Durham E-Theses

The location and kinematics of the emission line regions in Active Galactic Nuclei

Mullaney, J.R.

How to cite:

Mullaney, J.R. (2008) *The location and kinematics of the emission line regions in Active Galactic Nuclei*, Durham theses, Durham University. Available at Durham E-Theses Online: http://etheses.dur.ac.uk/2250/

Use policy

The full-text may be used and/or reproduced, and given to third parties in any format or medium, without prior permission or charge, for personal research or study, educational, or not-for-profit purposes provided that:

- a full bibliographic reference is made to the original source
- a link is made to the metadata record in Durham E-Theses
- the full-text is not changed in any way

The full-text must not be sold in any format or medium without the formal permission of the copyright holders.

Please consult the full Durham E-Theses policy for further details.

Academic Support Office, Durham University, University Office, Old Elvet, Durham DH1 3HP
e-mail: e-theses.admin@dur.ac.uk Tel: +44 0191 334 6107
http://etheses.dur.ac.uk

The location and kinematics of the emission line regions in AGN

J. R. Mullaney

Abstract

This thesis contains the results from a study of the optical emission lines of various samples of active galactic nuclei (AGN). We have used three separate techniques to determine the precise kinematics and the relative location of the emission line regions of AGN: a detailed study of a small sample (10) of AGN, a study of the general emission line properties of two larger samples, and the interpretation of the results from observations using numeric photoionisation models.

Although we present results on both the broad line and narrow line regions of AGN the main drive behind this work is the study of the poorly defined intermediate line region using emission from highly ionised species (high ionisation emission lines). Our results derived from observations indicate that a significant proportion of the emission from these species is produced within the central void of the putative dusty torus and that emission from more highly ionised species increases at radii closer to the central engine of the AGN. Furthermore, we find strong evidence that the intermediate region traced by these high ionisation emission lines is generally outflowing from the central engine but there is little evidence of any significant acceleration or deceleration of this material between the inner and outer regions traced by the higher and lower ionisation lines, respectively. Our results derived from numerical photoionisation codes support a model in which this outflowing material responsible for the high ionisation line emission is launched from the inner edge of the the dusty torus.

To Lilian Rodgers,
whose belief in the importance of
education never faltered.

Acknowledgements

None of what follows could have been achieved without the constant support of my supervisor, Prof. Martin Ward. I owe him a huge debt of gratitude for not turning away this ex-accountant when I turned up at his office door three and a half years ago. I would also like to thank Prof. Chris Done for the considerable insight she provided at various stages throughout my studies at Durham, and the particularly useful advice she gave regarding writing up; chocolate really does help a lot! Unfortunately, the helpfulness and approachability of every member of staff in the astronomy department at Durham University means that I am unable to thank everyone that supported me during these past 3 years. However, there are a couple whom I would particularly like to thank by name: Dr. Dave Alexander for providing me with plenty of advice and assistance, plus the incentive of a pay cheque to help me to finish (almost) on time, and Dr. Tim Roberts for joining me on my first observing run to the *WHT* on *La Palma* and surviving both an earthquake and a truly awful flight home with me.

I am indebted to my office mate of two years, Dr. Jonathan Gelbord, not only for putting up with my grumpy demeanour on occasion, but also for his lessons on statistics, without which this thesis would have been impossible to write. Whilst on the subject, I would like to thank Dr. Nick Schurch for rescuing my first paper from the brink of rejection with his statistical arguments.

My time at Durham would have been a lot less enjoyable had it not been for the presence of a large number of other Ph.D. students and post-docs. In particular, I would like to mention Mark Norris, Nick Ross, Tim Rawle, Bret Lehmer, John Stott, Craig Booth, Andy Goulding, Julie Wardlow, Rich Bielby, Jim Geach, Dave Wake, Rob Crain and Greg Davies for keeping me sane throughout this experience. A special mention must go to lovely Lynn for keeping my feet firmly on the ground by being the only *compos mentis* person in the department!

There's not many authors who are able to thank one-third of their readership personally: Mam, Dad thank you for all your support during the whole of my academic career. It's now time for me to get a real job (or at least one that involves paying income tax).

Finally, I would like to express my sincerest gratitude to Natalie. You, more than anyone else, have maintained my happiness throughout this endeavour. You will always be the most precious star in my Universe.

Declaration

The work described in this thesis was undertaken between 2005 and 2008 while the author was a research student under the supervision of Prof. Martin Ward in the Department of Physics at the University of Durham. This work has not been submitted for any other degree at the University of Durham or any other University.

Chapter 2 of this thesis has been published in the form of a paper:

- **Mullaney, J. R. & Ward, M. J.**, 2008, *Optical emission-line properties of narrow-line Seyfert 1 galaxies and comparison active galactic nuclei*, *Monthly Notices of the Royal Astronomical Society*, Volume 385, Issue 1, pp. 53-74.

The results of the line fitting routine described in chapter 3 has been submitted to *Monthly Notices of the Royal Astronomical Society* as Gelbord, Mullaney & Ward.

The last section of chapter 3 will form part of a *Letter* that is to be submitted to *Monthly Notices of the Royal Astronomical Society* as Ward, Mullaney & Gelbord.

The second half of chapter 5 is to be published in *Monthly Notices of the Royal Astronomical Society* as Mullaney, Ferland, Done, Ward and Schurch.

Part of this thesis is based on the results of two observation runs I performed during the 3 years of postgraduate study. The first, in October 2006, was performed at the *William Herschel Telescope* situated on the island of *La Palma, Spain*. The second, in January 2007, was based at the *Infrared Telescope Facility* on *Hawaii*.

The work described in chapters 2, 3, 4 and 5 was performed in collaboration with others. All text, excluding the discussion on the anomalous object in section 3.7, was written by myself. My contribution to section 3.7 involved the reduction of the raw spectrum taken by *ISIS* on the William Herschel Telescope (WHT) and the measurement of the emission lines in the SDSS and WHT spectra.

Chapter 2 is based on the results of an observing run initially proposed by my supervisor, Prof. M. Ward, with all data reduction and measurements performed by myself.

The procedures used to establish that Gaussian fits were preferable to Lorentzian fits described in 2.2.6 was initially suggested to me by Dr. N. Schurch, but all analysis was performed by myself.

The fitting routines described in chapters 3 and 4 were written by myself. Dr. J. Gelbord provided me with the samples obtained from the SDSS database and suggested ways to improve the fitting routine.

Prof. G. Ferland assisted me in both the implementation of the Cloudy routines described in chapter 5. He also suggested the decomposition of the emission lines into similar components to aide interpretation of the results produced by Cloudy. Prof. C. Done and Prof. M. Ward helped in the physical interpretation of the results provided by the models described in that chapter.

The copyright of this thesis rests with the author. No quotation from it should be published without prior written consent and information derived from it should be acknowledged

The location and kinematics of the emission line regions in Active Galactic Nuclei

by J. R. Mullaney

A thesis submitted to the University of Durham
in accordance with the regulations for
admittance to the Degree of Doctor of Philosophy.

Department of Physics
University of Durham
October 2008

The copyright of this thesis rests with the author or the university to which it was submitted. No quotation from it, or information derived from it may be published without the prior written consent of the author or university, and any information derived from it should be acknowledged.

17 APR 2009

Contents

List of Figures

List of Tables

Chapter 1 | *Introduction*

1.1 History

When, in 1908, E. A. Fath published the first spectrum of the nucleus of the (then-classified) spiral nebula, *NGC 1068* (described in Fath 1908), he began one of the most important lines of study in astronomy of the last 100 years. On inspection of the photographic plates onto which the image of the spectrum had been transferred, Fath noted that the emission from the nuclear region of this spiral nebula appeared distinctly different from the others in his sample. Included among the familiar absorption lines typical of other objects of this morphological type were strong *emission* lines.

During the years directly following the first discovery of this "emission line nebula", a small number of objects were added to this category, but the archives show no concerted effort to study them in any depth until C. K. Seyfert's seminal work (Seyfert 1943). His study of six of the nuclei of the brightest emission nebulae (which were, by then, known to be extragalactic) revealed that the emission lines in some of these objects were significantly broader than those observed in the "emission knots" in the periphery of other extragalactic nebulae- up to 8500 km s^{-1} full width zero intensity (FWZI). It is due to this study that these and similar objects came to be known as Seyfert galaxies (abbreviated to Sy).

Later, with the appreciation that these extragalactic nebulae were galaxies external to our own, it became evident that the nuclei of these emission line nebulae were highly luminous; it is not uncommon for the point-like nucleus of a Seyfert galaxy to have approximately the same luminosity as the host galaxy's combined stellar population (see Fig. 1.1). The fact that this nucleus is unresolved in even the most nearby Seyfert galaxies implies that there is an extremely large amount of activity within the central 100pc of these objects- hence the umbrella term 'active galactic nuclei' (AGN) for this class of object.

Although the evidence for the separation of Seyfert galaxies into two distinct sub-

DURHAM UNIVERSITY

Figure 1.1: Seyfert 1 galaxy, *NGC 5548* (left) plotted alongside an image of the non-active galaxy *NGC 3277*. Both galaxies are similar face on spirals that have been exposed for approximately the same period (500s and 600s, respectively) using the same instrument on the *Hubble Space Telescope*. The strong flux emitted by the AGN in the centre of *NGC 5548* has saturated the detector.

classes was present in Seyfert's early work, Khachikian and Weedman (1974) were the first to point out that these galaxies could be further categorised in terms of the profiles of the Hydrogen emission lines. In type 1 Seyfert objects (Sy1s) the hydrogen lines consist of a broad base which often has a superimposed narrow 'core', whereas in type 2s (Sy2s) only the narrow core is present (see Fig. 1.2). This sub-classification was to have important ramifications for the unification of the subcategories of active galaxies and the development of the standard model of AGN (see later).

It is a quirk of history that, as those key early studies of AGN in the optical wavebands were taking place, the development of radio astronomy was enabling astronomers to independently detect AGN without the acknowledgement that these objects were related (see Weedman 1976 for a review). During the 1950s, radio surveys of the sky were finding strong sources that could be identified as the radio counterparts of objects found in optical surveys and/or pointed observations. Although it was realised that some of these objects were associated with resolved extragalactic sources[1], a large number were found to have an almost star-like appearance when studied in optical wavelengths. This

[1]Of particular interest is that some of these resolved objects were, indeed, known Seyfert galaxies that had already been identified as having peculiar nuclear spectra, although little was made of this at the time.

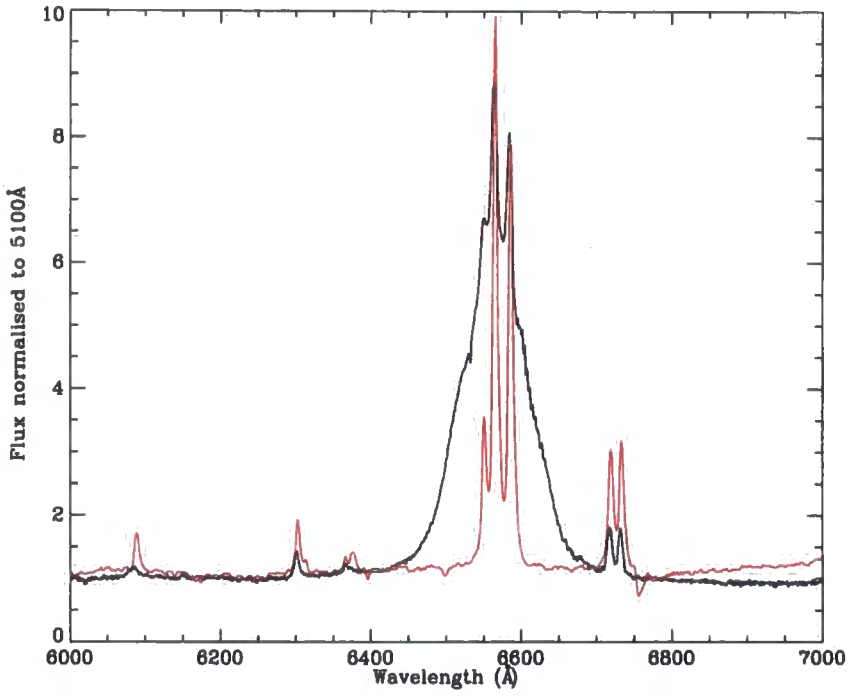

Figure 1.2: The Hα emission line of the Sy2 AGN *Mrk 573* (red) superimposed onto the Hα line of the Sy1, *NGC 985* (black). In both spectra, the narrow Hα core is bounded by the narrow [N II]$\lambda\lambda$6548,6584 lines, however, in the case of *NGC 985*, the broad base of the Hα extends well beyond these neighbouring lines.

led to these objects becoming known as quasi-stellar objects, shortened to "quasars". It wasn't until Schmidt (1963) recognised the very broad optical emission lines in the radio source *3C 273* as the hydrogen Balmer lines that the realisation dawned that these objects were the most distant objects yet to be discovered and, in turn, the brightest individual objects in the Universe yet observed at that time. So bright, in fact, that the nuclei of these objects far outshine their host galaxies' stellar populations.

It is beyond the scope of this brief history of the study of AGN to delve into the debate that surrounded the interpretation of the evidence associated with the study of quasars (i.e. the redshift controversy; see Weedman 1976) . It is sufficient to say that by the end of the 1970s, the large number of studies of Seyfert galaxies and quasars had shown that the earliest discovered Seyferts and quasars were, in fact, situated at opposing ends of a continuous scale of AGN luminosity.

With the development of electronic detectors and space based telescopes capable of observing the Universe from radio, through infra-red and optical wavelengths to X-ray and γ-ray energies, it became evident that AGN were powerful emitters across the full

electromagnetic spectrum. In particular, with the dawn of UV and X-ray astronomy, it became clear that AGN were strong emitters of high energy photons (i.e. wavelengths shorter than the optical bands). In fact, Elvis et al. (1978) showed that a common theme among type 1 AGN is their strong X-ray emission. Today, it is possible to plot the energy output of an AGN as a function of photon wavelength across more than ten decades of the electromagnetic spectrum, from the radio to γ-ray energies, as is shown in Fig. 1.3. These *spectral energy distributions* (hereafter SED) provide the evidence that all AGN are prodigious emitters of electromagnetic radiation, the total bolometric flux of which can far outstrip that of the combined output of all the stars in the host galaxy.

It is now accepted that the same underlying process, albeit with a considerable amount of variation in detail between objects, is at the heart of all AGN, producing the extreme luminosities, strong radio-to-X-ray emission and the broad emission line profiles. We will cover the details of this process in a later section. In the following section, however, we will give a brief introduction to the physics behind the production of emission lines in AGN.

1.2 Emission lines of AGN

We have already seen how the study of emission lines has played an important role in the discovery and classification of AGN. Produced by the release of photons as electrons fall from higher to lower atomic energy states, emission lines provide a wealth of information regarding the physical conditions of the atoms that produce them. Throughout this thesis, we will predominantly use the emission line spectra of AGN to deduce the kinematics and the relative location of the emitting gas.

Emission lines from astronomical sources typically fall into one of three different categories- permitted, forbidden and semi-forbidden. The fundamental differences between these categories are firmly rooted in the discipline of quantum mechanics, and as such we will not venture into a discussion into the causes of these differences. It is suffice to say that the type of lines that a given cloud of gas can produce is largely dependent on its density. While permitted lines can be produced in both high (electron density, $n_e \gtrsim 10^8 \mathrm{cm}^{-3}$) and low density clouds, only low density clouds ($n_e \lesssim 10^4 \mathrm{cm}^{-3}$) are capable of producing forbidden lines. The precise maximum density, however, is dependent on the forbidden line of interest. As the name suggests, semi-forbidden lines can be produced in somewhat higher density clouds than forbidden lines, but which are still significantly

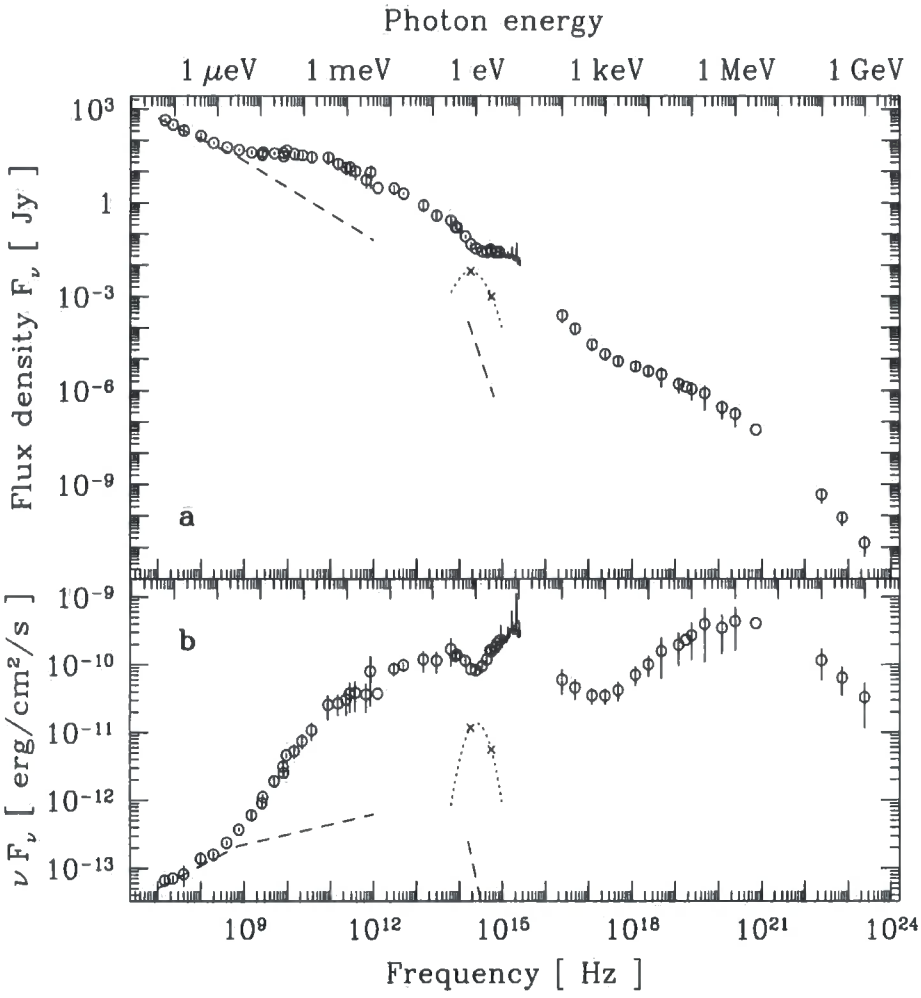

Figure 1.3: The average spectral energy distribution of the quasar, *3C 273* (taken from Türler et al. 1999). The upper plot (labelled (a)) shows the variation in flux density as a function of frequency and the lower plot (labelled (b)) shows the νF_ν representation. The lower plot gives a better representation of the *power* emitted as a function of frequency. The dashed line shows the contribution from the jet and the dotted curve shows the contribution from the host galaxy. Compared against starlight, the AGN emission is much more extended in frequency space.

less dense than permitted line clouds.

Of course, the relative strengths of the emission lines in a given spectrum will depend on many more parameters than simply the density of the emitting clouds. Clearly, the elemental abundances of a gas cloud will have a strong effect on the whether a given line can be produced. Furthermore, the ionisation state of that same cloud will have a strong influence on its emission line spectrum as energy level transitions within an atom are heavily dependent on its electron configuration. Even the temperature of an emitting region can be deduced by the careful measurement of a select few lines in its emission spectrum.

As emission lines are the result of the transition of atoms between quantised energy states, a given transition releases a photon with a very precise energy (or wavelength, or frequency, as all three are directly related). However, we have already seen that the emission lines observed in AGN are not detected at a single wavelength. Instead, they often have very broad profiles and are sometimes observed to be multi-peaked. These complications are introduced by the relative motions of emitting gas Doppler shifting the emitted photons to longer or shorter wavelengths as viewed by an observer. With this in mind, we can use precise measurements of the profiles of these emission lines to get a thorough understanding of the relative motions of the emitting gas clouds around AGN.

1.3 AGN Taxonomy, Unification and the Standard AGN Model

It was just over a decade after the discovery that AGN could be easily categorised on the profiles of their emission lines before it became clear that the properties of both types (1 & 2) could explained as different manifestations of the same object. Evidence for this "unification of AGN" came with the discovery that, when observed in polarised (reflected) light, the quintessential Seyfert 2 galaxy, *NGC 1068* (one of Seyfert's original six), showed evidence of having broad hydrogen lines- exactly as observed in type 1 AGN (Antonucci and Miller 1985). Based on this evidence a model was proposed in which the region responsible for the broad emission lines (broad line region or BLR) is located deep within the central regions of a heavily obscuring torus, whereas the region responsible for the narrow lines (narrow line region or NLR) seen in the spectra of both type 1 & type 2 AGN is extended outside this obscuring feature. In type 1 objects we have a clear line of sight into the central 'hole' to the BLR, whereas in type 2 objects we

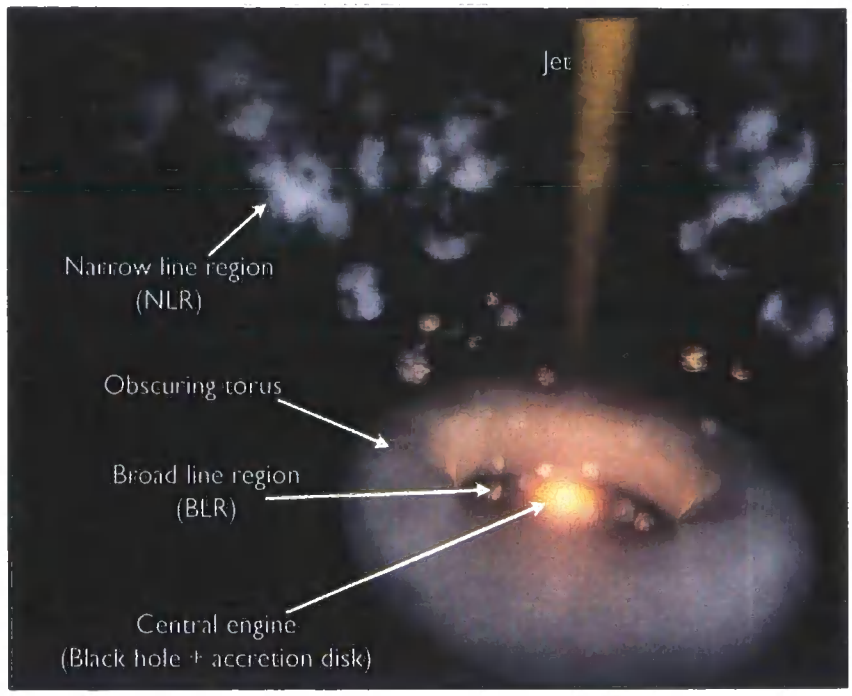

Figure 1.4: The standard (or unified) model of AGN. Printed with the kind permission of R. Smith and G. Collinson.

may only see this region indirectly by means of reflection (see fig. 1.4).

Being the more extended of the two, much more is known of the the NLR of AGN than the BLR. In some of the most local AGN this region has even been resolved and mapped with narrow band images (e.g. Tadhunter and Tsvetanov 1989, Wilson et al. 1993; see also Fig. 1.5). We therefore know that the spatial extent of this region can to up to 10s of kpc and represents the outer limits of the region in which central engine is the dominant source of ionising radiation. The wealth of forbidden lines in the optical wavebands from this region has enabled its physical properties to be determined in a large number of AGN. These emission line diagnostics tell us that the density and temperature of the NLR are of the order of $n_e \sim 10^{2-4}\mathrm{cm}^{-3}$ and $T \sim 10,000 - 25,000\mathrm{K}$ (Koski 1978). Combining these values with a filling factor of $\epsilon \sim 10^{-2}$ (i.e. the fraction of the overall volume of the NLR responsible for the emission) derived from the total luminosity of the NLR emission lines gives a typical mass of the NLR of $10^{5-6}\mathrm{M}_{\odot}$ (Peterson 1997).

In contrast to the extended nature of the narrow line region, the broad line region of AGN is known to be very compact and is unresolved in even the highest spatial resolution observations of the most local type 1 AGN. The best estimates we have of the spatial

extent of this region is based on reverberation mapping techniques, which rely on flux variations in the ionising continuum being 'echoed' in the broad emission lines. Due to the finite speed of light the delay of this light echo provides a direct measurement of the size of the region emitting the measured broad line (for a review of this work see Peterson 1994). Based on this technique, we now know that the BLR typically extends over just a few light days. However, despite its small size, this region is capable of producing highly luminous emission lines that can, in many type 1 spectra, outshine the total line emission from the (vastly more extended) NLR. This is testament to the high densities of the emitting clouds that form the BLR. We have already seen that only the permitted emission lines are broadened in type 1 spectra which implies that all the forbidden lines are collisionally suppressed. For this to be the case the clouds that make up the BLR must have densities of $10^{11}\mathrm{cm}^{-3}$ (Ferland et al. 1992). When one considers that the emissivity (energy emitted per unit volume per unit solid angle) of a line emitting cloud increases as a function of density *squared*, it is easy to see how such a small volume of gas can produce the vast amount of emission observed in type 1 AGN.

The simple model outlined above simultaneously explains both the appearance of AGN spectra and unifies two apparently disparate types of object into one. Its long-standing influence on AGN research over more than a decade means today almost all new models of the inner regions of AGN are refinements or advancement on this standard model. However, as explained out in the review article, Tadhunter (2008), it is likely that the model described here is a severe oversimplification of the true situation. Increasingly sensitive observations of AGN are now giving us a much more complicated picture their physical properties, one that includes (for example) variability, cloud dynamics and feedback with their host galaxies.

As currently presented, the model described above does not explain the most fundamental of all questions surrounding AGN – the source of the tremendous power at the heart of these objects. A remarkably accurate early insight into the source of the AGN's power is that given by Salpeter (1964). As it was known that a quasar's power was produced in a region "of relatively small size" [sic], he utilised the gravitational energy released as matter falls onto a compact body to theorise that such an infall onto a black hole of mass $10^8\mathrm{M}_\odot$ could produce the luminosities of the order of that produced by quasars and (although unknowingly at the time) other AGN (i.e. Seyfert galaxies). Despite its success in explaining the observed AGN luminosities from the unresolved centres of galaxies, it took a number of decades before the other major competing physi-

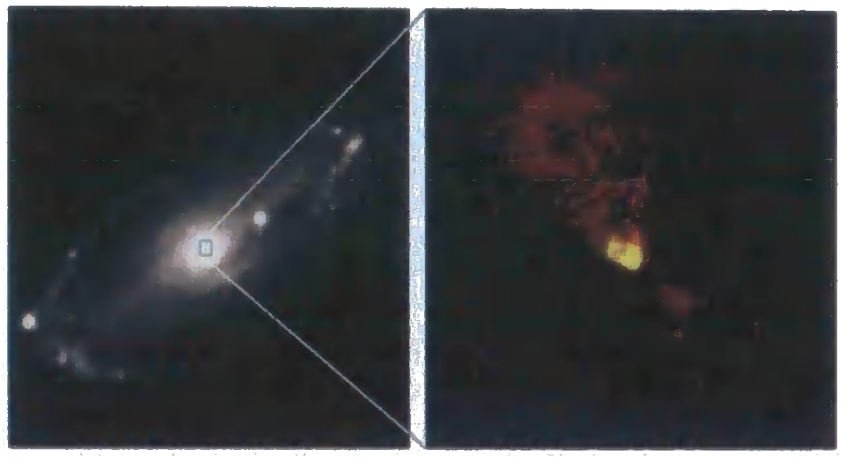

Figure 1.5: Left: Ground based image of the spiral galaxy *NGC 5728* which hosts a type 2 AGN. Right: *HST* image of the central regions of this AGN clearly showing the extended narrow line region ([O III]λ4959,5007 emission) illuminated by the strong ionising continuum of the obscured central engine. The overall extent of the [O III]λ4959,5007 emitting region is 1.8kpc (Wilson et al. (1993)). Image taken from STSci web pages.

cal model of AGN, that of the starbursts/supernovae (e.g. Terlevich and Melnick 1985), was abandoned and evidence supporting the presence of supermassive black holes in both active and non-active galaxies grew. Today, results from numerous independent techniques (e.g. reverberation mapping, stellar velocity dispersion) support the view that the central engine of the vast majority, if not all, AGN takes the form of an accretion disk converting gravitational potential energy into thermal energy and finally electromagnetic radiation as it falls onto the surface of a supermassive black hole. Studies using the reverberation mapping of the BLR and kinematics of the stellar component of active and non-active AGN (e.g. Gebhardt et al. 2000b and Gebhardt et al. 2000a) have shown that most, if not all, large galaxies contain supermassive black holes in their centres. It is therefore possible that all galaxies have gone through, or have the potential to go through, an active stage at some point during their evolution (e.g. Kormendy and Richstone 1995). This raises the question of the 'duty cycles' of AGN (the length of time that a given supermassive black hole will actively accrete and therefore appear as an AGN) and the processes that cause these objects to switch on and off. It has been argued that evidence of the duty cycles of AGN is present in the appearance of the radio 'bubbles' in the nearby radio galaxy *M87*- interpreted as showing that this galaxy has

Figure 1.6: Radio jets emitted by the quasar 3C175. The radio structure shown here is approximately 200kpc across. Image courtesy of NRAO/AUI.

been more active in the past (Churazov et al. 2001). Key to the study of the duty cycles of AGN is the source of their fuel; supermassive black holes may only become active if they have access to a reservoir of matter to accrete – a limited amount of fuel will lead directly to the apparent duty cycles. There is now strong evidence from observations of quasars that interactions between galaxies provide a means of supplying supermassive black holes with the material required to become active (e.g. Bahcall et al. 1997).

1.4 The importance of kinematics in AGN

We saw in the previous sections how studies of the internal kinematics of AGN have played an important role in their discovery (i.e. their strong, *broad* emission lines), in the interpretation of their spectra in terms of a basic standard model (i.e. incorporating broad and narrow line regions), and in the development of a theory to explain their immense luminosities (i.e. the *infall* of material onto a supermassive black hole). However, there is strong evidence of an additional form of kinematics in AGN that we have yet to mention but which forms a common theme throughout this thesis: that of *outflows*.

Outflows on the kiloparsec scale have been studied in AGN for over three decades

(for an early review see Bridle and Perley 1984). Dramatic radio images showing jets and lobes associated with AGN are direct evidence that these objects are capable of launching material from their energetic cores at relativistic velocities (see Fig. 1.6). Despite their dramatic appearance, objects with associated radio jets and lobes are relatively rare (constituting around 10% of the total quasar population, and an even smaller fraction of the low luminosity AGN population), however, there is evidence that outflows play an important role at much smaller scales in *all* AGN.

Evidence of outflows on much smaller scales than the extended radio jets and lobes have been detected in virtually all parts of the observable spectrum. In the X-ray and U.V. bands strong, blueshifted absorption lines[2] have been detected in the spectra of many AGN (e.g. Crenshaw et al. 2003). Although a range of blueshifts are detected in even a single object, typical values of this shift lie within the range of 1,000km s^{-1}-10,000km s^{-1}. Furthermore, as these lines are known to vary in both strength and velocity shift, it is evident that the material responsible for them passes in and out of our line of sight to the central object. Because absorption lines are formed by the presence of intercepting material, their blueshifts can be readily interpreted as evidence that the absorbing clouds are outflowing toward us from the source of continuum radiation.

In the optical and near infrared wavebands evidence of outflows emerges in the form of blueshifted, or blueshifted *components* of, emission lines. For example, it has been known for over two decades that the profiles of the strong forbidden [O III]λ4959,5007 lines show evidence of a blue *wing* in many type 1 (and some type 2) objects (e.g. Heckman et al. 1981; see Fig. 4.1 for an example of an [O III]λ5007 line that shows clear evidence of a blue wing). Evidence of outflows has also been detected in the broad line region: Morris and Ward (1989) detected asymmetries in the line profiles of the permitted O Iλ8446 line which they argue could be produced by radial outflows from the nucleus. Unfortunately, the blueshifting of emission lines does not directly imply the presence of an outflow. Unlike in the case of absorption lines, in which the absorbing material *must* lie between us and the continuum source, emission lines are produced isotropically. The question therefore arises why we should only observe blueshifted lines from the outflows (i.e. those coming toward us) rather than *both* blueshifted and redshifted lines from outflows on the near-side and far-side of the central engine (see Fig. 1.7). Tra-

[2]Contrary to emission lines, absorption lines are produced by clouds of gas intercepting our line of sight to a source of radiation. However, just as emission clouds *produce* photons of specific wavelength, absorption clouds remove photons of a specific wavelength from an underlying continuous spectrum.

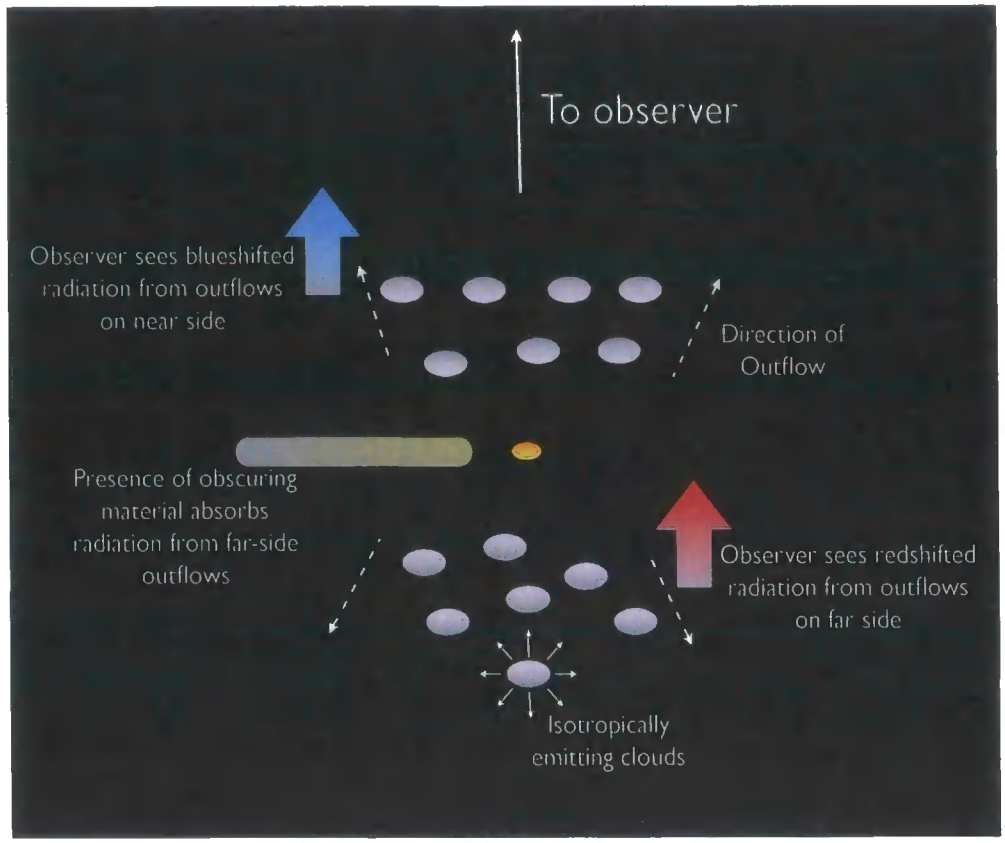

Figure 1.7: Without the presence of obscuring material, we should observe outflows on both the far and near sides of the central engine.

ditionally, this problem has been resolved by the assumption that obscuration must play an important role in dictating which 'side' of the outflow we can observe (e.g. Heckman et al. 1981). We have already seen that obscuration by the so-called 'dusty torus' plays an important role in how we perceive and categorise a given AGN. With this in mind, these obscuration effects mean we will preferentially observe emission arising from the near-side of the AGN than the far side. Therefore, blueshifts in the emission lines have typically been interpreted in terms of arising from outflowing material between us and the central engine of the AGN. Throughout this thesis we rely on this assumption to interpret the blueshift of emission lines as outflows.

As our ability to study the finer details of AGN spectra has improved with increasingly sophisticated instruments and telescopes, evidence of outflows in AGN has increased. It is therefore not unreasonable to consider that outflows are present (at some level) in the majority, if not all, AGN (whether in the form of relativistic radio jets, or more slowly moving winds detected in the NIR-X-ray wavebands). The ubiquity of outflows in AGN suggests they play an important role in the processes at the heart of these

objects- transporting matter around their central regions and aiding feedback processes (i.e. self-regulation) that could effect the evolution of AGN and their host galaxies.

1.5 Forbidden, high ionisation lines

The majority of the work within this thesis focusses on the study of forbidden, high ionisation lines (abbreviated to *FHILs*). As implied by their name these emission lines are produced by species of particularly high ionisation potentials ($\gtrsim$100eV) implying their production is limited to high energy astrophysical processes. Although these lines were first identified in the solar corona, in which they are produced by collisional processes, rather than photoionisation (hence their alternative name, coronal lines), our studies are focussed on the formation of these lines by the strong, highly ionising continuum radiation of AGN.

Although *FHIL* emission had been *detected* in the spectra of AGN at a relatively early period in the history of the study of these objects (unpublished, O.C. Wilson, circa. 1956), it took another decade before these lines were actually *identified* by Oke and Sargent (1968). Despite their early detection and identification it took another 16 years before the first concerted study of *FHILs* in more than a handful of objects was performed by Penston et al. (1984). In that work the authors showed that there existed a positive correlation between the [Fe VII]λ6087, [Fe X]λ6374 and [Fe XI]λ7892 *FHIL* strengths and other prominent optical emission lines (e.g. [O III]λ6300 and Hβ) in a sample of 29 *FHIL* emitting AGN. This supported the view that these lines are produced by photoionisation due to the strong high energy radiation from the AGN, rather than by collisional excitation (although the authors stressed that this latter mechanism could not be entirely ruled out at that time). It was also noted in that same study that the optical *FHILs* tend to be blueshifted with respect to the systematic velocity of the galaxy. Although this shift had earlier been detected in the [Fe XI] lines of a small sample of 13 bright Seyfert galaxies (e.g. Grandi 1978), Penston et al. (1984) showed that this blueshifting was typical to a much larger sample of *FHIL* emitting AGN.

With the availability of X-ray data from the *ROSAT* satellite, Erkens et al. (1997) (15 objects) and Porquet et al. (1999) (24 objects) were able to show that *FHIL* luminosities were positively correlated with the 0.1-2.4keV flux and that they were preferentially produced in AGN with a soft excess (i.e. the soft X-ray flux below $\sim$1keV rises above the apparently underlying power law extrapolated from higher X-ray energies; see chapter

5), which further reinforced the opinion that the *FHILs* were produced by photoinisation. Indeed, studies by Fosbury and Sansom (1983) and Osterbrock (1981) of the individual objects *Tololo 0109-383* and *III ZW 77*, respectively, use [Fe VII]$\lambda\lambda$3758,5158,6087 line diagnostics to show that the region responsible for at least this *FHIL* has a temperature indicative of photoionisation ($T \lesssim$40,000K), rather than $T \gtrsim$100,000K expected from collisional ionisation. Unfortunately, no similar diagnostics have been performed for the [Fe X] or [Fe XI] lines (indeed, in the case of the [Fe X] line this analysis is impossible, due to the lack of emission line diagnostics for this species).

1.6 Narrow Line Seyfert 1s

In the preceding sections, we have focussed our discussion of AGN around type 1s and type 2s. We have seen that type 1s have broad permitted lines (often with a narrow core superimposed onto the broad base), whereas type 2s have permitted lines that are just as broad as the forbidden lines. The widths of the permitted lines in type 1s are now known to vary considerably from object to object – typically having FWHM within the range of 500km s^{-1} to 10,000km s^{-1} (but objects with FWHM>30,000km s^{-1} have been discovered). Throughout this thesis we put some emphasis on the study of type 1 objects with permitted lines widths toward the low end of this range – known as narrow line Seyfert 1s (NLS1s). With this in mind, in the following paragraphs we provide a brief introduction to this particular class of AGN.

NLS1 galaxies are a sub-set of the AGN population which share a number of characteristic properties (Pogge, 2000). Superficially, their optical spectra resemble those of type 2s in that their permitted emission lines are quite narrow and only marginally wider than their forbidden lines - a property that has unfortunately led to numerous misidentifications as Sy2s in the literature (see Fig. 1.8). However, Osterbrock and Pogge (1985) noted that their strong permitted Fe II lines and high Hβ/[O III]λ5007 ratios were similar to the traditional type 1s. Although the velocity widths of the permitted lines in AGN spectra are observed to cover a continuous range, Goodrich (1989) placed a somewhat arbitrary limit of to the FWHM of Hβ of 2,000 km s^{-1} for an object to be classed as a NLS1. Since then, most studies have continued to use this value as the boundary between NLS1s and their broad line counterparts, here referred to as broad line Seyferts, or BLS1s, in order to distinguish them from NLS1s.

Studies of the continuum emission from NLS1 revealed interesting features across

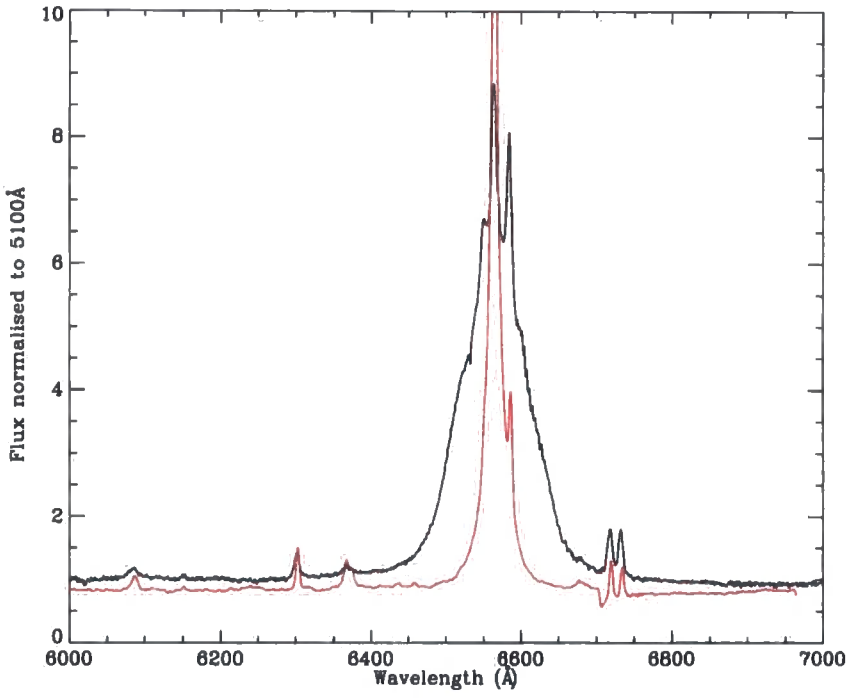

Figure 1.8: The Hα emission line of the NLS1 AGN *Ark 564* (red) superimposed onto the Hα line of the Sy1, *NGC 985* (black). Note the significantly narrower Hα line of the NLS1s, yet there is still clear signs of a broad base, unlike in the case of *Mrk 573* shown in fig 1.2.

the electromagnetic spectrum, for example, significant soft X-ray excesses, rapid X-ray variability and strong emission from FHILs (e.g. Stephens 1989; Puchnarewicz et al. 1992; Pogge 2000). Their X-ray properties encouraged searches using X-ray surveys with follow-up confirmation from optical spectroscopy. This showed that around 50% of all *ROSAT* soft X-ray selected AGN were NLS1s (Grupe et al. 1994; Pogge 2000). It should be noted, however, that this method introduces serious selection effects, since Boller et al. (1996) found that not all NLS1s display strong soft X-ray excesses.

The features described above, in particular the rapid X-ray variability and lack of highly broadened permitted emission lines, has led to speculation that NLS1s may harbour a lower mass central black hole than is typical in BLS1s ($10^{7-8}M_{\odot}$ and $10^{8-9}M_{\odot}$, respectively; e.g. Mathur et al. 2001). The maximum energy an accreting system can radiate is equal to the kinetic energy of the infalling matter, $GM\dot{m}/R_S$; where G is the gravitational constant, M is the mass of the black hole, $\dot{m}$ is the rate that matter falls onto the black hole and R_S is the Schwarzschild radius of the black hole. Therefore, if NLS1s harbour lower mass black holes than is typical in 'normal' Seyfert galaxies, their comparable bolometric luminosities imply a higher accretion rate. Indeed, it is possible that

NLS1s reach Eddington (or super-Eddington) luminosities (L_{Edd}) in which the inward gravitational force is balanced by the outward pressure imparted by the photons (radiated from the accretion process itself) on the accreting material[3]. It has been suggested (e.g. McHardy et al. 2006) that the key parameter in determining the distinctive physical properties of this class is their high ratio of L/L_{Edd} (which can be simplified to $\dot{m}/m$). Indeed high luminosity AGN which do not fulfil the velocity width criterion of NLS1s (i.e. <2,000km/s), but share many of their other characteristics, are also thought to have high $\dot{m}/m$, e.g. PDS456 (Reeves et al. 2003), consistent with the model of McHardy et al. (2006). It is partly for this reason that NLS1s have attracted much interest. In addition, we can potentially test the full extent of the relationships between observable parameters that have been established for the more general AGN population, such as relations between black hole mass and stellar bulge luminosity and velocity dispersion (see e.g. Ferrarese and Merritt 2000; Gebhardt et al. 2000a). Also, evidence of some of the more dramatic features of AGN activity, in particular relativistic and non-relativistic outflows, is sometimes prominent in NLS1 spectra (e.g. Leighly 2001; Leighly and Moore 2004), although it is unclear whether this is an indication of a real propensity toward outflows in NLS1s, or whether other spectral features simply allow these features to be more easily measured in these AGN. This has encouraged their study as laboratories for some phenomena present in general in AGN, but exhibited in a more extreme form in the NLS1s.

1.7 This thesis

In the chapters that follow, we describe the various techniques we employed to advance our knowledge of the relative locations and kinematics of the various emission line regions mentioned above. In particular, we have focussed our attention on constraining the (as yet poorly studied) properties of the *FHIL* emitting region. In the next chapter, we discuss the analysis and results obtained from a detailed study of a small sample of AGN observed with the *ISIS* spectrometer on the 4.2m William Herschel telescope, La Palma. In chapters 3 and 4 we describe the results obtained from a systematic search of the *SDSS* database for strong *FHIL* emitting objects. We describe the results of our work with photoionisation models of the *FHIL* emitting regions in chapter 5. Finally, we

[3]The situation described here is for the simple case of spherical accretion system, super-Eddington systems can arise by the formation of an accretion disk.

summarise our main findings and discuss possible future work in chapter 6.

Chapter 2

Forbidden, High Ionisation Line Profiles[1]

2.1 Introduction

The optical spectra of NLS1 provide a wealth of information. The large number of permitted and forbidden lines give information on the kinematics and physical properties of the various emitting regions, as well as the shape of the (unobscured) ionising continuum emitted by the central engine. For example, Dietrich et al. (2005) compared the low ionisation (<100eV) emission lines of NLS1 to show that the far-UV continuum of NLS1 was not significantly different from that of BLS1s, thereby indicating that the soft X-ray excess, seen in many NLS1s, is unlikely to extend to significantly lower energies approaching 100eV. However the true extent of this continuum feature, which is likely to contribute a significant fraction of the bolometric luminosity in a large proportion of NLS1s, is still unknown.

With ionisation potentials greater than 100eV, *FHILs* offer the possibility of determining the true shape of the soft X-ray excess. Previous studies of the optical *FHILs* in NLS1s, most notably [Fe VII]λ6087 (ionisation energy: 99eV), [Fe X]λ6374 (235eV), [Fe XI]λ7892 (262eV) and [Fe XIV]λ5303 (361eV) noted that these lines were significantly blueshifted and broadened, with respect to the low-ionisation forbidden lines, suggesting the possibility of outflows between the traditional broad- and narrow- line regions (e.g. Ward and Morris 1984, Erkens et al. 1997; Porquet et al. 1999; Nagao et al. 2000). However, despite the fact they often display broad wings and have prominent profile asymmetries, little effort has been directed towards modelling the *FHILs* using multiple component fits. This could yield insights into the detailed kinematics of the highly ionised gas close to the AGN. The information gained from gas kinematics would help us to constrain the location of the *FHIL* emitting gas with respect to other emitting regions, and also help us

[1]Note: This chapter is based on the work published in Mullaney & Ward (2008)

obtain a better understanding of outflows from AGN.

In this chapter, we examine the optical emission line spectra of 10 nearby ($z < 0.1$) AGN at sufficiently high spectral resolution and signal to noise to permit us to model their *FHILs* using multiple components. Six of these AGN have previously been classified as NLS1s. We also observed three BLS1s to facilitate comparison between the Seyfert groups. In an attempt to determine whether the *FHILs* are affected by the obscuration of the putative dusty molecular torus, we also observed one Seyfert 2 galaxy, *Mrk 573*, which has been shown to contain a hidden broad line region by Nagao et al. (2004). The high S/N of our spectra facilitates the accurate definition of the both the continuum level and other emission lines that are blended with those of interest. This reduces the systematic errors that plague the measurement of weak emission lines such as the *FHILs* and weak He lines measured here. Furthermore the high quality of the spectra allows the parameterisation of the emission line profiles via the fitting of multiple Gaussian components (we discuss our choice of Gaussian components in section §2.2.6). We point out, however, that this *parameterisation* is precisely that; a convenient method by which to compare the profiles of the emission lines within a given object or between objects. When we discuss the FWHM and velocity components of the multiple components we do not wish to imply that the emitting regions of AGN are split into discrete components with well defined velocity structures. Indeed, each component represents the average of an amalgam of emitting clouds. With this in mind, the broadest components of each emission line is a measure of the most extreme kinematics present in the regions where that line is most effectively produced.

2.2 Observations

The ten AGN in our sample were observed using the *ISIS* long slit spectrograph on the William Herschel Telescope during the nights of the 17^{th} and 18^{th} of October 2006. Basic information on these objects is listed in Table 2.1. Both the red and blue arms of the *ISIS* instrument were used, with a 600 lines/mm grism in each case. The CCD detectors used were the EEV12 and the Marconi CCD in the blue and red arms respectively. In order to cover the wavelengths of all four principal optical *FHILs* ([Fe VII], [Fe X], [Fe XI], [Fe XIV]) using this instrument, it was necessary to observe each galaxy with two different grating angles in one of the arms. Based on previous studies of *FHILs* in NLS1 galaxies (Erkens et al. 1997), it was apparent that the [Fe XIV]λ5303 line was likely to be the

weakest species of those observed. For this reason this line was observed twice using the blue arm, whilst the grating angle in the red arm was initially set for the measurement of the [Fe VII]λ6087 and [Fe X]λ6374 species, followed by a grating angle change to allow measurement of the [Fe XI]λ7892 line at a longer wavelength. This procedure thus resulted in a longer integration time for the weaker [Fe XIV] line than for the other iron species. The choice of beam-splitting dichroic was based on the observed wavelengths of the *FHILs*. Objects with $z \leq 0.035$ were observed using the 5700Å dichroic, while objects of $z > 0.035$ were observed using the 6100Å dichroic. This choice ensured that the lines of most interest always lay in a wavelength region of high dichroic throughput. The instrumental set-up provided almost complete spectral coverage between 4800Å and 8900Å. In order to minimise the stellar contribution from the host galaxy we used a slit width of 0.5″, resulting in an instrumental spectral resolution of $R = \lambda/\Delta\lambda = c/\Delta v \approx 3500 - 5500$, depending on wavelength (equivalent to 85-55 km/s FWHM). Corresponding standard star and telluric dividing star frames were taken for each galaxy observation. Wavelength calibration frames were taken using a CuNe + CuAr arc lamp.

2.2.1 CCD Image Reduction

The raw CCD images first had the bias level subtracted, then they were flat fielded and trimmed using the *IRAF* set of image reduction software. A two dimensional dispersion correction and wavelength calibration function was derived from the calibration arc frames. This was applied to each science frame, again using standard *IRAF* routines. The quality of the wavelength calibration was checked and corrected where necessary using the sky emission lines identified by Osterbrock et al. (1996). To extract the 1D spectrum from the 2D image, an extraction routine was written using the IDL programming language. We initially collapsed the 2D image along the direction of dispersion in order to obtain an indication of the spatial profile of the object within the slit. This 'average' profile was then fitted with a single Gaussian. We then returned to the original 2D image and extracted the 1D spectrum by summing the contribution of each pixel within 2σ limits of the average Gaussian profile, thus ensuring the same extraction window was used along the spectrum. The underlying sky background was determined by extrapolation of the region between 3σ and 20σ either side of the object spectra. These spectra were then flux calibrated using the standard star observations and the *IRAF* routines *noao.onedspec.standard*, *noao.onedspec.sensfunc* and *noao.onedspec.calibrate*. An attempt was then made to correct for telluric absorption by the division of a normalised, continuum

Galaxy	Type	z	R.A.	Dec	Exposure Times (s)			Ref.
			(J2000)		Blue	Red/Short	Red/Long	
Ark 564	NLS1	0.0247	22:42:39.3	+29:43:31	1080	540	540	1
1H1934-063	NLS1	0.0106	19:37:33.0	-06:13:05	1800	900	900	1
IIZW136	NLS1	0.0633	21:32:27.8	+10:08:19	2400	1200	1200	2,3
IZW1	NLS1	0.0611	00:53:34.9	+12:41:36	2400	900	1200	4
Mrk 335	NLS1	0.0261	00:06:19.5	+20:12:10	1600	600	1000	1,6
Mrk 573	Sy2	0.0172	01:43:57.8	+02:21:00	1800	900	900	5
Mrk 618	NLS1	0.0354	04:36:22.2	-10:22:34	3000	1500	1500	6
NGC 985	Sy1	0.0432	02:34:37.8	-08:47:15	1800	1200	1600	7
NGC 7469	Sy1	0.0163	23:03:15.6	+08:52:26	900	450	450	8
VIIZW118	Sy1	0.0803	07:07:13.1	+64:35:59	4000	2000	2000	9

Table 2.1: AGN observed using *ISIS* on the WHT. Target co-ordinates taken from *NASA/IPAC Extragalactic Database.* Spectral classifications taken from: 1. Rodríguez-Ardila et al. (2002), 2. Boroson and Green (1992), 3.Constantin and Shields (2003), 4. Rudy et al. (2000), 5. *NASA/IPAC Extragalactic Database,* 6. Ryan et al. (2007), 7. de Vaucouleurs and de Vaucouleurs (1975) 8. Riffel et al. (2006) 9. Kunth and Sargent (1979). Redshifts measured from the [SII]$\lambda\lambda$6717/32 doublet (assumed to represent the systemic velocity of the galaxy), with heliocentric correction. A typical error on these redshifts is $\sim$45km/s

removed (i.e. flat) spectrum of a standard star. However, since this introduces large uncertainties in the spectra between the wavelengths affected by telluric absorption features, we have not attempted to obtain strengths for coronal lines within these regions.

2.2.2 General Corrections

Due to the procedure used to obtain the required wavelength coverage, there are three associated spectra for each galaxy; blue (4400-5600Å), red-short (5700-7000Å) and red-long (7300-8600Å), which we have joined together to form a single, almost continuous spectrum. During the spectral joining process, it was noted that no significant corrections were needed to force the spectra covering the three wavelength ranges to align, thus giving us confidence in the flux calibration procedure and the photometric accuracy. All our spectra have been corrected for redshift, which was calculated from the average observed wavelength of the [S II]λ6717, 6732 doublet, and geocentric velocities have

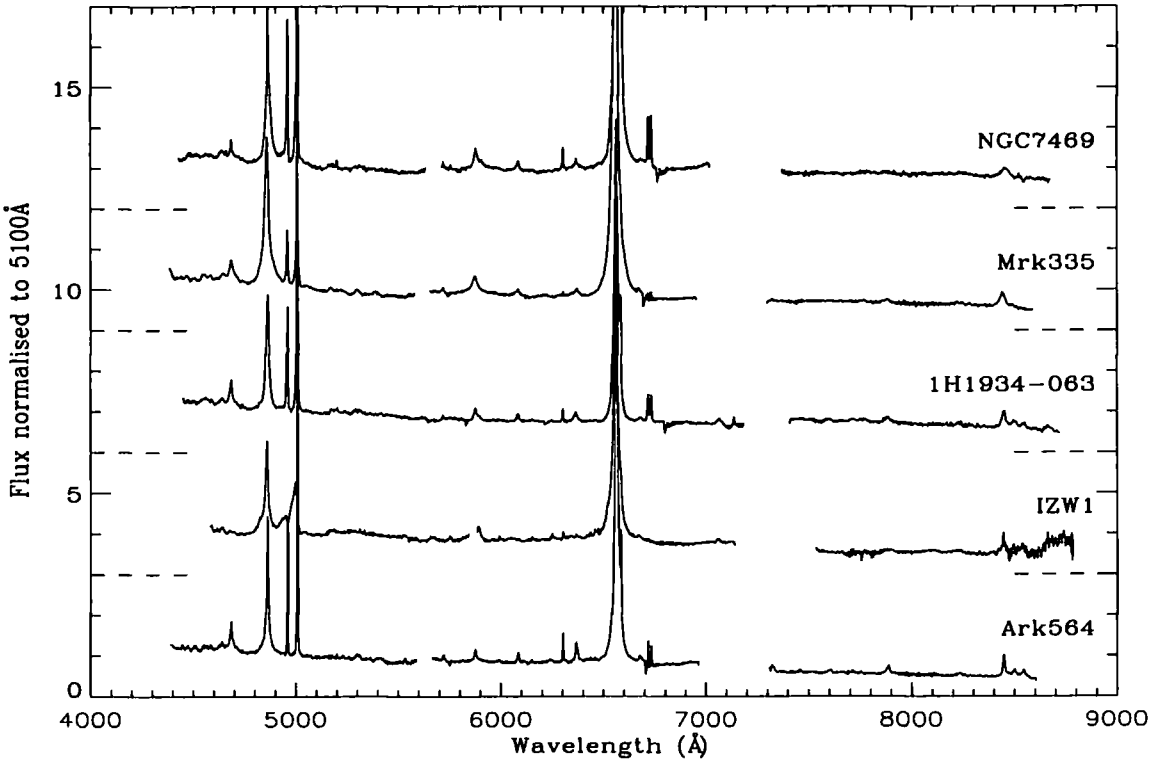

Figure 2.1: Flux calibrated, redshift corrected, FeII subtracted spectra. Flux has been normalised to the level at 5100Åand offset for clarity. The dotted lines either side of the plot show the level of the offset. For a clearer depiction of the lines discussed here, we refer the reader to Figs. A.1 - A.8

been taken into account. All velocities published here are therefore relative to the [S II]λ6717, 6732 doublet, which we assume is representative of the host galaxy. This is based on the fact that it has a low excitation potential and low critical density, meaning that it is likely to be formed away from the AGN.

The spectra have been corrected for Galactic extinction using the wavelength dependent absorption function of Cardelli et al. (1989) and the Schlegel et al. (1998) $E(B-V)$ values obtained from NASA/IPAC Extragalactic Database. Due to the narrow slit widths used, we expect that the spectra suffer only minor contamination from the host galaxy. To test this assumption, we searched for the stellar absorption feature Mg b at λ5170Å, but only found evidence of it in *Mrk 573* (the only Seyfert 2 in our sample), in which it has an equivalent width of $\sim$5Å . Because we concentrate on the profiles and relative strengths of emission lines at wavelengths which are largely unaffected by the stellar features, we have not corrected for this contamination.

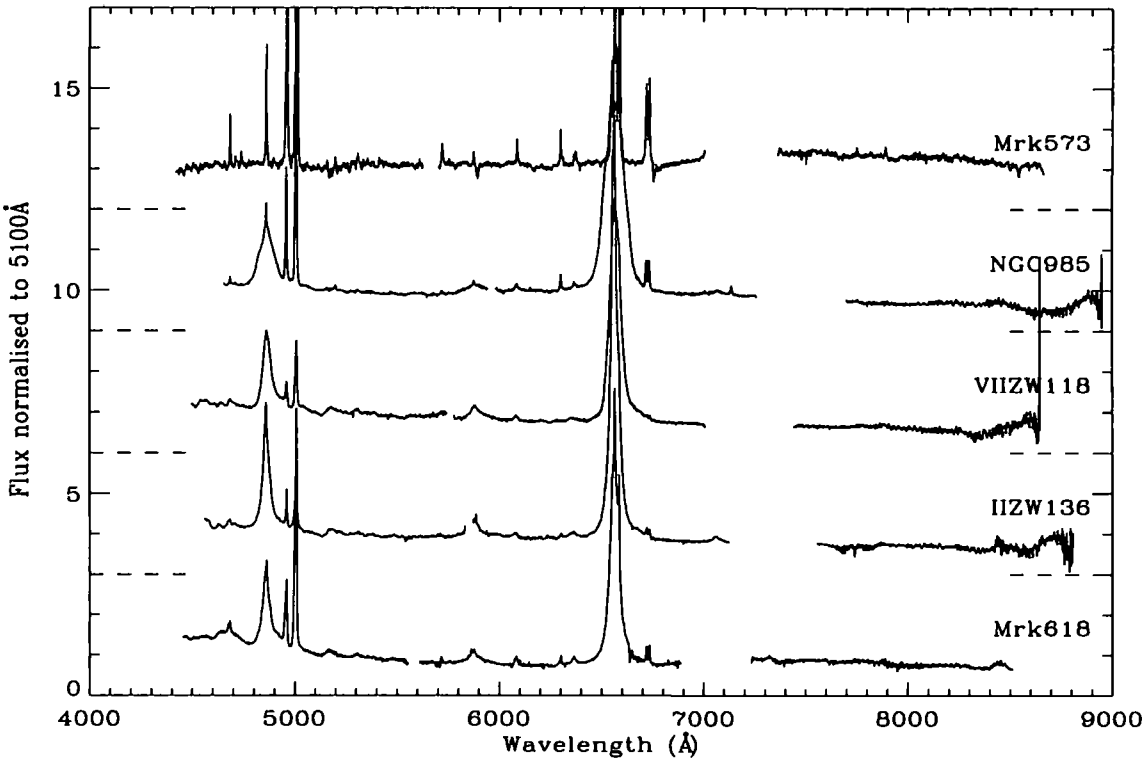

Figure 2.2: As for 2.1

2.2.3 Continuum Fitting

Since we wish to measure the total flux and profile of the emission lines, it was necessary to accurately fit and subtract the underlying continuum. For blends of weak lines, this can be problematic as it is difficult to distinguish between the continuum and extended line wings, thereby making the continuum fit somewhat subjective. In an attempt to more objectively determine the continuum levels, we modelled the whole spectrum with a gently inflecting fourth order polynomial fitted to regions of the spectrum that were perceived by eye to be free of emission features. Each fit was then inspected at the wavelength of the lines of interest to check that it was a sensible fit to the local underlying continuum. As some of the weaker emission lines lie on the broad wings of the Hα profile, we first fit the Hα line and remove the contribution of the broad wings from the weak lines.

2.2.4 Fe II Lines

Permitted emission from Fe II is often detected in the optical spectra of AGN, and is particularly strong in many NLS1s, in which multiplets of broad lines blend together

to form a pseudo-continuum. As some of our lines of interest lie close to strong Fe II features, we decided to remove them by using a method closely based on that outlined in Boroson and Green (1992). In their study of the strong Fe II lines in the spectrum of IZW1, Véron-Cetty et al. (2004) show that this emission contains two velocity components. To account for this we used their published line lists as a template, and broadened the two sets of lines by convolving this template with two Gaussians with independent variables of velocity width and intensity. In their method, Boroson and Green (1992) produced a matrix of Fe II spectra, from which they selected the one that most closely matched the Fe II emission in a particular object's spectrum. Increasing computing processing speeds since their original work fortunately means that we can now produce the broadened Fe II spectrum 'on the fly' using an IDL based GUI *REMOVEFEII*, developed by myself. This enables much more control over the range of input variables, making the Fe II feature removal a more dynamic and controlled process. As was noted by Landt et al. (2008), it is difficult to determine the true widths of the Fe II lines as, above a certain velocity width, the lines blend together into a single broad feature. To counter this it was noted that by fitting a single line that was unique to either the narrow or broad component templates and that was not part of an Fe II blend, a reasonably independent estimate of the strength and width of the two templates could be determined. A limitation to this method is that it is dependent on the assumption that all our AGN display the same Fe II emission lines, with the same relative strengths, as found in IZW1.

In practice it was found that, in general, this procedure was able to remove a significant proportion of the narrow Fe II emission component, but it was difficult to fully account for the broad component of the emission lines. A qualitative assessment of the line profiles affected by Fe II emission is therefore possible, but the level of uncertainty does not allow reliable measurements in cases where the FeII blends are strong – between $\lambda\lambda$4100-4600 and $\lambda\lambda$5150 -5400 (in particular the region of [Fe XIV]λ5303).

2.2.5 Line fitting

All the emission lines discussed in detail in the subsequent sections were modelled by fitting multiple Gaussian profiles, which we argue in the next section is more statistically robust than the Lorentzian component fitting method used in some previous NLS1 studies (also see Gonçalves et al. 1999, Véron-Cetty et al. 2001). Blends (excluding the Fe II lines discussed above) were dealt with by simultaneously fitting the blended lines. This method worked well for the majority of blended lines. In regions of the spectra

where broad lines are blended together with narrow lines, (in particular the Hα and [NII]$\lambda\lambda$6548,6584 lines), once we had fitted these lines we compared the widths of the blended narrow lines with those of the unblended narrow [OIII]$\lambda\lambda$4959,5007 lines as a check that the fit that been performed correctly.

The 90% confidence errors associated with the parameters derived for each fitted Gaussian (i.e. intensity, width and central wavelength) were determined by deviating each of the parameters from their optimum values until a change in χ^2 equal to the published 90% confidence level for the appropriate number of free fitting parameters was obtained. In addition to these random errors, we found that uncertainties in the continuum model leads to significant systematic errors for the line parameters (especially the broadest components). To estimate this, we rescaled the continuum by $\pm 1\sigma$ (adopting RMS as 1σ) and refit the line models, thereby quantifying the impact of continuum levels that are set too high or too low.

The intensities, widths and shifts of the multiple Gaussian fits for the lines discussed in this paper, along with their associated random and systematic errors, are listed in Tables 2.2 - 2.7, which we discuss in turn below. We note that, in Tables 2.4 & 2.5 we have not corrected for instrumental broadening as none of the components of the lines of interest had widths close to the instrumental broadening determined from the sky lines (~2Å). Therefore, when considered in quadrature, instrumental broadening would have an insignificant effect on the measured line widths.

2.2.6 Multiple component fits to the permitted emission lines

A statistical goodness-of-fit test is required in order to conclusively determine whether multiple Gaussians or a Lorentzian plus Gaussian model best represent the shape of the observed broad permitted emission line profiles.

In the literature the principal statistical test for this is the χ^2 fit statistic, which takes account of both the data points and their associated errors. When we apply this statistic to our Balmer line data we find that the χ^2 values of the three-Gaussian (3G) models are significantly lower than those of the Lorentzian-plus-1-Gaussian (L+1G) models. For example, in the case of the Hβ line in *Ark 564*, the χ^2 statistic for the 2 Gaussian is 6077.97, L+1G: 2249.38 and 3G: 2186.66. The best-fitting L+1G and 3G models both provide a much better description of the data than the two-Gaussian model. Comparing these two models, we find that the 3G model improves the fit by $\Delta\chi^2 = 62.72$ with the addition of just three additional free parameters. The probability of three extra parameters improv-

ing the χ^2 by as much as 21.10 purely by chance is 0.01%. The $\Delta\chi^2$ is at least this large for each line in tables 2-4 that is described with three components. Thus, we assert that the 3G model provides a better fit with >99.99% confidence.

We emphasise that the *reduced* χ^2 of all of the above models is $\gg 1$, so none of these provide a formally good fit to the data. This is an inherent problem when fitting simple models to large-scale features in high signal-to-noise data. The random error associated with the flux in each spectral bin is small and thus the potential contribution of any individual bin to the total χ^2 is large. Small 'bumps-and-wiggles' in the data that are not reproduced in the model will thus contribute strongly to the total χ^2. Although each of these deviations may well be a real feature of the source, we are not presently interested in complicated models that could reproduce such details. The inevitable consequence of leaving such features unmodelled is that the reduced χ^2 of the best-fitting model will invariably be larger than 1. In this paper we are only interested in the large-scale structure of the lines. If we want our relatively simple models to fit the spectra well we need to minimise the impact of the small-scale bumps-and-wiggles. This can be accomplished by smoothing the data. So long as the smoothing radius is not too large, the gross features in which we are interested will be preserved.

To further test the L+1G and the 3G models we have applied both to a sequence of increasingly smoothed spectra. We convolve each spectrum with a range of Gaussian kernels, varying the Gaussian FWHM from 1.0Å to 25.0Å in 0.5Å steps. To the lines in each we fit the L+1G and 3G models and measure the resulting reduced χ^2. We note that by using the reduced χ^2 we take into account the greater number of free parameters (and therefore greater flexibility) associated with the 3G model. As the smoothing radius increases, (1) the small-scale structures in the data get washed out, (2) the information content of the spectrum decreases, and (3) the reduced χ^2 of the best-fitting large-scale line models decreases.

With the appropriate amount of smoothing, the reduced χ^2 of a model will approach 1.0 and the model can then be said to provide a good description of the (remaining) data. Any additional smoothing will decrease the reduced χ^2 below 1. When this happens the model is no longer appropriate because the spectrum has lost so much information that it no longer requires a model of this complexity. In effect, the model has too many degrees of freedom for such a simplified spectrum and its use over-interprets what is left of the data. We find that for the lines measured, the 3G models require less smoothing than the L+1G models to reach a reduced χ^2 of 1. We therefore consider the 3G model to be the

more appropriate model because it describes the spectra well when less of the original information content has been lost.

As an example, fig. 2.3 shows a comparison of the reduced-χ^2 values for both the 3G and L+1G models applied to the Hβ profile of *Ark 564* as a function of smoothing width. The reduced-χ^2 of the 3G model reaches 1 with a smoothing kernel of ~4.0Å FWHM whereas that of the L+1G model requires a kernel of ~5.6Å FWHM. Thus the 3G model reflects more of the information contained in the original spectrum. Quantitatively, when the 3G model fitted to the smoothed spectrum has a reduced-χ^2 of 1.00 the reduced-χ^2 of the L+1G model is 1.35, indicating that the former is a better representation of the data with >99% confidence. Moreover, the fact that the reduced-χ^2 curve of the 3G model is always below that of the L+1G model indicates that the 3G model always provides a better representation of the data regardless of the level of smoothing applied.

It should be noted that we have only smoothed our data to show that 3G models are more appropriate than L+G models. Throughout the process described in this section we did not adjust the errors associated with each data point as the smoothing length changed. The χ^2 values therefore cannot be taken to be formally accurate. Furthermore, smoothing the data inevitably changes the properties of the fitted components; in particular, the FWHM of the narrow component significantly increases as the smoothing length approaches the width of that component. Therefore, we have only used the prcoesses described in this section as a convenient method to compare the different component models (i.e. 3G and L+G). With this in mind, all the results presented in the remainder of this chapter are based on the un-smoothed spectra.

2.3 Emission Line Results

2.3.1 The Broad Emission Lines

Due to the clear distinction between the spectrum of the only Seyfert 2 in our sample, *Mrk 573*, and all the other galaxies we observed (Seyfert 1s, with a range of broad emission line widths), we will discuss this galaxy in a separate section.

Balmer Lines

As expected, all our spectra are dominated by strong Hα and Hβ lines, which we show, together with their Gaussian fits, in figs A.1 and A.2, respectively (see Appendix). We

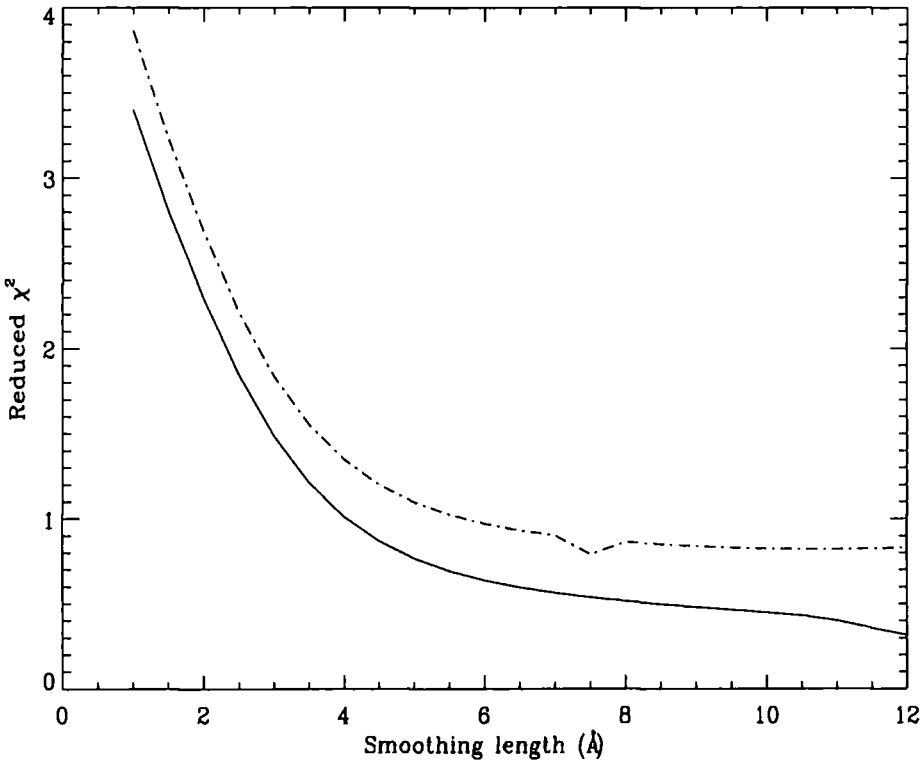

Figure 2.3: The effect of smoothing on the reduced-χ^2 statistic for the *Ark 564* Hβ line (here, smoothing length refers to the FWHM of the Gaussian smoothing kernel). The dotted line corresponds to the L+1G fit, and the solid line refers to the 3G fit. It is evident that, irrespective of the smoothing length used, the 3G fit is statistically better than the L+1G fit. That the reduced-χ^2=1.0 point is reached by both fitting methods at smoothing lengths significantly below the maximum smoothing length revealed in fig. 2.4 confirms this is still within the regime at which the narrow component of the Hβ remains in tact after smoothing

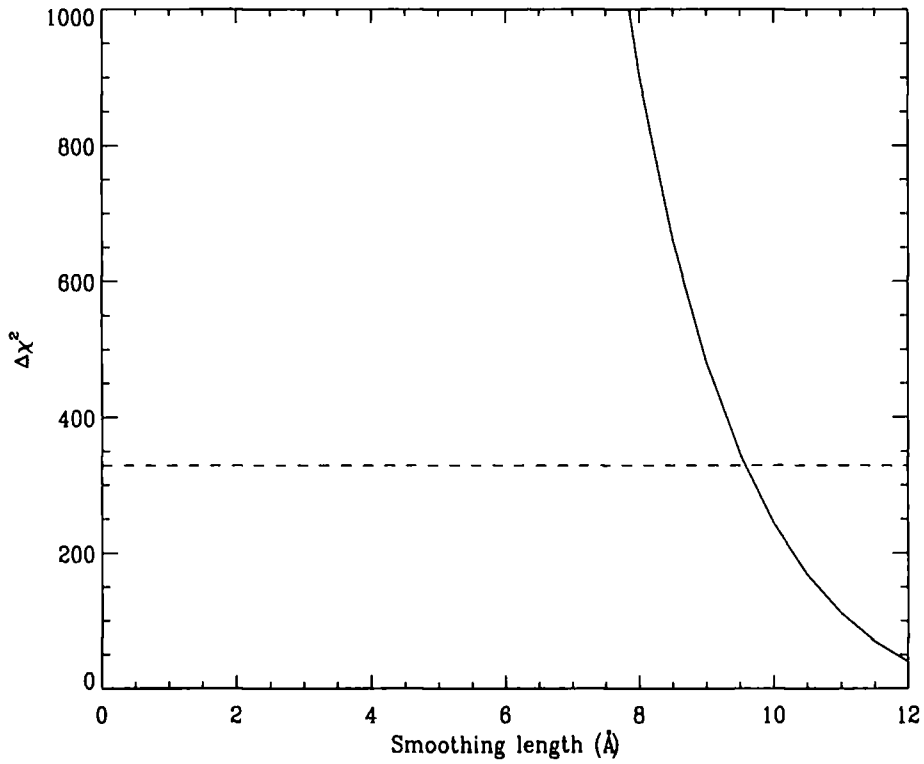

Figure 2.4: Change in χ^2 after the removal of the narrow component of the Hβ line of *Ark 564* when fitted with a 3G model. The dotted line shows the 90% confidence level that the narrow component is detectable when performing the fit. Using smoothing lengths significantly less than point at which the two lines intersect effectively ensures that we are smoothing out the small deviations discussed in the text, but retaining the overall profile of the Hβ line.

Line	*Ark 564*	*IZW1*	*1H1934-063*	*Mrk 335*	*NGC 7469*
Hβ Flux	2.76	2.62	6.11	6.70	5.43
H$_\alpha$ λ6563	454.2 ± 5.0 (5%)	453.8 ± 3.3 (15%)	320.4 ± 1.5 (5%)	350.1 ± 2.4 (<2.5%)	487.5 ± 3.2 (5%)
Broad	184.9 ± 2.5 (<2.5%)	228.0 ± 1.9 (10%)	76.06 ± 0.78 (<2.5%)	155.0 ± 1.4 (<2.5%)	424.1 ± 2.8 (5%)
Intermediate	169.1 ± 2.1 (10%)	175.5 ± 1.4 (5%)	198.03 ± 0.86 (5%)	139.4 ± 1.1 (<2.5%)	-
Narrow	100.2 ± 1.3 (5%)	50.33 ± 0.59 (50%)	46.27 ± 0.38 (<2.5%)	55.77 ± 0.66 (5%)	63.41 ± 0.64 (<2.5%)
H$_\beta$ λ4861	100.0 ± 1.4 (10%)	100.00 ± 0.92 (10%)	100.00 ± 0.48 (15%)	100.00 ± 0.74 (5%)	100.00 ± 0.83 (5%)
Broad	46.80 ± 0.92 (5%)	61.66 ± 0.69 (15%)	43.10 ± 0.30 (10%)	60.16 ± 0.52 (5%)	85.76 ± 0.74 (5%)
Intermediate	36.36 ± 0.58 (10%)	28.18 ± 0.33 (5%)	50.75 ± 0.25 (20%)	28.92 ± 0.30 (5%)	-
Narrow	16.84 ± 0.33 (20%)	10.16 ± 0.19 (10%)	6.15 ± 0.10 (15%)	10.92 ± 0.20 (5%)	14.24 ± 0.24 (<2.5%)
[O III]λ5007	88.50 ± 0.96 (5%)	65.10 ± 0.61 (15%)	38.87 ± 0.21 (<2.5%)	29.32 ± 0.25 (5%)	111.13 ± 0.77 (<2.5%)
Broad	44.02 ± 0.54 (<2.5%)	48.66 ± 0.49 (15%)	28.19 ± 0.17 (<2.5%)	18.19 ± 0.20 (5%)	46.32 ± 0.44 (5%)
Narrow	44.48 ± 0.51 (5%)	16.45 ± 0.26 (10%)	10.679 ± 0.098 (<2.5%)	11.13 ± 0.12 (5%)	64.80 ± 0.45 (<2.5%)
He Iλ5876	17.0 ± 1.1 (45%)	-	12.22 ± 0.34 (35%)	23.27 ± 0.81 (30%)	23.33 ± 0.89 (35%)
Broad	12.81 ± 0.99 (60%)	-	8.59 ± 0.30 (40%)	16.45 ± 0.74 (35%)	18.05 ± 0.80 (40%)
Narrow	4.15 ± 0.37 (<2.5%)	-	3.63 ± 0.17 (25%)	6.82 ± 0.32 (15%)	5.27 ± 0.38 (10%)
He IIλ4686	25.54 ± 0.64 (15%)	-	22.52 ± 0.24 (15%)	12.18 ± 0.29 (10%)	10.71 ± 0.39 (40%)
Broad	18.97 ± 0.57 (10%)	-	15.26 ± 0.21 (5%)	8.07 ± 0.25 (5%)	8.83 ± 0.36 (45%)
Narrow	6.57 ± 0.25 (25%)	-	7.25 ± 0.11 (35%)	4.11 ± 0.15 (20%)	1.88 ± 0.15 (5%)
[Fe VII]λ6087	3.95 ± 0.29 (25%)	-	3.44 ± 0.14 (30%)	3.12 ± 0.26 (65%)	5.35 ± 0.66 (40%)
Broad	3.95 ± 0.29 (25%)	-	3.44 ± 0.14 (30%)	3.12 ± 0.26 (65%)	2.79 ± 0.55 (50%)
Narrow	-	-	-	-	2.56 ± 0.35 (30%)
[Fe X]λ6374	9.36 ± 0.66 (25%)	-	6.26 ± 0.21 (25%)	5.68 ± 0.59 (55%)	7.29 ± 0.68 (70%)
Broad	8.03 ± 0.56 (25%)	-	6.26 ± 0.21 (25%)	4.80 ± 0.54 (60%)	7.29 ± 0.68 (70%)
Narrow	1.32 ± 0.33 (25%)	-	-	0.88 ± 0.24 (15%)	-
[Fe XI]λ7892	8.83 ± 0.57 (30%)	-	7.80 ± 0.23 (35%)	2.24 ± 0.17 (60%)	-
Broad	5.96 ± 0.49 (30%)	-	7.80 ± 0.23 (35%)	2.24 ± 0.17 (60%)	-
Narrow	2.88 ± 0.30 (35%)	-	-	-	-
[Fe XIV]λ5303	1.81 ± 0.33 (35%)	-	1.81 ± 0.11 (60%)	-	-
Broad	1.81 ± 0.33 (35%)	-	1.81 ± 0.11 (60%)	-	-

Table 2.2: Modelled line flux, as a percentage of the Hβ line. Where no value is listed, there was no significant indication of the presence of the line or component. The ± errors refer to the 90% confidence interval of the measurement, the (%) errors refer to the systematic errors associated with the estimation of the continuum flux levels. The Hβ line flux has units of 10^{-13} ergs/s/cm^2

Line	*Mrk 618*	*IIZW136*	*VIIZW118*	*NGC 985*	*Mrk 573*
Hβ Flux	1.84	4.64	1.47	3.63	0.400
Hα λ6563	331.1 ± 3.4 (5%)	383.0 ± 2.3 (5%)	412.8 ± 3.4 (10%)	527.5 ± 1.9 (<2.5%)	382. ± 10.0 (<2.5%)
Broad	184.1 ± 2.2 (5%)	116.2 ± 1.00 (<2.5%)	122.0 ± 1.6 (10%)	501.4 ± 1.8 (<2.5%)	-
Intermediate	136.5 ± 1.6 (10%)	209.7 ± 1.3 (5%)	-	-	242.8 ± 6.8 (<2.5%)
Narrow	10.54 ± 0.42 (<2.5%)	57.15 ± 0.47 (<2.5%)	290.8 ± 2.3 (10%)	26.09 ± 0.32 (5%)	138.9 ± 4.0 (<2.5%)
Hβ λ4861	100.0 ± 1.2 (20%)	100.00 ± 0.76 (5%)	100.0 ± 1.0 (5%)	100.00 ± 0.46 (10%)	100.0 ± 3.3 (10%)
Broad	76.37 ± 0.95 (10%)	34.50 ± 0.46 (5%)	41.11 ± 0.66 (10%)	95.07 ± 0.43 (10%)	-
Intermediate	22.03 ± 0.48 (45%)	55.84 ± 0.42 (10%)	-	-	66.0 ± 2.5 (5%)
Narrow	1.61 ± 0.24 (40%)	9.66 ± 0.17 (<2.5%)	58.89 ± 0.60 (5%)	4.926 ± 0.095 (10%)	34.0 ± 1.4 (15%)
[O III] λ5007	80.54 ± 0.78 (5%)	23.94 ± 0.26 (5%)	20.54 ± 0.37 (10%)	60.36 ± 0.27 (<2.5%)	1216. ± 28. (<2.5%)
Broad	65.06 ± 0.64 (5%)	12.97 ± 0.21 (5%)	11.08 ± 0.28 (10%)	25.85 ± 0.18 (<2.5%)	785. ± 18. (<2.5%)
Narrow	15.48 ± 0.23 (<2.5%)	10.97 ± 0.12 (5%)	9.46 ± 0.22 (5%)	34.51 ± 0.15 (<2.5%)	431. ± 10. (<2.5%)
He I λ5876	26.0 ± 1.1 (35%)	-	25.4 ± 1.1 (20%)	15.68 ± 0.62 (40%)	9.1 ± 1.4 (45%)
Broad	18.8 ± 1.0 (40%)	-	17.48 ± 0.94 (25%)	14.77 ± 0.59 (40%)	9.1 ± 1.4 (45%)
Narrow	7.22 ± 0.53 (25%)	-	7.94 ± 0.51 (5%)	0.91 ± 0.18 (15%)	-
He II λ4686	18.83 ± 0.63 (20%)	5.00 ± 0.24 (45%)	5.28 ± 0.39 (35%)	1.145 ± 0.050 (25%)	35.6 ± 1.9 (20%)
Broad	13.51 ± 0.57 (25%)	3.00 ± 0.21 (65%)	3.16 ± 0.33 (55%)	1.145 ± 0.050 (25%)	22.0 ± 1.5 (25%)
Narrow	5.32 ± 0.26 (5%)	2.00 ± 0.11 (20%)	2.12 ± 0.21 (10%)	-	13.7 ± 1.0 (10%)
[Fe VII] λ6087	4.29 ± 0.30 (35%)	4.27 ± 0.26 (40%)	2.81 ± 0.31 (40%)	2.80 ± 0.15 (50%)	28.0 ± 1.9 (20%)
Broad	4.29 ± 0.30 (35%)	4.27 ± 0.26 (40%)	2.81 ± 0.31 (40%)	2.80 ± 0.15 (50%)	28.0 ± 1.9 (20%)
Narrow	-	-	-	-	-
[Fe X] λ6374	6.60 ± 0.45 (30%)	6.47 ± 0.32 (45%)	5.57 ± 0.59 (80%)	-	15.4 ± 2.1 (30%)
Broad	6.60 ± 0.45 (30%)	6.47 ± 0.32 (45%)	5.57 ± 0.59 (80%)	-	15.4 ± 2.1 (30%)
Narrow	-	-	-	-	-
[Fe XI] λ7892	-	-	-	-	11.1 ± 1.4 (80%)
Broad	-	-	-	-	11.1 ± 1.4 (80%)
Narrow	-	-	-	-	-
[Fe XIV] λ5303	-	-	-	-	-
Broad	-	-	-	-	-

Table 2.3: As for table 2.2

have been able to deconvolve these lines into their narrow and broad components for all the observed Seyfert 1 nuclei. For six of the nine Seyfert 1s we observed the Balmer lines are best fitted with three components. The three galaxies that do not fit this trend are *NGC 7469*, *VIIZW118* and *NGC 985*, in which a third component does not provide a significant improvement to the fit. In general, we find equivalent velocity width components (to within errors) in both the Hα and Hβ lines, giving us further confidence in the reality of each of the components. The only case of which this is not strictly true is the intermediate component of *1H1934-063*, although here the discrepancy is <20%- typical of the size of the systematic errors on Balmer line components in other galaxies considered here.

To assist in the discussion we have arranged our results in order of increasing Hα intermediate component velocity width, which we find most closely matches the crude FWHM of the whole line. Fitting the Balmer lines with Gaussians is complicated by the presence of a number of blended narrow and broad lines emitted by other species.

Line	*Ark 564*	*IZW1*	*1H1934-063*	*Mrk 335*	*NGC 7469*
H_α λ6563					
Broad	2578. ± 24. (10%)	3247. ± 16. (20%)	2837. ± 26. (10%)	3920. ± 27. (5%)	2066.1 ± 6.4 (<2.5%)
Intermediate	963.1 ± 7.3 (5%)	918.3 ± 4.1 (25%)	1271.7 ± 3.7 (<2.5%)	1333.4 ± 7.3 (<2.5%)	-
Narrow	320.9 ± 3.2 (<2.5%)	328.2 ± 3.2 (20%)	411.4 ± 3.2 (<2.5%)	707.1 ± 8.2 (<2.5%)	230.4 ± 2.3 (<2.5%)
H_β λ4861					
Broad	3175. ± 60. (25%)	4049. ± 43. (15%)	2624. ± 18. (25%)	3838. ± 29. (<2.5%)	2046. ± 15. (5%)
Intermediate	897. ± 12. (15%)	967. ± 11. (5%)	1059.7 ± 4.3 (10%)	1292. ± 12. (<2.5%)	-
Narrow	290.1 ± 5.6 (10%)	388.8 ± 7.4 (5%)	317.8 ± 6.2 (10%)	685. ± 14. (<2.5%)	329.6 ± 6.2 (<2.5%)
[O III] λ5007					
Broad	336.1 ± 2.4 (5%)	2044. ± 20. (5%)	538.0 ± 3.0 (<2.5%)	893. ± 11. (5%)	744.2 ± 6.6 (10%)
Narrow	161.2 ± 1.2 (<2.5%)	759. ± 13. (5%)	191.1 ± 1.8 (<2.5%)	246.3 ± 2.4 (5%)	284.6 ± 1.2 (<2.5%)
He I λ5876					
Broad	3250 ± 510 (25%)	-	1852. ± 72. (45%)	6970 ± 380 (30%)	2910 ± 160 (25%)
Narrow	475. ± 46. (<2.5%)	-	576. ± 31. (15%)	1336. ± 76. (10%)	665. ± 57. (5%)
He II λ4686					
Broad	2305. ± 76. (20%)	-	2535. ± 37. (20%)	2666. ± 93. (5%)	1700 ± 110 (25%)
Narrow	474. ± 22. (20%)	-	686. ± 12. (20%)	957. ± 40. (10%)	290. ± 25. (5%)
[Fe VII] λ6087					
Broad	446. ± 37. (15%)	-	572. ± 27. (20%)	1380 ± 140 (45%)	1270 ± 360 (45%)
Narrow	-	-	-	-	518. ± 85. (20%)
[Fe X] λ6374					
Broad	749. ± 62. (25%)	-	1127. ± 42. (15%)	2680 ± 420 (35%)	2560 ± 300 (35%)
Narrow	268. ± 73. (10%)	-	-	510 ± 170 (10%)	-
[Fe XI] λ7892					
Broad	1140 ± 110 (40%)	-	1457. ± 48. (20%)	1330 ± 120 (35%)	-
Narrow	428. ± 51. (20%)	-	-	-	-
[Fe XIV] λ5303					
Broad	540 ± 110 (30%)	-	623. ± 55. (35%)	-	-

Table 2.4: Line widths in km/s. As above, the random errors are the 90% confidence interval and the systematic uncertainties arising from the continuum model are given in parenthesis. measurement.

In particular, the Hα line is blended with two often quite strong, narrow [N II] lines at λ6548 and λ6584. Fortunately, as they are narrow these lines are easily fitted and removed when fitting the Hα line. More difficult to account for is the broad He I λ4922 line that forms the 'red shelf' of the Hβ line, and is discussed in detail by Véron et al. (2002). If, during the initial fitting, there was evidence of a broad, redshifted component to the Hβ line, we assumed that it was the result of this Helium line. We then refit the blend, adding an additional Gaussian with its central wavelength fixed to 4922Å (rest frame). This component is then excluded from further analysis of the Hβ line. A similar procedure was used to remove the less prominent red shelf on the Hα line, caused by the presence of He I λ6678 emission.

Line	*Mrk 618*	*IIZW136*	*VIIZW118*	*NGC 985*	*Mrk 573*
H_α λ6563					
Broad	3221. ± 26. (5%)	4474. ± 30. (5%)	5242. ± 59. (20%)	4987.5 ± 7.8 (<2.5%)	-
Intermediate	1681. ± 15. (<2.5%)	2093.1 ± 5.9 (<2.5%)	-	-	533.9 ± 9.1 (<2.5%)
Narrow	191.1 ± 8.2 (<2.5%)	675.1 ± 4.6 (<2.5%)	2503.1 ± 8.7 (<2.5%)	519.3 ± 8.7 (5%)	180.1 ± 3.7 (<2.5%)
H_β λ4861					
Broad	3343. ± 35. (10%)	5130. ± 68. (20%)	4543. ± 70. (20%)	5003. ± 18. (5%)	-
Intermediate	1360. ± 33. (30%)	2353. ± 14. (5%)	-	-	546. ± 19. (20%)
Narrow	240. ± 64. (5%)	649. ± 12. (<2.5%)	2293. ± 18. (<2.5%)	467. ± 12. (10%)	185.8 ± 7.4 (5%)
[O III] λ5007					
Broad	810.1 ± 4.8 (5%)	1379. ± 26. (15%)	772. ± 22. (10%)	803.5 ± 5.4 (5%)	523.1 ± 2.4 (<2.5%)
Narrow	267.2 ± 3.6 (<2.5%)	339.1 ± 3.6 (5%)	442. ± 11. (<2.5%)	309.8 ± 1.2 (<2.5%)	169.6 ± 1.2 (<2.5%)
He I λ5876					
Broad	5500 ± 340 (35%)	-	5470 ± 360 (15%)	5150 ± 280 (25%)	254. ± 45. (30%)
Narrow	1600 ± 130 (10%)	-	1810 ± 140 (<2.5%)	520 ± 130 (10%)	-
He II λ4686					
Broad	4110 ± 190 (10%)	2990 ± 270 (45%)	2070 ± 260 (25%)	423. ± 22. (15%)	430. ± 30. (20%)
Narrow	920. ± 50. (5%)	1061. ± 68. (5%)	940 ± 100 (10%)	-	198. ± 17. (5%)
[Fe VII] λ6087					
Broad	775. ± 63. (15%)	2020 ± 190 (20%)	1060 ± 140 (25%)	980. ± 65. (35%)	378. ± 30. (15%)
Narrow	-	-	-	-	-
[Fe X] λ6374					
Broad	1290 ± 130 (15%)	2740 ± 180 (25%)	2980 ± 400 (45%)	-	387. ± 58. (20%)
Narrow	-	-	-	-	-
[Fe XI] λ7892					
Broad	-	-	-	-	330. ± 43. (45%)
Narrow	-	-	-	-	-
[Fe XIV] λ5303					
Broad	-	-	-	-	-

Table 2.5: As for table 2.4

Helium Emission

Our spectra also cover a number He lines, of which He Iλ5876 and He II λ4686 are two of the strongest. Plots of these lines, including their Gaussian fits, are shown in Figs A.3 and A.4, respectively. We have been able to measure both these emission lines in seven of the nine observed Sy1 galaxies (the redshifts of *IZW1*and *IIZW136* place their He Iλ5876 between the ranges of the Blue and Red/Short spectral settings). Unfortunately, He IIλ4686 suffers from strong blending with the Fe II lines and the $H\beta$ line just blueward and redward of it, respectively. Despite our attempts to remove the blended Fe II emission there are still some remnants of this procedure (seen either in emission, or in absorption caused by overcompensation). There also appears to be an unidentified broad line present in the blue wing for the majority of the observed He IIλ4686 that does not seem to change after the Fe II removal. Where this unidentified line is blended with the He IIλ4686 line, we have fit it with a single Gaussian and have not included it in the interpretation of the He II line intensity and width. Aware of these complications,

Line	*Ark 564*	*IZW1*	*1H1934-063*	*Mrk 335*	*NGC 7469*
H_α λ6563					
Broad	-71. ± 13.	234.4 ± 8.2	-108. ± 14.	118. ± 14.	-249.2 ± 0.00
Intermediate	-32.4 ± 4.1	99.6 ± 2.3	10.5 ± 1.8	298.3 ± 0.00	-
Narrow	-7.3 ± 1.8	-19.2 ± 1.8	-0.5 ± 1.8	-8.4 ± 4.6	-81.5 ± 0.00
H_β λ4861					
Broad	-35. ± 31.	461. ± 21.	-76.3 ± 9.9	90. ± 12.	-312.7 ± 6.2
Intermediate	-7.3 ± 6.8	252.1 ± 5.6	0.8 ± 2.5	257.5 ± 6.2	-
Narrow	-10.4 ± 3.1	72.0 ± 3.7	-63.9 ± 3.1	37.9 ± 6.2	-91.9 ± 0.00
[O III]λ5007					
Broad	13.6 ± 1.8	1375.8 ± 9.6	105.9 ± 1.8	149.0 ± 5.4	215.5 ± 3.6
Narrow	-42.12 ± 0.60	537.2 ± 6.6	-37.9 ± 1.2	-15.1 ± 1.2	-20.44 ± 0.60
He Iλ5876					
Broad	-220 ± 180	-	-369. ± 38.	-230 ± 190	-754. ± 79.
Narrow	-8. ± 25.	-	52. ± 16.	141. ± 37.	-81. ± 29.
He IIλ4686					
Broad	-23. ± 38.	-	30. ± 19.	-428. ± 45.	59. ± 45.
Narrow	55. ± 11.	-	133.5 ± 6.4	161. ± 19.	35. ± 13.
[Fe VII]λ6087					
Broad	73. ± 19.	-	179. ± 14.	359. ± 69.	520 ± 150
Narrow	-	-	-	-	99. ± 39.
[Fe X]λ6374					
Broad	256. ± 31.	-	510. ± 19.	450 ± 190	440 ± 150
Narrow	86. ± 41.	-	-	228. ± 83.	-
[Fe XI]λ7892					
Broad	424. ± 55.	-	396. ± 23.	473. ± 60.	-
Narrow	170. ± 26.	-	-	-	-
[Fe XIV]λ5303					
Broad	425. ± 59.	-	720. ± 24.	-	-

Table 2.6: Line shift from systemic velocity shift (in km/s), as determined from the [S II]λ6718 doublet. We use the convention that negative numbers indicate a net redshift.

we fit the He II line with multiple Gaussians where the addition of a second component provides a statistically better fit.

When it is present, the broad component is generally redshifted with respect to the narrow component of the line, however, this may be an artefact of line asymmetries caused by the Fe II removal. For the galaxies in which He IIλ4686 is detected its strength relative to Hβ varies considerably between galaxies, ranging from almost 25% in *Ark 564*, to less than 2% in *NGC 985*.

More accurately measured is the He Iλ5876 line. It is well detected in all our spectra that cover the region, and is easily deconvolved into its constituent velocity components. In 4/9 of the Sy1-type AGN the broadest of these components is considerably broader than the broadest Hβ velocity component, although the level of the continuum fit has a considerable effect on the width of the fitted broad component (see §5.3.3). As explained in §2.2.5 we account for the possible influence of the continuum fit on the He I line by

Line	*Mrk 618*	*IIZW136*	*VIIZW118*	*NGC 985*	*Mrk 573*
H_α λ6563					
Broad	20. ± 14.	32. ± 16.	-553. ± 32.	-88.9 ± 4.6	-
Intermediate	-5.1 ± 8.2	-29.9 ± 3.2	-	-	-137.5 ± 4.6
Narrow	-96.9 ± 4.6	177.1 ± 2.3	-186.6 ± 5.0	-20.4 ± 4.1	-57.6 ± 0.00
H_β λ4861					
Broad	125. ± 22.	525. ± 35.	-704. ± 38.	-195.0 ± 9.3	-
Intermediate	85. ± 17.	44.1 ± 7.4	-	-	-135.1 ± 6.2
Narrow	-84. ± 54.	189.0 ± 6.8	-126.5 ± 9.9	-16.7 ± 5.6	-100.0 ± 0.00
[O III] λ5007					
Broad	235.2 ± 2.4	222. ± 12.	106. ± 11.	104.1 ± 0.00	-131.2 ± 1.2
Narrow	-49.3 ± 2.4	-0.3 ± 2.4	-89.3 ± 6.0	9.4 ± 0.00	-69.51 ± 0.60
He I λ5876					
Broad	-410 ± 170	-	-1520 ± 170	-260 ± 130	-61. ± 23.
Narrow	202. ± 68.	-	-146. ± 68.	-27. ± 62.	-
He II λ4686					
Broad	-651. ± 97.	-870 ± 130	-920 ± 130	21.2 ± 6.4	-109. ± 17.
Narrow	261. ± 26.	426. ± 36.	133. ± 57.	-	-61.4 ± 9.0
[Fe VII] λ6087					
Broad	258. ± 30.	691. ± 74.	279. ± 69.	81. ± 30.	-73. ± 15.
Narrow	-	-	-	-	-
[Fe X] λ6374					
Broad	387. ± 52.	640. ± 80.	480 ± 180	-	-78. ± 28.
Narrow	-	-	-	-	-
[Fe XI] λ7892					
Broad	-	-	-	-	-64. ± 23.
Narrow	-	-	-	-	-
[Fe XIV] λ5303					
Broad	-	-	-	-	-

Table 2.7: As for table 2.6

recording the impact that changing the level of the continuum has on the measured line parameters. In all of the 4 Syl-type AGN mentioned above, the broad He I component remains broader than the broadest Hβ component even when the underlying continuum level is shifted well above any reasonable continuum fit would be placed. Admittedly, the possibility remains that there exists some underlying features that we have not taken into account in modelling the continum+He I line (e.g. a weak blending of lines similar to the Fe II complexes). Bearing these points in mind we cautiously maintain that, in a large minority of our type 1 objects, the He I line is appropriately modelled with a component that is broader than the broadest of the Hβ components.

2.3.2 Narrow Emission Lines

The narrow emission line region has been well studied in the past, and is therefore much better understood than the other two non-spatially resolved regions discussed in this paper. Because of this we do not provide a full analysis of the narrow emission lines. Instead we will simply mention the main points of the most prominent of these narrow

lines.

[O III] $\lambda\lambda$4959,5007

All our spectra, with the possible exception of IZW1, display strong [O III] $\lambda\lambda$4959, 5007 lines, whose profiles all show asymmetries or have low intensity broad wings that cannot be modelled by a single Gaussian. These asymmetries tend toward a blue wing, which, when fitted using two Guassians, suggests a narrow (200km/s < FWHM < 400km/s) component centred on the systemic wavelength, plus a broader component (350km/s < FWHM < 1000km/s) that is generally blueshifted with respect to the narrow component. The latter fact was first noted by Heckman et al. (1981), in which they attribute the effect to outflows with preferentially absorbed redshifted components, supported by the tight correlation between line asymmetry and Hα/Hβ ratio.

[S II] λ6717, 6732 doublet

As this feature is commonly used to determine the densities of the NLR of AGN, we chose to fit these lines with separate Gaussians, using multiple components if there was evidence of broad wings or inflections. Comparing the [S II] 6717/6731 line ratio with published density relationships revealed no correlation between electron density and AGN type or width of Hβ. This finding is consistent with the large scatter in the [SII] ratio vs. line width plot of Xu et al. (2007) at low values of Hβ FWHM.

Balmer line narrow component

As a test to determine whether the narrow component of the Balmer emission is arising from the same region of the AGN as the narrow forbidden line emission, we compare in detail the widths of the narrow components of the Balmer and [O III] lines. Tables 2.4 2.5 and shows that 7/9 of the observed Seyfert 1s have narrow Balmer components that either lie in between or very close to the velocity widths of the narrow and broad components of the [O III] component widths. The two galaxies in which this is not the case are *IZW1* and *VIIZW118*. As mentioned in the previous section, *IZW1* has very broad, highly blueshifted [OIII] lines, so it is not surprising that the widths do not match in this case, and there is no evidence of a narrow component in the Balmer lines of *VIIZW118*.

2.3.3 Forbidden High Ionisation (Coronal) Lines (*FHILs*)

We detect the [Fe VII] λ6087 emission line in every galaxy. The line profile in *NGC 7469* is best described by a two-Gaussian model. Additionally, *Ark 564* and *Mrk 335* both appear to have a slight blue wing, but the improved fit of a 2 component model is not statistically significant.

We detect the [Fe X] emission line in seven of our spectra. Our measurements are complicated by blending with the [O I]λ6363 line. An estimate of the contribution from the [O I] line can be made by using the nearby [O I]λ6300 line as a calibration. From atomic physics these two lines should have exactly the same profile, and the intensities must have a ratio of 1:3. Using this information we are able to remove the contribution of [O I] from the [Fe X] blend. As with the He I and He II lines, measuring the broad component of the [Fe X] line is complicated by uncertainties in setting the local continuum levels and blends of multiple lines that form a pseudo-continuum. Despite these difficulties, we have measured the [Fe X] lines using Gaussian fits, which are shown in Fig. A.6. Our analysis includes a 2^{nd} Gaussian component when its addition is statistically significant, although the majority of the spectra only require a single component. All the [Fe X] lines we measure contain broad components that are broader than the [Fe VII] broad components. The two galaxies that show the narrowest Balmer lines also have the narrowest [Fe X] lines of the sample. All the [Fe X] lines are blueshifted in the range between $\sim$150 and $\sim$700km/s, although there does not appear to be any correlation between blueshift and velocity width or relative intensity of the line between galaxies.

Unfortunately, about half of our spectra have rather poor S/N ratios in the region containing the [Fe XI] line. This is partly attributed to telluric absorption (as discussed in §2.2.1), and partly to interference fringes on the CCD chip around these wavelengths. Due to this, we only have measurements of this line for three galaxies, *Ark 564*, *1H1934-063* and *Mrk 335*, as shown in Fig. A.6. The widths of the [Fe XI] lines reveals that they are similar to the [Fe X] line velocity widths in *Ark 564* and *1H1934-063*. *Mrk 335* seems to have a wider broad component in [Fe X], but this value is uncertain because of poor continuum determination.

The highest ionisation line species we observe, [Fe XIV]λ5303, lies within a region that is heavily affected by the presence of Fe II emission. Despite our attempts at mitigating the effects of Fe II emission, we have still had great difficulty in isolating the [Fe XIV]λ5303 line. The [Fe XIV] line is also strongly blended with the [Ca V]λ5309

line. Although we cannot measure the [Fe XIV] line accurately enough to give robust quantitative results, we are confident of its presence in two of our sample, *Ark 564* and *1H1934-063* ($\Delta\chi^2$ >500 and >1000, respectively, for 1 added Gaussian- corresponding to a $\gg 10\sigma$ detection in both targets). In both cases we are able to separate the feature into 2 Gaussian components ($\Delta\chi^2$=52 and =85 between 1- and 2- component fit, again, corresponding to a $>10\sigma$ detection of two separate lines in both targets), which we interpret as [Fe XIV] and [Ca V]. We take further confidence in this from the fact that the velocity shift of the [Fe XIV] line is similar to that of the [Fe X] and [Fe XI] lines. Differentiation of the [Fe XIV] and [Ca V] lines is helped by the fact that the former is more strongly blueshifted thereby increasing the observed separation from the intrinsic 6Å to 15-20Å. That the ionisation potential of [Ca V] is significantly less than that of [Fe XIV] (67eV and 361eV, respectively) provides further evidence that blueshift increases with the ionisation potential of the emitting species.

2.3.4 *Mrk 573*

Mrk 573 is a relatively well studied nearby ($z = 0.0170$) Seyfert 2 galaxy, which has been shown to contain a hidden BLR that is detectable in polarised light (Nagao et al. 2004) suggesting the presence of obscuring matter along our line of sight to the BLR, possibly the putative torus. We therefore observed this galaxy as a comparison for the Seyfert 1s, but without the complication of broad emission components on both the permitted lines and the *FHILs*.

As Erkens et al. (1997) had already found, this Seyfert 2 contains strong *FHILs*. We chose to observe this galaxy at higher spectral resolution and S/N levels, to determine if these lines had any structure in their profiles that might indicate outflows or turbulence in the *FHIL* emitting regions of Seyfert 2s.

The various line profiles extracted from the spectrum of *Mrk 573*, with their associated Gaussian fits are shown in the last panel of the all the figures discussed previously.

Narrow Emission Lines

As expected for a Seyfert 2 spectrum, all the emission lines in *Mrk 573* are considerably narrower than the permitted lines observed in Seyfert 1 galaxies. However the strong [O III] and Balmer emission lines show signs of symmetric, broad wings and were modelled with multiple Gaussian components, while all the weaker lines were satisfactorily

fit with a single component. Excluding the broad wings of the strongest lines, all the emission lines had similar velocity widths of FWHM ~300km/s. We also detect strong He IIλ4686 emission in this galaxy.

Forbidden High Ionisation Lines

Of note is the large number of *FHILs* that we detect in *Mrk 573*. They are comparable to the most highly ionised Seyfert 1 spectrum in our study, *Ark 564*. In addition to [Fe VII]λ6087 both [Fe VII]λ5159 and [Fe VII]λ5722 are well detected. In contrast to the trend found in the Seyfert 1s, the highest ionisation lines in Mrk 573 show no sign of asymmetry or wing broadening, and have thus been fitted with a single Gaussian. The resulting profiles of [Fe X] and [Fe XI] have widths and velocity shifts similar to that of [Fe VII]. We note that these lines appear to be redshifted relative to [S II], but are consistent with the velocity of the Mgb absorption lines. We do not detect [Fe XIV]λ5303 in this object.

2.4 Discussion

As described in detail in the previous sections, we have been able to decompose many of the optical emission lines into multiple components that span a range in velocity widths and velocity shifts – indicating that the spectra of Seyfert galaxies cannot be considered simply in terms of narrow and broad emission lines. This is clearly shown in Fig. 2.5, in which we display the range of the component widths for each line species which we will discuss in detail.

While traditionally the permitted lines of Seyfert galaxies were considered to be a blend of emission from both the broad and narrow line regions, we find evidence of a very broad (2500km/s $\lesssim$ FWHM $\lesssim$ 7000km/s) third component in 6/9 of the Seyfert 1s (all six of them NLS1s) we observed. This extra component was previously noted in the NLS1 galaxy *KUG 1031+391* by Mason et al. (1996) with a measured FWHM (~2500km/s) more typical of the broad lines in a Seyfert 1. It was suggested by Gonçalves et al. (1999) that the broad wings of the Balmer lines in *KUG 1031+391* were better fit with a single Lorentzian profile, although Dietrich et al. (2005) have since shown that this function's profile overestimates the core of the line, while underestimating the flux in the wings, in their study of 12 NLS1 galaxies. We defend our use of a 3 Gaussian component fit in §2.2.6. These models reveal a very broad component in a further 6 NLS1

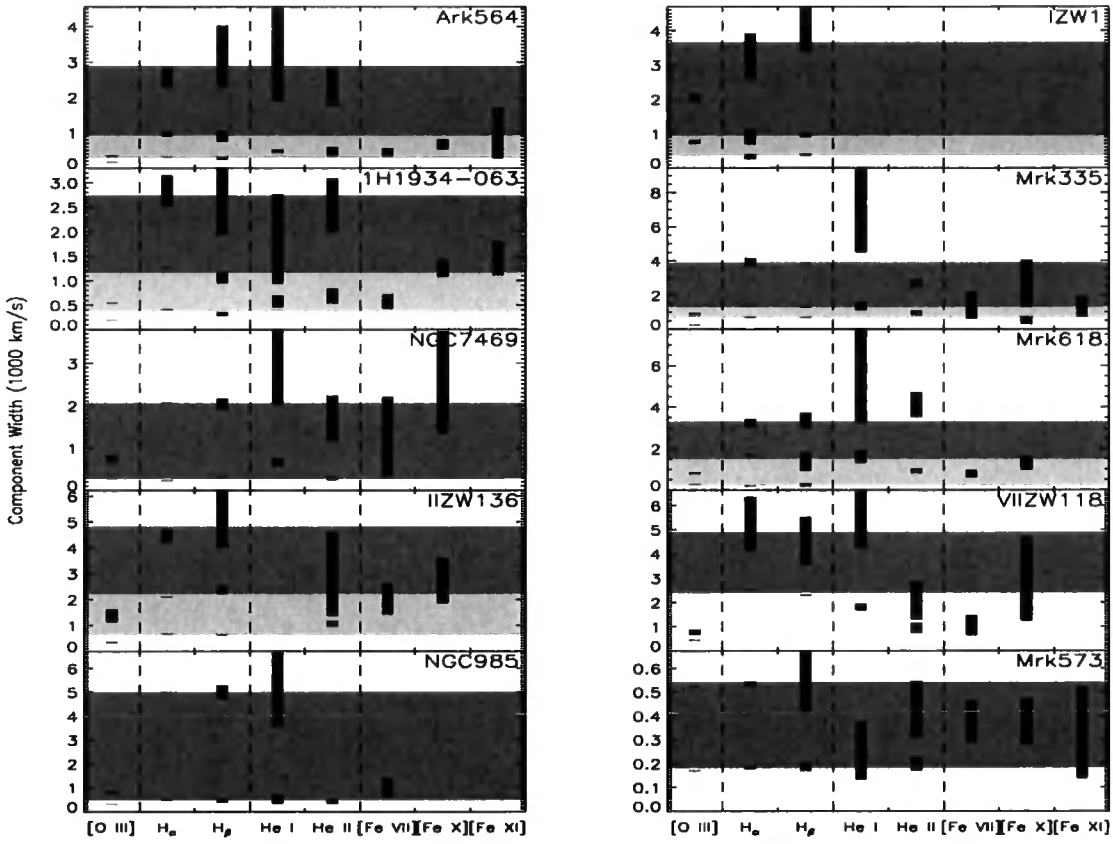

Figure 2.5: The component widths of each of the lines discussed in detail in this paper. The vertical height of each block represents the extent of both the systematic and random errors associated with each line model component. The shaded areas represent the regions between the 'narrow' and 'intermediate' and 'intermediate' and 'broad' widths, averaged between the Hα and Hβ components (only one shaded region is shown in cases where the permitted line fit required only 2 components). This clearly shows that the *FHILs* tend to have widths between those of the traditional broad and narrow emission lines.

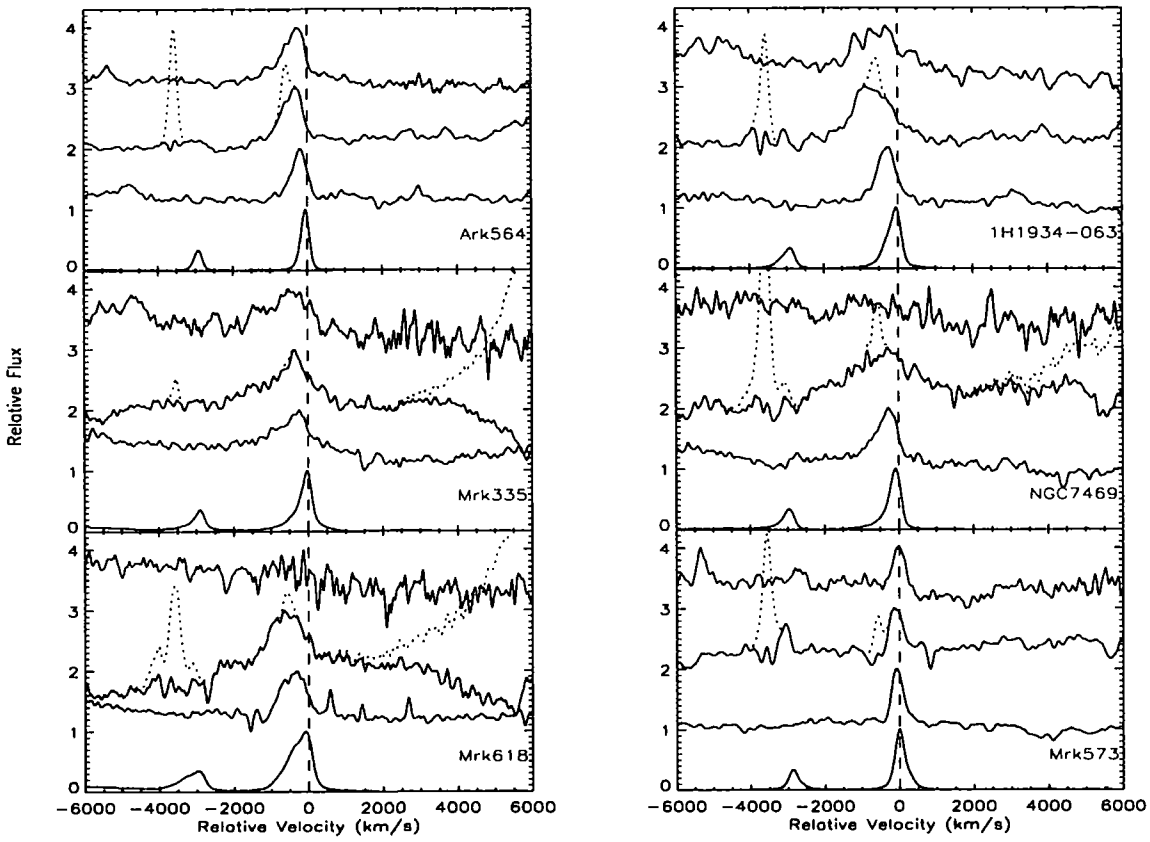

Figure 2.6: Comparing the profiles and velocity shifts of the high ionisation lines. We include the narrow [O III] line as a comparison. Profiles shown are (from bottom) [O III]λ5007, [Fe VII]λ6087, [Fe X]λ6374 and [Fe XI]λ7892. The dotted lines indicate removed features, such as the [O I]λ6363 line that is often blended with the [Fe X]λ6374 line and the blue wing of the Hα line. It is generally seen that line widths and shifts increase with ionisation potential.

galaxies, in which we measure broad components of similar widths when fitting both the Hα and Hβ lines independently. We note that care must be taken when interpreting lines with multiple components. It is unlikely that the dense emitting gas around the central engine can be simply divided into discrete velocity-width bins (in this case, three). The true situation is that we see an amalgam of emission from a ensemble of clouds along our particular line of sight with a wide range of velocity widths (see, for example, Osterbrock 1993).

As discussed by Dietrich et al. (2005), the fact that we see emission line components with widths similar to those of the broad emission lines of BLS1 galaxies indicates that emission from this BLR may be reduced in NLS1s, rather than absent altogether. This could imply either:

- that we should no longer assume that black hole masses in NLS1s are smaller than in BLS1s. This may appear to contradict other evidence of reduced black hole masses in NLS1s, including values derived from stellar velocity dispersion (σ) and X-ray variability measurements. It has been claimed, however, that the validity of the M_{BH}-σ relation shown in Figure 2 of Barth et al. (2005) is uncertain at low values of values of σ. This is particularly evident when one considers that the M_{BH} estimate for M33 is a hard upper limit (and more likely that this galaxy does not contain a central black hole; Gebhardt et al. 2001) and the mass of the black hole in NGC4395 has been revised upwards by an order of magnitude (Peterson et al. 2005). Taking this into account, it is possible that the M_{BH}-σ relationship shows an upturn at low values of σ, strengthening the claim that we may expect broader components in the Balmer lines of NLS1s. Also, although detailed long term X-ray variability measurements can be used to derive black hole masses using their power density spectra (see e.g. McHardy et al. 2006), isolated short term X-ray variability may not be a reliable indicator of the black hole mass. This has recently been shown by Reeves et al. (2002).

- that NLS1 galaxies *do* contain lower mass black holes, but the radius of the broad line region scales in proportion to the mass of the black hole. This would then mean that other factors determine the observed widths of the lines.

For both these explanations, we would need a theory to explain the reduced relative luminosity of the very broad component. This could be disruption by the inner parts of an energetic wind originating from within the accretion disc that would have the largest

effect on a nearby broad line region, or the strong UV/soft X-ray flux seen in the SED of many NLS1s in the form of the soft-excess, or a mixture of both.

We find that the permitted Helium line profiles differ considerably from the Balmer lines for the sub-set of galaxies (6/7) in which the Helium line can be measured. This fact has been reported by Shuder (1982), and has since been briefly mentioned in the course of a number of permitted line studies (e.g. Almog and Netzer 1989, Dietrich et al. 2005), in which the broad component of the He I λ5876 line was found to be broader than the corresponding Balmer line component. We too find that this is the case in three of the galaxies in which this line was observed. This suggests some form of segregation of the broad line region, in which different species of permitted lines are emitted preferentially in regions with differing conditions and kinematics. This is also suggested by the results of the locally, optimally emitting cloud (LOC) models of Baldwin et al. (1995). Because we are uncertain of the processes that cause broadening of the permitted lines we cannot rule out diverse explanations, for example, that a greater proportion of the He I emitting region lies closer to the central engine than the Balmer line emitting region, because of the higher ionisation of Helium compared with Hydrogen, or alternatively whether the Helium clouds are undergoing greater turbulent motion or are outflowing/inflowing at higher speeds as has been discussed by e.g. Collin-Souffrin et al. (1988). However, caution must be taken when interpreting the widths of the He lines, as we have shown that the level of the underlying continuum can have a considerable effect on the properties of the fitted components.

Due to the difficulties with blending, we have been unable to measure the broad component of the He IIλ4686 line to the same degree of accuracy as He I and Balmer lines. Despite this, there is some evidence that it has a broad component with a FWHM which is significantly less than the corresponding He I and Balmer line components (see, in particular, *Ark 564*, *Mrk 335*, *NGC 7469* and *VIIZW118* in Fig. 2.5). If this is the case, and is not the result of measurement errors or Fe II removal, then this runs counter to the prediction from photoionisation models of Korista and Goad (2004)- that the broad components of the permitted lines should increase in width with increasing ionisation potential. Landt et al. (2008) find a similar situation when comparing the widths of the permitted lines in both optical and near-infrared spectra. They speculate that this effect may be caused by an accelerating outflow, in which the He^{+} gas is closer to the source of the ionising continuum than He^{0}, but is outflowing more slowly as it has yet to be accelerated to its terminal velocity. This would be a very important result, but clearly

much more work is necessary to determine the true kinematics of the He I, He II and the Hydrogen emitting clouds.

Evidence of emission components with widths between the conventional broad and narrow lines is also seen in the forbidden lines of all the objects we observe, in the form of a broad blue wing. This is a well known feature that has been studied in depth since its first detection and description by Heckman et al. (1981), in which they attribute the blue wings of the [O III] lines to outflowing gas, which is likely to have a density similar to the traditional NLR (i.e. $n_e \sim 10^4 \mathrm{cm}^{-3}$), interspersed with dust that preferentially obscures the gas outflowing in a direction away from us. More recent studies (Whittle 1992, Christopoulou et al. 1997, Veilleux et al. 2001, Véron-Cetty et al. 2001) confirm that the [O III] emission is likely to arise from an ambient region at the same redshift and rotational velocity as the host galaxy, and an 'outflowing' region that is distributed in two wide angle ionisation cones. We note that the critical densities of [O III]λ5007, [Fe VII]λ6087 and [Fe X]λ6374 ($\log(n_e) \sim 5.8$, ~ 7.6, ~ 9.7, respectively; Appenzeller and Oestreicher 1988) suggest that the outflowing gas responsible for [O III] blue wings is likely to have a lower density than the *FHIL* outflows.

Strong evidence of gas with kinematics between the classic narrow and broad emitting regions is found in the form of the *FHILs*. As was noted in Erkens et al. (1997) and Rodríguez-Ardila et al. (2006), we find that as well as being significantly broader than the lower ionisation forbidden lines, these lines show increasing blueshift with increasing ionisation potential. This is clearly shown in Fig. 2.6, in which we plot the line profiles in terms of velocity shift from systemic for the [O III]λ5007 and the Fe *FHILs*, which suggests an outflow that is possibly related to that responsible for the broad, blue wing of the [O III] lines.

We note that, where it is measured, the width of the [FeVII]λ6087 line is generally between that of the narrow and intermediate Balmer line components. This, combined with findings that this line also tends to be blueshifted with respect to the permitted and low ionisation forbidden lines suggest this line is emitted from a kinematically distinct region. We find that the relative intensity of the [Fe VII]λ6087 is reasonably constant among our small sample, at 2-4% flux of the Hβ line in all the galaxies we observed. A larger, more homogenous sample would be required to fully determine correlations between the [Fe VII] line properties and AGN classes, such as NLS1s and BLS1s.

Our fits to the [Fe X]λ6374 line suggest that this species is formed in yet another kinematically distinct region, as was noted by Rodríguez-Ardila et al. (2006) for nearby

Seyfert 1 and Seyfert 2 galaxies. Although approximately twice as strong as [Fe VII]λ6087 in all the galaxies in which it is detected, this line is more poorly defined because of its much broader profile and its blending with other emission lines. In many of the galaxies it has a broad component that approaches the FWHM of typical of broad permitted lines, and shows little or no evidence of a narrow component, possibly implying that the Fe^{9+} ion is only created in regions near to the central source of ionisation, which would agree with the predictions of the photoionisation models of Ferguson et al. (1997). As found for [Fe VII], the relative intensity of the [Fe X] line appears to be similar in all the galaxies we observed ($\sim$8% Hβ, or 2$\times$[Fe VII]λ6087). We note that the almost constant value of [Fe X]λ6374/[Fe VII]λ6087$\sim$2 appears at odds with the findings of Nagao et al. (2000), who generally found lower values for this ratio in a larger sample of AGN (including NLS1s, BLS1s and Sy2s). We note, however, that the systematic errors associated with the fitted continuum level has a significant effect on the measured intensity of the broad components of these weak lines, which could account for these differences.

In contrast to generally similar relative [Fe X]λ6374 line intensities among our sample, we find that the [Fe XI]/[Fe X] ratio covers a wide range e.g. from $\sim$1 in *1H1934-063* to < 0.03 in *NGC 7469* (taking 90% upper confidence limits for the [Fe XI] line). This is despite the fact that these two species have similar ionisation potentials (235eV and 262eV for [Fe X] and [Fe XI], respectively). The origin of this wide range of ratios is not well understood. However, it is in agreement with the photoionisation models of Ferguson et al. (1997), who point out that the [Fe XI]λ7892 line is highly sensitive to the density and ionisation parameter of the *FHIL* emitting region. In addition, if we assume that [Fe XI] is produced by photoionisation (as suggested by Penston et al. 1984) it is possible that the range in the line ratio is also a function of the continuum shape in this energy region.

Despite the difficulties in extracting the [Fe XIV]λ5303 mentioned in §2.3.3, we are able to qualitatively confirm the presence of this line in two of our sample, *Ark 564* and *1H1934-063*. These galaxies also display strong [Fe X]λ6374 and [Fe XI]λ7892 lines, and we are able to show that the blueshift of the [Fe XIV]λ5303 line is similar to the blueshift of these other lines, giving us further confidence in this detection. However, it should be emphasised that the systematic errors associated with this measurement caused by the removal of the FeII blend is unknown and are likely to be large, we therefore make no attempt to interpret the intensity or width of this line.

Finally, turning to the case of the only Seyfert 2 in our sample, it is clear from Fig.

2.5 that the highest ionisation lines in *Mrk 573* trace a kinematically different region than both the permitted and other forbidden lines. Apart from a weak, broad component of the [Fe VII]λ6087 line, the widths of *FHILs* are all relatively low (FWHM $\sim$ 400km/s). These results agree with those of Almudena Prieto et al. (2005) and Rodríguez-Ardila et al. (2006), who found that there is significant [Si VII] (a *FHIL* observed in the near-IR) emission in regions up to $\sim$150pc from the nuclei in four nearby type 2 galaxies. However, it is difficult to reconcile their results with our findings for BLS1s and NLS1s in terms of the standard AGN model. Strong [Fe XI]λ7892 is detected in all four type 2 galaxies observed by Rodríguez-Ardila et al. (2006) and in our work. However, this line is detected in less than half of the type 1s that have been observed by us and in Erkens et al. (1997). If, using the standard model we expect that the NLRs of both type 1 and type 2 galaxies are essentially the same then we would expect from the type 2 results to detect a narrow [Fe XI]λ7892 line in a much larger proportion of type 1 galaxies. Of course, sample selection effects may be important and it will be necessary to observe larger samples of the various AGN types at comparable signal to noise to make further progress in this area.

2.5 Summary

The main conclusions from our study can be summarised as follows;

- The emission lines in the spectra of both BLS1s and NLS1s appear to be emitted from more zones than the traditional narrow and broad line regions. This is particularly evident in the profiles of the *FHILs*, but also in the profiles of the broad, permitted lines of Hα and Hβ. The lines from the *FHIL* region typically have a FWHM of 1000 - 3000km/s, and are significantly narrower than the broadest components of the permitted lines observed in the same object.

- All of the NLS1s in our sample show evidence of a very broad component in their permitted lines. This component has a FWHM that is more typical of that observed in the broad lines of BLS1s, i.e. $\sim$3000km/s. Although the FWHM measurements are a product of our line modelling process, the point that the broad wings of the permitted lines extend to up to 3000km/s in even the 'narrowest' NLS1s indicates that there exists emitting clouds with much higher relative velocities than has typically been assumed in this sub-set of Seyferts. However, this component appears

to be greatly suppressed in the case of NLS1s. We speculate this suppression might be either a result of the destruction of the standard BLR by an energetic wind or by the increased high energy photon flux of NLS1s, or both. We propose two methods of production of this extra broad component: 1) a higher mass black hole than is expected for NLS1s and a BLR radius more typical of BLS1s, or 2) a low mass black hole and an equivalently smaller BLR radius.

- We detect [Fe XI]λ7892 in a few cases where the data has sufficiently high signal to noise. Despite [Fe X] and [Fe XI] having similar ionisation potentials, the [Fe X]/[Fe XI] ratio covers a wide range within our sample. It is therefore possible that this ratio is very sensitive to the physical conditions of the emitting region as well as the shape of the ionising continuum.

- Strong, narrow *FHILs* are also detected in the Seyfert 2 *Mrk 573* (as also noted by Rodríguez-Ardila et al. 2006). Since it has been shown that this AGN contains a hidden BLR, this result indicates that *FHILs* can be formed in regions beyond the extent of the putative dusty molecular torus.

Chapter 3

A novel method of searching the SDSS catalogue for FHIL emitters[1]

3.1 Introduction

A large proportion of modern astronomy is now based on astronomical surveys. The dawn of this era was brought about by the use of photographic plates and the arrival of telescopes with wide fields of view (e.g. the Palomar Observatory Sky Survey, completed in 1958, which later became the Digitised Sky Survey). However, in the last two decades, the development of highly automated telescopes, detector technology and space-based missions has brought about significant advancements in our ability to map the sky. Astronomers now have free access to a large number of exhaustive surveys sampling almost all detectable portions of the electromagnetic spectrum; at radio wavelengths (e.g. *FIRST*, *NVSS*), through the far- and near-IR (e.g. space-based *IRAS* mission and ground-based *2MASS*, respectively), optical (see later), UV (e.g the space based *IUE* mission) to X-ray energies (e.g. the space-based *ROSAT* mission).

Two of the most recent dedicated sky surveys, the 2-degree field survey (*2dF*; taken with the Anglo-Australian Telescope at Siding Springs, Australia; Lewis et al. 2002) and the Sloan Digital Sky Survey (*SDSS*; taken with the dedicated *SDSS* telescope at the Apache Point Observatory, New Mexico, US; Stoughton *et al.* 2002) brought about a new era in astronomical surveys with their ability to obtain, analyse and catalogue the spectra of multiple objects by combining state-of-the-art instruments with robust data

[1]Note: This chapter is based on work that is to be published in Gelbord, Mullaney & Ward (submitted to *MNRAS*)

reduction pipelines. By providing access to vast searchable databases which together contain spectral information on over a million individual objects, these surveys enable astronomers to study both general trends among different classes of objects, and search for the proverbial 'needles in the haystack'- rare objects which would otherwise take a lifetime of pointed observations to find.

Prior to the advent of large spectral surveys, studies of *FHILs* were limited to objects which had previously had their spectra taken during pointed observations (e.g. Morris and Ward 1988). This introduces a strong selection effect as these objects are likely to fall into one or both of the following categories:

- they are bright, and therefore easily observed
- they are particularly interesting objects (e.g. strange morphologies, undergoing collisions, particularly broad/narrow emission features, strong X-ray/UV/IR emitters etc.)

Today, the largest dedicated studies of *FHILs* to date are those described in Murayama and Taniguchi (1998) and Nagao et al. (2000), which are based on compilations of spectra from such pointed observations. By compiling a sample of AGN from the available literature, these studies avoided preferentially selecting AGN with very strong *FHILs*. This enabled the study of AGN with a full range of *FHIL* luminosities. For example, in the larger of these two samples (described in Nagao et al. 2000) out of 227 objects, only 124 (or 55%) showed any sign of *FHIL* emission. In those studies, the authors separate their analysis by AGN type, noting systematic differences between the *FHIL* emissions of type 1s and type 2s. In particular, they note an apparent weakening of the *FHILs* (most prominently [Fe VII]) relative to the lower ionisation lines ([O III]λ5007, [S II]$\lambda\lambda$6717,6731 and [O I]λ6300) in their type 2 population compared to their type 1 populations. They go on to suggest that this is the result of the *FHILs* being produced on the inner wall of the dusty obscuring torus, i.e. the same obscuring torus that keeps type 2 nuclei hidden from our view would also partially obscure the *FHIL* emitting region.

The placing of the *FHIL* emitting region on the inner wall of the torus, between the broad and narrow line regions, has important consequences for our understanding of the structure and kinematics of the immediate AGN environment. The blueshifting of the *FHILs* implies a general outflowing of this material and it has been suggested (e.g. Porquet et al. 1999) that the *FHIL* emitting region could represent a link between the inner and outer AGN regions.

With its database of over 900,000 AGN and galaxy spectra, the *SDSS* presents an excellent opportunity to study the *FHIL* emitting objects without the constraints and biases associated with previous samples. In this chapter we considerably improve on the number statistics of previous surveys of *FHIL* emitters by introducing a novel method of extracting AGN spectra that show evidence of *FHILs* from the *SDSS* database.

It should be noted that the work described in this chapter led directly onto that described in Chapter 4. In that chapter, we describe how we used the analysis techniques developed in section 3.3.1 to a much larger pool of spectra from emission line objects that is less affected by the biases described in the following sections. In this respect, this chapter should be considered as preparatory work prior to the creation of our larger sample.

3.2 Sample selection

The sample discussed in this chapter was obtained by applying filtering criteria to the *SDSS* database produced by the spectral fitting pipeline described in Stoughton *et al.* (2002). In brief, this automated pipeline attempts to model each spectrum with a 5^{th} order polynomial fit to the continuum and a single Gaussian for each fitted emission or absorption line. Although a large number of strong emission lines are fitted by the pipeline, it does not attempt to fit any of the optical *FHILs*. Therefore, in order to obtain our sample of strong *FHIL* emitters, an indirect method of querying the database was used.

One of the optical *FHILs*, namely [Fe X]λ6374, lies close enough to the low ionisation [O I]λ6363 emission line to form a blend in low resolution spectra. In the *SDSS* spectral fitting pipeline, no account is taken of this blend, meaning the corresponding Gaussian fit to the [O I]λ6363 line incorporates the [Fe X] line, if both lines are present in the spectrum. As the [O I]λ6363 line is the weaker line of a fixed-ratio doublet, we were able to use the *SDSS* pipeline measurement of the [O I]λ6300 (the other emission line of this [O I] doublet) to search for AGN with [O I]λ6300/[O I]λ6363 ratios lower than the fixed ratio of 3 (given by atomic physics), thereby revealing the presence of the [Fe X] emission line.

Prior to performing our extraction based on the measured [O I] lines, we queried the *SDSS* database for all spectra that displayed Balmer and [O III] emission lines as, in this study, we are principally interested in *FHILs* emitted from AGN. We also applied a

redshift cut of z<0.3 to ensure that all sample spectra contained the Hα emission line. Following these steps, we then queried the resulting database for spectra that contained both of the [O I] emission lines. On inspection of the results produced by this initial cut, it was noted that a large proportion of the spectra with [O I]λ6300/[O I]λ6363 < 3 (i.e. those potentially indicating the presence of the [Fe X] line) had low [O I] equivalent widths and the deviation from the expected ratio was due to large uncertainties in the measurement of these lines. To deal with this problem, we concentrated our later queries to return spectra with high confidence measurements of the [O I] lines (i.e. with peak modelled line flux greater than 10σ above the continuum level).

On inspection of the resulting spectra with [O I]λ6300/[O I]λ6363 < 3 ratios, it was clear that a considerable number of these were misidentified as [Fe X] emitters because the broad wings of the Hα lines were fitted with the [O I]λ6363 Gaussian. This has the effect of producing apparently stronger [O I]λ6363 measurements in the pipeline. To mitigate this effect, we placed an upper limit to the velocity width of the Hα ($\sigma < 50\AA$) in our final query.

Our final query produced a sample of 120 objects with [O I]λ6363 stronger than that predicted by the fixed [O I] flux ratio. On inspection, 65 of these showed clear evidence of an [Fe X] emission line.

Clearly this sample is not complete. Due to the limitations of the *SDSS* spectral database, we are only able to search for one *FHIL*. We are therefore likely to be missing a significant number of objects with strong [Fe VII] and (less likely) [Fe XI] lines. Also, by being constrained to limit our queries to remove AGN with broad Balmer lines, we preferentially select narrow line AGN (narrow line type 1s and type 2 objects). Despite these limitations, this sample is unique in terms of its lack of bias with respect to previously studied objects.

3.3 Analysis

3.3.1 Fitting routine

Each spectrum from our selected sample was analysed using an automatic emission line fitting routine developed by myself. The first attempts at this involved modelling the shape of the underlying continuum across the entire region of interest (i.e just blueward of the Hβ line to redward of the [Fe XI] line) with a third order polynomial. After removal of this fitted continuum, all the emission lines of interest were fit simultaneously

with progressively complex models incorporating increasing numbers of Gaussian components (up to three per emission line in the case of Hα). After each fit the change in χ^2 ($\Delta\chi^2$) was used to determine whether the addition of a given Gaussian component caused a significant improvement to the spectral fit.

Although this complex routine was able to accurately fit the strong Hα and [O III] emission lines, it became clear that it was unable to produce accurate measurements of the weaker emission lines, particularly [Fe VII] and [Fe X]. Both these *FHILs* are frequently contaminated by other emission features; the [Fe VII] line by TiO from stellar sources and the [Fe X] line by weak Hα wings. This means that spectral line fitting routines employing global continuum fits (as described in the previous paragraph) often overestimate the flux of these lines by attributing the overabundance of flux from the contaminant to the [Fe VII] or [Fe X] line. To overcome this problem we chose to break up the spectral fitting process to focus on narrow spectral 'windows' centred on individual lines or small numbers of blended lines. By doing so we were able to define the local underlying continuum irrespective of contaminants and obtain a more precise measurement of the weaker emission lines in our spectrum.

As with the more complex routine described at the start of this section, in cases where more than one Gaussian was fitted to a given spectral window we continued to build up the model by increasing the number of components and use $\Delta\chi^2$ to determine whether the addition of an extra Gaussian component produced a significant improvement to the fit . In the following we describe the steps we followed for each spectral window. A summary of the fit components is given in Table 3.1. In what follows, the collective 'Gaussian parameters' refers to the full width half maximum (FWHM), velocity shift from systemic and normalisation above the continuum-removed spectrum.

[O III]

1. Fit the local continuum with a third order polynomial, anchoring the fit to the spectrum within the wavelength windows: [4900Å, 4935Å], [4975Å, 4985Å] and [5040Å, 5090Å]. These were chosen for their lack of strong emission or absorption features (the Hβ wings, if present, were fitted as an underlying continuum feature).

2. Fit the [O III]λ5007 emission line with a single Gaussian of fixed width (200km s^{-1} FWHM) and velocity shift (0 km s^{-1}), allowing its normalisation to vary to the best fit value. The choice of FWHM=200km s^{-1} was used as it is a reasonable, if a little

Table 3.1: Lines fitted by the *FHIL* modelling routing and a summary of the component parameters.

Emission line	Number of Components	Final Fit Details
[O III]λ5007	≤ 2	All params. free
[Fe VII]λ6087	≤ 2	All params. free
[O I]λ6300	1	All params. free
[Fe X]λ6374	1	All params. free
[N II]λ6548	1	Shift and FWHM fixed to [O I] values
Hα λ6563	≤ 3	Shift and FWHM of one component fixed to [O I] values
[N II]λ6584	1	Shift and FWHM fixed to [O I] values
[S II]λ6717	1	FWHM fixed to [O I] values
[S II]λ6732	1	Shift and FWHM fixed to [O I] values

low, initial guess for the FWHM of the narrow lines in AGN spectra. We preferred to start to the model components with FWHM slightly less than typically observed, to reduce the likelihood that the fitted components become too broad and fit the underlying continuum.

3. Allow the FWHM and velocity shift of the Gaussian fitted in step 2 to vary from the assigned values.

4. Introduce an additional Gaussian component. Allow all parameters (normalisation, FWHM and velocity shift) of both components to vary.

[Fe VII]

1. Fit the local continuum with a first order polynomial, anchoring the fit to the spectrum within the wavelength windows: [6030Å, 6055Å], [6120Å, 6160Å].

2. Proceed using the same process as for the [O III] fit.

[O I] and [Fe X]

1. Fit the local continuum with a third order polynomial, anchoring the fit to the spectrum within the wavelength windows: [6250Å, 6280Å], [6325Å, 6350Å] and

[6400Å, 6430Å]. These windows ensured that any broad Hα wings are fitted as the local underlying continuum.

2. In order to deblend the [Fe X] and [O I]λ6363 lines, the [O I]λ6300 is initially fit with a single Gaussian. In the following steps this first Gaussian is scaled by a factor of 1/3 and placed at 6363Å to account for the blended [O I] line, around which the [Fe X] component is fit.

3. Introduce a Gaussian to model the [Fe X] line, allowing all its parameters to vary.

[O I], Hα, [N II] and [S II]

As the Hα line is a blend of narrow and broad components (in the case of type 1s) and [N II] emission lines, a more complicated fitting process was required to yield the best fit model.

1. Fit the local continuum with a third order polynomial, anchoring the fit to the spectrum within the wavelength windows: [6250Å, 6290Å], [6760Å, 6800Å], again, selected for their lack of strong emission and/or absorption features in the sample spectra.

2. Initially fit the Hα line with a single Gaussian, allowing all its parameters to vary. This forms an initial estimate of the Hα FWHM and normalisation. Fit the narrow lines ([O I]λ6300, [N II]$\lambda\lambda$6548,6584 and [S II]$\lambda\lambda$6717,6732) each with a single Gaussian of fixed FWHM (200km s^{-1}) and velocity shift (0km s^{-1}).

3. Allow FWHM and velocity shift of the [O I]λ6300 line to vary. The resulting fit determines the FWHM and velocity shift of the [N II] lines and narrow Hα component and the FWHM of the [S II] lines in the following steps.

4. Introduce a second Hα component. Allow only its normalisation to vary- its FWHM and velocity shift are fixed to the values determined from the [O I] line in step 3. This restriction ensures that this second Gaussian can only model the narrow Hα component and prevents it from becoming broad and weak enough to model the Hα wings or excess continuum flux. Allow all three parameters of the first fitted Gaussian to vary. Allow only the normalisation of the [N II] lines to vary

5. Allow the velocity shift of both [S II] lines to vary, yet keep their velocity shifts linked to each other (i.e. both components must shift by the same velocity). We

use this [S II] shift as a measure of the systematic redshift of the source.

6. Introduce a third Hα component. Allow all its parameters to vary, along with all the parameters of the first Gaussian. Allow only the normalisation of the second Gaussian (introduced in step 4) to vary.

[Fe XI]

1. Fit the local continuum with a third order polynomial, anchoring the fit to the spectrum within the wavelength windows: [7790Å, 7860Å], [7910Å, 8090Å].

2. Introduce a single Gaussian to model the [Fe XI]λ7892 line. Allow all its parameters to vary.

3.3.2 Parameter analysis

Due to the relatively small size of our sample we were able to check each fit to ensure that the fitted component parameters were indeed providing a reliable measure of the emission line properties. By far the most common cause of failure was the broadening of second (or third) components to fit residual continuum. In cases where this occurred we reverted to using the line component parameters of a previous, more simple fit with fewer components. For example, if it was noted that the final [Fe VII] fit contained a very weak, broad additional component that was modelling continuum rather than a broad emission line asymmetry, then we reverted to using the results of the single component [Fe VII] fit in further analysis.

After fitting each spectrum with the model described above, we rejected a further three sources from our original sample of 65. One was rejected because its redshift placed the [S II] lines outside the *SDSS* spectral range; the other two were found to have no significant [Fe X] emission, once the [O I]λ6363 emission line had been fully taken into account.

3.3.3 Dust reddening

The line fluxes (and consequent luminosities) presented here have not been corrected for reddening. Based on measurements of the Balmer decrement and the continuum shapes of the spectra we estimate that the impact of reddening is generally small. Of the few spectra that appear to be affected by dust, by far the most reddened object has an estimated A_V value of 3.2. For no other object do we measure $A_V > 2$. To mitigate the

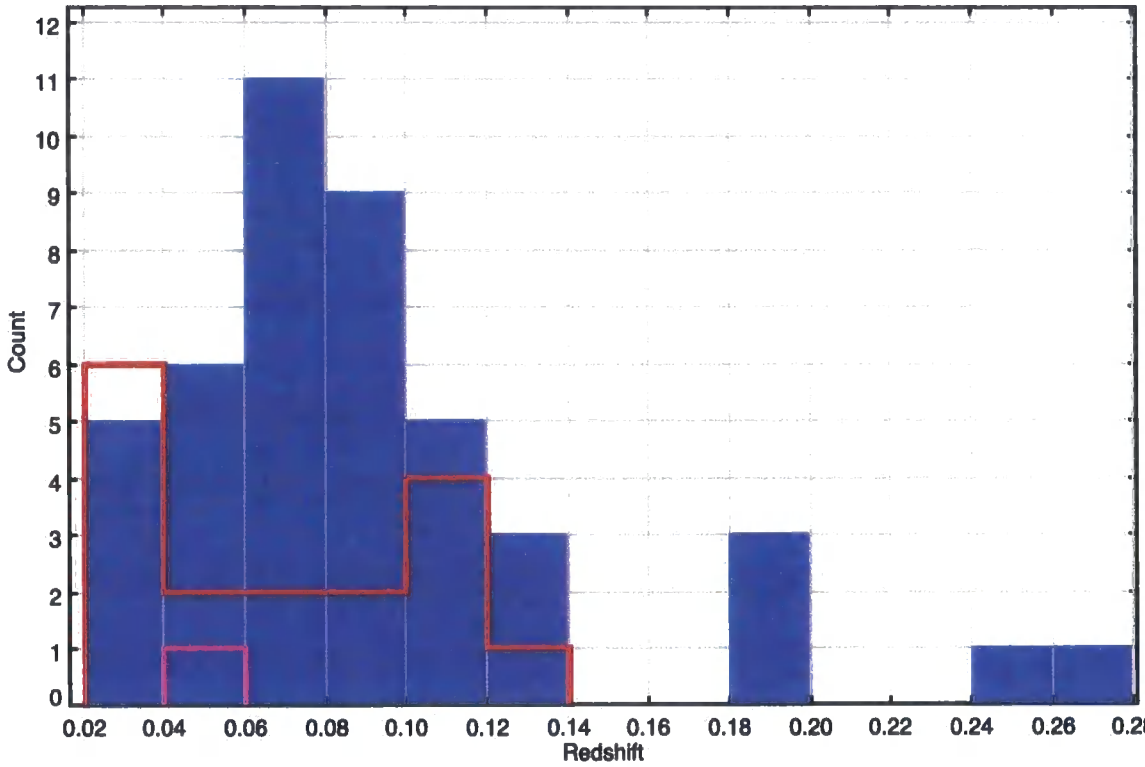

Figure 3.1: Redshift distribution of our [Fe X] selected sample. In all figures in this chapter, blue lines/points represent type 1s, red represents type 2s and (in this figure only) purple represents the object that cannot be attributed to either of these classifications.

effect of uncorrected reddening in our final conclusions, we will place greater emphasis on those derived from lines that are close in wavelength (e.g. [Fe VII], [Fe X] and Hα). For reference, in the case of objects with $A_V < 2$ the [Fe VII]/[Fe X] measurement is influenced at less than the 10% level; this is always smaller than the measurement uncertainty.

3.4 Results

The fitting routine produced best fit values, including 1-σ errors, for the normalisation, FWHM and velocity shift of the various Gaussian components of all the lines listed in Table 3.1. In the following sections we describe the key results from comparison of the *FHIL* properties against each other, against the properties of the other modelled emission lines and against archival X-ray data, where available.

3.4.1 Sample Statistics

The final sample of 62 spectra consisted of 44 type 1 and 17 type 2 AGN and one object with extremely strong high ionisation lines that did not fit into any AGN category. This latter object is discussed separately in §3.7; in the discussion that follows we only concentrate on the results from the AGN of our sample. We present the redshift distribution of our sample, determined from the [S II]λ6717,6732 doublet[1], in Fig. 3.1. The number of type 1 AGN peaks strongly at $z \sim 0.1$. This is a result of the combined effects of an increasingly large survey volume plus the reduced apparent brightness of sources at higher redshift. The type 2 population has a much more even redshift distribution which tends toward lower redshifts than the type 1s. This systematic difference is most likely the result of selection effects; type 2s are generally weaker optical emitters, a result of the strong obscuration along our line sight to the nucleus.

It should be noted here that the redshift distribution of the type 1s in our sample is similar to the sample described in Nagao et al. (2000). However, our type 2 AGN sample span a narrower, but higher, range of redshifts: $0.02 < z < 0.2$ compared to $0.001 < z < 0.2$. This is because the *SDSS* typically avoids very low redshift AGN due to the upper flux limit of $V \sim 15$ that is built into its spectral target selection system. The literature-based sample of Nagao et al. (2000), on the other hand, would have led to the preferential selection of bright objects at low redshifts.

3.4.2 *FHIL* luminosity correlations

In their study of *FHIL* emitting AGN Murayama and Taniguchi (1998) showed that the 18 type 1s in their sample were stronger [Fe VII] emitters, relative to the [O III] emission line, than the 17 type 2s (see their Fig. 1). This result was later confirmed using a larger sample of AGN consisting of 32 type 1s (11 NLS1s; 21 BLS1s), 34 type 2s and 38 type 1.5s (Nagao et al. (2000)). As their sample was composed of previously well studied AGN it was subject to the biases discussed in §4.1. We therefore wished to determine whether such a systematic difference between *FHIL* emission in type 1s and type 2s exists in a sample specifically selected on the basis of their *FHIL* line strengths.

In Fig. 3.2 we present histograms of the [Fe VII]/[O III] ratio and the [O III] luminosity for our sample, equivalent to Figs. 1 and 2 of Murayama and Taniguchi (1998) and

[1]We note that the velocity shift of the [O III] narrow component agrees very well with that of [S II]. In the [S II] frame, the [O III] line has, on average, a velocity shift of -5±40km s^{-1}. We use this result in the following chapter to justify our use of the stronger [O III] line as an indication of object redshift.

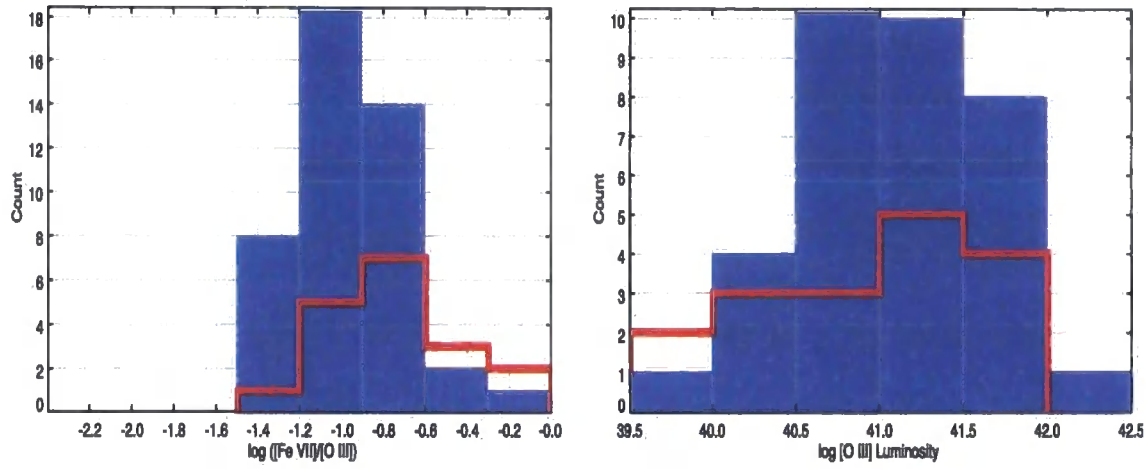

Figure 3.2: Histograms showing the distribution of [Fe VII]/[OIII] ratios and [O III] luminosities of our sample of Seyfert AGN. These are equivalent to Figs. 1 and 2 of Murayama and Taniguchi (1998) and Figs. 3 and 5 of Nagao et al. (2000). Despite our sample having a similar distribution of [O III] luminosities, the difference in [Fe VII]/[OIII] ratio between type 1s and type 2s presented in their plots is not evident in our sample. In the text, we explain how this may be attributed to the selection effects of both samples.

Figs. 3 and 5 of Nagao et al. (2000). Despite covering a similar range of [O III] luminosities, the [Fe VII]/[O III] ratio shows little or no systematic difference between the type 1 and type 2 populations when they are selected on *FHIL* strength.

In order to explain the difference between our results and those of these earlier studies, we now look more closely at the selection effects inherent in both samples. As our principal selection criterion is a strong [Fe X] line, we systematically choose AGN with strong [Fe VII] emission (Fig. 3.4 shows that the strengths of these lines are positively correlated). Although Fig. 3.3 indicates that [Fe VII] and [O III] line strengths are also positively correlated for this sample, in the general AGN population (both type 1s and type 2s) a strong [O III] line does not necessarily imply a strong [Fe VII] line. This latter point is clear from the statistics presented in Nagao et al. (2000): in general, only ~50% of AGN show detectable [Fe VII] lines, yet the [O III] line is present in all Seyfert spectra. Therefore, our selection criteria implies we are sampling the upper tail of the type 2 histograms presented in Fig. 1 of Murayama and Taniguchi (1998) and Fig. 5 of Nagao et al. (2000).

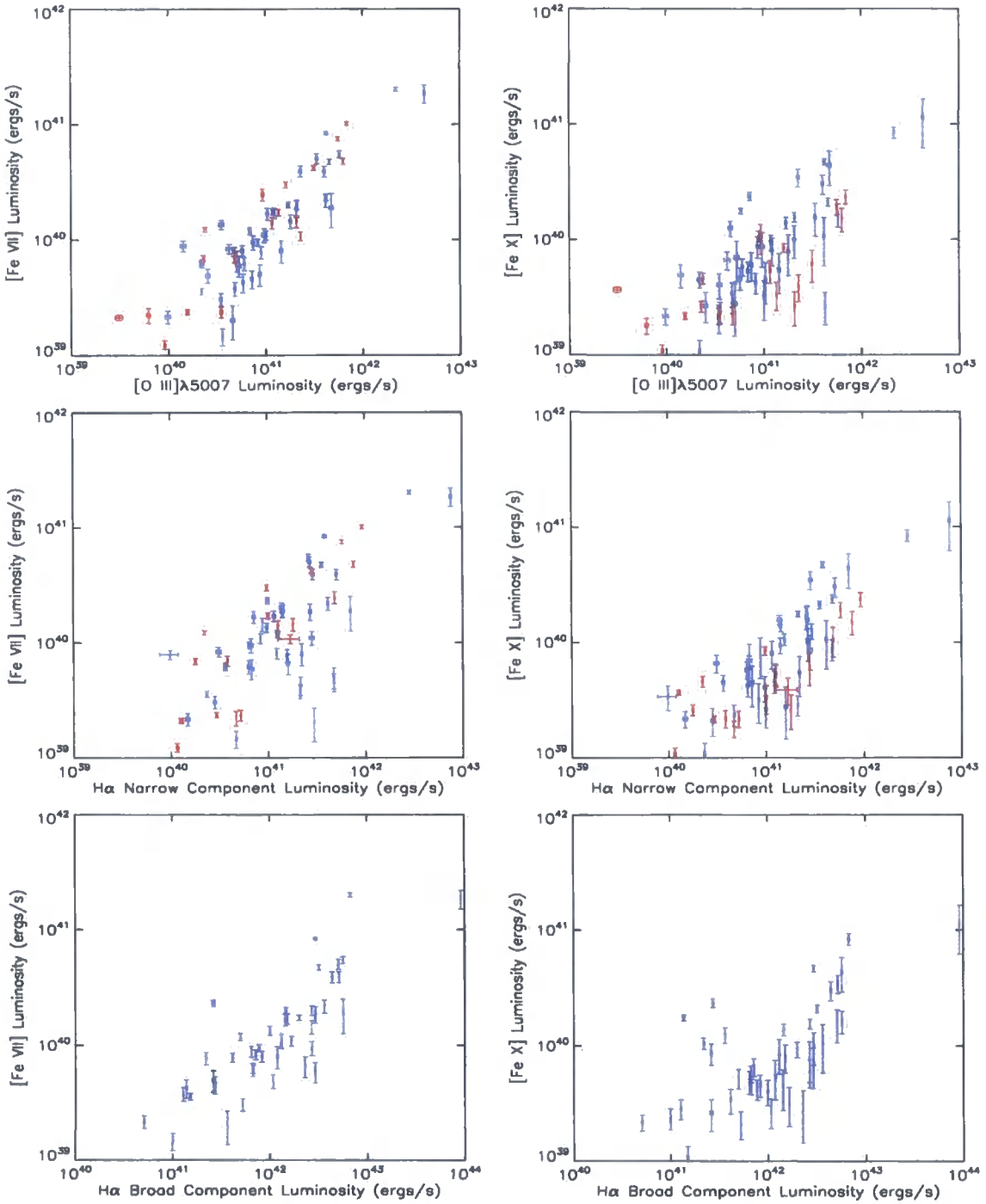

Figure 3.3: Line luminosity plots. Although a general positive correlation is evident between the *FHIL* luminosities and the [O III] and Hα broad and narrow components, there is no strong evidence that the *FHIL* luminosities are more correlated with either the narrow or the broad emission lines.

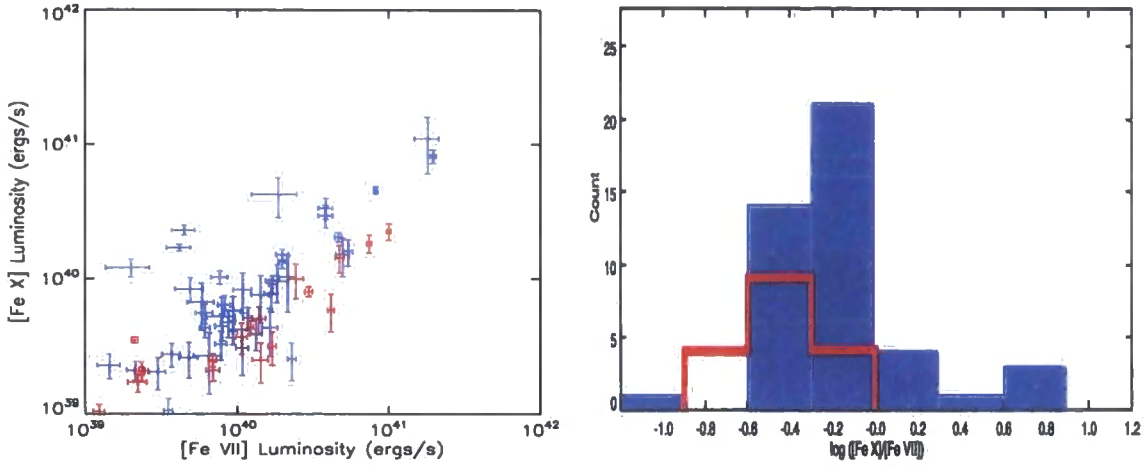

Figure 3.4: Left: [Fe X] luminosity plotted against total [Fe VII] luminosity. The type 2s have a systematically weaker [Fe X] line for a given [Fe VII] luminosity. Right: Histogram showing the distribution of [Fe X]/[Fe VII] ratio for both Seyfert types in our sample. This confirms the systematic weakening of the [Fe X] line in type 2s compared to type 1s. A KS test on these distributions reveals that there is less than a 0.001% chance that they are drawn from the same underlying populations.

We note that the [Fe VII] and [Fe X] line luminosities are positively correlated with those of the Hα and [O III] emission lines (see Fig. 3.3). As we modelled the Hα line with multiple components, we are able to determine whether the luminosities of the measured *FHIL* strengths are better correlated those of the broad or narrow emission lines. This is a pertinent question, as previous studies (e.g. Murayama and Taniguchi 1998, Porquet et al. 1999) have suggested that the *FHIL* emitting region lies between the broad and narrow line regions, but it is unknown which, if either, of these are more closely related to the *FHIL* emitting region in terms of their emission properties.

It is evident from the plots in Fig. 3.3 and the correlation statistics given in Table 3.2 that neither the broad nor narrow components of Hα or the [O III] line is significantly better correlated with the strength of either the [Fe X] or [Fe VII] lines. Of note, however, is the significantly stronger correlation between the [Fe VII] line luminosity and [O III] line luminosity (for both type 1s and 2s) than between [Fe X] and [O III]. The [Fe X] line luminosity shows a poorer correlation with the Hα broad component than does [Fe VII], indicating that the [Fe X] emitting region is not necessary more closely associated to the broad line region than the [Fe VII] emitting region.

Correlation	Spearman's ρ	Significance
[Fe VII]-[O III]$_1$	0.86	3.8×10^{-14}
[Fe VII]-[O III]$_2$	0.90	2.1×10^{-7}
[Fe VII]-Narrow Hα_1	0.51	4.8×10^{-4}
[Fe VII]-Narrow Hα_2	0.87	2.4×10^{-6}
[Fe VII]-Broad Hα_1	0.81	1.7×10^{-11}
[Fe X]-[O III]$_1$	0.72	2.9×10^{-8}
[Fe X]-[O III]$_2$	0.77	1.9×10^{-4}
[Fe X]-Narrow Hα_1	0.81	6.6×10^{-11}
[Fe X]-Narrow Hα_2	0.77	2.0×10^{-4}
[Fe X]-Broad Hα_1	0.63	5.2×10^{-6}
[Fe X]-[Fe VII]$_1$	0.62	7.1×10^{-6}
[Fe X]-[Fe VII]$_2$	0.89	9.7×10^{-7}
[Fe XI]-[Fe VII]$_1$	0.37	6.8×10^{-2}
[Fe XI]-[Fe VII]$_2$	0.89	9.7×10^{-7}
[Fe XI]-[Fe X]$_1$	0.86	4.0×10^{-8}
[Fe XI]-[Fe X]$_2$	0.92	6.9×10^{-6}
[Fe X]-0.1-2.4keV$_1$	0.82	5.7×10^{-8}
[Fe VII]-0.1-2.4keV$_1$†	0.53	2.5×10^{-3}
[Fe VII]-0.1-2.4keV$_1$‡	0.75	9.2×10^{-6}
Hα-0.1-2.4keV$_1$†	0.57	1.2×10^{-3}
Hα-0.1-2.4keV$_1$‡	0.83	1.5×10^{-7}
[O III]-0.1-2.4keV$_1$†	0.71	1.3×10^{-5}
[O III]-0.1-2.4keV$_1$‡	0.80	8.2×10^{-7}

Table 3.2: Luminosity-luminosity correlation statistics. The associated scatter diagrams are presented in Figs. 3.3-3.7. ρ is a measure of the strength of the correlation and can take values between -1 and +1; -1 and +1 refer to a strong negative and positive correlation, respectively. The significance is a measure of the likelihood of obtaining the observed correlation by selecting the points at random from an evenly distributed underlying population. Subscripts refer to AGN type. †Sample includes outliers discussed in §3.4.2 (indicated as triangles in Fig. 3.7). ‡ Sample excludes outliers.

Type	Mean	σ	Error in mean
1	0.98	1.2	0.18
2	0.50	0.39	0.09

Table 3.3: Statistics of the [Fe X]/[Fe VII] ratio for the two types of AGN explored here.

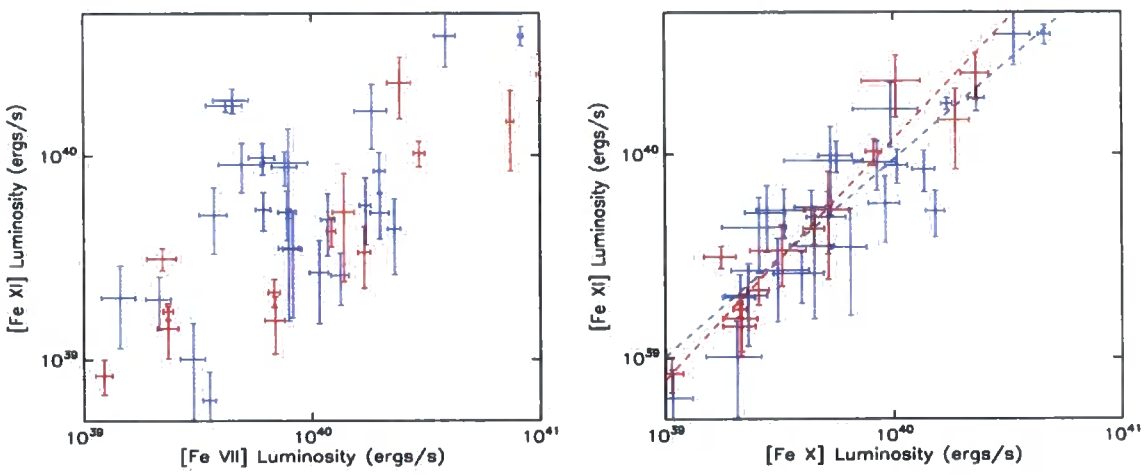

Figure 3.5: Left: [Fe XI] luminosity plotted against total [Fe VII] luminosity. The [Fe XI] line appears to show a similar, although not as pronounced, weakening as [Fe X] in type 2s. Left: [Fe XI] luminosity plotted against total [Fe X] luminosity. No systematic difference between the *FHILs* of type 1s and type 2s is evident on comparison of the [Fe X] and [Fe XI] line luminosities.

Comparison of the [Fe VII] and [Fe X] line luminosities reveals a positive correlation exists between these lines for both types of AGN explored here (see Table 3.2), but also that the type 2s in our sample have systematically weaker [Fe X] lines for a given [Fe VII] luminosity. This is evident in the left hand plot of Fig. 3.4. To investigate this difference further we produced a histogram of [Fe X]/[Fe VII] values, shown in the right hand plot of Fig. 3.4. This indicates that, indeed, the [Fe X]/[Fe VII] ratio shows less scatter in the type 2 population and is generally offset to lower values. Quantitatively, the [Fe X] line is on average 51% weaker (relative to [Fe VII]) in type 2 AGN than in type 1s (for a summary of these statistics see Tables 3.2 and 3.3). We therefore typically miss ~50% of the [Fe X] flux in type 2 AGN, although the considerable scatter on the [Fe X]/[Fe VII] ratio for the type 1 objects makes it difficult to assess how much [Fe X] emission is obscured in an individual type 2 object. As a final test of this result, we determined the Kolmogorov-Smirnov (KS) statistic for the two populations. This revealed a probability of $< 0.001\%$ that the type 1s and type 2s were drawn from the same underlying population.

A similar, yet less striking relationship is evident in the upper left and upper right plots of Fig. 3.3, which show how the [Fe VII] and [Fe X] line strengths are correlated with that of the [O III] line. Although there is no apparent difference between the type 1 and type 2 population in terms of the relative strength of the [Fe VII] line (as discussed above), type 2s appear to have a weaker [Fe X] line for a given [O III] strength. However, the probability that this represents two separate populations is much lower than the [Fe X]/[Fe VII] ratio (90%; less than 2σ significance).

The difference between the [Fe X]/[Fe VII] ratios of the type 1 and type 2 populations is reinforced in the left-side plot of Fig. 3.5, showing the correlation between [Fe XI] and [Fe VII] line luminosities. Although less clear than the [Fe X] vs. [Fe VII] separation of Fig. 3.4, the type 2s tend to have a lower [Fe XI] luminosity for a given [Fe VII] luminosity. Unfortunately, the low number of [Fe XI] measurements within our sample means a KS test would provide unreliable statistics. A plot of [Fe XI] vs. [Fe X] line luminosities reveals a strong correlation between these lines. This same plot, however, displays no systematic difference in the [Fe XI]:[Fe XI] ratio exists between the type 1 and type 2 populations (see right-hand plot of Fig. 3.5). The correlation statistics for the [Fe X] - [Fe XI] lines (see table 3.2) also reveal that there is a strong, almost 1:1, relation between their respective luminosities (a linear regression to log([Fe XI]) vs. log([Fe X]) gives a gradient of 0.96 ± 0.05 and 1.2 ± 0.1 for the type 1s and type 2s, respectively).

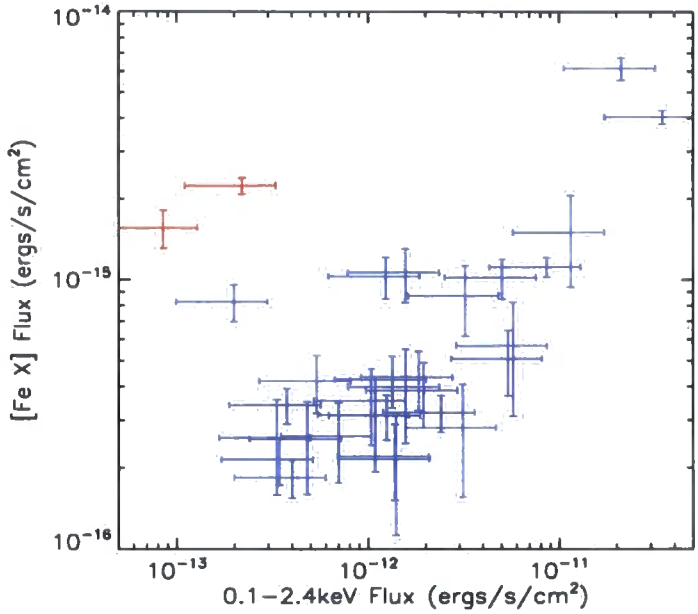

Figure 3.6: [Fe X] line flux plotted against X-ray flux. The flattening of the left-hand edge of the plot at low [Fe X] fluxes is due to the sensitivity limit of our method of extracting the sample from the *SDSS* database

FHIL correlations with X-rays

To investigate the relationship between *FHIL* emission and X-rays we cross-referenced our [Fe X] selected *SDSS* sample with the *ROSAT* all-sky X-ray survey database (described in Voges et al. 1999; for completeness, we also searched for objects with more recent X-ray detections with the current generation of X-ray telescopes, *XMM* and *Chandra*, but found no matches). On checking, it was found that 29/44 type 1s and 2/17 type 2s had associated X-ray measurements. In the discussion that follows, we have converted the *ROSAT* count rates in the 0.1-2.4keV band into flux measurements by assuming a power law index of Γ=1.5 and an absorbing column of n_H=3×10^{20}cm^{-2}. Given this assumed model, the conversion from *RASS* (*ROSAT* All Sky Survey) count rates is equivalent to a multiplicative factor of 1.3×10^{-11} ergs cm^{-2} count^{-1}.

In Fig. 3.6, we plot [Fe X] vs. X-ray flux scatter plot for our sample. This shows a clear positive correlation between these parameters for type 1 objects. A similar correlation exists for the [Fe XI] line (not shown). The correlation between the [Fe X] line and X-rays becomes even more pronounced when one compares their luminosities (see top left plot of Fig. 3.7). In order to determine whether this correlation was specific to [Fe X], we also present in Fig. 3.7 plots of the [Fe VII], [O III]λ5007 and Hα luminosities vs. X-ray luminosity. These plots show that, in general, the luminosities of these other lines are

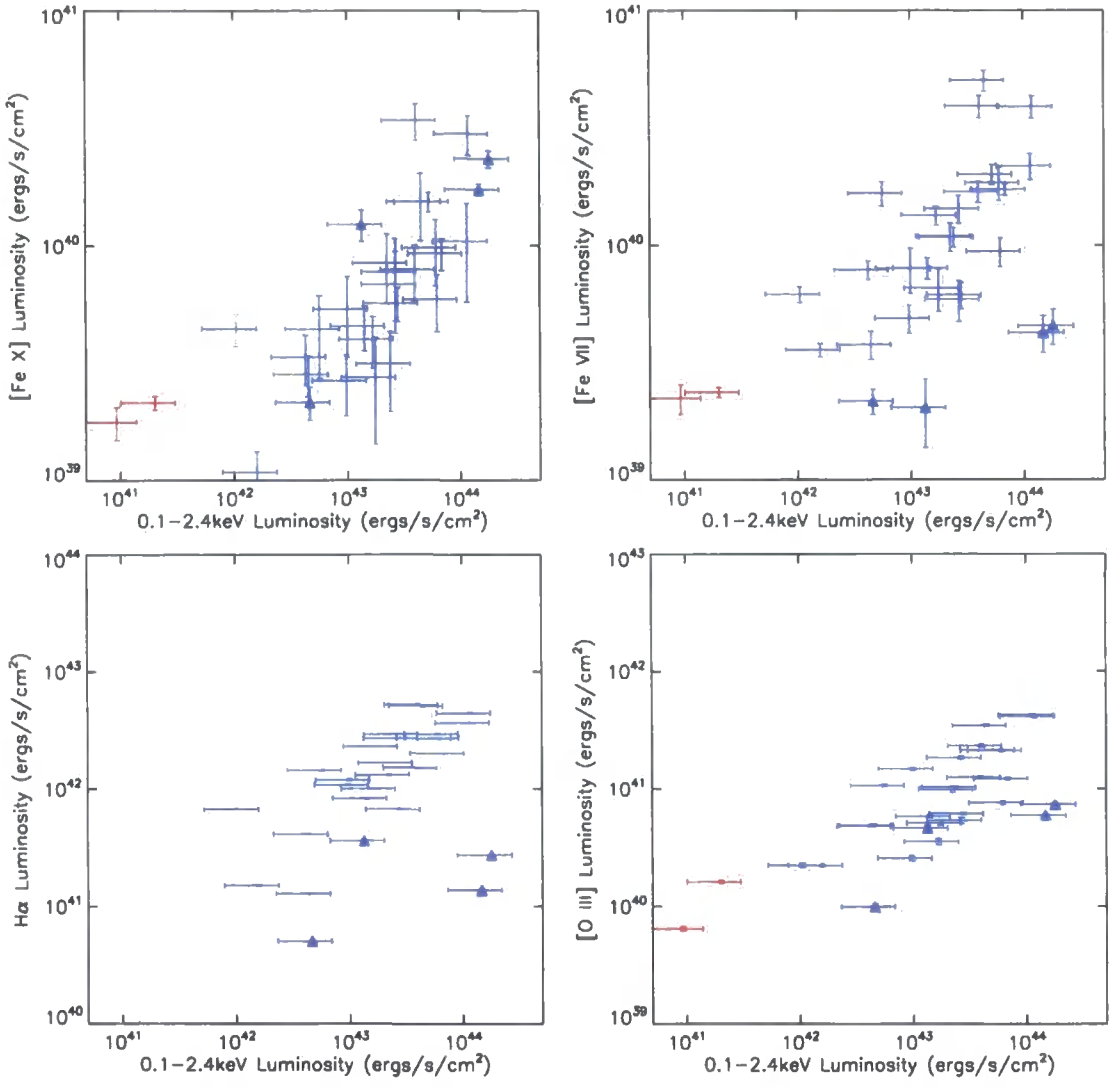

Figure 3.7: Various line luminosities plotted against X-ray luminosity. All plots show positive correlations of various strengths between the measured parameters (see correlation statistics in table 3.2. In all but the [Fe X] vs. X-ray plot there are distinct outliers. These same objects are distinguished with triangular points in all plots (initially defined using the [Fe VII] vs. X-ray measurements). We interpret this as an indication that the [Fe X] line is a more reliable indicator of X-ray luminosity than any of the other lines shown here. The possible causes of this are discussed in §3.5

also correlated with X-ray luminosity in our sample. However, the luminosities of these lines are less well correlated with the X-ray luminosities. Of note are four clear type 1 outliers that lie below the general trend indicated by the the remaining points of the [Fe VII] vs. X-rays plot. Three of these objects are also outliers in the Hα vs. X-rays and [O III] vs. X-rays plots. On inspection, these outliers proved to have some of the narrowest permitted lines of all the type 1s in our sample (Hα FHWM of 1700km s^{-1}†, 1900km s^{-1}, 2900km s^{-1}, 3200km s^{-1}compared to the type 1 population mean of 4000 $\pm$ 200km s^{-1}). If these outliers are excluded when determining the correlation statistics the Hα and [O III] line luminosities are found to be as strongly correlated with the X-ray luminosities as the [Fe X] line luminosity.

3.4.3 *FHIL* kinematics

In Chapter 2 we mention that in our study of a smaller sample of AGN there appears to be a qualitative link between the blueshifts and widths of the *FHILs*. Although the spectral resolution and signal to noise of the spectra from the *SDSS* aren't as high as those in our smaller sample, by fitting Gaussian components to the emission lines we were able to study how the kinematics of the *FHILs* in this much larger sample are related. In the following discussion any line shift is reported relative to the [S II]λ6717,6732 emission lines, which we assume represent the systematic redshift of the source (see Chapter 2 for further justification).

The upper left hand plot of Fig. 3.8 shows the relationship between the shifts of the [Fe VII] and [Fe X] lines. Correlation statistics associated with the kinematic parameters (given in table 3.4) reveal that the velocity shifts of the [Fe VII] and [Fe X] lines are strongly correlated in the case of type 2 objects, but poorly correlated for type 1s. Furthermore, a linear regression to these values reveal an almost 1:1 correlation between the shifts of these lines (for both types, although considerable scatter creates a large degree of uncertainty in this correlation for type 1s). There is a slight tendency among the type 2 objects for the [Fe X] line to be more blueshifted than the [Fe VII] line (as shown in table 3.5), although the mean relative shift of [Fe X] to [Fe VII] is consistent with 0km s^{-1} (in both type 1 and 2) when errors are taken into account.

The shifts of the [Fe XI] and [Fe VII] lines are less strongly correlated (in the case of both type 1 and type 2 objects) than the [Fe X]-[Fe VII] line shifts. Of particular note in the plot of [Fe XI] vs. [Fe VII] shifts (Fig. 3.8 and the bottom section of table 3.5) is the

†Only [Fe VII]

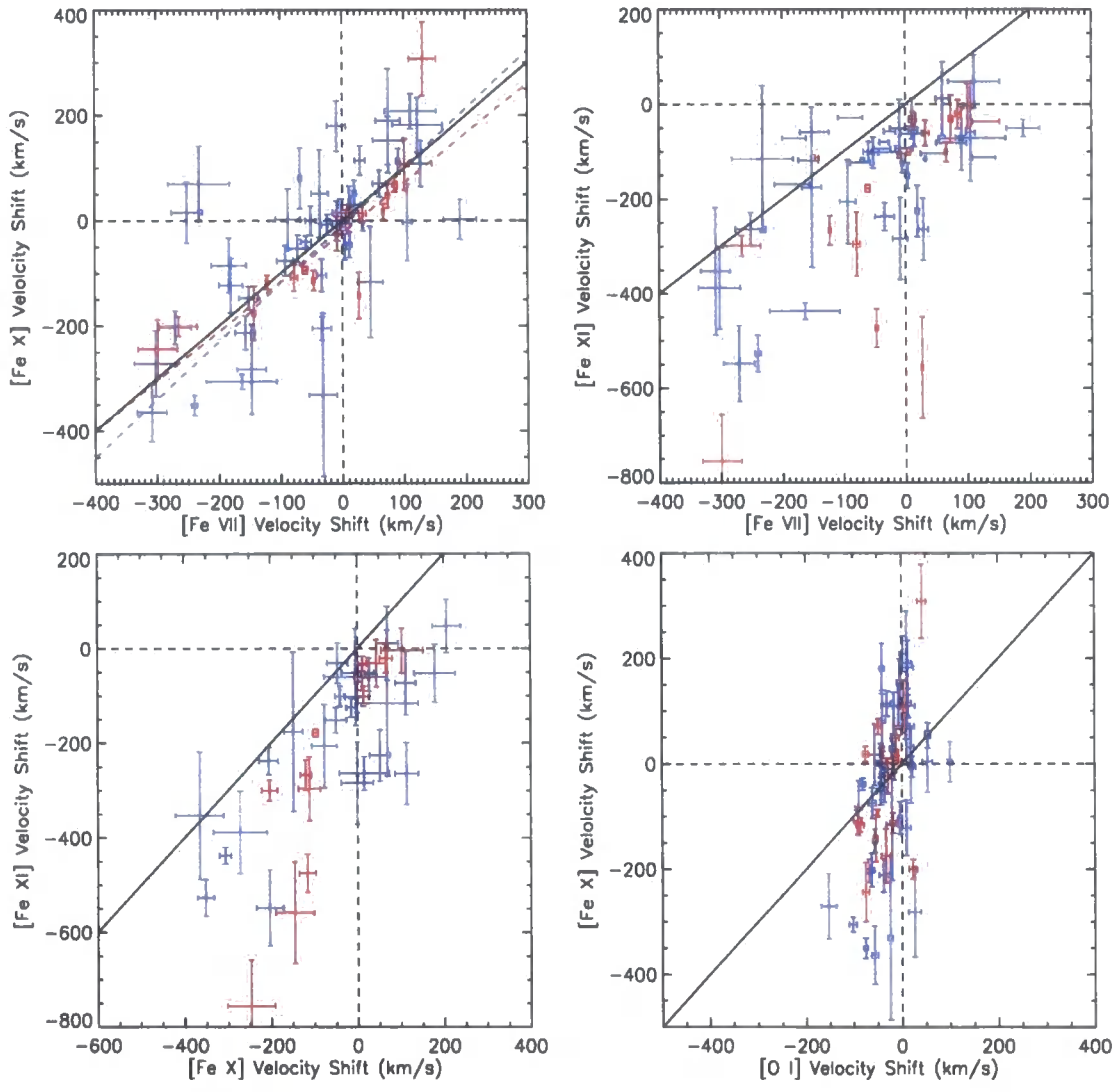

Figure 3.8: Top left: Velocity shifts of the [Fe VII] and [Fe X] *FHILs* relative to the [S II] emission lines (black dotted lines are used to show the transition between blueshift and redshift, red and blue dashed lines show the results of a linear regression to the data for type 2 and type 1 objects, respectively). This trend is also seen in the velocity shifts of the [Fe XI] vs. [Fe VII] and [Fe XI] vs. [Fe X] line (top right, bottom left, respectively). We note a general positive correlation between *FHIL* velocity shifts. To ensure this correlation is not introduced by the velocity correction derived from the [S II] lines, we also plot the [Fe X] vs. [O I] velocity shifts (bottom right).

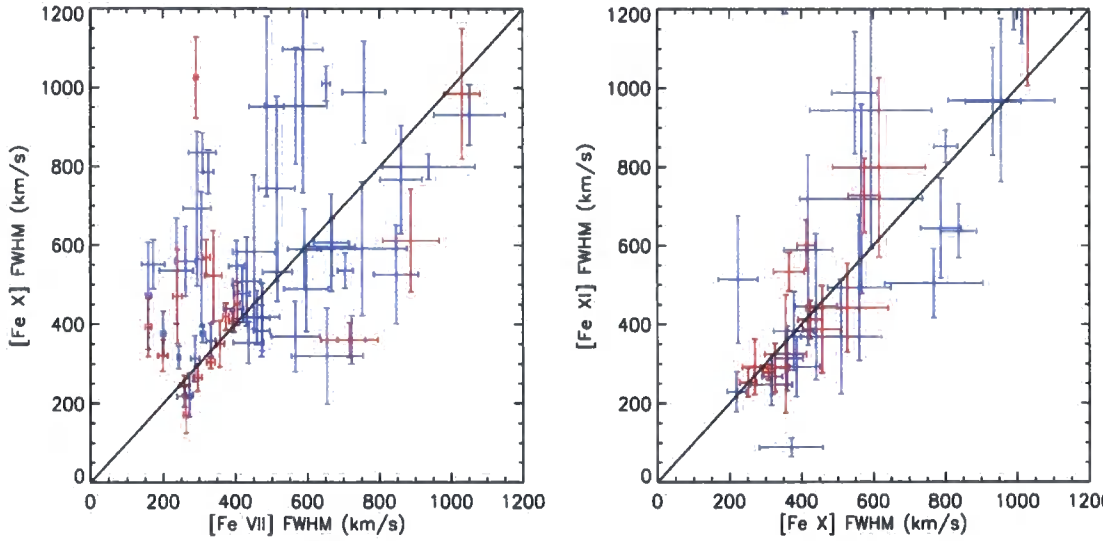

Figure 3.9: *FHIL* FWHM plots: Left: There is no clear correlation between the FWHM of the [Fe VII] and [Fe X] emission lines. 26/44 type 1s (59%) and 9/17 type 2s have (53%) have an [Fe X] line that is broader than the [Fe VII] line. Right: Equivalent plot for [Fe XI] and [Fe X] lines showing that the FWHMs of these lines are approximately equal in the majority of our sample. A line of equality is shown on each plot.

systematic blueshifting of the [Fe XI] line relative to the [Fe VII] line (only 1/17 type 2s and 5/44 type 1s have [Fe VII] lines that are *more* blueshifted than the [Fe XI] line).

To ensure that the shift-shift correlations discussed above are real and have not been introduced by normalising the shifts with respect to the velocity shift of the [S II]λλ6716, 6732 lines, we also plot the [Fe X] vs. [O I]λ6300 velocity shifts (corrected using the same method; see bottom plot of Fig. 3.8). This shows no trends capable of producing the shift-shift correlations of the *FHILs* shown in the other plots of Fig. 3.8.

In Fig. 3.9 we present plots showing the FWHM of the *FHILs* in our sample. Although a strong correlation exists between the FWHM of the [Fe X] and [Fe XI] lines, no such correlation exists between the [Fe X] and [Fe VII] lines. The large difference in Spearman's ρ statistic for each of these correlations (see table 3.4) is confirmation of this point.

Finally, we return to the results discussed at the start of this section, i.e. the possible existence of a correlation between the blueshifts and FWHM of the *FHILs*. The scatter diagram of Fig. 3.10 and the last two rows of table 3.4 show the correlation between FWHM and velocity shift of the [Fe X] line is very weak (particularly for the type 2

Correlation	Spearman's ρ	Significance
[Fe X] Shift-[Fe VII] Shift_1	0.65	2.0×10^{-6}
[Fe X] Shift-[Fe VII] Shift_2	0.9	1.9×10^{-7}
[Fe XI] Shift-[Fe VII] Shift_1	0.55	1.2×10^{-4}
[Fe XI] Shift-[Fe VII] Shift_2	0.79	1.6×10^{-4}
[Fe XI] Shift-[Fe X] Shift_1	0.64	5.5×10^{-4}
[Fe XI] Shift-[Fe X] Shift_2	0.95	1.1×10^{-6}
[Fe X] FWHM-[Fe VII] FWHM_1	0.43	3.6×10^{-3}
[Fe X] FWHM-[Fe VII] FWHM_2	0.40	0.11
[Fe XI] FWHM-[Fe VII] FWHM_1	0.66	3.0×10^{-4}
[Fe XI] FWHM-[Fe VII] FWHM_2	0.89	3.5×10^{-5}
[Fe X] FWHM-[Fe X] Shift_1	-0.24	0.11
[Fe X] FWHM-[Fe X] Shift_2	-0.17	0.50
[Fe XI] FWHM-[Fe XI] Shift_1	-0.56	$3.2\times10^{-}3$
[Fe XI] FWHM-[Fe XI] Shift_2	-0.66	0.01

Table 3.4: Line kinematics correlation statistics. The associated scatter diagrams are presented in Figs. 3.8-3.9. For a description of the column headings, see the caption of Table 3.2 Subscripts refer to AGN type.

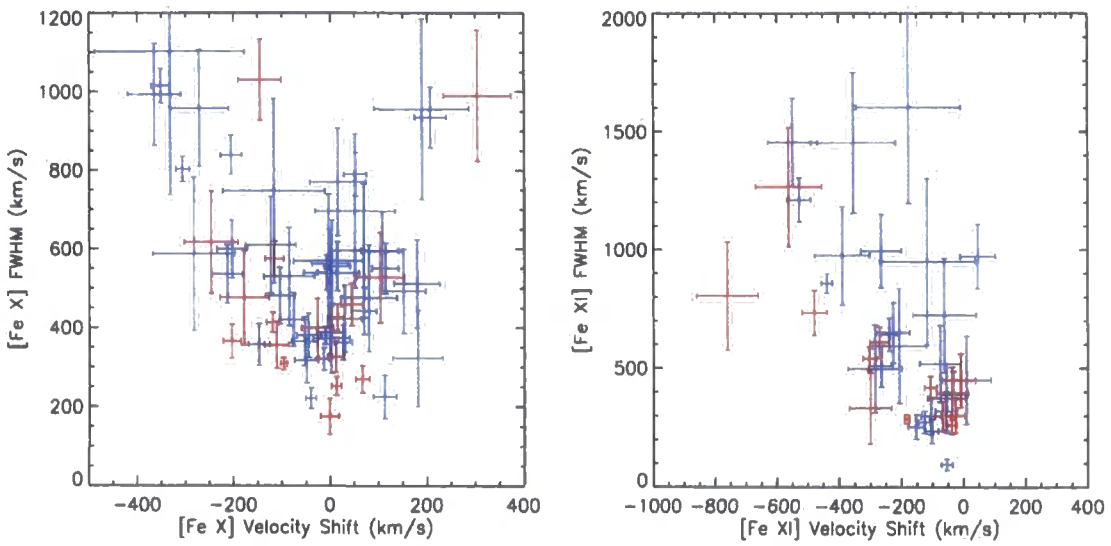

Figure 3.10: Emission line FWHM plotted against velocity shift for the [Fe X] (left) and [Fe XI] (right) lines.

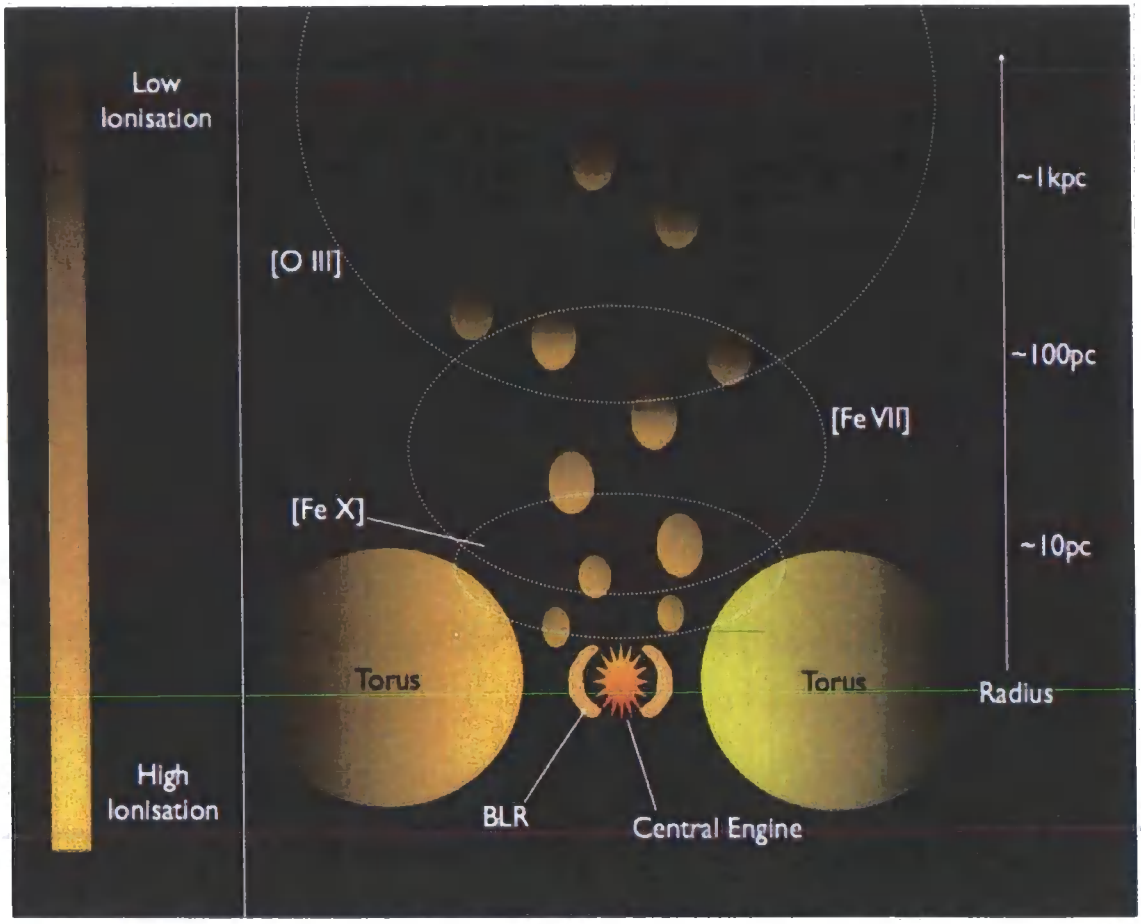

Figure 3.11: Schematic showing the locations of the regions in which the various *FHIL* emission dominates, relative to the obscuring torus. The results in the chapter suggest that the [Fe X] line is predominantly produced within the central 'void' of the obscuring torus, whereas the [Fe VII] emitting region extends to larger radii. There is, however, considerable overlap between these regions in which the various *FHILs* are produced.

	[Fe VII]			[Fe X]			[Fe XI]		
Type	Mean	σ	Err.	Mean	σ	Err.	Mean	σ	Err.
1	-47	120	19	-40	150	23	-150	130	20
2	-27	122	31	-39	130	34	-204	220	54

	[Fe X]-[Fe VII]			[Fe XI]-[Fe VII]			[Fe XI]-[Fe X]		
Type	Mean	σ	Err.	Mean	σ	Err.	Mean	σ	Err.
1	7	110	17	-100	110	16	-110	130	20
2	-11	69	17	-176	160	41	-164	150	38

Table 3.5: Top: Mean velocity shifts of the measured *FHILs* (relative to [S II]) and (bottom) the velocity difference between the [Fe XI], [Fe X] and [Fe VII] lines for both types of AGN discussed in the text. All shifts are given in km s^{-1}. Negative values refer to blueshifts. σ refers to standard deviation and Err. is the error in the mean ($= \sigma/\sqrt{(N-1)}$; where N is the size of the population).

objects) and is only marginally stronger for the [Fe XI] line. The same analysis of the [Fe VII] line reveals a similarly weak correlation as the for [Fe X] line.

3.5 Discussion

Once selection effects are taken into account, the results presented here generally agree with the findings of *FHIL* emitting AGN. Although we do not find the differences in the [Fe VII]:[O III] ratios for type 1s and type 2s such as those of Nagao et al. (2000), we have identified systematic difference between type 1s and type 2s when the [Fe X]/[Fe VII] ratio is considered. If this is interpreted using the model described in Murayama and Taniguchi (1998) (pictured in Fig. 3.11), then it implies that in general, the [Fe X] emission is produced in a region that is closer to the nucleus than the [Fe VII] emission. The geometry of the *FHIL* emitting regions and the putative obscuring torus then implies that in type 2s, a larger fraction of the [Fe X] emission is obscured from our view. This is consistent with a significant fraction of the [Fe X] emission being produced within the central void of the obscuring torus.

These findings are counter to the those of Nagao et al. (2000) who did not find a significant difference in the [Fe X]/[Fe VII] ratio between type 1s and type 2s. In that

study this was explained by assuming that 'a significant fraction of the [Fe X] emission arises from low density ISM' and would therefore be more spatially extended than the [Fe VII] emitting region. Their interpretation goes against the findings of Ferguson et al. (1997) (and chapter 5) who used photoionisation models to show that for a typical AGN spectral energy distribution, the [Fe X] line is preferentially produced at smaller distances from the source of ionising radiation (peak [Fe VII] emission radii: 0.64-102.5pc, [Fe X]: 0.04-20.44). Although these photoionisation models show that low density ($n_H \sim 2 - 4 cm^{-3}$) clouds are capable of producing significant [Fe X] emission at large radii ($R \sim 350pc$), these same clouds would also contribute significantly to the [Fe VII] flux. This is indeed what the results presented here show: the [Fe X] line *is* produced in extended regions (i.e. outside the region obscured by the dusty torus) in some type 2 AGN (and probably some type 1s, based on unification arguments). However, for the type 2 objects of our sample, the strong correlation between [Fe X] and [Fe VII] about a mean [Fe VII]:[Fe X] ratio of 2:1 indicates that these tenuous, extended regions are also strong emitters of [Fe VII]. Therefore, from arguments based on both photoionisation models and the results presented here, it is difficult to understand how, in the Nagao et al. (2000) model, the [Fe X] emitting region could be more spatially extended yet still produce the observed relative line luminosities.

The same arguments, when applied to the [Fe X]/[Fe XI] luminosities, suggest that both these lines are produced in approximately the same region. This is reasonable when one considers the similar ionisation potentials of these species (232eV and 262eV). Our results derived from the relative luminosities of the *FHILs* therefore suggest that more highly ionised emission lines are produced closer to the central black hole.

The model described above is corroborated by the results derived from the FWHM of the lines. The lack of correlation between the FWHM of the [Fe X] and [Fe VII] lines indicate that these lines are produced in distinct regions. On the other hand the strong correlation between the FWHM of the [Fe X] and [Fe XI] supports the concept that the regions responsible for these higher ionisation lines are co-spatial.

The findings based on the X-ray luminosities of our sources extend the results of Porquet et al. (1999), i.e. a strong correlation exists between [Fe X] and X-ray luminosity. Although they represent a small minority of our sample, and therefore hard to interpret, it is possible that the outliers of the Hα , [Fe VII] and [O III] vs. X-ray plots (that aren't present in the [Fe X] vs. X-ray plot) are the result of the varying degrees of sensitivity of these lines to different portions of the continuum SED. The Hα and [O III] lines have

relatively low ionisation potentials (13.6eV and 54.9eV, respectuvely), therefore these lines should scale more directly with the UV or *bolometric* AGN luminosity, rather than just the soft X-rays used here. The [Fe X] ionisation potential (235eV), on the other hand, is well within the upper and lower bounds of the X-ray bands we have used here (0.1-2.4keV) and our results show that this line responds well to the soft X-ray luminosities. Bearing these results in mind, the presence of outliers in the [Fe VII] vs. X-rays plot indicates that the response of this line to the underlying SED is similar to that of Hα and [O III]. Unfortunately, the low number of outliers in these plots makes interpretation of these results difficult, however, this result is suggestive of a break in the form of the underlying SED between 100eV ([Fe VII]) and 235eV ([Fe X]) in some AGN, particularly those with narrow permitted lines (i.e. those more likely to have a strong soft excess).

Analysis of the velocity shifts of the *FHILs* in our sample provides us with further information about the environment of the *FHIL* emitting region. The correlated shifts of the [Fe X] and [Fe VII] *FHILs* around a 1:1 relationship indicate that these lines typically outflow at approximately the same velocities. It is therefore possible that they arise from different regions of a continuous flow; we have already shown that these lines are predominantly produced in separate regions. This suggests a scenario in which the *FHIL* emitting clouds are 'coasting' at a given velocity and undergo little or no acceleration or deceleration between the regions in which the [Fe X] line is strongly produced, to those in which the [Fe VII] emission dominates the *FHIL* spectrum.

3.6 Summary

In this chapter we have introduced a novel way of extracting AGN spectra with strong *FHILs* and have presented the results derived from such a sample. Although selection effects bias our sample toward AGN with strong [Fe X] lines, the sample presented here is less susceptible to other selection effects which were inherent in earlier sample of *FHIL* emitting AGN, i.e. simply the brightest and most studied AGN

To analyse the spectra an automated process was used that emphasised the use of χ^2 minimisation techniques. This enabled a large sample of spectra to have an arbitrary number of emission lines to be fit with an arbitrary number of components in an unbiased manner. It is hoped that this process will be used in future projects to measure other emission and/or absorption line properties in even larger samples of spectra (for example, future large sky surveys).

The main conclusions drawn from the sample presented here can be summarised as follows:

- the [Fe X] line appears to be suppressed relative to the [Fe VII] line in type 2 AGN as compared to type 1s. We interpret this as evidence that the [Fe X] region is partially obscured from our view in type 2 AGN. This can be seen as further evidence that a proportion of the *FHIL* emitting region lies within the central void of the dusty torus.

- there is no significant difference in the ratio of the [Fe X] to [Fe XI] lines between type 1s and type 2s, suggesting that these lines are produced in the same regions relative to the obscuring torus. This is supported by the similar FWHM of these lines in both type 1 and type 2 AGN.

- there is some evidence that the [Fe X] line is more closely related to the X-ray luminosity of an AGN than the broad component of the Hα line and the (full) [O III] and [Fe VII] lines. The outliers of the plots from which this conclusion is derived have some of the narrowest Balmer lines in the sample. We interpret this as possible evidence of a break in the SED between the ionisation potentials of the [Fe VII] and [Fe X] lines (100eV and 235eV) in NLS1s (i.e. those AGN with a tendency to has a strong soft excess). However, a much larger sample of outliers is needed to fully test this hypothesis.

- The similarity between the velocity shifts of the [Fe VII] and [Fe X] lines is indicative of these emission lines being produced in different regions of a continuous outflow. The average relative velocity shifts of the lines suggest that there is little or no acceleration or deceleration of this outflowing gas between the region where [Fe X] dominates to that where [Fe VII] dominates the *FHIL* emission.

3.7 An anomalous object with extremely strong *FHILs*

We would like to end this chapter by returning to the non-AGN object we discovered during our search for *FHIL* emitters described above. At the time when the SDSS spectrum was taken on the 27^{th} February, 2004, this object (*SDSSJ1241+4426*) had unusually strong *FHILs* (only the [O III]λ5007 and Hα lines had higher fluxes than the [Fe X]λ6374 line; see Fig. 3.12). To determine whether the emission lines were variable, a

second observation of this object was obtained on the 27^{th} May, 2008 using the ISIS dual-beam spectrometer on the William Herschel Telescope (WHT), La Palma. In order to provide spectral coverage similar to that of the SDSS, a low dispersion grating was used in both the red and blue arms (R157R and R158B, repectively) in conjunction with the 5700 dichroic. A 1.3" wide slit width provided an average instrumental FWHM of 9Å (measured from arc lines). An IDL routine, *KRISIS*, was written by myself to reduce the data. Telluric features were corrected for by dividing the object spectra by a normalised, high S/N spectrum of a standard star. The reduced, wavelength and flux calibrated spectrum is shown, along with the SDSS spectrum for comparison, in Fig. 3.12 at the end of this chapter.

As the principal aim of the second epoch observation was to establish whether the emission lines had varied in flux since the SDSS spectrum was taken. It was necessary to ensure that the any measured variations were intrinsic to the source and were not caused by the different aperture size employed for the WHT observation (1.3" long-slit vs. a 3.0" diam. SDSS fibre). To do this we extracted regions of increasing projection (0.5"-3.0") parallel to the slit, and then measured the emission line fluxes for each extraction width. We note that for all but the Hα line, an extraction width of 2.0" includes $> 95\%$ of the flux contained within the 3.0" extraction dimension. We therefore assume that our final choice of extraction width of 3.0" contains all the nuclear emission line flux of the target. This same test reveals a 20% reduction in emission line flux between the 3.0" and 1.3" extraction widths. By assuming circular symmetry can therefore place an upper limit of about 20% on the uncertainty in the measured line fluxes introduced by the reduced aperture size of the WHT observation.

All the emission lines discussed in this paper were fit with a single Gaussian in order to measure their total flux. A local continuum was defined by fitting a fourth order polynomial to the continuum flux either side of each measured emission line. The results of these measurements for both the SDSS and ISIS observations are given in Table 3.6. It is evident from these results and Fig. 3.12 that, in general, the fluxes of the emission lines have fallen. In particular, we note that the relative drops in the [Fe X] and [Fe XI] lines are the highest among the all the measured forbidden lines.

3.7.1 What is the Origin of the strong Coronal Lines?

In the course of our search for AGN with strong coronal lines contained in the SDSS described in this chapter, the galaxy, *SDSSJ1241+4426*, is unique in several respects. Its

	SDSS	WHT	
Line	*27-02-2004*	*27-05-2008*	% Change
[Fe VII]λ3758	0.53 ± 0.14	0.25 ± 0.05	-53%
[Ne II]λ3868	0.73 ± 0.11	0.51 ± 0.06	-30%
Hγ	0.22 ± 0.07	0.11 ± 0.04	-50%
[O III]λ4363	0.63 ± 0.09	0.52 ± 0.07	-17%
He IIλ4686	0.4 ± 0.08	0.17 ± 0.04	-58%
Hβ	0.46 ± 0.07	0.34 ± 0.06	-26%
[O III]λ4959	0.66 ± 0.07	0.73 ± 0.07	11%
[O III]λ5007	2.08 ± 0.11	1.95 ± 0.07	-6%
[Fe VII]λ5721	0.3 ± 0.06	0.34 ± 0.05	13%
[Fe VII]λ6087	0.54 ± 0.06	0.41 ± 0.04	-24%
[O I]λ6302	0.31 ± 0.06	0.27 ± 0.04	-13%
[Fe X]λ6376	0.91 ± 0.07	0.4 ± 0.04	-56%
Hα	3.03 ± 0.11	2.15 ± 0.05	-29%
[N II]λ6584	0.37 ± 0.05	0.41 ± 0.05	11%
[Fe XI]λ7892	0.72 ± 0.09	0.23 ± 0.04	-68%

Table 3.6: Line fluxes in units of $\times 10^{-15}$ ergs/s/cm^2 and the relative change in these fluxes between observations.

optical spectrum is not consistent with an AGN. First, its emission line profiles (FWHM) over a range of ionisation potentials, from [O I] up to [Fe X], are all around 200km s^{-1}. These values are typical of starforming galaxies, and far less than found in Seyferts of both type 1 and type 2. Second, the ratio of [N II]λ6584 to Hα is 0.12, which is typical of a starforming galaxy and far lower than found for typical ratios of Seyferts. The third point is that in the SDSS spectrum the [Fe X] line is stronger than Hβ. However, in the SDSS spectrum, the emission from HeIIλ4686 is almost as strong as Hβ. Such a ratio has been observed in the most extreme cases of Seyfert 2s, but never in the spectra of galaxies powered by star formation.

Tidal Disruption

If, therefore, *SDSSJ1241+4426* is not some form of AGN then what could be responsible for its exceptional high ionisation line properties? One possibility is that this could be

a rare example of a tidal disruption event in which a star is shredded by the strong gravitational gradient that exists close to a black hole (eg. Rees 1988, Komossa and Bade 1999). During a tidal disruption event the layers of the passing star are stripped away and accreted onto the SMBH. Unlike in the case of "steady state" AGN, this results in a sudden flare of radiation, predominantly in the UV and X-rays, reaching up to $10^{44} M_6$ ergs s^{-1} in luminosity for a period of $t_{pk} \sim 0.5 M_6^{-0.1} \epsilon_{0.1}^{0.4}$ yr (where M_6 is the mass of the SMBH in units of 10^6 $M_\odot$ and $\epsilon_{0.1}$ is the efficiency of the accreting system in units of 0.1). This is followed by a rapid decline in luminosity as the remainder of the star is accreted over a more extended period of time (Rees 1988).

Following such a rapid increase in ionising radiation we would expect to see the surrounding gas respond by a sudden increase in the flux of the emission lines produced via photoionisation. In particular, as models of tidal stripping predict that most of the radiation emitted by this event is produced in the UV to X-Ray portion of the electromagnetic spectrum, the flux of the high-ionisation lines would increase dramatically. The length of time that this suddenly ionised gas will produce emission lines is inversely proportional to both the electron density and the recombinations coefficient of the lines in question. As the recombination coefficient of the [Fe X]λ6374 line is of the order of 10^{-10} cm^3 s^{-1} (Jacobs et al. 1977) we would expect the emission of this line to have reduced significantly during the 4 years between the observations of *SDSSJ1241+4426* for all but the most extremely low density environments ($n_e \sim 10^2$ cm^2). However, inspection of Table 3.6, shows that these lines have decreased in flux by only a factor of 2-3.

Although tidal distruption remains a possibility if the duration of the enhanced accretion onto the supermassive central black hole is extended, and/or the density of the ionised gas is low, another, perhaps more plausible explanation would be a supernova event in a high density enviroment near to the centre of the galaxy. The SDSS spectrum and the SDSS follow-up spectrum are centred on the nucleus of the galaxy. It is known that supernova can produce strong coronal line emission (eg. SN 1987A; Gröningsson et al. 2006).

In either case (ie. tidal disruption or an extreme supernova event) the spectrum of *SDSSJ1241+4426* is very rare, and its interpretation deserves further consideration. However, because it is clearly not an AGN, based on several criterion discussed above, it does not fit logically into any of the samples that we discuss in this thesis. But it does demonstrate the power of our novel detection methods aimed at finding very extreme objects within the SDSS database. Such needles-in-a-haystack provide a challenge for

the conventional emission line galaxy classification schemes, and clearly need to be understood.

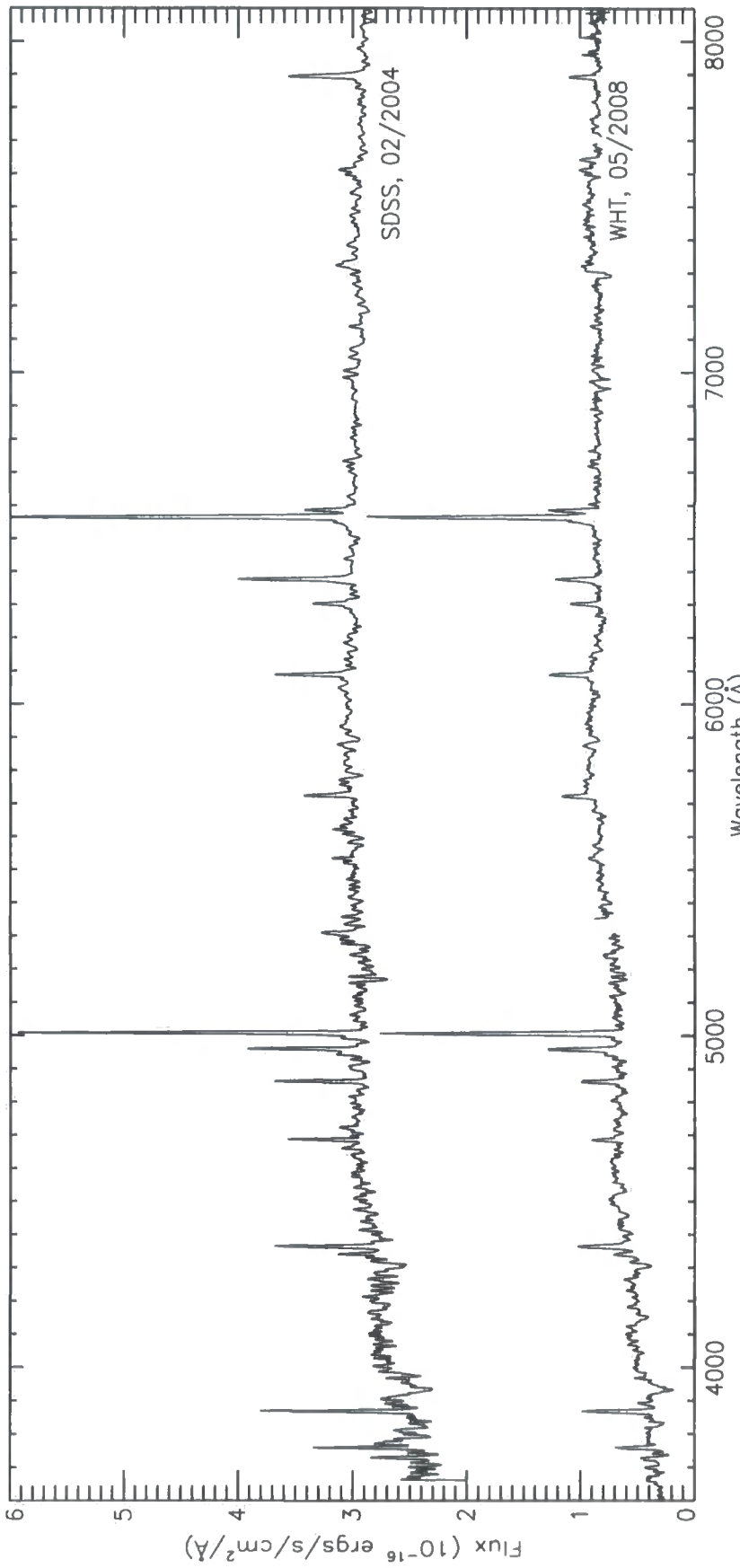

Figure 3.12: Top: SDSS spectrum, convolved with a Gaussian of FWHM=4Å and shifted upwards in flux by an additional 2×10^{-16}ergs/s/cm^2/Å for clarity. Bottom: Second epoch spectrum taken with ISIS. The region around 5300Å has been masked due to low instrumental throughput between the blue and red arms. Additionally, the region around 7700Å has been masked as it suffered from a strong cosmic ray that could not be corrected for.

Chapter 4

A systematic search for FHIL emitters in the SDSS database

4.1 Introduction

In the previous chapter we described how we used the results from the SDSS pipeline to extract the *FHIL* emitting sources from the SDSS spectral database. Unfortunately, a consequence of using this method to find these sources is the introduction of significant selection effects that prevent us from performing a full analysis of the results from these spectra. In particular, by selecting the spectra on the basis of strong [Fe X]λ6374, we are strongly biased toward spectra with strong [Fe VII] emission. Therefore, any analysis based on lines other than [Fe X] is inherently compromised – as is evident in our comparison of the [Fe VII]λ6087:[O III]λ5007 luminosity ratios against those derived from the Nagao et al. (2000) sample. In addition to the selection effects introduced by selection on [Fe X]λ6374 line flux, forcing our analysis on spectra with Hα lines with FWHM<50Å (introduced to ensure that the [Fe X] was not included in the wing of the Hα emission line) means we could only find AGN spectra with relatively narrow emission lines. As one of the principal questions associated with our investigation into *FHIL* emitting AGN is whether the presence of these lines is in any way related to the properties of the broad permitted lines, this is clearly a major shortfall of the sample described in the previous chapter.

Despite its flaws, the work described in the previous chapter is proof that we are able to use the SDSS spectral database to obtain useful measurements of the *FHIL* emission from a moderately large sample of objects that are *not* subject to the usual selection effects associated with previous samples of *FHIL* emitting AGN (see the introduction of Chapter 3). One of the key benefits of the study described in the previous chapter is that

it required the development of an automated emission line fitting routine that quickly measured the flux, width and velocity shift of a pre-selected sample of SDSS spectra. In developing this routine, it became clear that the rapidity of the fitting facilitated its use on a much larger sample containing (potentially) hundreds of thousands of SDSS spectra. By avoiding the use of the SDSS spectral fitting routine, we are much less susceptible to the selection effects of our previous sample and by focusing our search on the [Fe VII]λ6087 line as well as the (blended and typically weaker) [Fe X]λ6374 line, we are able to obtain a less biased sample of *FHIL* emitting objects from the SDSS database.

Although our automated script facilitates the search of *FHILs* in (potentially) the whole SDSS database, this could be deemed as overkill; in this current study we are uninterested in the spectra of a large proportion of the SDSS database, such as those of non-emission line objects or objects with redshifts such that our lines of interest are outside the wavelength coverage of the SDSS detectors. Therefore, in the following section we describe how and why we limited the size of our initial sample by placing constraints on the parameters obtained from the SDSS spectral fitting pipeline.

4.2 Sample Selection and Line Fitting

In order to find as large a number of *FHIL* emitting galaxies as possible, we set very loose constraints on our initial query to the SDSS database. Firstly, a redshift limit of 0.36 was set to ensure that the full Hα line was included in all the spectra. It was also required that the [O III]λ5007 line was in emission to ensure that we were only measuring emission line objects (predominantly starbursts and AGN). Finally, a continuum S/N>20 (at [Fe VII]λ6087) limit was applied. This was necessary as the *FHILs* are generally weak features that are easily lost in the continuum noise of a low S/N spectrum. These restrictions provided an initial sample of 31328 spectra.

To determine which of these spectra contained *FHIL* emission, we attempted to fit a single Gaussian at the wavelengths at which these emission lines would be expected. This was done on the assumption that the redshift given in the SDSS spectrum header is a fair approximation of the true value. By evaluating the χ^2 difference between a simple continuum fit and a continuum+Gaussian fit, we were able to determine the likelihood that an individual *FHIL* existed at a given wavelength.

4.2.1 Reliability of the *FHIL* measurements

Using an automated process to find spectra with inherently weak emission lines from a large sample such as ours is prone to risks. Using $\Delta\chi^2$ as an indication of the likelihood of the presence of an emission line means our chosen procedure, whilst computationally undemanding, is heavily dependent on the quality of the continuum fit. Although our fitting procedures (described in the following sections) are robust against false positives, they return numerous spectra with low continuum signal to noise (hereafter S/N) and non-existent emission *FHILs*. We therefore wanted to include in our fitting routines an estimate of the systematic error in our line measurements introduced by the (potentially poor) fit to a low S/N underlying continuum.

To estimate the systematic errors associated with our line fits, after each *FHIL* had been identified and measured with the nominal continuum fit, we increased, then decreased, the level of the continuum by one standard deviation (calculated during the continuum fitting process). The emission line was then fit again with a single Gaussian at the same position as the 'optimal' fit, but with its normalisation and FWHM allowed to vary. The logic behind this was that the position of the peak of a Gaussian should change little if the level of the underlying continuum is raised/lowered by a constant value, although the width and normalisation would change considerably. This was indeed found to be the case when we tested the procedure on spectra with strong *FHILs* and allowing the central position of the Gaussian to vary (we note that we couldn't free all parameters for all spectra as, in those spectra in which the measured *FHILs* were weak, allowing the position of the Gaussian to vary meant it would often settle on other, stronger emission lines when the continuum level was raised).

In establishing the total errors (random + systematic) on each of the fit parameters introduced by both the emission line and continuum fits, we were able to rank our spectra in terms of the confident limits associated with each parameter. Although the choice of relative error cut-off is arbitrary, we chose to only work with results with $\frac{\Delta F}{F}$ <50%[1] as, after inspection of the fits, we were confident that all objects satisfying this criterion have strong, well measured *FHILs*. In cases where more than one *FHIL* are compared, we apply the same limits to *both* lines. We note that the measurements of the much stronger Hα, Hβ and [O III]$\lambda\lambda$4959,5007 lines were not treated to the rigourous error analysis as the strength of these lines mean the relative errors associated with the assumed contin-

[1]Where F is the flux in the line

uum level are negligible.

4.2.2 [Fe VII]λ6087

We initially attempted to measure the [Fe VII]λ6087 line as it is typically the strongest of the optical *FHILs*. This line was initially fit with a single Gaussian. If a χ^2 test showed a significant improvement of the fit on the addition of this first component a second component was added. This second component was retained if a further χ^2 revealed it provided a significantly better fit. From our initial sample the fitting process described above found 1607 spectra with [Fe VII]λ6087 emission at a confidence level of >99%. This number was reduced to 269 when the systematic + random error selection criteria (i.e. $\frac{\Delta F}{F}$; described in the previous subsection) was applied.

4.2.3 [Fe X]λ6374

Following the search for [Fe VII] lines we also attempted to detect evidence of [Fe X]λ6374 emission in all the 31328 spectra of the original sample. A key difference between the work described in this chapter and the previous chapter is that, by avoiding the use of the results from the SDSS fitting routine, we have the potential to measure the [Fe X] lines in all objects with broad Hα lines (we were forced to impose a limit of FWHM < 50Å in the previous chapter which corresponds to 2285km s^{-1} at zero redshift).

Defining the continuum underlining the [Fe X] line is a particular challenge. Because this line can lie on the curved wings of the Hα line, the local continuum cannot be modelled with a simple power law, as in the case of [Fe VII]λ6087. To account for the potential curvature to the underlying continuum, we introduced higher order terms to a simple first order polynomial fit. On addition of these higher order terms we had to ensure that the continuum fit did not become too flexible and fit non-continuum features. As a compromise, we fit the local continuum underlying the [O I]λ6300 line with a first order polynomial, while at wavelengths between 6340Å and 6500Å we fit the continum-plus-Hα wing with either a Gaussian or a lorentzian profile- the one that provided the best fit in terms of χ^2 statistics was then carried forward into the rest of the [O I]+[Fe X] fitting routine. The two continuum functions (first order polynomial plus guassian/lorentzian) were joined in such a way that they formed a smooth, continuous continuum fit.

The actual [O I] and [Fe X] lines were fit using the same routine as outlined in Chapter 3. The [O I]λ6300 line was fit first and [O I]λ6363 component was then given the same

profile (its normalisation reduced by a factor of 1/3). A component was then added to model the [Fe X]λ6374 line. A χ^2 statistical test was used after the addition/variation of each component to determine whether the new component provided a better fit to the data.

Our search for [Fe X]λ6374 emission returned 8086 spectra with emission at 6374Å detected at >99% confidence (determined from $\Delta\chi^2$). After selection based on the relative size of the systematic + random errors this number was reduced to 157.

Once we had defined two separate samples based on the detection of [Fe X] and [Fe VII] we cross matched the results from each to ensure we had [Fe X] measurements for the [Fe VII] sample (and vice versa). Furthermore, we also measured the Hα , [N II]$\lambda\lambda$6548,6584, Hβ and [O III]λ5007 lines (described below) in each spectrum contained in our *FHIL* detected samples.

4.2.4 Hα, Hβ and [O III]λ5007

As well as measuring the *FHILs* in our sample we wished to compare the properties of these lines with other prominent emission lines in the spectra. To do this we produced an automated line fitting routine which modelled the Hβ, [O III]λ5007, Hα and [N II]$\lambda\lambda$6548,6584 lines with multiple Gaussian components. To produce a procedure that would accurately model these lines' complex profiles with the minimum number of components proved challenging; it had to be robust enough to fit these lines in potentially thousands of spectra that were unlikely to be checked by eye, yet quick enough to facilitate such numbers of spectra to be fit in short period of time (hours, rather than days or weeks). After trying a number of different fitting procedures it was found that the following was most effective at accurately fitting these lines:

- Fit the underlying continuum with a first order polynomial fit between the wavelengths 4500Å-5100Å(under the Hβ and [O III]λ5007 lines) and 6250Å-6800Å (under the Hα and [N II] lines). Outside these regions the continuum fit was set to be equal to the spectrum- this ensures that there is no possibility of a component fitting features outside the region of interest.

- Fit the Hα line with a single Gaussian. The shift, FWHM and normalisation of this component are all allowed to vary. This produces a baseline fit to the Hα line onto which other components are added as the model becomes more complex.

- Fit the [O III]λ5007 line with a single Gaussian, allowing all its parameters to vary.

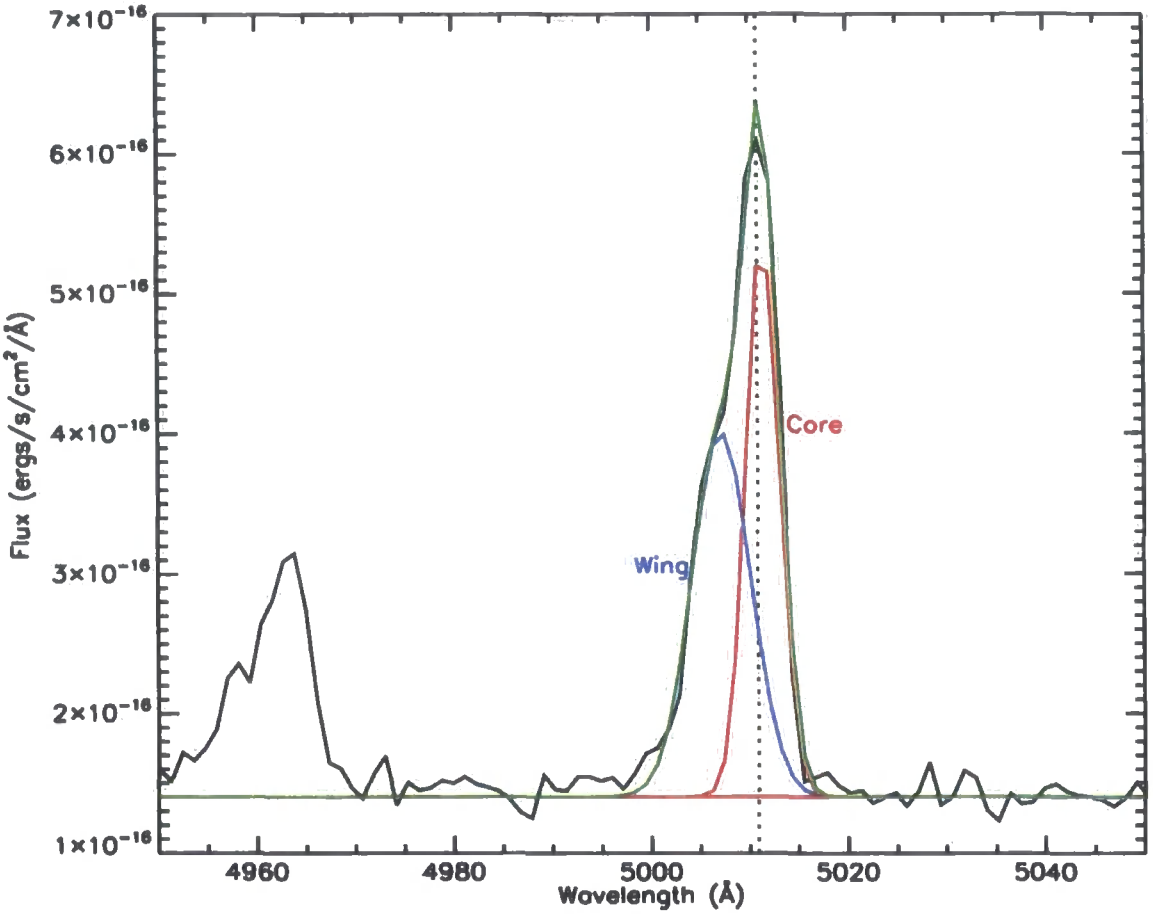

Figure 4.1: The [O III]λ5007 line was fitted with up to two Gaussian components. The core component was defined as peaking nearest (in terms of wavelength) to the peak of the overall modelled line profile, shown in green. This provided more consistent results over designating the narrowest or largest amplitude component as the core.

- As the [O III]λ5007 line in AGN spectra often has a broad base (which is generally blueshifted with respect to the stronger narrow component, but is known to be redshifted in a minority of cases) we fit a second component to the [O III]λ5007 fit. We define each component as being either a wing or a core: the core is that component who's maximum lies nearest (in λ) to the peak of the overall modelled line profile (see Fig. 4.1).

- The [N II] lines and the narrow component of the Hα line were then fit with a single Gaussian, the velocity shift (wrt. systematic; determined from the SDSS redshift measurement) and FWHM of which was fixed to that of the [O III]λ5007 core.

- Although the velocity shift of the strong [O III]λ5007 line is a good first order approximation for the shift of the Hα and [N II] lines, it was evident in a number of spectra that a better fit would be obtained if the velocity shift of these lines were allowed to vary slightly to more appropriate values. This was done by holding the width of these components fixed to the [O III]λ5007 FWHM, but allowing their velocity shift and normalisation to change.

- Due to their proximity to one another, the [N II] and Hα lines are often blended in AGN spectra (even in the case of type 2 spectra). It is therefore necessary to determine what fraction of the flux of the blend is attributable to the Hα lines and [N II] lines. To assist in determining the flux attributable to each line we initially assumed that the [N II] lines had the same profile as the [O III]λ5007 line by adding the wing (with the same FWHM and velocity shift relative to the refitted Hα and [N II] lines) with the same relative core:wing normalisations. This had the result of minimising the requirement of a third, broad component, especially in type 2 AGN spectra.

- In Chapter 2 we showed that the [O III] lines had a greater tendency to have a broad base as compared to the other low ionisation forbidden lines. It is therefore reasonable to assume that the wing of the [O III]λ5007 line is an upper limit to the relative normalisation of this component in other lines. Indeed, in fitting the [N II] profiles it was noted that the [O III] profile was often too broad for these lines. We therefore allowed the relative normalisation of the [N II] lines to vary from the [O III]λ5007 wing:core ratio. However, to prevent the wing component fitting the

broad Hα line in the case of type 1 objects, we prevented the wing:core of the [N II] line from rising above that defined for the [O III] line.

- Throughout the above process, the model has been allowed to vary all the parameters of the initial Hα component (introduced in the first step). In the case of type 2 AGN this component should now be either broad, yet weak (wrt. the narrow components) or a third, narrow component that provides a better fit to the narrow Hα line. In the case of type 1 (or type 1.x) AGN spectra, this component should now be precisely modelling the broad component of the Hα line. As a further check to determine whether this component is required, it is removed in this step and the normalisations of all other components are allowed to vary. A $\Delta\chi^2$ test is used to determine whether this component is, indeed, necessary.

- Although we have taken care to avoid the broadest of the three Hα components becoming broad enough to form a pseudo continuum, it is possible that this could occur (especially in type 2 objects in which weak, real broad components are poorly defined). To avoid this false component being passed onto other steps, we prevent the broad Hα component being added back to the fits after the previous step if it has a FWHM $>$ 15,000km/s.

- Until now we have ignored the Hβ line and have concentrated our fitting routine on the [O III] and Hα/[N II] complex. Although the Hα line would appear to be the more complicated of the Balmer lines to model, the fact that the blended [N II] lines are narrow (and therefore relatively easy to model with the [O III] template employed here) makes the modelling of this line preferable over that of Hβ which, in some of the more highly ionised AGN spectra, is often blended with a broad He II that is difficult to distinguish from a broad Hβ wing. To avoid these problems we model the Hβ line with the same number of components used for Hα, forcing their velocity and FWHM to remain fixed to those of the equivalent Hα components but allowing their respective normalisations to vary.

4.3 Control Sample

At the outset of this work we wished to determine the principal causes of *FHIL* emission. In Chapter 3 we saw that a small minority of AGN in the SDSS database contained [Fe X] emission strong enough to be detectable via the results of its data processing pipeline.

Although we stressed that our earlier sample was incomplete, it showed that strong *FHIL* emission is not ubiquitous even among the AGN spectra with the highest S/N. Unfortunately, the limitations of how that sample was selected made it difficult to make a fair comparison between the confirmed *FHIL* emitters and the general AGN populations. Alternatively, with the sample presented in this chapter, a comparison with the underlying sample from which the *FHIL* emitting AGN were extracted is straightforward. To do this, we randomly selected 1000* spectra from the underlying population and fit the Hα, Hβ and [O III]λ5007 lines using the same fitting routines as those used on the confirmed *FHIL* emitting AGN. We also determined the 2σ upper limits on the [Fe VII] and [Fe X] lines. The control sample was then cross checked against our lists of confirmed *FHIL* emitters to ensure that none of the latter had been included by chance.

4.4 AGN categorisation

Having identified a sample of *FHIL* emitting objects, it was necessary to classify them in terms of the standard Seyfert/Quasar categories. This enables us to determine trends associated with the *FHIL* emission lines with respect to these classifications. In particular it was necessary to identify the Sy1s and Sy2s (hereafter type 1s and type 2s). Unfortunately this process is complicated by the presence of so-called Sy1.5 - Sy1.9 (AGN that show the clear presence of a broad component in the Hα lines, but which is weak or non-existent in the Hβ lines[2]) in all our samples and H II regions in our control samples.

To differentiate between the H II regions and AGN in our control samples, we used the line ratio plots described by Baldwin et al. (1981) and the loci given in Kewley et al. (2001) (see Fig. 4.2). Although these ratio-ratio plots have in the past been principally used to distinguish between H II regions and narrow line (type 2) AGN, the narrow band across the parameter space in which the H II regions lie mean that they can be also be used to quickly distinguish the majority of broad line (type 1) AGN from H II regions and type 2 AGN. This leaves a small number of 'ambiguous' type 1 AGN that lie in the region of the parameter space populated by the H II objects. It is possible to then use the widths of the Gaussian components fitted to the Hα , Hβ and [O III]λ5007 lines to determine which of the objects with H II-like line ratios are indeed type 1 AGN. As H

*A random selection of 1000 spectra provided 57 type 1s, 25 type 1.9s and 85 type 2s- sufficient to provide us with reasonable statistics for the underlying AGN population.

[2]The differences between the profiles of the Hα and Hβ profiles in Sy1.x AGN is attributed to absorption along our line of sight that has a stronger effect on bluer parts of the optical spectrum.

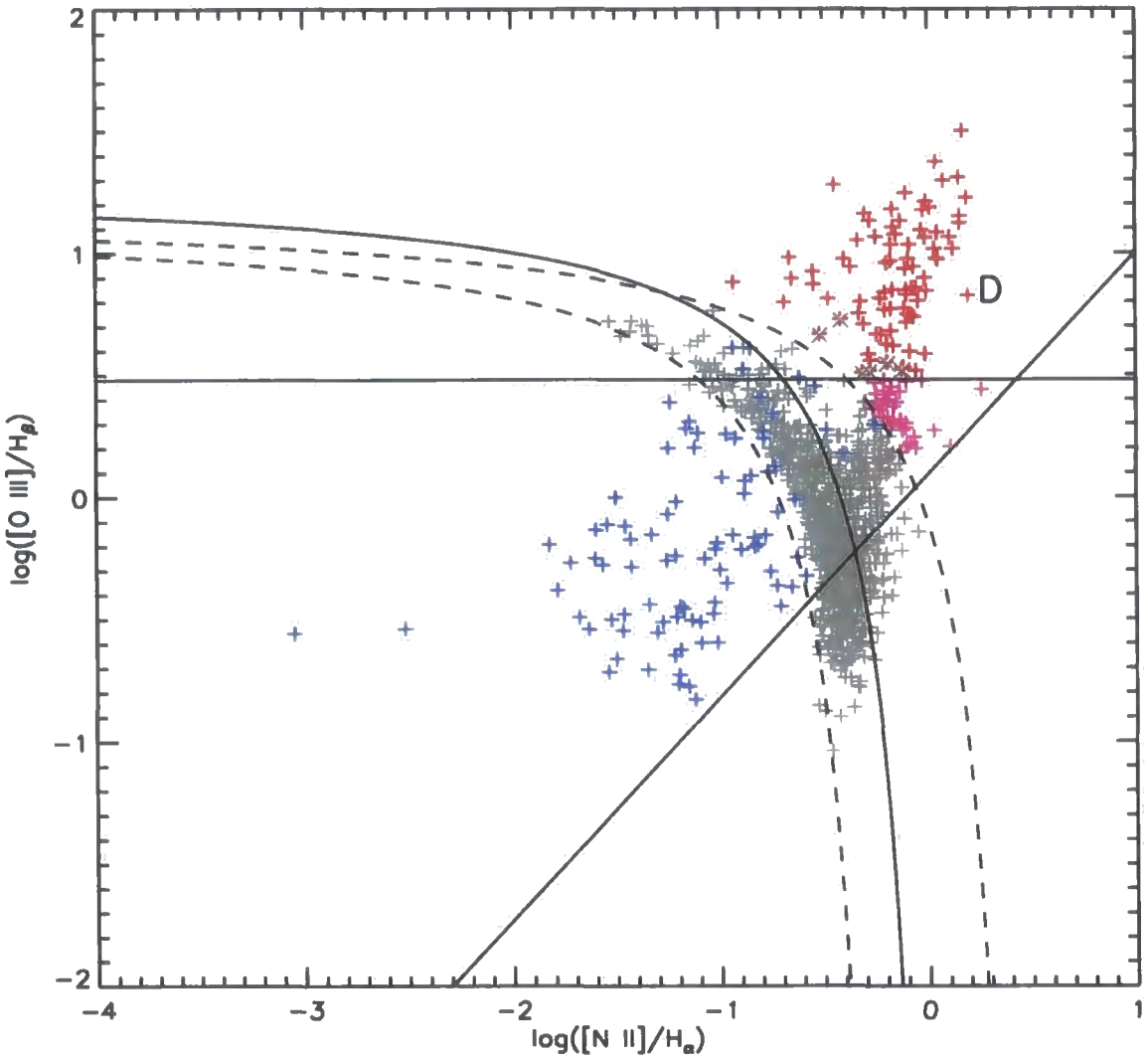

Figure 4.2: Line ratio (BPT) plot showing the distribution of AGN in our control sample. Blue points represent Sy1s, red points Sy2s, grey points HII regions and magenta points LINERS. Red points with grey 'X's show points that would be identified as Sy2s using the characteristics described here but on inspection were identified as HII regions. We use the loci of Kewley et al. (2001) (upper dashed line) to differentiate between narrow line objects (Type 2 AGN and HII regions). We define our own set of loci below which no HII regions are found (lower dashed lines)- only Type 1 objects populate this region. Type 1 objects can lie between the two sets of loci described here. These are differentiated from HII regions by having FWHM > 1000 km s^{-1}. The horizontal solid line represents the loci below which Type 2 objects are categorised as LINERS. We do not find any AGN below the solid diagonal line.

II objects typically have emission lines that are much narrower than type 1 AGN we visually inspected any object in the 'H II' region of the parameter space with Hα FWHM $>$ 1,000 km s^{-1}. Each of these were found to be type 1 AGN. As there is a risk that we could miss some type 1 AGN with very narrow lines by setting the the FWHM limit at 1000 km s^{-1} we inspected the Hα and Hβ lines of the rejected (i.e. H II) objects. Only one further type 1 AGN was found to be included in the rejected sample. We are therefore confident that the AGN and H II classifications shown in Fig. 4.2 are correct.

After testing a number of possible methods of distinguishing between Sy1.9s, NLS1s and Sy1s (such as the relative ratios of the broad and narrow components in the Hα and Hβ lines) it was found that the most robust was to classify these objects by simple visual inspection. This was possible as after the removal of H II regions from the control sample, the total number of spectra contained in our 3 samples was of the order of a few hundred, rather than thousands, of spectra. Objects that showed a clear weakening of the Hβ broad component (compared with the Hα line) were classified as Sy1.9 objects. We did not make any further subclassifications (e.g. 1.5 or 1.8) as our principal interest was to determine whether the broad component was being absorbed along our line of sight rather than complicate our results by using these somewhat arbitrary classifications.

Rather than use an arbitrary cut-off value for the Hβ or Hα FWHM to separate Sy1s and NLS1s, we chose use a weighted average Hα FWHM as an indication of the overall FWHM of the line. The characteristic width of the Hα line was determined by weighting the measured FWHM of a component with its luminosity. We excluded the narrow component of the Hα line from this calculation as its relative strength and FWHM bears no relation to the broad component. This weighted average is less sensitive to the presence of a weak, broad component in many Hα lines (especially in the case of NLS1s; see Chapter 2) than choosing the FWHM of the broadest component as an indication of the total FWHM of the emission line.

4.5 Reddening

As was the case with the smaller sample derived in the previous chapter, based on the measurements of the Balmer decrement we estimate that the impact of dust on this larger sample is relatively small. In Fig. 4.3 we show the distribution of the Balmer decrements for both the [Fe VII] detected sample and the [Fe X] detected sample. In the case of type 1 objects, the intrinsic Balmer decrement of the broad line region can be as large as

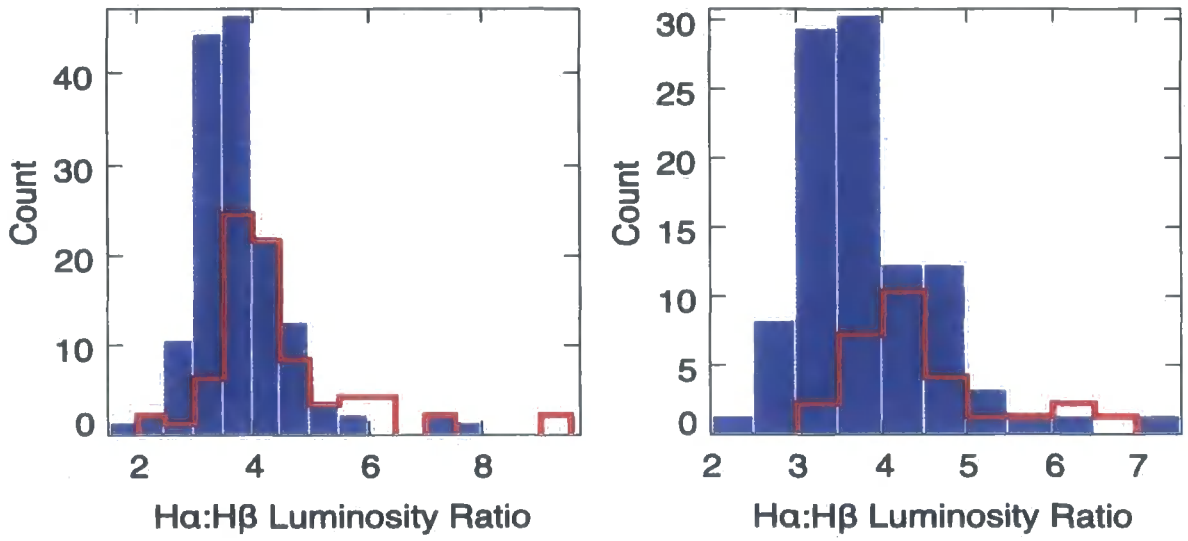

Figure 4.3: Balmer decrements for both the [Fe VII] detected (left) and the [Fe X] detected (right) samples. The blue bars represent type 1s, the red line type 2s.

~5. This is due to the high densities and optical depths of the BLR resulting in deviations from simple Case B recombination. Only six type 1 objects in our [Fe X] detected sample and eight in our [Fe VII] detected sample have Hα:Hβ ratios greater than this value. The highest Balmer decrement of either sample is 7.6. If we assume the intrinsic Hα:Hβ ratio for this object is 5, then the [Fe X]:[O III], [Fe VII]:[O III] and [Fe X]:[Fe VII] ratios will decrease by 29%, 25% and 5%, respectively, which is smaller than the relative systematic+random error associated with the luminosities of the *FHILs* (see §4.2.1)[3].

In the case of the type 2 objects, we assume that the Case B recombination ratio applies due to the lower densities of the narrow line regions. This implies that the intrinsic Hα:Hβ for these objects is 2.87 (assuming a temperature of 10,000K; Osterbrock and Ferland 2006). In both the [Fe X] and [Fe VII] samples, the majority of the type 2 objects have Balmer decrements less than 6 (71/81 for the [Fe VII] sample 25/31 for the [Fe VII] and [Fe X] detected samples, respectively) giving reductions in the [Fe X]:[O III], [Fe VII]:[O III] and [Fe X]:[Fe VII] ratios of 45%, 40% and 8%, respectively.

Based on our analysis of the Balmer decrements described above we choose not to attempt to correct the spectra for reddening as our main conclusions would not be affected. Furthermore, there is an inherent uncertainty in correcting for reddening, especially in

[3]If we assume a more typical intrinsic Hα:Hβ ratio of 4, then these ratios are decreased by 40%, 36% and 7%, respectively

the case of type 1 objects, as it is impossible to know the true intrinsic Balmer decrement (due to the deviation from Case B recombination in the BLR).

4.6 Results

4.6.1 Comparison with control sample

Fluxes/Luminosities

As we used the diagnostic powers of the BPT diagram to distinguish between type 1 & 2 AGN and H II regions in our samples, it was natural to consider whether the [Fe VII] and [Fe X] emitters differed from the control sample in terms of their locations on this plot. In Fig. 4.4 we show the BPT diagnostic plot for both the [Fe VII] emitters and the control sample. This plot shows that the type 1 [Fe VII] emitters cover the same region of the plot as the equivalent objects in the control sample. There is, however, a slight tendency for the [Fe VII] emitters to have higher [O III]λ5007:Hβ ratio than the control sample (at a given [N II]/Hα ratio; the mean [O III]λ5007:Hβ /[N II]/Hα values for the type 1 objects in the control and [Fe VII] samples are 0.09 ± 0.03 and 0.1 ± 0.01, respectively). With the exception of one object, the type 2 [Fe VII] emitters are only detected in objects with $\log\left(\frac{[O\,III]}{H\beta}\right) > 0.85\log\left(\frac{[N\,II]}{H\alpha}\right) + 0.95$ (i.e. typically stronger [O III]λ5007 relative to Hβ). Furthermore, there are no [Fe VII] emitters in the LINER region of the plot.

In Fig. 4.5 we show the equivalent plot showing the distribution of the [Fe X] on the BPT diagram. This shows that the type 2 [Fe X] emitters lie in the same region as the type 2 [Fe VII] emitters (i.e. apparently preferentially produced in objects with strong [O III] relative to Hβ at a given [N II]/Hα ratio). The type 1 [Fe X] emitters appear to lie in the same region of the parameter space as the [Fe VII] emitters and the control sample, yet again showing a slight tendency toward higher [O III]λ5007:Hβ ratios.

The distribution of type 2 [Fe VII] and [Fe X] emitters could be seen as confirmation that objects that emit strong *FHILs* avoid the regions of the BPT plot with low [O III]λ5007 :Hβ ratios at a given [N II]:Hα ratio. However, it is possible that this result is produced by selection effects introduced by our line fitting models. If we assume for now that the [Fe VII]:[O III]λ5007 and [Fe X]:[O III]λ5007 ratios in type 2 AGN are roughly constant (our results from Chapter 3 suggest that the both the [Fe VII] and [Fe X] fluxes are typically 1-5% that of [O III]λ5007), then we will be unable to detect [Fe VII] emission in objects with weak [O III] lines- i.e. those which are more likely to have

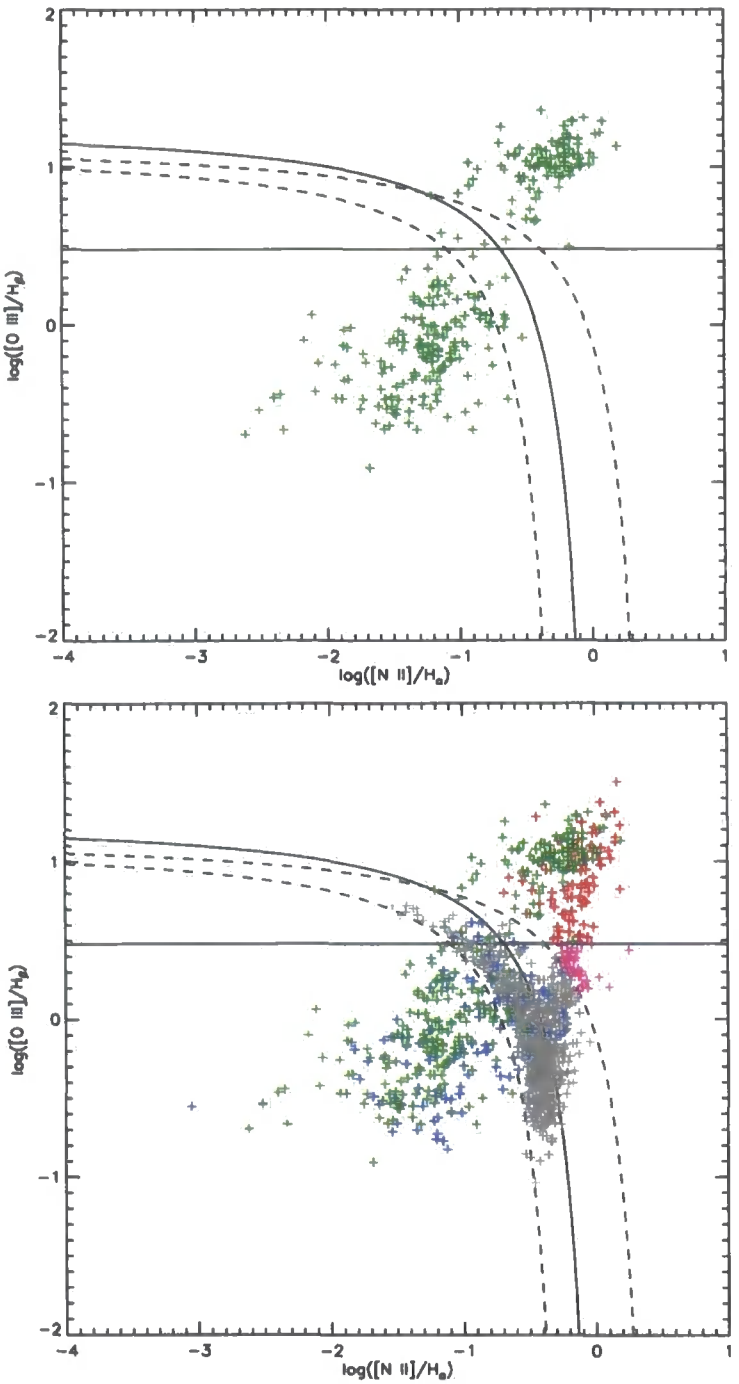

Figure 4.4: Same as Fig. 4.2 but now we include the sample showing the most clear evidence of [Fe VII] emission ($\frac{\Delta F}{F}$<50%) in green (we include the blue, red and grey points of Fig. 4.2 in the lower plot to enable comparison between the [Fe VII] emitting sample and the control sample). The type 1 [Fe VII] emitters are distributed over the same region of the plot as the control sample, although there is a slight tendency to lie above (i.e. have higher [O III]λ5007:Hβ ratios) than the control sample. The type 2 [Fe VII] emitters aparently avoid the low ionisation region of the plot (low [O III]λ5007:Hβ ratio Type 2 AGN and LINERS). This 'area of avoidance' is explored in the text.

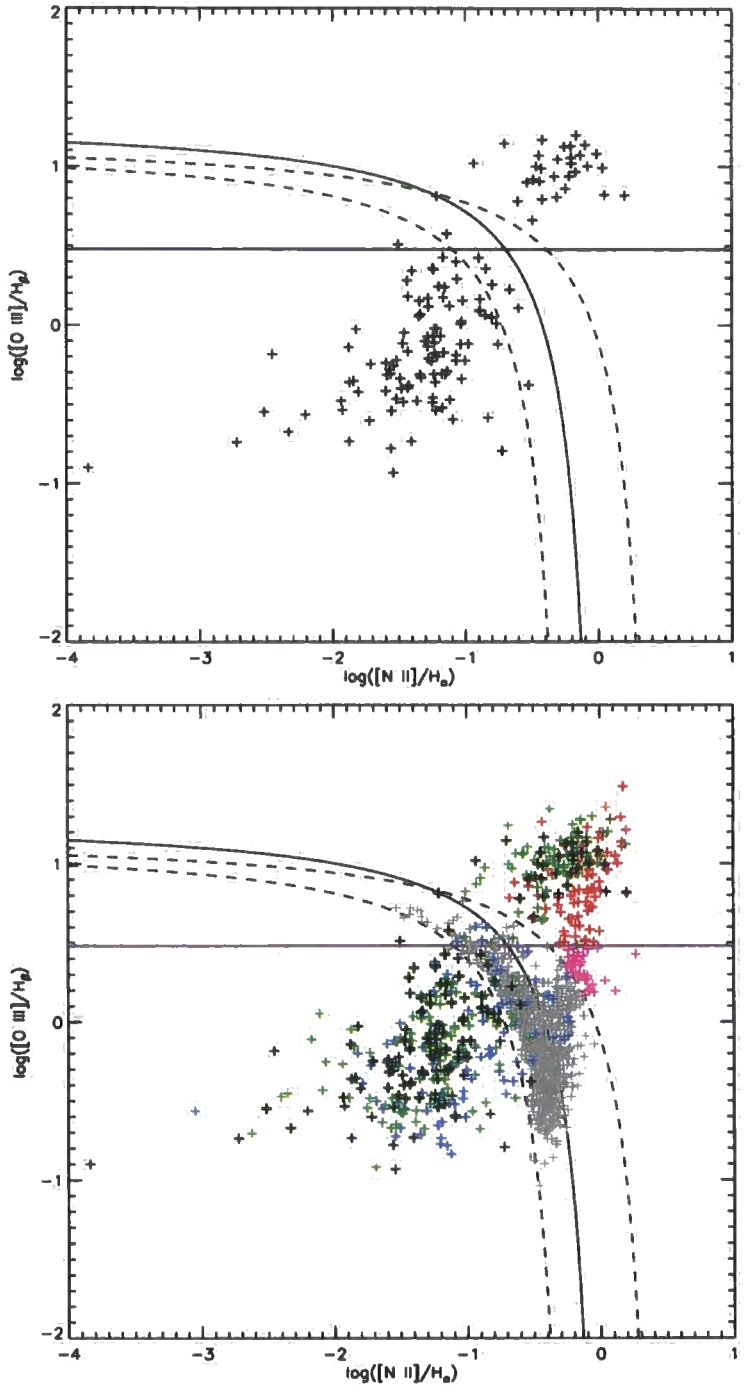

Figure 4.5: Same as Fig. 4.4 but now we include the [Fe X] emitting objects in black

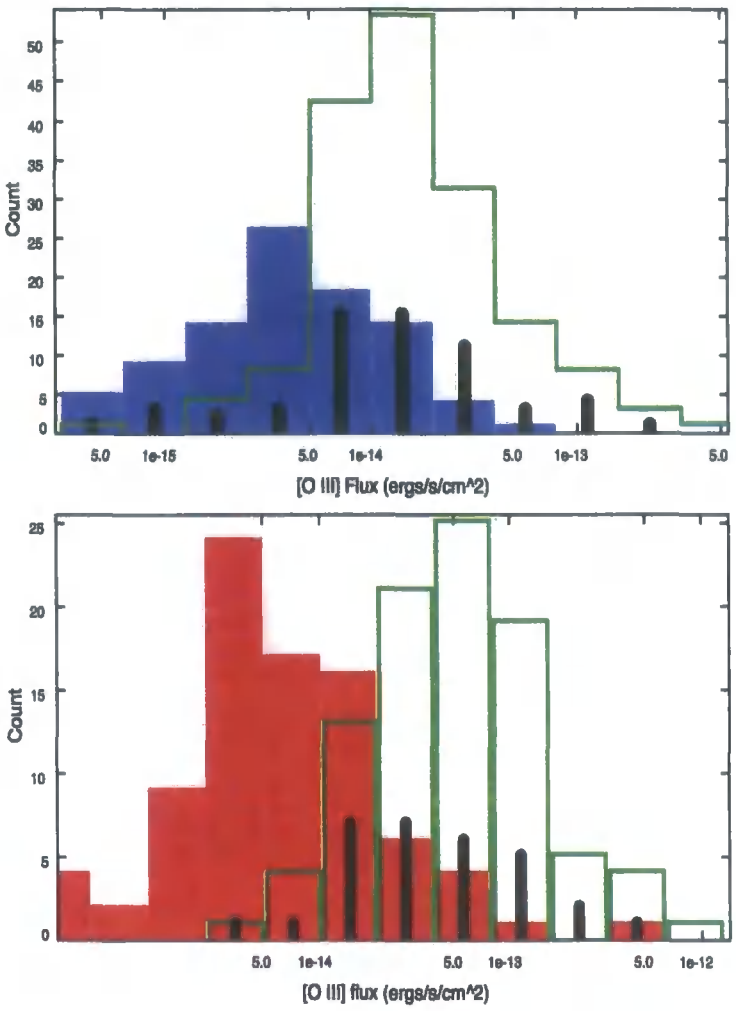

Figure 4.6: Distribution of [O III]λ5007 flux for type 1 AGN (top) and type 2 AGN (bottom) within our control sample (CS1) (blue and red bars, respectively) and the [Fe VII] (green) and [Fe X] (black) samples.

low [O III]/Hβ values. To determine whether this is the case, we investigated whether the objects with [Fe VII] detected by our fitting routine had systematically higher [O III] flux as compared to the control sample. Fig. 4.6 shows that this is indeed the case; the number of type 1 (type 2) [Fe VII] and [Fe X] emitters peaks at an [O III] flux that is ∼4 (∼16) times that of the control sample.

Despite showing that there is a large difference in [O III] flux between the *FHIL* emitting and control samples we cannot yet rule out that the *FHIL* emitters could preferentially populate sub-regions of the BPT parameters space. With the systematic differences between the control and *FHIL* emitting samples in mind, we produced a second control sample (CS2) by selecting only objects with [O III]λ5007 flux $> 1 \times 10^{-14}$ ergs/s/cm^2.

This more closely matches the range of [O III] fluxes displayed by the *FHIL* detected samples (see Fig. 4.6) and is therefore a more reasonable comparison sample. The BPT diagram for this new sample (with the [Fe VII] and [Fe X] emitting sources included) is shown in Fig. 4.7. Although the number of type 2 objects in CS2 that populate the *FHIL* detected AGN 'zone of avoidance' is significantly fewer than is the case for CS1, there remain 19 type 2 objects in the region of the BPT diagram in said region. On obtaining 2σ upper limits for the flux of the [Fe VII] line in these 19 objects, 18 were found to have upper limits on their [Fe VII]/[O III] ratios that are consistent with the type 2 [Fe VII] emitting sample ([Fe VII] flux > 0.25% of the [O III] flux). This is consistent with [Fe VII] emission roughly scaling with [O III] emission for the vast majority of sources, but falling below our detection limit at low [O III] flux levels.

The above test revealed a single object for which the upper limit on the [Fe VII]/[O III] sample was inconsistent with the general [Fe VII] emitting population . This could suggest a bi-modal distribution of [Fe VII]/[O III] ratios among the AGN sample. To investigate this further we plot the upper limits on the [Fe VII]/[O III] ratio for a sub-sample of objects in CS2 with [O III] flux spanning a similar range as those in the [Fe VII] and [Fe X] detected samples (see Fig. 4.8). There is no indication of any bimodality to the [Fe VII]/[O III] ratio in either type 1 or type 2 AGN- the distribution of [Fe VII]:[O III] upper limits from each sample blend into one another in both plots, revealing a continuous range of [Fe VII]:[O III] ratios spanning two orders of magnitude. A KS test reveals (with a confidence >99.9%) that we are preferentially selecting objects with high [Fe VII]:[O III] ratios in the case of our [Fe VII] sample ($\gtrsim$0.03 and $\gtrsim$0.01 for type 1s and 2s, respectively).

Conversely, the bottom panel of Fig. 4.8 reveals that, although we tend to select objects of both type with slightly higher [Fe X]/[O III] ratios than average (based on upper limits) we also miss a significant proportion of targets within the control sample having a similar range of [Fe X]/[O III] values. On inspection all the objects that we are missing in the control samples were, in fact, flagged by the fitting routine as possessing [Fe X] lines (i.e. based on χ^2 statistics), but were removed from the samples during the $\frac{\Delta F}{F}$ >50% cut described in §4.2.1. This is a clear indication that our [Fe X] sample is not complete. In particular, our $\frac{\Delta F}{F}$ cut preferentially excludes objects with broad [Fe X] lines, as shifting the level of continuum under a broad line will have a larger effect on a line spanning a large range in wavelengths. Despite this we defend our choice of imposing a selection criterion based on the systematic errors as without it the results

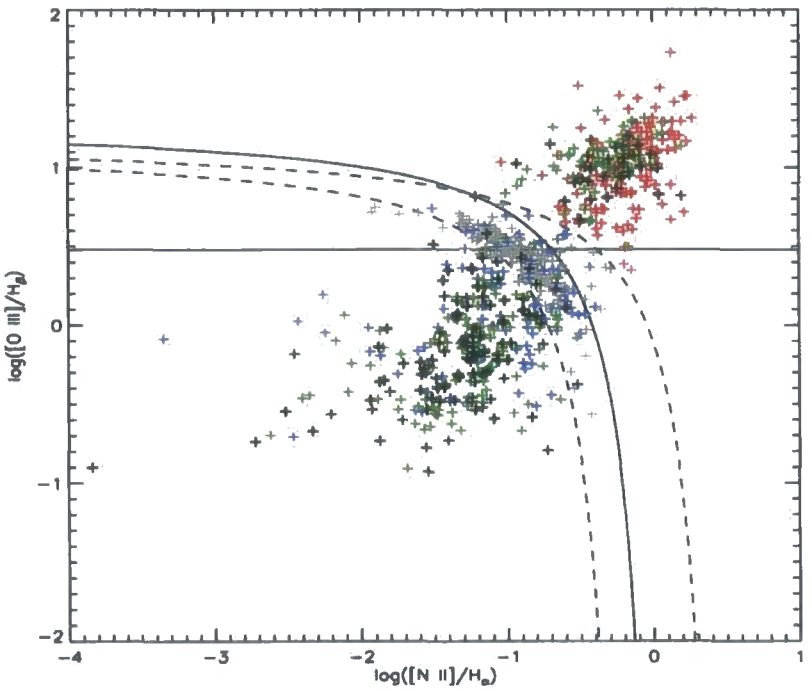

Figure 4.7: BPT diagram with CS2 as the control sample which only contains objects with [O III]λ5007 $> 1 \times 10^{-14}$ ergs/s/cm^2. 19 type 2 objects lie in the region above the horizontal line (to the bottom) which is avoided by both [Fe VII] and [Fe X] emitters. On further inspection, 18 of these objects had upper limits on the [Fe VII]/[O III] ratio that are consistent with the general [Fe VII] emitting population.

described in the following sections would be dogged by uncertainties associated with these errors. Throughout the following sections we consider the effects of this selection bias and mitigate its influence on our results.

Aside from informing us of the completeness of our sample, the lower panels of Fig. 4.8 gives us a clear indication of the range of (the upper limits of) the [Fe X]/[O III] ratios in AGN in general (i.e. not just the [Fe X] and/or [Fe VII] samples). In type 1 AGN, there is a continuous distribution of [Fe X]/[O III] values that spans more than an order of magnitude ($0.01 \gtrsim$[Fe X]/[O III]$\gtrsim 0.3$, peaking at $\sim$5%). In the case of type 2 objects, this same ratio extends over a slightly broader range of values (over 2 orders of magnitude) and peaks at a slightly lower value of $\sim$2%.

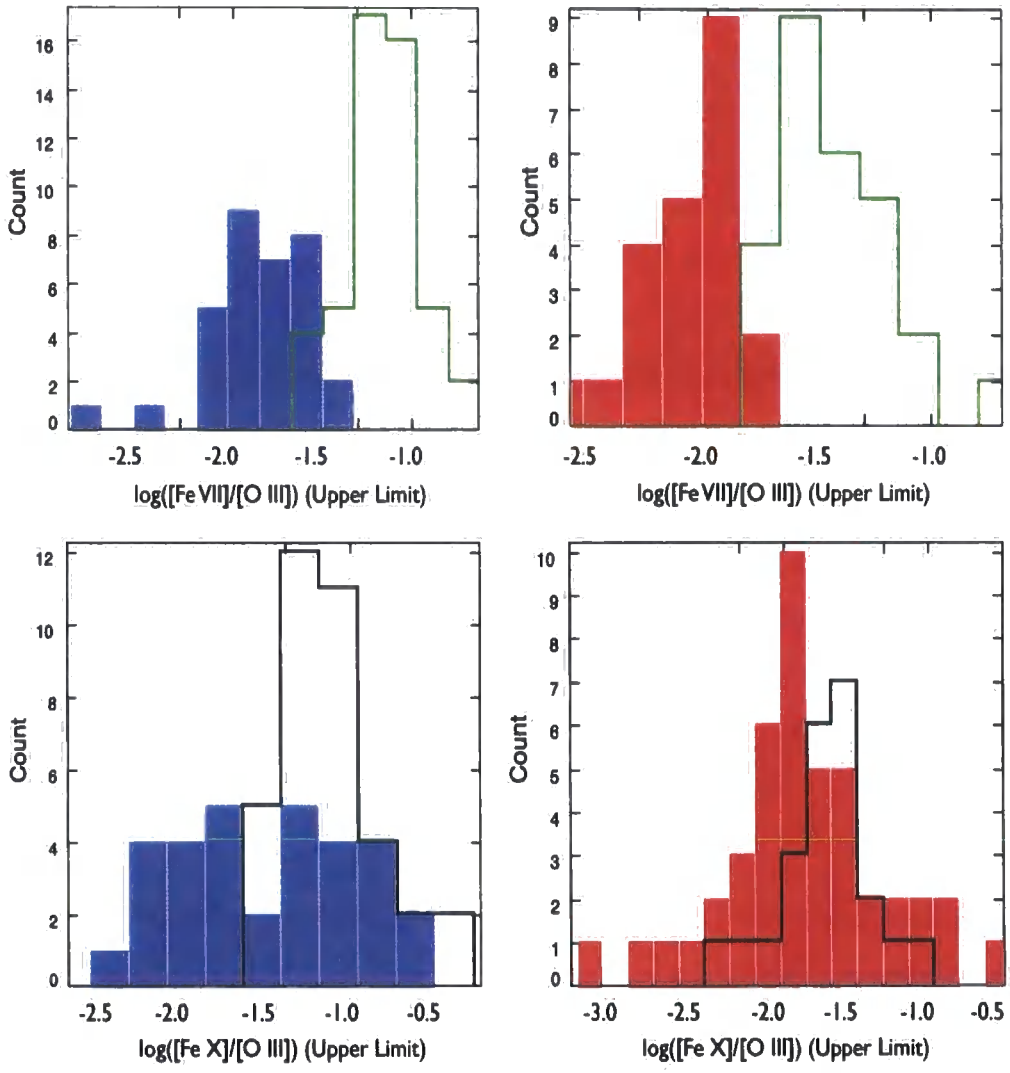

Figure 4.8: Top: Distribution of [Fe VII]/[O III] upper limits for type 1 objects (blue bars) and type 2 (red bars) objects in CS2. Overplotted in green is the distribution of [Fe VII]/[O III] for both type 1s (left) and type 2s (right) (with [O III] $>10^{-14}$ergs/s/cm^2) from the [Fe VII] selected sample. Bottom: Distribution of [Fe X]/[O III] upper limits for type 1 objects (blue bars) and type 2 (red bars) objects in CS2. Overplotted in black is the distribution of [Fe X]/[O III] for both type 1s (left) and type 2s (right) (again, with [O III] $>10^{-14}$ergs/s/cm^2) from the [Fe X] detected sample.

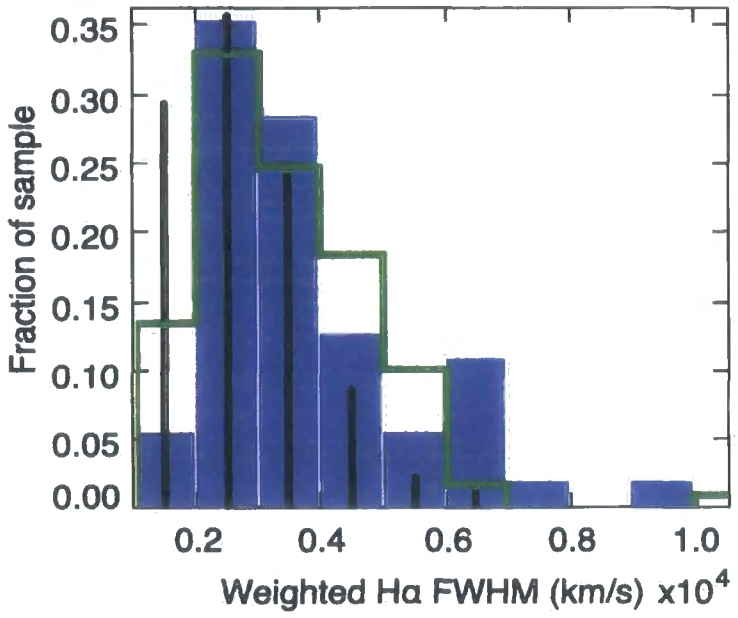

Figure 4.9: Weighted average FWHM of the two broadest components of the Hα lines of type 1 AGN in the control sample (CS1; blue), [Fe VII] emitting sample (green) and [Fe X] emitting sample (black).

Line Widths

Although it has never been examined systematically, there is a general impression that *FHILs* are preferentially produced in NLS1 AGN. With the samples we have obtained, we are now in the position to test this hypothesis. In Fig. 4.9 we show the relative proportions of each of our samples of type 1 AGN which lie in each characteristic weighted Hα FWHM bin. In terms of Hα FWHM, both the [Fe VII] and [Fe X] samples are skewed, relative to the control sample, towards objects with narrower Hα lines. In particular, the lowest FWHM bin (<2000 km s^{-1}) contains 29% of [Fe X] and 15% of [Fe VII] emitters compared to only 6% of the control sample. This apparently supports the view that the most highly ionising AGN are those with narrow permitted lines.

To test this, we must consider the selection effects incorporated into our fitting routine that may bias us towards detecting such lines in objects with narrow Hα lines. Throughout this discussion we will concentrate on the [Fe X] line over the [Fe VII] line because of its stronger tendency to being detected in narrow objects and because it is more likely to be affected by selection effects due to its proximity to the Hα line (r.f. Chapter 3).

A possible selection effect was outlined in Chapter 3- the measurement of the [Fe X] lines could be influenced by the wings of the nearby Hα line. This can be tested by

producing a set of simulated spectra with increasingly broad Hα lines which also include typical [Fe X] and [O I] emission lines. These latter two lines were given average profiles and fluxes derived from the [Fe X] sample. The model spectra were then degraded by the addition of random noise and the same fitting routine was then used to determine the level of accuracy the fitting routine can achieve at each value of Hα FWHM. On fitting this mock sample with the same [Fe X] line fitting routine as for the general sample, it was found that the continuum fitting routine was accurately tracing the underlying continuum and the wings of the Hα line where these extended to the [Fe X] and [O I] lines. This conclusion is based on ten fits performed on two otherwise identical spectra with Hα FWHM of 3000km s^{-1} and 7000km s^{-1}. The mean χ^2 values associated with the continuum fit to these spectra are 239±20 and 246±15 (across 137 bins), respectively. Any biasing of the sample due to the fit of the Hα wing and continuum can therefore be ruled out as an explanation for the increased proportion of [Fe X] emitters at low values of Hα FWHM (compared against our control sample). Our continuum fitting routine is just as good at tracing spectra with broad Hα wings as those with narrow.

In §4.6.1 we show that, with the exclusion of a minority of outlying sources, the flux of the [Fe X] line is typically 1-5% the flux of the [O III] line in the objects in which the [Fe X] line is detected. If we therefore assume that the upper limit for the [Fe X]:[O III] ratio is 5% in the majority of sources (i.e. excluding the small number of outliers) we would be unable to detect [Fe X] lines in objects with low [O III] flux. Furthermore, if it were found that the objects with the broadest Hα lines were also those that had, on average, lower [O III] flux, this would explain why the fitting process and analysis preferentially detects [Fe X] lines in type 1 objects with narrower lines. A similar argument could also be applied to the distribution of continuum flux among the sample – if the objects with broad Hα lines had a weaker continuum and thus lower S/N around [Fe X] then, again, we would preferentially detect [Fe X] line objects with narrow Hα. Why would we expect broad objects to be fainter on average? Fig. 4.9 shows that type 1 objects with Hα FWHM > 4000km/s become increasingly rare at higher FWHM values. Furthermore, the AGN with the broadest lines also tend to be the brightest. We should therefore expect that these objects have, on average, a higher redshift than the more common (per unit area on sky) objects with Hα FWHM < 4000km/s. We may therefore suspect that these broader objects may be fainter due to geometric dilution of their intrinsic luminosity.

Fig. 4.10 shows that it is not the case that type 1 objects with broad Hα (FWHM > 4000km/s) have either systematically fainter continuum S/N ratios or [O III] lines. In

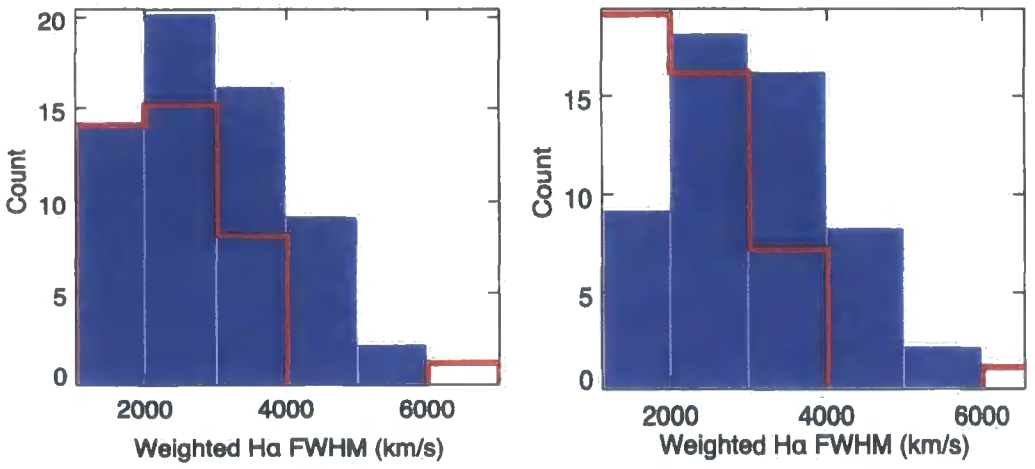

Figure 4.10: Left: Hα FWHM distribution of the [Fe X] sample. The sample has been split according to the flux of the [O III]λ5007 line. The red line represents sources with [O III]$<1 \times 10^{-14}$ergs/s/cm^2, the blue bars represent sources with [O III]$>1 \times 10^{-14}$ergs/s/cm^2. Right: Same as *left*, in this case, however, the sample has been split according to the S/N level in the continuum. The red line refers to spectra with S/N$<$40, the blue bars refer to those with S/N$>$40.

fact, there is some evidence that the sources with *higher* continuum S/N ratios and [O III] fluxes are those with Hα FWHM$>$4000km/s. This rules out the possibility that the [Fe X] lines are undetected in broad line objects because they are systematically fainter.

A further selection effect that could produce the increased proportion of [Fe X] emitters with low Hα FWHM is that the fitting routine may be missing objects with very broad [Fe X] lines. Consider two similar spectra both of which have [Fe X] lines containing equal flux. If the [Fe X] line in one spectrum was twice as broad as that in the other, then the contrast between the continuum noise and the [Fe X] line will be reduced in this object. It is therefore possible that the fitting routine is missing objects with broader [Fe X] lines- particularly when we determine the errors associated with the quality of the continuum fit and remove those with large systematic errors (see §4.2.1). If it were the case that the FWHM of the [Fe X] line was correlated with the FWHM of the Hα line, then we may expect to miss a large proportion of the [Fe X] emitters that had broad Balmer lines. However, Fig. 4.11, shows that there is no correlation between the measured [Fe X] FWHM and the Hα FWHM. This rules out the possibility that broader [Fe X] lines in objects with broad Hα lines are the cause of the bias towards detecting [Fe X] lines in

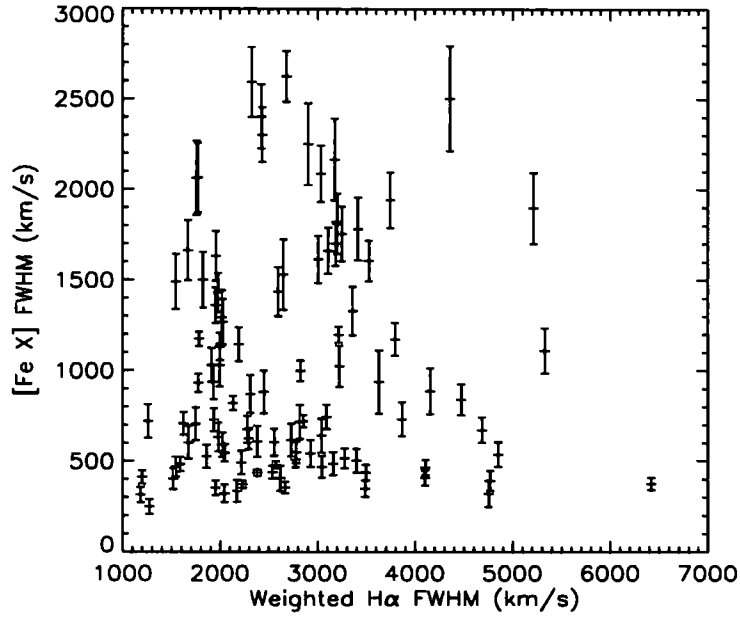

Figure 4.11: [Fe X] FWHM plotted against weighted Hα FWHM for the [Fe X] detected sample.

narrow line type 1 objects – broad [Fe X] lines are just as likely to be detected in objects with small Hα FWHM values as with large. Even if we include the objects from CS2 that were rejected in our $\frac{\Delta F}{F}$ cut (which we found in §4.6.1 to have systematically broader [Fe X] lines), no significant correlation between the [Fe X] FWHM and Hα FWHM is found (Spearman's ρ=0.18).

To rule out the possibility that the [Fe X] lines are being missed in broad line objects because of differences in the continuum S/N levels in the broad- and narrow-line type 1 objects we split our sample of [Fe X] emitters into sub-samples according to the S/N of the spectra around the [Fe X] line (between 6250Åand 6450Å). In Fig. 4.12 we show the effect this splitting has on the relative populations of [Fe X] detected type 1s in each Hα FWHM bin. When we analyse the data in this way, the relative population of [Fe X] emitters in the narrowest Hα bin drops to 17% (of a total sample size of 53 in the highest S/N bin, S/N>40; representing about one half of the overall [Fe X] emitting Sy1 population). [Fe X] detected spectra with lower S/N tend to populate the lower Hα FWHM bins. This result supports the suggestion that the increased proportion of [Fe X] sample having low Hα FWHM widths (see Fig. 4.9) are caused by selection effects. However, the proportion of spectra with the highest S/N (>40) with Hα FWHM <2000km s^{-1} is still almost three times greater in our [Fe X] sample (17%) as in our control sample (6%).

Even at high S/N levels, it is still possible that the fitting routine preferentially de-

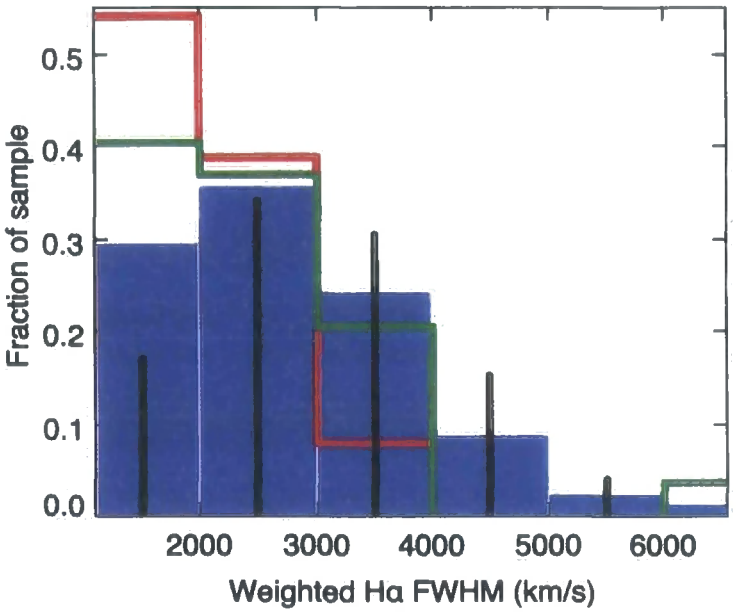

Figure 4.12: Hα FWHM distribution of the sample with detected [Fe X] lines. The blue bars refer to the whole [Fe X] sample, whereas the other indicators (lines/spikes) show the FWHM distribution as a function of S/N in the continuum. The red lines refer to spectra with 20<S/N< 30 (13 objects), the green line refers to spectra with 30<S/N< 40 (30 objects) and the black spikes refer to objects with S/N>40 (53 objects). The proportion of objects in the narrowest Hα FWHM bin drops as the S/N of the spectrum increases. The S/N>50 sample (not shown) has the same proportion of objects in the narrowest Hα FWHM bin.

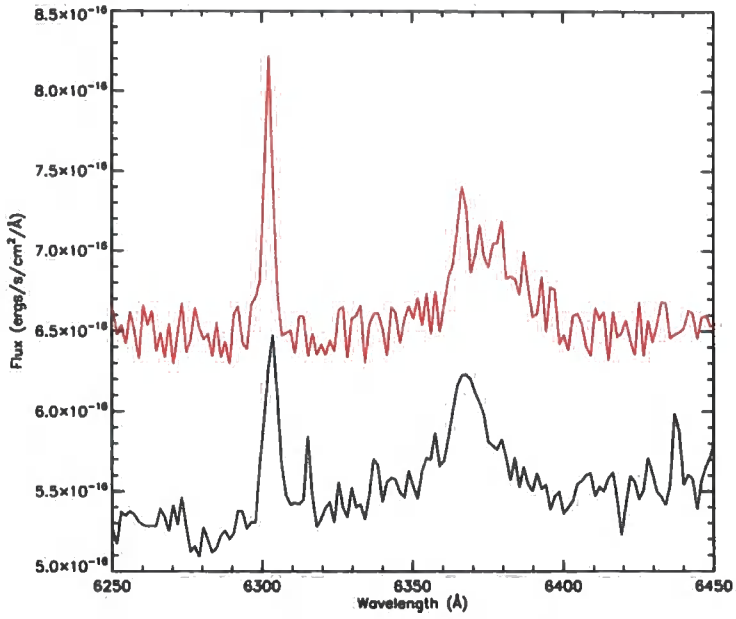

Figure 4.13: A typical S/N=40 spectrum with from our sample of spectra with [Fe X] detected (black) and a typical S/N=40 mock spectrum (red, offset). Throughout our sample of mock spectra the flux in the [Fe X] line was kept constant while the FWHM of the line was increased from 200km s^{-1} to 3000km s^{-1}.

tects [Fe X] lines in narrow line type 1 objects over broad. In order to test whether this is the case we created a mock sample of spectra, each having a S/N of 40 in the continuum. To this we added the [O I] lines, a broad Hα line (we used two values for Hα FWHM, 3000km s^{-1} and 6000km s^{-1} to determine what effect, if any, this had on the [Fe X] detection) and an [Fe X] line with an equivalent width of 2.5Å- the average for the [Fe X] sample with S/N=40 in the continuum (a typical mock spectrum is shown in Fig. 4.13). The FWHM of the [Fe X] line was varied between 250km s^{-1} and 3000km s^{-1} between the spectra in the mock sample to determine at which point the our fit routine ceased to detect [Fe X]. Five spectra were produced for each combination of Hα and [Fe X] FWHM in order to determine the likelihood of detection. The [Fe X] fitting routine was then run on this mock sample. Fig. 4.14 shows the success rate of the detection routine – 100% of the sample are detected at [Fe X] FWHM < 1600 km s^{-1}. Is there a systematic difference in Hα FWHM values between objects in our [Fe X] detected, type 1, S/N > 40 sample with FWHM < 1600km s^{-1} and FWHM > 1600km s^{-1}? When we split this sample according to the measured [Fe X] FWHM, i.e. greater than or less than 1600km s^{-1}, we find that the two sub-samples have consistent mean Hα FWHMs (3000±1000km

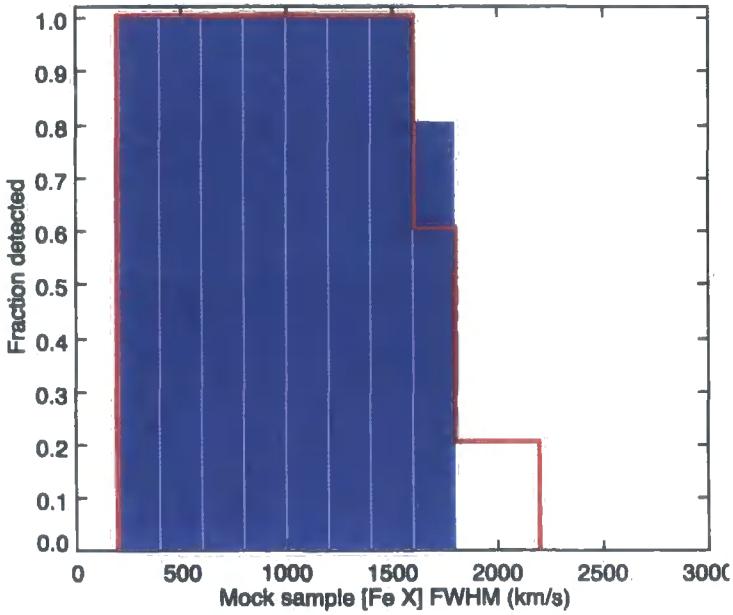

Figure 4.14: Detection rate of the fitting routine as a function of [Fe X] FWHM for a sample of mock spectra with S/N = 40. All the detections shown here have a total error (random plus systematic) of <50% (i.e. the same as the [Fe X] and [Fe VII] emitting samples discussed here). The blue bars and red line correspond to spectra with Hα FWHM of 3000km s^{-1} and 6000km s^{-1}, respectively.

s^{-1} and 3180±760km s^{-1} for the [Fe X] FWHM >1600km s^{-1} and <1600km s^{-1} samples respectively). This indicates there is no significant difference in Hα FWHM between objects that are expected to be detected ([Fe X] FWHM < 1600km s^{-1}) and those that are less likely to be detected ([Fe X] FWHM > 1600km s^{-1}; based on the results of our mock sample). We are therefore confident that the difference between the relative populations with low Hα FWHM for the [Fe X] and control samples is real and has not been introduced by selection effects or the fitting routine.

Having ruled out all likely selection effects, we can confirm that the [Fe X] lines are preferentially produced in type 1 objects with narrower Hα lines. However, Fig. 4.15 indicates that there is no direct correlation between the strength of the [Fe X] lines and the FWHM of Hα . Instead, this plot shows that although broad line objects are apparently restricted to producing weak [Fe X] (relative to other emission lines), this restriction does not exist in narrow line type objects (with weighted Hα FWHM < 3600km s^{-1}) – they are capable of producing very strong [Fe X] lines relative to the other, less highly ionised emission lines. To ensure that the dearth of broad line objects with strong [Fe X] lines

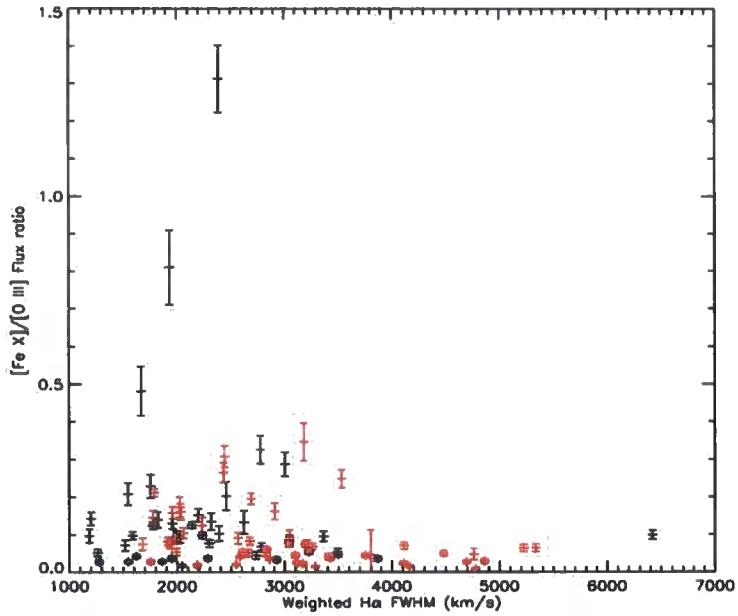

Figure 4.15: [Fe X]/[O III] ratio plotted as a function of weighted Hα FWHM. The sources with narrow Hα lines (FWHM<3600km s^{-1}) have a much larger spread of relative [Fe X] strength extending to higher values than the broad line objects. Red points refer to objects with S/N>40 in the continuum.

is real and is not produced by the lower relative numbers of broad line objects we split the [Fe X] detected sample into those with Hα FWHM $<$ 3600km s^{-1} and those with Hα FWHM $>$ 3600km s^{-1}. We then performed a KS test on these sub-samples based on the [Fe X]/[O III] flux ratio. This revealed that there is a 0.1% probability that these two samples are drawn from the same underlying distribution of [Fe X]/[O III] values making the difference between the two populations (in terms of the [Fe X]/[O III] ratio) significant at the 3σ level. If we only take those sources with continuum S/N>40, this probability increases to 1% and the significance reduces to 2.6σ.

4.6.2 *FHIL* luminosity/flux correlations

In Chapter 3 we investigated the correlations that exist between the *FHILs* and other emission lines in a smaller sample selected purely on the [Fe X] line. We now briefly revisit some of these correlations using the larger, more homogeneously selected sample presented here. Furthermore, as one of these new samples has been selected based on the detection of the [Fe VII] line (rather than only the [Fe X] line) we are now able to determine how the method of selection effects these correlations.

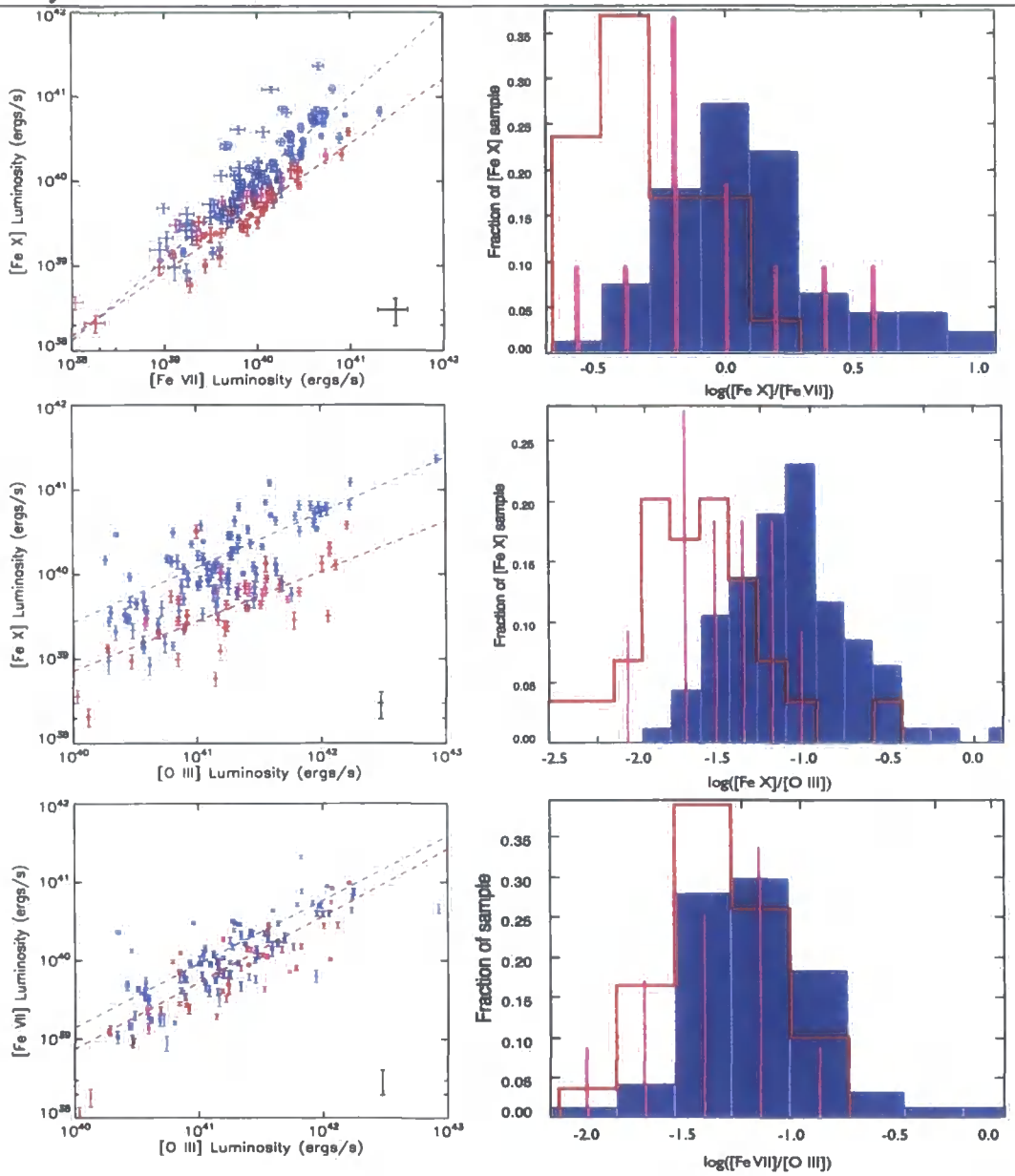

Figure 4.16: Line luminosity-luminosity plots (left) and ratio histograms (right) for the [Fe X] sample. Blue points/ bars refer to type 1 AGN, red points/lines refer to type 2 AGN and magenta points/lines refer to type 1.9 AGN. The error bars in the plots refer to random errors associated with the measurements. The black error bars in lower right of the scatter diagrams show the typical size of the systematic error described in the text.

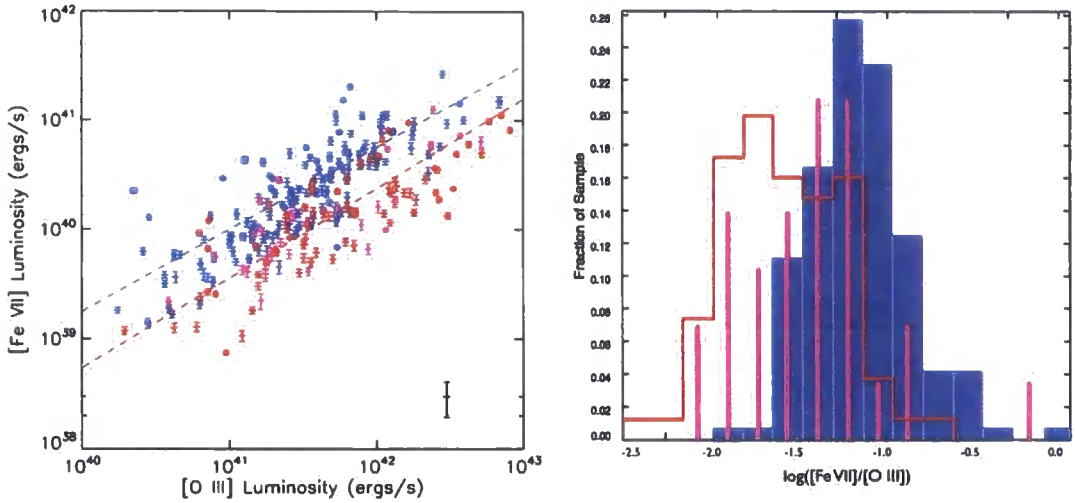

Figure 4.17: Left: [Fe VII] line luminosity plotted against [O III] line luminosity for the [Fe VII] sample. Right: Histogram showing the distribution of [Fe VII]:[O III] ratio for each type of AGN studied (blue:1s, red:2s, magenta:1.9s)

The difference between the [Fe VII]:[Fe X] flux ratio between type 1 and type 2 AGN was one of the main conclusions of the previous chapter. In Fig. 4.16 we show the equivalent plot for the objects in our larger sample in which both these lines have been detected. The difference in this flux ratio between type 1 and type 2 is again evident. A KS test indicates the likelihood that the type 1 and type 2 objects were drawn from the same underlying population (in terms of [Fe X]:[Fe VII] flux ratio) is $\ll$0.01%. The same test reveals that the type 1.9s are better described as belonging to the same underlying population as the type 1s, rather than the types 2s, although the difference is marginal (9.5% and 6.9%, respectively). In Table 4.1 (at the end of this chapter) we give the statistics of the samples associated with the measured parameters. On average, the [Fe X] line in type 1 objects is 25^{+125}_{-62}% stronger than the [Fe VII] line, although there is considerable scatter around this value (the errors are derived from the standard deviation of this ratio). The [Fe X] line in type 2 AGN is considerably weaker- having, on average, only 50^{+30}_{-18}% of the flux of the [Fe VII] line. Furthermore, there is considerably less scatter in this ratio in the type 2 objects. In the case of type 1.9 AGN the mean ratio of these lines is approximately mid way between that of type 1s and type 2s.

Fig. 4.16 shows that when a sample is selected based on the presence of the [Fe X] line, there is a distinct difference between the [Fe X]:[O III] ratio between the type 1 and type 2 AGN. The scatter of this ratio is larger than in the case of the [Fe X]:[Fe VII] in

both type 1s and 2s making the distinction between the two population less clear. A KS test still reveals that the chance that these two populations are drawn from the same underlying sample (in terms of this line ratio) is $\ll$0.01%. The same test shows that the type 1.9 AGN are significantly more likely to be a subset of the same underlying population as the type 2 AGN (15% likelihood, as opposed to 0.7% likelihood they are a subset of type 1s). Again, the mean ratios show that the [Fe X] line is stronger (with respect to [O III]) in type 1 AGN than type 2s.

In the previous chapter we showed that when the *FHIL* emitting sample is selected based on the presence of the [Fe X] line, there is no significant difference between the [Fe VII]:[O III] ratio in type 1 and type 2 AGN. We find that this remains to be the case in this larger sample (see Fig. 4.16). However, if we now turn to the sample selected on the detection of the [Fe VII] line, we find that there is a significant difference between the type 1 and type 2 population in terms of the [Fe VII]:[O III] ratio (a KS test reveals a $\ll$0.01% probability that the two types are drawn from the same underlying population in terms of the [Fe VII]:[O III] ratio). This is shown in both plots of Fig. 4.17. The statistics of the [Fe VII] sample are given in Table 4.2. The mean [Fe VII]/[O III] ratio of the type 1 AGN is a factor of 2.5 higher than the type 2s. This is in agreement with the findings of Murayama and Taniguchi (1998) and Nagao et al. (2000). A further KS test (and the histogram in Fig. 4.17) supports the suggestion that the type 1.9s are a subset of the type 2 AGN, rather than type 1s, in terms of the [Fe VII]:[O III] flux ratio (27.9% compared to 0.05%, respectively).

4.6.3 *FHIL* kinematics

One of the main advantages of our fitting routines is that the use of Gaussian components provides information on the kinematics of the emitting region. In Fig. 4.18 we show the distribution of [Fe X] FWHM in our [Fe X] selected sample and how this property relates to the [Fe VII] FWHM in the three classes of AGN we distinguish between. It is evident in both plots of Fig. 4.18 that the [Fe X] FWHM shows considerable scatter in type 1 AGN, whereas in type 2s the [Fe X] line is typically restricted to $\lesssim$500 km s^{-1}. The two type 2 AGN with [Fe X] FWHM significantly greater than this limit were inspected ensure that the measurements were valid. Both of the type 2 outliers in this plot have broader than average [O III] wing components ($\sim$1000 km s^{-1}, compared to the average of 710 km s^{-1}). It is therefore feasible that we are seeing the [Fe X] line being produced in a region with similar kinematics as that responsible for the [O III] wing in these objects.

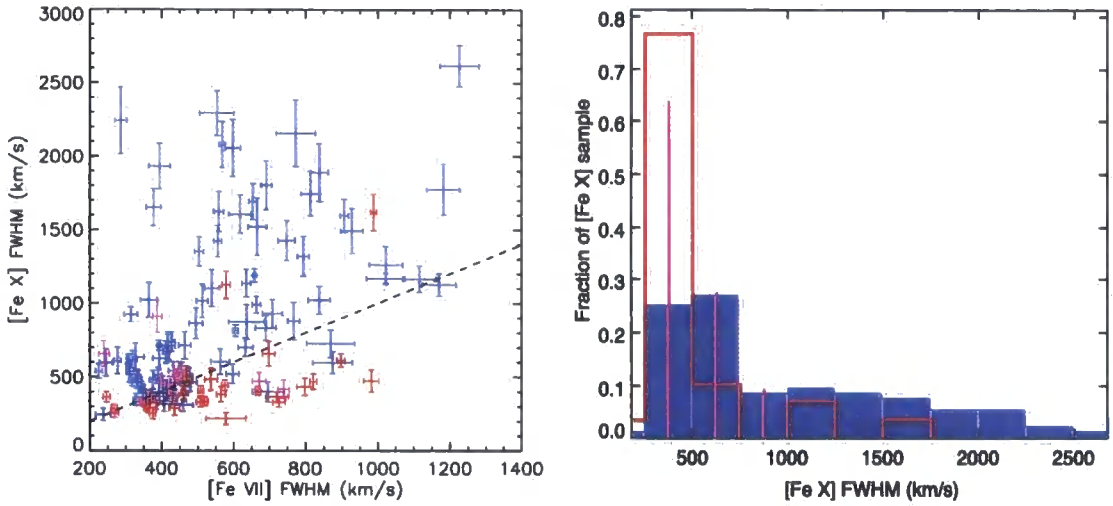

Figure 4.18: [Fe X] kinamatics: Left: [Fe X] FWHM plotted against [Fe VII] FWHM. Right: Distribution of [Fe X] FWHM among the studied AGN types (blue: 1s, red:2s, magenta:1.9s).

There is no significant correlation between the [Fe X] and [Fe VII] FWHM in any of the classes of objects we have identified. Furthermore, we see no correlations between the *FHIL* FWHM and the FWHM of any of the components of the other measured emission lines.

In Fig. 4.19 we show the velocity shift distribution of the [Fe X] and [Fe VII] lines for our [Fe X] selected sample. These velocities have been normalised with respect to the velocity shift of the [O III] line, which we noted in the previous chapter is very close to the systemic velocity shift of the galaxy determined from the [S II]$\lambda\lambda$6717,6732 doublet. We chose to use the core of the [O III] line, rather than [S II] directly, as it is generally the much stronger of these lines, plus our selection criteria guarantees that it is present in all our spectra. We find that, in the case of all AGN classifications considered here, both the [Fe VII] and the [Fe X] lines are blueshifted with respect to systematic (or, more precisely, the core of the [O III] line) in the vast majority of sources. We note that there is a slight tendency for the [Fe X] line in type 1 AGN to be more blueshifted than the [Fe VII] line (see Fig. 4.19 and Table 4.1), although there is considerable scatter in this measurement. There is no tendency for the [Fe X] line to be more or less blueshifted than the [Fe VII] line in either type 2 or type 1.9 AGN. A Spearman's rank test indicates that the [Fe X] and [Fe VII] shifts in type 1 AGN are correlated, although this correlation is not strong (ρ=0.66).

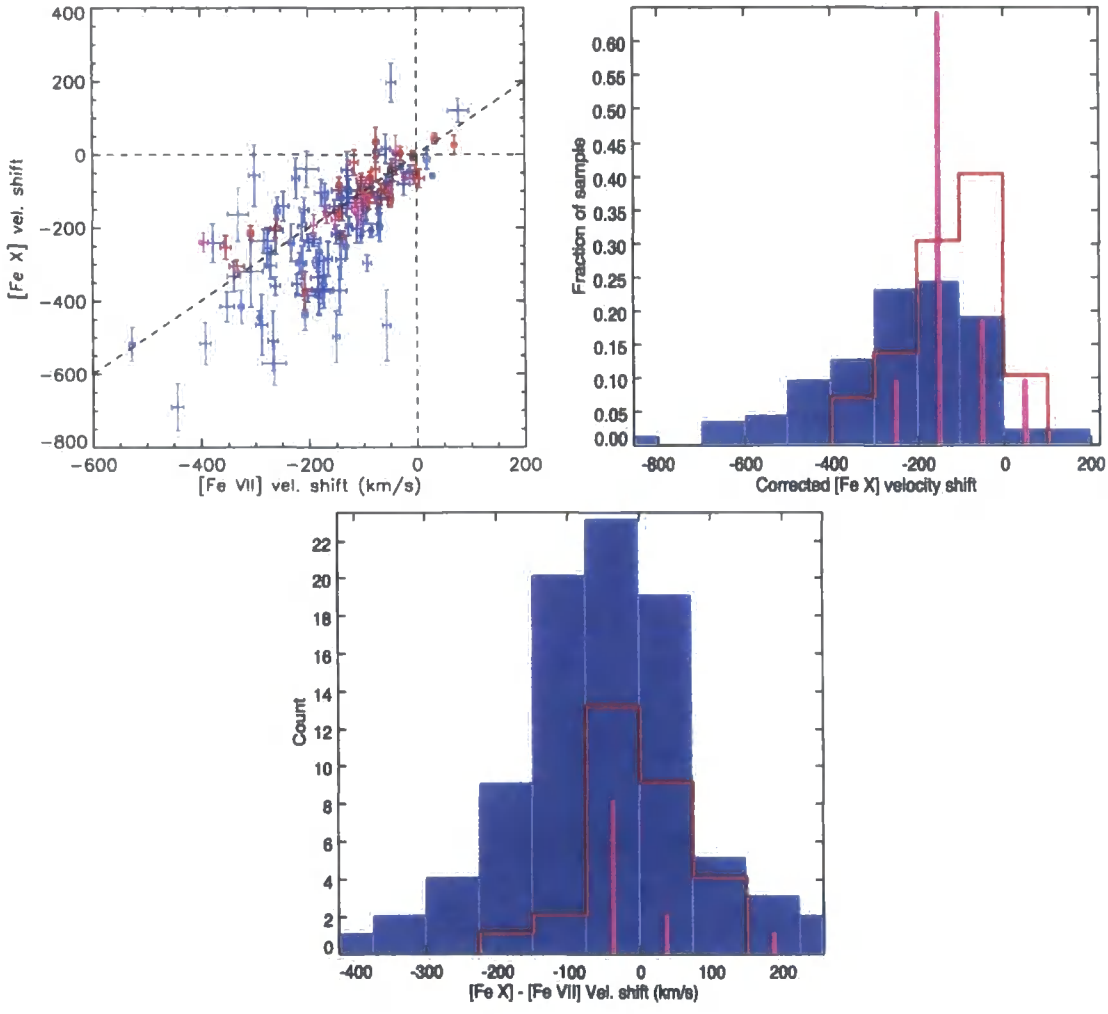

Figure 4.19: Velocity shifts of the *FHILs*: Upper left: [Fe X] shift plotted against [Fe VII] shiift. Shifts are relative to the [O III] core defined in the text and negative values refer to blueshifts. Upper right: Distribution of *FHIL* shifts as a function of AGN type. Bottom: Distribution of [Fe X] shift-[Fe VII] shift. In all plots, blue refers to type 1s, red to type 2s, magenta to type 1.9s.

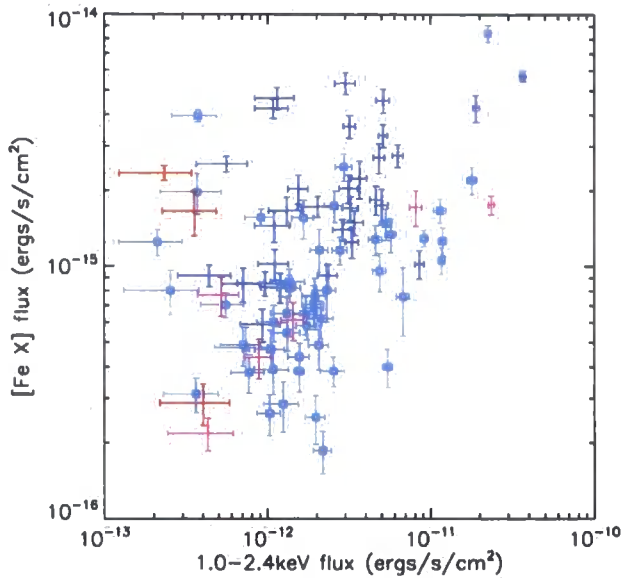

Figure 4.20: [Fe X] flux plotted against soft X-ray flux determined from *ROSAT* detections. Red points refer to type 2 AGN, magenta to type 1.9s. We have split the type 1s into to subsamples to enable comparison with the results presented in the previous chapter (see text): dark blue to type 1s with [Fe X] FWHM $>$ 1100km s^{-1}and light blue to type 1s with [Fe X] FWHM $<$ 1100km s^{-1}

4.6.4 Comparison with X-rays

In the previous chapter we noted that a strong correlation exists between both the [FeX]/X-ray fluxes *and* luminosities. We now wish to explore this relationship further using the new, larger sample. The X-ray fluxes were determined by assuming an intrinsic spectral model with spectral index Γ=1.6 and a hydrogen column density, N_H, of 5×10^{20}cm^{-2}. In Fig. 4.20 we plot the [Fe X] flux against the X-ray flux of the 90 sources of the 142 in our [Fe X] sample that have *ROSAT* detections. In our larger sample, we do not see a good correlation between [Fe X] and X-rays fluxes. To investigate the loss of this strong correlation, we returned to the previous sample to determine if there were any significant differences between the two samples that could cause this difference. The [Fe X] FWHM of the larger sample extents to considerably larger values than the smaller sample (up to 2700 km s^{-1} compared to 1100 km s^{-1}). When we overplot the objects from the larger sample with [Fe X] FWHM $<$ 1100 km s^{-1} we reduce the scatter of this plot (the ρ value of a Spearman's rank test increases from 0.3 to 0.6) and the remaining points lie in a similar region of the plot as occupied by the smaller sample (the 'narrow [Fe X]' points of

the larger sample are coloured light blue in Fig. 4.20).

Turning to the X-ray luminosities, we note that the [Fe X] line luminosity is more highly correlated with the X-ray flux than both the Hα and [Fe VII] line luminosities (Fig. 4.21; Spearman's ρ= 0.72, 0.68 and 0.58, respectively). This echoes a similar result based on the smaller sample described in the previous chapter. Again, we note a number of outliers in the Hα -X-ray plot that do not appear as outliers in the [Fe X] vs. X-ray (top right and top left plots of Fig. 4.21). Two of these outliers are the same as those in Fig. 3.7 and are those with the narrowest Hα lines of even this larger sample. Added to these original outliers are three others. Although the widths of the Hα lines in these objects means they are classed as NLS1s, they are not amongst the narrowest objects in this group, having Hα FWHM in the range of 1700-2000 km s^{-1}.

4.7 Discussion

One of the major advantages of the selection method described here (over that described in the previous chapter) is that it has enabled the comparison the properties of the [Fe X] and [Fe VII] detected objects with a set of control samples containing spectra selected from the same initial sample. These comparisons have led us to the conclusion that the objects with detected *FHIL* emission are not *significantly* different from the rest of the AGN population in terms of the relative strengths of the other permitted and forbidden lines we measured. We do note a tendency for objects with detected *FHILs* to also have stronger [O III]λ5007 lines (in both relative and absolute terms). However, this does not reflect a constant *FHIL*:[O III]λ5007 ratio; in all types of AGN explored here, the strengths of the *FHILs* relative to [O III]λ5007 spans a continuous distribution across almost two orders of magnitude. As we have explored in this and the previous chapter, this large range in relative *FHIL* strengths can in part be explained in terms of (observer-source) orientation and the extent of the *FHIL* emitting region, although, as we will see in the following chapter, the shape of the ionising SED also has a strong effect on the relative strengths of these lines. Unfortunately, we are currently unable to determine which of these influencing factors have the strongest effect.

Our detailed treatment of the relative widths of the permitted lines of our *FHIL* detected and control samples indicates that these lines are preferentially produced in objects with narrower permitted lines (Hα FWHM$\lesssim$3500, although the strongest *FHIL* emitters have Hα FWHM$\lesssim$2000). This supports the concept that the *FHILs* respond to

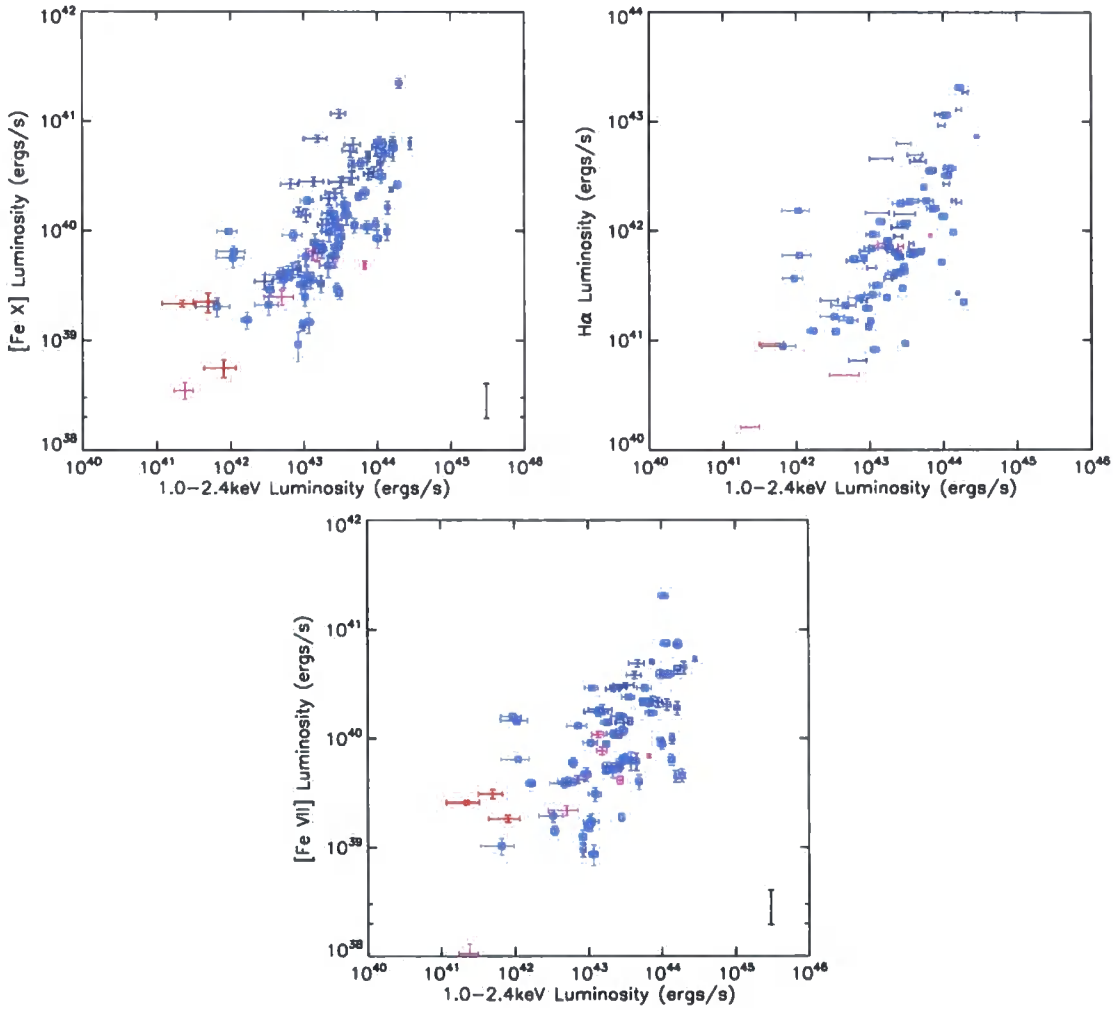

Figure 4.21: Line luminosities plotted agains soft X-ray luminosity: Upper left: [Fe X]. Upper right: Hα. Bottom: [Fe VII]. Symbol colours and shapes have the same meaning as those used in Fig. 4.20.

the stronger soft X-ray emission that is typically found in objects with narrow permitted emission lines (NLS1s, ;Boller et al. 1996). Indeed, our Fig. 4.21 shows the soft X-rays are more strongly correlated with the [Fe X] line than either Hα or [Fe VII].

Our results derived from the *FHIL-FHIL* correlations in general corroborate the main results from the previous chapter. Again, we see a striking difference in the [Fe X]:[Fe VII] ratios between type 1 and type 2 AGN. Furthermore, the increased size of the samples has enabled the identification of 11 type 1.9 AGN with detected [Fe X] lines (i.e. those that show some degree of absorption between the Hα and Hβ lines). Although this remains a relatively small subsample, initial results indicate that these AGN have *FHIL* properties between types 1 & 2, both in terms of line ratios and kinematics. This further supports the claim that the differences in *FHIL* properties between type 1 & 2 is orientation based- with the [Fe X] emitting region becoming increasingly obscured as we move from type 1s, through 1.9s to 2s.

A major difference between the results presented in this and the previous chapter is that a sample derived from the [Fe VII] line, rather than [Fe X], shows a similar distribution of [Fe VII]:[O III] ratios as that presented in Murayama and Taniguchi (1998) and Nagao et al. (2000). This result is a clear example of the role that selection effects can play in work of this type. By selecting on the [Fe VII] line we obtain a more complete sample of [Fe VII] emitters, rather than preferentially obtaining those with strong [Fe VII] by selecting on [Fe X]. The results from this chapter therefore support the model of Nagao et al. (2000) – that the [Fe VII] emitting region is somewhat obscured by obscuration in type 2 AGN, but in the case of type 1s we observe the full [Fe VII] emission.

The lack of correlation between the *FHIL* FWHM and the FWHM of Hα suggests that both the [Fe X] and [Fe VII] emitting regions are not linked to the broad line emitting region. In our final chapter we will discuss in more detail the origins of the *FHIL* emitting regions. As well as a strong tendency for the *FHILs* measured here to be blueshifted relative to systematic, there is some weak evidence that the outflow of velocities of the [Fe X] and [Fe VII] regions are linked. However, it is not necessarily the case the [Fe X] line is blueshifted more than the [Fe VII]. This suggests that the *FHIL* emitting clouds form part of the same general outflow, but the spatial separation of the [Fe X] and [Fe VII] emitting regions (evident from the suppressed [Fe VII] and [Fe X] emission in type 2s) is caused by the various *FHILs* being preferentially produced at different radii.

4.8 Summary

In this chapter we have extended the work described in Chapter 3 by using our own fitting routines to directly search for the presence of the [Fe VII] and [Fe X] in SDSS spectra. This has considerable advantage over using the results of the SDSS pipeline as we no longer rely on the blending of the [O I]λ6363 with the [Fe X] line to detect the presence of the latter line. This removes the influence of a number of selection effects that were inherent in the previous, smaller sample. In particular we have been able compile separate samples containing sources with detected [Fe X] lines and sources with detected [Fe VII] lines, i.e. we no longer rely on the presence of [Fe X] to find [Fe VII]. Furthermore, as the [Fe X] fitting routine we have implemented in this chapter is more robust against the curvature of the spectrum around [Fe X] due to the presence of a broad Hα wing, our sample is no longer constrained to objects with narrow (FWHM $<$ 50Å) Hα lines. We are therefore able to fully investigate the relationship between *FHIL* emission and the widths of the permitted emission lines. It should be noted that, although some selection effects are still present within our samples, we have been able to mitigate their influence on our final conclusions, which are summarised below:

- In terms of relative line luminosities, our *FHIL* detected AGN show no significant difference from the AGN with undetected *FHILs* (based on Hβ/[O III] vs. Hα/[N II] ratio plots).

- The range of *FHIL*:[O III] ratios cover a large range of values (typically spanning $\sim$two orders of magnitude). This, and the fact that our samples of *FHIL* emitting AGN have systematically higher [O III] fluxes than the control samples, strongly suggests that all AGN emit *FHILs* at some level, but they are too faint to detect in objects with generally weaker emission lines.

- When compared against our control samples, we note that we detect a higher proportion of *FHIL* emitters in AGN with narrow permitted lines (i.e. weighted Hα FWHM $<$ 2000km s^{-1}). After careful consideration of the selection effects that could effect this result, we find that at least 17% of the [Fe X] emitters have Hα FWHM $<$ 2000km s^{-1}, compared to just 6% of the control sample. On investigation of the causes of this increased proportion of [Fe X] emitters in the lowest Hα FWHM bins, we note that the [Fe X] luminosities (relative to [O III]) are *not* anti-correlated with the width of the permitted lines. However, we note that large [Fe

X]:[O III] ratios (i.e. $\gtrsim$0.1) are *only* measured in objects with weighted Hα FWHM < 3500km s^{-1}.

- We find a strong systematic weakening of the [Fe X] line relative to [Fe VII] in the type 2 AGN compared to the type 1s, confirming our results from the previous chapter. A similar, although not as large, difference in the *FHIL* ratios in the type 1.9s of our samples provides increased evidence that this disparity is caused by obscuration effects, rather than differences intrinsic to the sources or method of detection.

- We note that by selecting a sample of *FHIL* emitters based on the presence of the [Fe VII] line (rather than the selection criteria employed in the previous chapter) we obtain [Fe VII]:[O III] ratio distributions similar to those presented in previous work (Murayama and Taniguchi 1998 and Nagao et al. 2000). The work presented in this chapter therefore supports the main conclusion of these earlier works: that a proportion of the [Fe VII] emission is obscured from our view by the dusty torus in the case of type 2 (and type 1.9) AGN.

- Although the correlation between [Fe X] and X-ray luminosities is weaker in the sample derived here compared to that defined in the previous chapter, we still note that the the soft X-ray luminosities are more strongly correlated with [Fe X] luminosities than with either Hα or [Fe VII]. This strongly supports the concept that the *FHIL* emitting region is photo- rather than collisionally ionised.

	AGN Classification		
Parameter	Type 1	Type 1.9	Type 2
[Fe X]-[Fe VII]			
log-log Fit Gradient[1]	0.97±0.01	0.65±0.05	0.76±0.02
log-log Spearman's Rank[2]	(0.86, 1.2×10^{-26})	(0.96,1.8×10^{-6})	(0.94, 5.6×10^{-14})
Mean $\log\left(\frac{[FeX]}{[FeVII]}\right)$	0.1	-0.1	-0.3
σ $\log\left(\frac{[FeX]}{[FeVII]}\right)$	0.3	0.3	0.2
Max $\left(\frac{[FeX]}{[FeVII]}\right)$	8.5	3.3	1.4
Min $\left(\frac{[FeX]}{[FeVII]}\right)$	0.3	0.4	0.2
[Fe X]-[O III]			
log-log Fit Gradient[1]	0.65±0.01	0.53±0.03	0.59±0.02
log-log Spearman's Rank	(0.7, 1.2×10^{-15})	(0.65,0.03)	(0.7, 3.3×10^{-5})
Mean $\log\left(\frac{[FeX]}{[OIII]}\right)$	-1.1	-1.5	-1.7
σ $\log\left(\frac{[FeX]}{[OIII]}\right)$	0.4	0.3	0.4
Max $\left(\frac{[FeX]}{[OIII]}\right)$	1.3	0.1	0.3
Min $\left(\frac{[FeX]}{[OIII]}\right)$	0.01	0.01	0.002
[Fe X] kinematics			
Mean FWHM (km/s)	940	500	470[3]
σ FWHM (km/s)	570	170	280[4]
Mean shift (km/s)	-220	-136.	-110
σ shift (km/s)	160	67	100
Mean [Fe X]-[Fe VII] shift (km/s)	-50	-6	-6
σ [Fe X]-[Fe VII] shift (km/s)	120	60	60

Table 4.1: Various parameter statistics associated with each AGN classification in our [Fe X] detected sample. [1]Gradient of the linear fit to the log-log plot of the data. [2](ρ, significance), ρ is a measurement of the strength of the correlation (values of -1,0,1 refer to strongly anti-correlated, no correlation and strongly correlated, respectively) and the significance gives the probability (between 0.0 and 1.0) that the null hypothesis is true (i.e. that the correlation could arise by the random selection of points from an evenly distributed underlying population). [3&4] Mean reduces to 400km/s and σ reduces to 100km/s, respectively, on exclusion of outliers.

	AGN Classification		
Parameter	Type 1	Type 1.9	Type 2
[Fe VII]-[O III]			
log-log Fit Gradient[1]	0.71±0.02	0.58±0.01	0.83±0.02
log-log Spearman's Rank	(0.83 3.5×10^{-37})	(0.77±1.2×10^{-6})	(0.83, 7.6×10^{-22})
Mean $\log\left(\frac{[FeVII]}{[OIII]}\right)$	-1.2	-1.5	-1.6
σ $\log\left(\frac{[FeVII]}{[OIII]}\right)$	0.3	0.4	0.3
Max $\left(\frac{[FeVII]}{[OIII]}\right)$	1.0	0.7	0.2
Min $\left(\frac{[FeVII]}{[OIII]}\right)$	0.01	0.07	0.003
[Fe VII] kinematics			
Mean FWHM (km/s)	630	520	680[3]
σ FWHM (km/s)	220	270	280[4]
Mean shift (km/s)	-220	-104	-90
σ shift (km/s)	150	93	140

Table 4.2: As for Table 4.1 but for the [Fe VII] detected sample.

Chapter 5

Photoionisation models of the FHIL emitting region

5.1 Introduction

Along with the rapid development of telescope technology in the last four decades, the study of astronomy has greatly benefitted from the advancement of computer processing power and software development over the same period. Modern astronomy relies heavily on the availability of fast (often parallel) processors to perform simulations of complex physical processes, the results of which are compared with observations. The ability to test hypotheses via the production of 'simulated universes' is one of the most powerful tools today's astronomers can use to develop their understanding of the Universe.

In previous chapters we have concentrated on results based purely on observations. In this final science chapter we will turn to computational photoionisation models to help interpret some of the results we have already outlined. This chapter is organised into two distinct sections. The first is based on our investigations into how the *FHIL* emission is affected by changes in the shape of the ionising SED. Following this, we choose to concentrate on an individual object, *Ark 564*, in an attempt to determine what physical processes are at work in producing the observed profiles of the strong *FHILs* in the spectrum of this object.

5.2 *FHILs* and the shape of the ionising SED

The development of space-based astronomy and huge advancements in detector technology has opened up virtually the whole of the electromagnetic spectrum to today's astronomers. However, irrespective of detector or telescope location, there will always remain a region of the electromagnetic spectrum that is hidden from view. Between the

extreme ultraviolet and soft X-ray wavebands, neutral gas within our own Galaxy becomes highly opaque as the effective atomic cross sectional area increases dramatically at these wavelengths . This has the result of effectively obscuring all the radiation within this broad waveband (13.6eV $\lesssim h\nu \lesssim$ 300eV).

Although the issue of EUV-SXR absorption affects all multiwavelength astronomical observations, the problem is particularly acute for AGN. Within this obscured region of the spectral energy distribution (SED) the big blue bump (BBB) apparently reaches its maximum luminosity before falling to join the observed X-ray continuum beyond 300eV. As it is believed that the BBB is emitted directly by the accretion disk, our inability to determine its point of turnover means we are currently unable to place strong constraints on the total energy radiated by an AGN.

Some work has been done in exploring the obscured region of the AGN SED as it shifts into the observable windows in highly redshifted sources (see Telfer et al. 2002). This method has, however, a number of shortfalls, not least that at increasingly high redshifts, the observed fluxes of these objects become vanishingly small. This has the result that only the most intrinsically bright sources can be studied at photon energies deep into the obscured region of the spectrum, thereby introducing a considerable selection effect. Furthermore, UV to X-ray photons will also be absorbed by gas intrinsic to the source meaning the observed flux will not be a true representation of the radiation produced by the central engine. Finally, as emitted photons are redshifted into our observable windows, we lose information on the soft X-ray emission of individual objects as photons in this waveband are, in turn, redshifted into the obscured region of the electromagnetic spectrum.

The problem of placing constraints on the bolometric luminosity of AGN is further complicated by the presence of an apparent excess of X-ray emission when the hard (2-10keV) X-ray power law is extrapolated to lower energies (0.3-2keV) (e.g. Turner and Pounds 1988). This so-called soft excess (SXS) is particularly strong in narrow line Seyfert 1s (NLS1s)- a class of AGN that show narrow permitted lines and strong emission from more highly ionised species (e.g. Stephens 1989, Pogge 2000). The magnitude of the SXS, up to a factor of $\sim$6 above the extrapolated X-ray power law in some AGN (e.g. KUG 1034+398 described in Pounds et al. 1995), implies that it could, depending on its spectral extent, provide a significant contribution to the bolometric flux of the AGN. In early studies (e.g. Pounds et al. 1986), it was suggested that the SXS was the high energy tail of the BBB. However, at present, there is no general agreement on what is

producing this strong feature. As the SXS extends into the region of the SED obscured by Galactic absorption, we are unable to determine whether it is a localised feature on the AGN SED (e.g. blackbody emission from a hot accretion disk corona), or whether it extends to much lower energies to join the BBB. By being able to place constraints on the spectral extent of the SXS, we would be in a much better position to determine the physical source of the feature.

As Galactic obscuration is strongest between ~20eV and ~300eV the potential exists to use the relative strengths of the *FHILs* emitted in the optical and near-infrared wavebands to determine the form of the EUV-SXR continuum, as the species responsible for these lines have ionisation potentials between 100eV and 300eV. With this in mind we will use the photoionisation code Cloudy (v. 07.02.01; last described in Ferland et al. (1998)) to test how the *FHILs* react to changes in the form of the obscured SED.

In the following sections, we describe the details of our models, including the form of the input SEDs (§5.3.1) and analyse how the *FHILs* are affected by changes in the shape of the obscured SED (§5.3.2). We provide a sumary of our results in §4.8.

Throughout this chapter we use the convention that [Fe VII] refers to the [Fe VII]λ6087 line (ionisation potenial: 100eV), [O III] to [O III]λ5007 (35eV), [Fe X] to [Fe X]λ6374 (235eV) and [Fe XI] to [Fe XI]λ7892 (262eV).

5.2.1 The models

We have based our input SEDs on the observed continuum properties of the NLS1, *Ark 564*. This AGN was chosen as it is known to have very strong *FHILs* that have been measured in both the near infrared and optical wavebands (e.g. Erkens et al. 1997, Mullaney and Ward 2008, Riffel et al. 2006, Landt et al. 2008) and therefore provides one of the best objects on which to test the hypothesis that *FHILs* can be used as a diagnostic to the EUV-SXR continuum. As well as emitting strong *FHILs*, *Ark 564* also displays a strong SXS that has recently been discussed by Dewangan et al. (2007), who show it as rising by a factor of three (at 0.3keV) above an extrapolated power law fit ($\Gamma = 2.5$) constrained by the 2-10keV emission.

Cloud Geometry

We take as a model emitting clouds in a series of thin, concentric spherical shells of radius, R (cm), from the continuum source (here, we define 'thin' as cloud thickness,

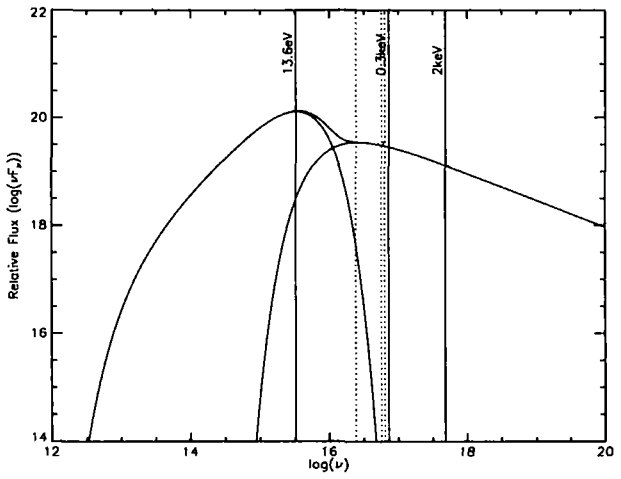

Figure 5.1: SED for Baseline model, which consists of a BBB component with $T_{fall} = 1.2 \times 10^5$ and a soft X-ray power law of $\Gamma = 2.5$ ($\nu F_\nu \propto \nu^{-0.5}$)

$t = R/10$). As the luminosity of any individual SED was fixed, the area density of the incident ionising photons on the front face of the cloud is defined solely by R. For each SED modelled, we varied log(R) between 15.5 and 20.5 ($\sim 10^{-3}$pc to $\sim$100pc) in steps of Δlog(R)=0.0414, corresponding to $\Delta R = 0.1R$ (requiring 121 separate models for each value of n_H and SED shape). The lower and upper limits of R were chosen based on the inner limit of the typical size of the broad line region and the outer limit of the traditional narrow line region, respectively.

As each model was performed independently, no self-sheilding was taken into account. In §5.3.2 we show that this is a reasonable assumption as any *FHIL* emitting clouds heavily absorb the ionising continuum. Although modelling a full gas shell is likely to overestimate the covering factor of the *FHIL* emitting region, as we compare the model results with observed *FHIL ratios* rather than absolute fluxes, the covering factor will be divided out during the analysis stage.

Cloud density

In their paper, Ferguson et al. (1997) showed that the *FHILs* are most effectively produced in clouds with a wide range of densities (2<log(n_H)<10). Therefore, we chose to model this region of the log(n_H) parameter space here. For each value of R, we performed 40 simulations covering 2.0<log(n_H (cm^{-3})<10.0 in steps of Δlog(n_H)=0.2. Therefore for each modelled SED we performed 40 $\times$ 121 = 4840 simulations covering (n_H,R) param-

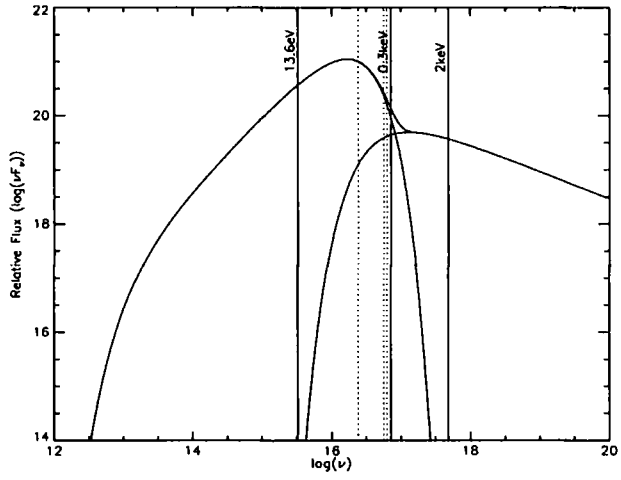

Figure 5.2: Hot BBB with high energy tail of the BBB extending far enough into the X-rays to (partially) account for the SXS. The soft X-ray power law is the same as in the Baseline model.

eter space.

SEDs

To test whether the *FHILs* could be used as a diagnostic of the EUV-SXR AGN continuum emission, we initially chose to model the *FHIL* emission from a set of three widely differing SEDs. Each of the SEDs (with the exception of the baseline model, which does not attempt to account for the observed SXS) are potential solutions to the observed continuum features of *Ark 564* in the EUV and SXR wavebands.

1. **Baseline (Fig. 5.1):** An accretion disk BBB peaking at a characteristic temperature of 1.2×10^5K (~13.6eV, log(ν)~15.5) . From FUSE/HST observations, we know that the BBB rises to at least this point. This SED therefore represents the lowest possible temperature BBB. We have not attempted to recreate the SXS in this SED. Instead, we have simply modelled the soft X-ray emission by extrapolating the 2-10keV power law ($\Gamma = 2.5, \nu F_\nu \propto \nu^{-0.5}$) to meet the BBB. We have normalised the X-ray emission at 1keV relative to the UV emission according to the observed fluxes in these bands (i.e. $\nu_U F_U / \nu_X F_X$ ~10).

2. **Hot BBB (Fig. 5.2):** With this SED, we have attempted to model the SXS as the high energy tail of the BBB. It should be noted that studies of SXR variability now disfavour this theory as an explanation of the SXS. In this work, we would like to determine whether the optical *FHIL* fluxes also rule out this possible explanation

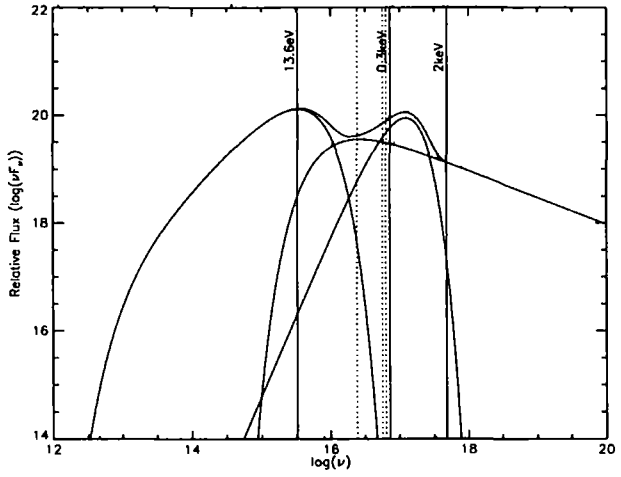

Figure 5.3: Baseline model + SXS represented by a simple black body spectrum at T_{BB}=1.5×10^6 which introduces an inflection to the EUV-SXR continuum.

for the SXS. Here, we increase the peak temperature of the BBB (T_{fall}) to the point where the total soft X-ray flux rises above the extrapolated 2-10keV power law by a factor of ~3 at 0.3keV. This was found to be the case at T_{fall}=6.0×10^{5}K. However, it should be noted here that this model does not accurately predict the full broad extent of the SXS. Observations show that the SXS in *Ark 564* extends upwards in energy to 2keV, whereas this model cannot account for any SXS beyond ~500eV. The photon index of the X-ray power law was held at Γ = 2.5.

3. **Thermal SXS (Fig. 5.3):** In order to produce a more realistic representation of *Ark 564*'s SXS, the last of our initial SEDs models consists of a Baseline+thermal component. Here, we have attempted to reproduce the SXS with a simple black body of characteristic temp, T_{BB}. The form of the SXS in *Ark 564* required T_{BB}=1.5×10^{6}K. Although this model does not accurately reproduce the observed SXS (over-predicting the X-ray flux at 500eV), it is a much better representation than that provided by the 'hot BBB' model. Again, Γ was held at 2.5.

Other input parameters

The results of this study are dominated by variations in the input parameters described above. However, we varied a small number of the other input parameters from their default values to be more consistent with properties expected in the gas surrounding AGN. These are:

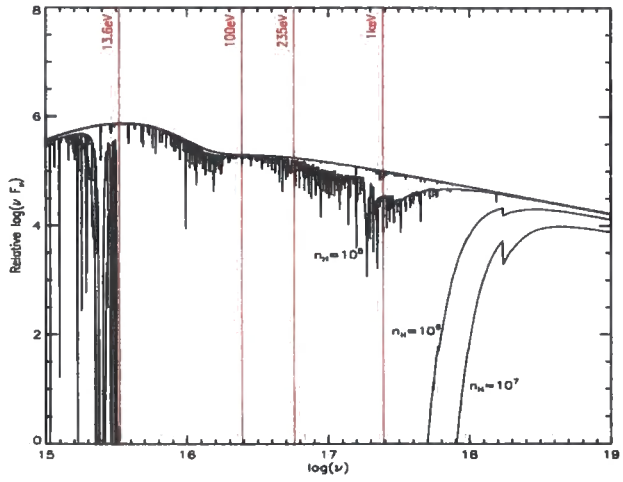

Figure 5.4: Transmitted spectrum from the baseline model. Spherical cloud, 3.2×10^{18}cm (~1pc) from central flux source, 3.2×10^{17}cm thick. Black lines show various transmitted SEDs for varying cloud densities: $2.0 < \log(n_H) < 7.0$. The densities are shown where the lines are resolvable from the incident spectrum.

- A background SED provided by the CMB at z=0. This is negligible compared to the ionising flux, but ensures that there is non-zero flux across the whole of the modelled spectrum.
- The models are stopped if the temperature of a cloud falls below 3000K.
- The models are stopped if the column density of a cloud reaches N_H=10^{24}cm^{-2}. At this point the cloud is considered to be optically thick to the ionising radiation.
- Assumed solar metallicities.

5.2.2 Results

Transmitted spectrum

In Fig. 5.4 we present the transmitted spectrum from a set of models produced by the baseline SED. This plot shows that for high density clouds, the radiation capable of producing the most highly ionised species is severely attenuated, meaning that any *FHIL* emission arising from dense clouds is produced on the side facing the continuum source, as described by Murayama and Taniguchi (1998). It should be noted that the degree of absorption produced by the $\log(n_H)$ = 6 and $\log(n_H)$ = 7 would be easily detected in the 0.3-10 keV SXR emission from *Ark 564*. The fact that it is not detected implies that

such clouds are unlikely to lie along our line of sight to the active nucleus (the expected source of soft x-ray continuum) unless they have a very low covering factor. The striking difference between the absorption from the log(n_H) = 5 and log(n_H) = 6 clouds is largely the result of the fraction of ionised hydrogen at the back edge of the respective cloud. In the case of the log(n_H) = 5 cloud, > 99% of this hydrogen is ionised, hence the lack of a strong Lyman absorption feature from these clouds. Conversely, in the case of the log(n_H) = 6 cloud, only 2% of the hydrogen at the back edge of the cloud is ionised resulting in the strong absorption feature at 13.6eV.

Comparing the modelled transmitted spectrum with the modelled fluxes of [Fe VII]λ 6087 (Fig. 5.5) reveals that the region of the n_H, R parameter space that produces the strongest *FHILs* is also the region that causes significant absorption of the SXR continuum. This implies that either the *FHIL* emitting region does not lie along our line of sight, or that it has a very low covering factor, such that the potential absorption from these clouds is heavily diluted by the strong SXR continuum emission. It has been shown that the *FHILs* are broadened to a FWHM~1000km/s (e.g. Erkens et al. 1997, this thesis). If they did indeed lie, or even temporarily pass, along our line of sight to the source of the SXR continuum, the predicted absorption signature of the strong *FHIL* emitting clouds would be easily detected in the 0.3-10keV waveband. This signature has yet to be detected in any AGN observed in the X-rays.

Emitted *FHILs*

The models described in §5.3.1 produce a prediction for the *FHIL* line luminosity emitted by every spherical cloud shell considered in our parameter space (L(n_H,R)). In figs. 5.5-5.7 we present contour plots indicating the luminosity (relative to the peak luminosity) for each of the *FHILs* modelled. Each plot includes data from all three modelled SEDs. Points are used to show the position within the parameter space at which the luminosity of the line peaks. We present the coordinates of these positions along with the corresponding luminosities in Table 5.1. Contours are used in figs. 5.5-5.7 to show the regions of the parameter space at which the line luminosity is greater than 10% of the peak luminosity. In the following discussion, we refer to the region enclosed by these contours as strongly producing the *FHIL* in question.

It is clear from figs. 5.5-5.7 that changing the shape of the ionising SED has limited effect on the extent of the region of parameter space that can produce any of the *FHILs* strongly. In particular, the range of densities at which these lines are strongly produced

			Baseline			HotBBB			ThermalSXS		
FHIL	I.P.	n_{cr}	L_{pk}	R_{pk}	n_{pk}	L_{pk}	R_{pk}	n_{pk}	L_{pk}	R_{pk}	n_{pk}
[Fe VII]	99eV	7.3	41.7	19.1	5.6	43.0	19.5-19.6	5.6	42.0	19.1-19.2	5.6-5.8
[Fe X]	235eV	9.7	42.2	17.9-18.2	6.0-6.6	42.9	18.3-18.7	5.6-6.4	42.7	18.2-18.5	5.8-6.4
[Fe XI]	262eV	10.4	41.6	18.0-18.1	6.0-6.2	42.2	18.4-18.5	5.6-5.8	42.1	18.4	5.8
[Si VI]	170eV	8.8	41.3	18.9	6.6	42.5	19.4	6.4	41.6	18.9	6.8
[Si X]	351eV	8.8	41.7	18.3	5.8	42.1	18.6-18.7	5.4-5.6	42.2	18.7	5.4
[S VIII]	281eV	10.6	41.1	18.4	6.6	42.0	18.8-19.1	6.0-6.6	41.4	18.5-18.6	6.8-7.0
[S IX]	328eV	9.4	41.6	18.9	5.2	42.1	19.1-19.5	4.6-5.4	42.0	19.0-19.2	5.0-5.4

Table 5.1: Peak luminosities in log(ergs/s) (L_{pk}) and the corresponding densities (n_{pk}; log(cm^{-3})) and radii (R_{pk}; log(cm)) of the *FHILs* discussed in this chapter. We also give the ionisation potential of the species responsible for each line (I.P.) and each lines' critical density n_{cr} (taken from Rodríguez-Ardila et al. (2002))

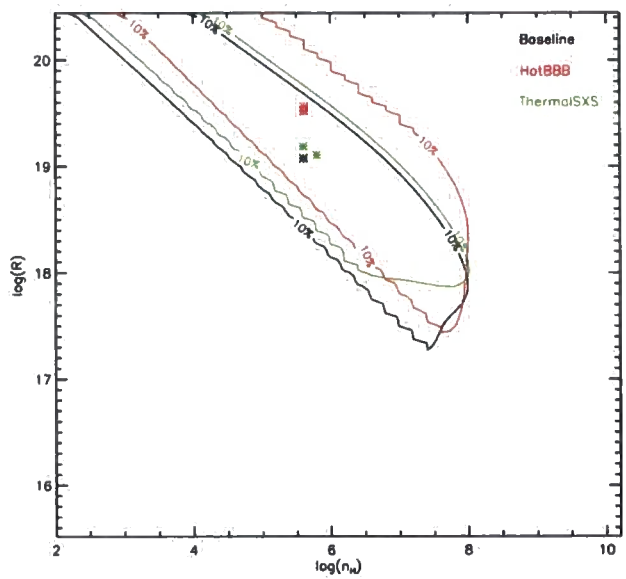

Figure 5.5: [Fe VII]λ6087 emission line strength. The points refer to the position of the peak luminosity, which are given in Table 5.1. The contours show the region in which the line luminosity is greater than 10% the peak value.

changes little, even between the two most extreme SEDs modelled here (baseline and hot BBB). Where any change occurs it is generally parallel to the radius axis of figs. 5.5-5.7. Although the magnitudes of these changes are dependent on the *FHIL* in question, in general, the radius of the strongly emitting region increases as the incident flux at 0.1keV $< h\nu <$ 1keV increases.

The position of the peak luminosity within the parameter space is dependent on the

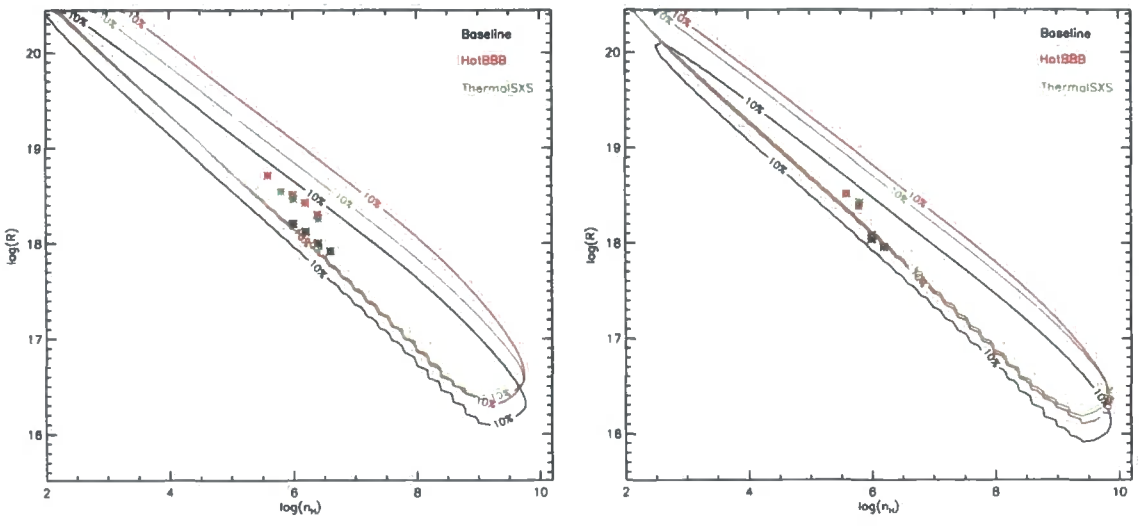

Figure 5.6: Same as Fig. 5.5 but for the [Fe X] (left) and [Fe XI] (right) lines.

shape of the input SED. The density at which the peak luminosity is produced, n_{pk}, decreases as the ionising flux increases (Baseline→ThermalSXS→HotBBB). This shift to lower density values is more prominent for more highly ionised species. It should also be pointed out that for all the SEDs and lines modelled here, $n_{pk} \ll n_{crit}$, indicating that emission lines are not produced most efficiently at or near their critical densities.

All the lines modelled here show that the radius at which their luminosities peaks, R_{pk}, increases with ionising flux. Notable is the factor of three increase in R_{pk} between the Baseline/ThermalSXS and the HotBBB models for the lower ionisation lines ([Fe VII] and [Si VI]). This is principally due to the difference between the Baseline/ThermalSXS and the HotBBB SEDs being greatest around the ionisation potentials of these species. A similar effect is seen for the higher ionisation lines ([Fe X], [Fe XI], [Si X], [S VIII] and [S IX]) between the Baseline and the ThermalSXS/HotBBB SEDs. The figures presented here therefore indicate that the radius of the dominant *FHIL* emitting region (i.e. that radius at which a particular *FHIL* is emitted most strongly) is dependent on the incident flux at $h\nu \sim$I.P. and therefore the shape of the incident SED.

All the SEDs used here reflect the results of Ferguson et al. (1997), i.e. that R_{pk} decreases with ionisation potential. This agrees with observational evidence derived from the relative luminosities of the *FHILs* emitted from type 1 and type 2 AGN (under the assumption that some of the *FHIL* emitting region is obscured from our view by the putative dusty torus; see chapters 3 and 4). The difference in R_{pk} between the higher and lower I.P. lines modelled here is dependent on the shape of the incident SED. For exam-

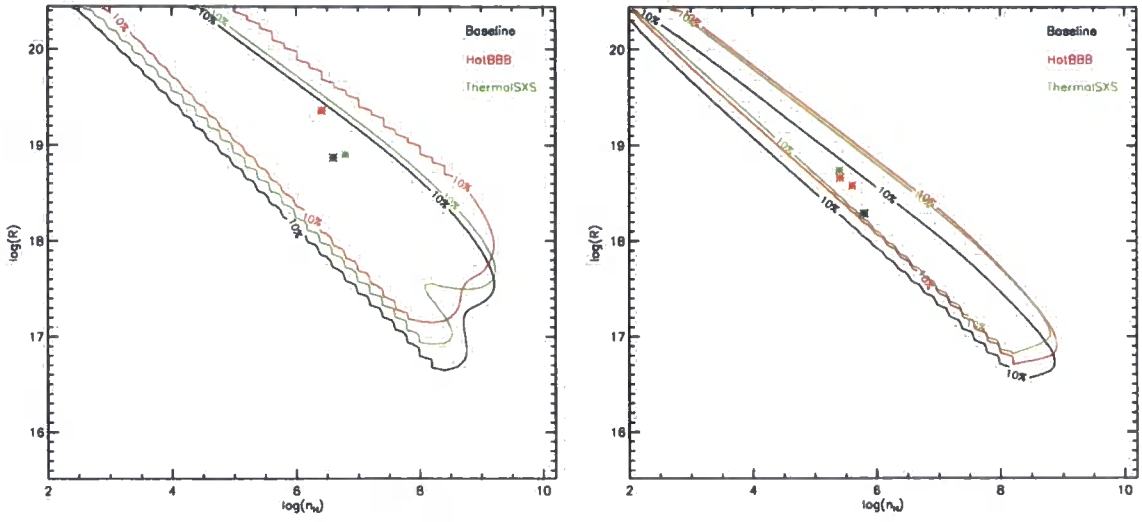

Figure 5.7: Same as Fig. 5.5 but for the [Si VI] (left) and [Si X] (right) lines.

ple, the Baseline model predicts a (maximum) factor of ~13 difference between the R_{pk} values for the [Fe X] and [Fe VII] lines, whereas the ThermalSXS and HotBBB models predict a factor of ~10 and ~20, respectively. If we assume a scale height of the central torus of ~1pc (or 3.085×10^{18}cm; as observed by Gallimore et al. 1997 and justified theoretically in Krolik and Begelman 1988) all the SEDs used here produce R_{pk} values that are consistent with the concept that a significant proportion of the higher ionisation lines (e.g. [Fe X], [Fe XI] etc) are produced within the region bounded by the dusty torus, whereas the luminosities of the lower ionisation lines peaks at regions outside the torus.

The peak luminosity (L_{pk}) of various emission lines is highly dependent on the shape of the incident SED. Table 5.1 indicates that, for example, the predicted peak luminosity of the [Fe VII] line changes by a factor of ~20 between the Baseline and HotBBB models. This reflects the factor of ~30 difference between the incident flux of these SEDs around the ionisation potential of [Fe VII]. A more modest change in L_{pk} between the different SEDs is noted for the higher ionisation lines- the [Fe X] and [Fe XI] change only by a factor of ~3 (Baseline/ThermalSXS) and ~5 (Baseline/HotBBB). This strong response to the incident SED lends weight to the possibility that the ratios of the *FHIL* emission lines could be used to constrain the SED in the region of 0.1keV $< h\nu <$ 1keV. This is discussed further in the following section. The results discussed in this section show that all of the *FHILs* referred to in this chapter can be produced, to some extent, by all the modelled SEDs. In particular, our results produced using the baseline SED shows that a strong soft excess is not a requirement for the production of *FHILs*, although its presence will boost

the luminosities of these lines considerably, thus making them more easily detectable in such objects.

Comparison with observed *FHIL* ratios

One of the major findings of the previous two chapters was that the [Fe X]:[Fe VII] ratio was systematically lower in type 2 AGN than in type 1s. We concluded that was due to a significant proportion of the [Fe X] emission being produced within a region obscured by the same dusty torus structure that blocks our view of the BLR in type 2 AGN. From the results presented above, we can now test whether our photoionisation models of the *FHIL* emitting region can reproduce these observations. Furthermore, as we have determined the response of the emitting species as a function of a changing SED, we can also examine the influence the SED has on the observed *FHIL* emission in both type 1 and type 2 AGN. Throughout the following analysis we will concentrate on only the [Fe X]:[Fe VII] line ratio; both Chapter 3 and the results described in this section indicate that the [Fe XI] line largely follows the [Fe X] line in terms of its flux/luminosity.

By summing the total [Fe X] line and [Fe VII] line luminosities produced by the photoionisation models over all values of n_H and R, we can determine the overall [Fe X]:[Fe VII] predicted by a given model. These values are given in the 'Total' column of table 5.2. These values clearly show that the [Fe X]:[Fe VII] line ratio is heavily dependant on the incident SED. Both the Baseline and ThermalSXS models significantly overproduce the [Fe X] relative to [Fe VII] compared to the observed mean value of $\sim$1-1.25 determined in earlier chapters. However, we note that those observed [Fe X]:[Fe VII] ratios showed significant scatter about these values, and ratios of $\gtrsim$5.0 were detected. It is possible that these extreme ratios are the direct result of different incident SEDs; an indication that the underlying continuum of these objects possess either a strong, localised soft excess (i.e. ThermalSXS) or a soft X-ray power law continuum combined with a low temperature BBB (i.e. Baseline). The input SED that most closely reproduces the mean observed [Fe X]:[Fe VII] ratio is the HotBBB. However, this model slightly *under*produces [Fe X] relative to [Fe VII]. A better agreement with the observations can be obtained by the reduction of the relative strength of incident flux around 100eV (possibly by using a cooler BBB). In terms of the total [Fe X]:[Fe VII] ratios, the three SEDs used here (or a combination of their various features) are capable of producing the full range of values measured in the previous chapters.

In the remaining columns of table 5.2 we give the [Fe X]:[Fe VII] ratios calculated from

5.3 Dynamic Models

Early studies of *FHILs* (e.g. Osterbrock 1981, Penston et al. 1984, De Robertis and Osterbrock 1984) revealed that their profiles differed from the more prominent low ionisation forbidden lines (such as [O III]λ5007 and [N II]λ6584) *and* the permitted broad lines (e.g. Hβ and Hα). In addition to having widths between these two extremes, they were often observed to be blueshifted with respect to the low ionisation lines or to possess an asymmetric blue wing, suggesting a net flow to the gas producing these lines. Irrespective of the interpretation of the source of these kinematics, it is clear that at least part of the *FHIL* emission arises from a region of the AGN distinct from the traditional broad line and narrow line regions (BLR and NLR, respectively; see Chapter 2 for a more detailed discussion of the profiles of emission lines from AGN). Further evidence that *FHILs* arise from an 'intermediate' region (i.e. between the BLR and NLR) is provided by integral field observations of the near infrared *FHILs* in two of the closest AGN: the Circinus galaxy and *NGC 4051* (Mueller Sánchez et al. 2006 and Riffel et al. 2008, respectively). These studies showed that these *FHILs* were being emitted at up to 75 pc from the nucleus.

In their study of the *FHILs*, Ferguson et al. (1997) used photoionisation codes to show that a typical AGN spectral energy distribution (hereafter SED) could produce these lines in clouds covering a wide range of distances from the central engine (or radii, R); from just outside the BLR to the extended NLR. However, as their study focussed on the *relative* positions of the emitting regions of various *FHILs* it did not address the issue of the source of these clouds or explain the kinematics of these clouds evident in the profiles of the lines.

Here, we extend the work of Ferguson et al. (1997) by presenting the results of a new set of photoionisation models that, when combined with the observed properties of the *FHILs*, produce a self-consistent picture of the source and kinematics of the *FHIL* emitting clouds around AGN.

5.3.1 The models

In a slight departure from the input conditions of our static models, for our dynamic models we have tried to match the input to the models as closely as possible to the observed properties of *Ark 564*. The reason for this change is that we now attempt to reproduce the profiles and strengths of the emitted *FHILs* rather than simply investigate

Model	Total	$R > 18.5$	$R > 19.0$	$R > 19.5$
Baseline	2.4	0.9	0.7	0.5
HotBBB	0.7	0.4	0.3	0.2
ThermalSXS	4.9	2.1	1.6	1.3

Table 5.2: [Fe X]:[Fe VII] ratios for each of the SEDs used in our models. The 'Total' column is the ratio determined by the integration of lines' luminosities across the whole parameter space (R, n_H), where as the other three columns give the ratios produced by regions beyond typical scale heights of the torus (in log(cm)). These values are therefore indicative of the ratios we would expect to observe in type 2 AGN.

regions beyond the particular R values that have been selected as representative heights for the obscuring torus (between 1-10pc). In physical terms, this means we are effectively obscuring any line emission from the inner regions of the AGN, as if the dusty torus was blocking our view of these regions. These values therefore give some indication of the [Fe X]:[Fe VII] ratios we would expect in typical type 2 AGN with the incident SEDs used here. We find that this ratio changes by a factor ≤ 2 despite, in effect, changing the height of the torus by a factor of 10. Depending on the torus height employed, both the Baseline and HotBBB SEDs can recreate the mean ratio of 0.5 for the type 2 objects studied in the previous two chapters. Again, the scatter about this mean can be explained in terms of varying SED shape, but also in terms of size/orientation of the obscuring torus. The HotBBB SED, combined with a large torus scale height, is capable of recreating the lowest [Fe X]:[Fe VII] ratios observed in our earlier samples, whereas the ThermalSXS SED can easily recreate the highest [Fe X]:[Fe VII] ratios found in type 2 objects. Differences in the scale height of the torus can also explain the increased numbers of type 1.9s (relative to type 2s) with [Fe X]:[Fe VII]>1.0. In the case of 1.9s we are likely observing the torus at a slightly more pole-on orientation than type 2s, i.e. more like a "grazing" incidence angle from the edge of the torus to the nucleus. This change in relative orientation is effectively the same (in terms of the results presented here) as changing the scale height of the torus. The results shown in table 5.2 therefore support the higher (on average) [Fe X]:[Fe VII] ratios of type 1.9s compared to 2.0s.

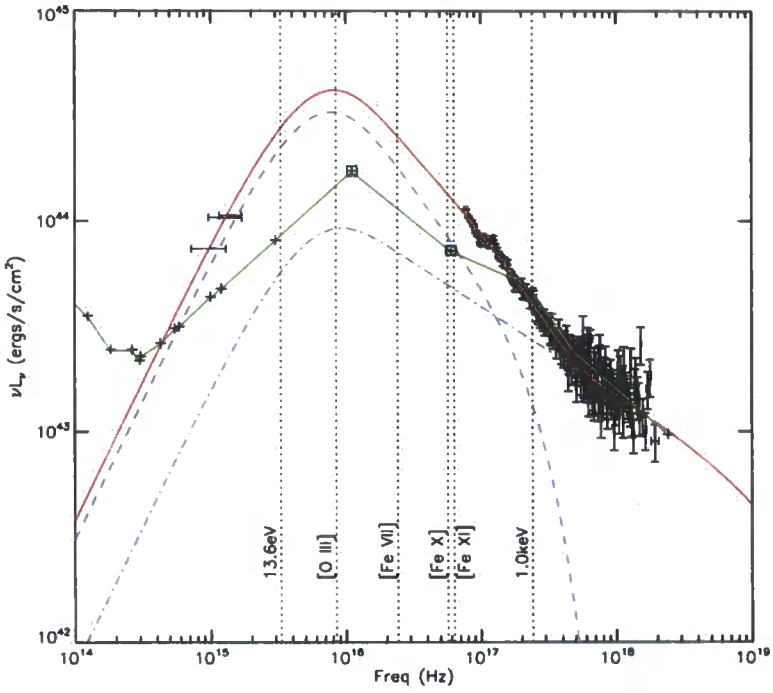

Figure 5.8: The two SEDs used in our models. The green line represents SED-R04 of Romano et al. (2004). Points surrounded by squares have been extrapolated from the observable portions of the SED. The red line represents SED-X which was constructed using optical/UV/X-ray data obtained with the XMM-Newton satellite. Dashed and dash-dot lines show the components of SED-X produced by Compton scattering of the photons emitted by the accreting system by low and high temperature gas, respectively. Dotted lines indicate the ionisation potentials of the species discussed here. Lines showing the 13.6eV and 1keV are included for reference.

how varying a small number of input parameters effects the *FHIL* ratios *in general.*

Calculations were performed with version 08.00 of Cloudy, last described by Ferland et al. (1998), to predict the emission lines shown in the optical spectrum of *Ark 564* taken with the *ISIS* spectrometer on the WHT telescope (see Chapter 2 for more details regarding these observations).

Input SED

In their study of the low ionisation lines of *Ark 564* Romano et al. (2004) assembled an SED (hereafter SED-R04) that was constrained by their observations between the mid-IR–UV and 1–10keV (the gap between these wavebands cannot be directly observed due to strong attenuation caused by photoelectric absorption by neutral gas). They extrapolated the UV and soft X-ray continuum to form an SED that peaked at ~40eV in νF_ν space (see Fig. 5.8). This was used as our initial input SED. To determine the sensitivity of our results to the shape of the strongly absorbed portion of the SED, we assembled our own based on XMM observations of *Ark 564* taken on the 17$^{\text{th}}$ June, 2000 (hereafter SED-X). This SED peaks at approximately the same photon energy, but has a luminosity at this energy roughly twice that of SED-R04 (in νL_ν space). Because the major difference between the two SEDs occurs within the unobservable section of the electromagnetic continuum, SED-X conforms to the observed fluxes in the optical and X-ray wavebands. It should be noted, however, that SED-X overproduces flux at 1000Å as compared to SED-R04 by a factor of ~2, although this can be explained by reddening which is significant at these wavelengths . We normalised both SEDs to have a luminosity of 2.64×10^{43} ergs s^{-1} at 7000Å (Romano et al. 2004). For SED-X this corresponds to an Eddington ratio of $L/L_{Edd} = 3.9$

Cloud geometry and density

In their work on the line emitting regions of AGN Ferguson et al. (1997) showed that *FHIL* emission peaks along ridges of constant ionisation paramater, U ($= L/4\pi R^2 n_H h\nu c$; where R is the distance of the emitting cloud of density n_H from a continuum source of luminosity L; all other symbols have standard meanings). More specifically, they noted that the optical high ionisation iron lines all reached a maximum luminosity around $R \sim 10^{18} - 10^{19}$ cm (0.3 – 3 pc) and $n_H \sim 10^5 - 10^7$ cm^{-3} for a source of ionising luminosity $L_{Bol}^{ion} = 5 \times 10^{43}$ergs s^{-1}. These values act as a rough guide to the location of

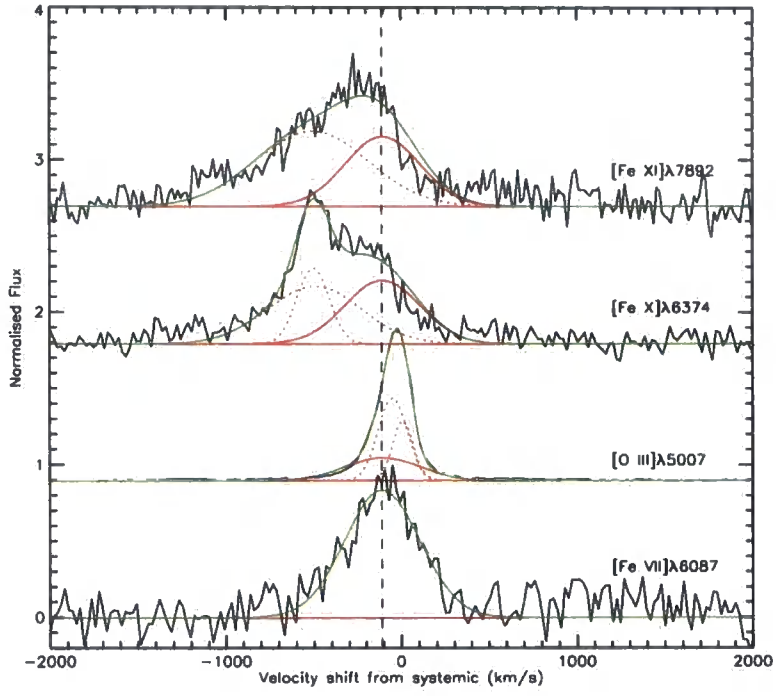

Figure 5.9: [O III], [Fe X] and [Fe XI] profiles decomposed into Gaussian components, one of which has the same kinematic parameters as the fit to the [Fe VII] line. This places upper limits on the flux produced with the same kinematics as the [Fe VII] line.

FHIL	Flux[a]	Shift[b] (km s^{-1})	FWHM (km s^{-1})
[O III]	6.2	-110	507
	4.3±0.3	6±2	133±2
	8.6±0.3	-52±16	193±1
[Fe VII]	1.00±0.03	-110±28	507±7
[Fe X]	1	-110	507
	1.1±0.1	-494±34	620±30
[Fe XI]	0.7	-110	507
	1.1±0.1	-510±31	750±28

Table 5.3: Component parameters for the emission lines. The [Fe VII] line was fit with a single component. The other line fits were then forced to contain a component with the same FWHM and velocity shift. [a]Component flux relative to [Fe VII]. [b]Velocity shift; negative values are blueshifts.

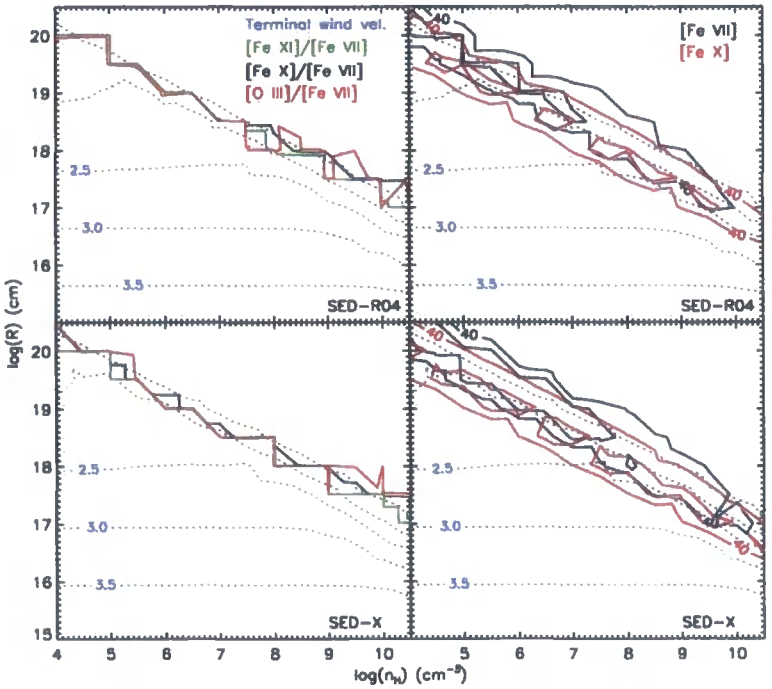

Figure 5.10: Contour plot showing the regions of the parameter space at which the observed k-ratios (see §5.3.1) are produced (left column) and the [Fe VII] and [Fe X] lines are most strongly emitted (right column). The dotted blue contours show the log(terminal velocity) of the clouds at each point in the parameter space.

the *FHIL* emitters in *Ark 564*. However, as we include radiative driving in our models which tends to reduce the density of the emitting clouds and the ionising luminosity is greater in *Ark 564* (4.8×10^{44} ergs s^{-1} for SED-R04), we chose to model a large portion of the parameter space covering $15 < log(R) < 20.5$ and $4 < log(n_H) < 11$ at low resolution (steps of 0.5 in both R and n_H) to ensure we cover all the possible *FHIL* emitting regions.

Cloud dynamics

As the high ionisation emission lines of *Ark 564* are blueshifted relative to the systemic velocity of the host galaxy (see Mullaney and Ward 2008 and Erkens et al. 1997 for more details) any model designed to reproduce the observed line ratios should also be able to reproduce the velocity structure of the *FHIL* emitting region. To account for this we included radiative driving in our models by using the 'wind' command in Cloudy and assuming a $2.6 \times 10^6 M_{\odot}$ black hole mass for *Ark 564* as reported by Botte et al. (2004). In adding this feature to the models, Cloudy determines the momentum transfer from

the incident photons to the absorbing/emitting gas clouds via photon capture, Compton and Rayleigh scattering, and free-free absorption. As the incident photons are emitted from a central source (whereas photons resulting from a scattering processes are emitted isotropically) a net radial force results. By providing the code with an estimate of the mass of the central object (in our case the central supermassive black hole) the vector sum of the radiative and gravitational forces can be calculated and, in turn, the acceleration and resulting terminal velocity determined. If the only source of photons were those produced by the central source, these calculations would be relatively straightforward. Unfortunately, however, the situation is complicated with the consideration that the scattered photons also carry momentum that can be absorbed in other regions of the absorbing cloud (especially in the case of emission line photons which are readily absorbed by neighbouring atoms/ions). With this in mind it is easy to see that a full treatment of the radiative driving process would be a very computationally expensive task. Cloudy largely avoids this problem by adopting a large velocity gradient approximation which assumes that the change in velocity of the material is so great that any emission line photons are doppler shifted out of the small range of wavelengths that are readily absorbed.

By conservation of mass, the density and velocity of a continuous column of gas is related such that $\rho_0 v_0 = \rho_1 v_1$, where $\rho_{0,1}$ and $v_{0,1}$ represent the density and velocity at two points. In including radiative driving we decrease the density of the emitting clouds as a function of depth as the gas is allowed to accelerate. This decrease in density allows the ionising radiation to penetrate deeper into the cloud. Therefore, by allowing the clouds to be radiatively driven, we drastically change the physical parameters of the emitting gas as compared to models involving only stationary clouds. This has corresponding effects on the modelled line ratios.

The profiles of the emission lines were used to further constrain our models. By decomposing the profiles of the iron *FHILs* and [O III] into Gaussian components we can place upper limits on the luminosity of these lines emitted from a region described by a single set of kinematic properties. To do this we fit the [Fe VII] line with a single Gaussian (a second component was found to be statistically unnecessary) and force the fits of the other emission lines to contain a component with the same FWHM and velocity shift (507 ± 7 km s^{-1} and -110 ± 28 km s^{-1}, respectively; see Fig. 5.9 and Table 5.3). From this analysis we note that our models of the [Fe VII] emitting gas must not produce [O III] luminosities greater than $\sim$6 times that of [Fe VII], while the [Fe X]/[Fe VII] and

[Fe XI]/[Fe VII] ratios of kinematically similar components (hereafter referred to as k-ratios) should be no more than unity and 0.61, respectively. To account for this and to reduce computation time our model calculations were stopped when [O III]/[Fe VII]$\geq$6. Furthermore, we note that Fig. 5.9 shows little or no [Fe X] or [Fe XI] flux being produced at blueshifts lower than the [Fe VII] component.

Because photons that are most capable of producing Fe^{6+} to Fe^{10+} are readily absorbed, *FHILs* will be produced nearer the front face of the clouds (i.e. facing the continuum source) while the lower ionisation lines will be preferentially produced at larger depths. By placing an upper limit on the flux of the [O III] emission from the *FHIL* emitting cloud we can therefore limit the size of the modelled cloud.

Other parameters

We refer the reader to §5.2.1 for a description of the other input parameters that were varied from their default values.

5.3.2 Results

In Fig. 5.10 we present contour plots showing the regions of the parameter space at which SED-R04 and SED-X produce the observed k-ratios (defined in §5.3.1) and the [Fe VII] and [Fe X] lines are most strongly produced. The [Fe XI] contours lie close to the [Fe X] contours and have been removed for clarity. Also shown on these plots is the velocity the modelled clouds reached by the end of the calculation. It should be noted that this could represent either the true terminal velocity of the cloud or the velocity that the cloud reached at the point when the calculation was stopped because the [O III]/[Fe VII] k-ratio reached 6 (these two values may not be the same). Furthermore, the *FHILs* are not necessarily strongest at the terminal velocity- in general they peak at lower velocities (see figs. 5.11 and 5.12).

Both SEDs are capable of producing the observed k-ratios along a line of constant $\log(U)$=-0.4 stretching from $\log(n_H)$=5.0, $\log(R)$=19.5 to $\log(n_H)$=10, $\log(R)$=17.0. This suggests that when kinematics are included in the models, the *precise* shape of the illuminating SED has little effect on these ratios. However, since both SEDs were produced to match the observed emission of a single object, this does not rule out the possibility that *FHIL* ratios will be affected by the large differences in overall SED shape between different AGN.

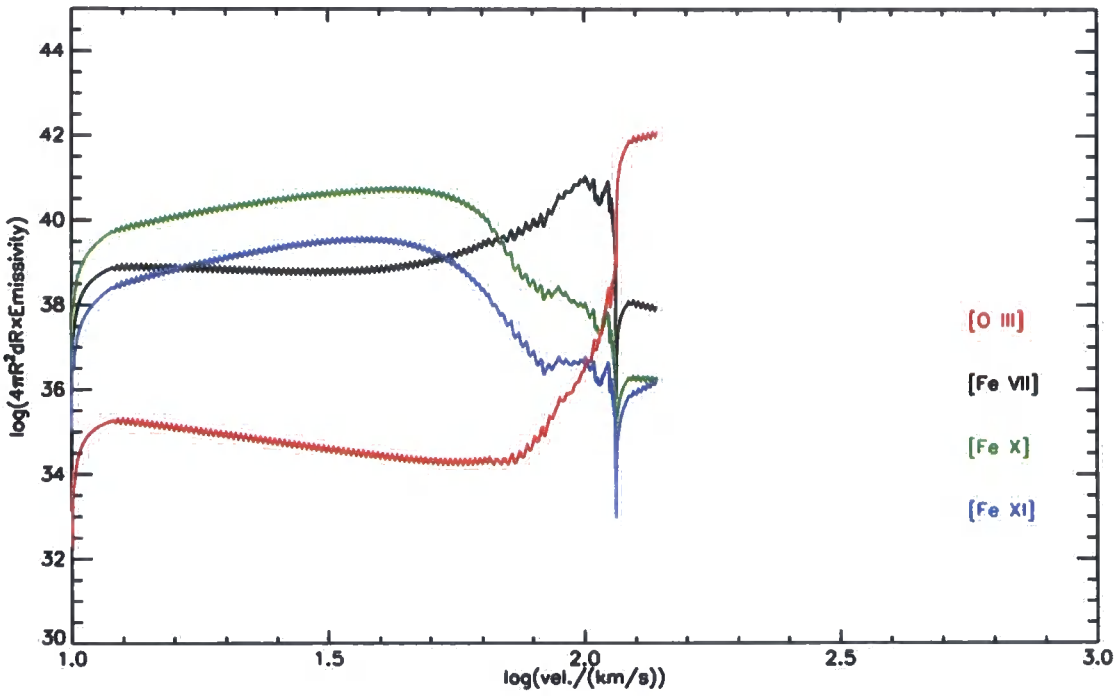

Figure 5.11: Emission line luminosity as a function of gas velocity for a cloud at $R = 10^{19}$ cm with $n_H = 10^6$ cm^{-3} illuminated by SED-X. The overproduction of [Fe X] and [Fe XI] at low velocities implies that in this model the gas *cannot* be undergoing acceleration at this R and n_H.

Neither SED is capable of (radiatively) driving the emitting clouds to the observed blueshifts of the *FHILs* in the regions of the parameter space where these lines are most strongly produced. Even the higher velocities produced by the increased EUV flux of SED-X are at least a factor of 2 below the observed [Fe X] and [Fe VII] blueshifts in these regions.

Although contour plots are a useful way of exploring the parameter space for regions of interest, they only give a representation of the final results from Cloudy and may conceal important details of the models. In figure 5.11 we show how the *FHIL* luminosities vary as a function of velocity through an emitting cloud at R=10^{19} cm and n_H=10^6 cm^{-3}. This shows that if a cloud were to undergo acceleration from 10 km s^{-1} in this region of the parameter space, the [Fe X] line would be overproduced relative to the [Fe VII] line at low velocities and the [Fe VII] line would be observed at *higher* blueshifts. This is the opposite of what is seen in the spectra (see Fig. 5.9) and implies that the *FHIL* emitting clouds *cannot* be undergoing acceleration in the regions of the parameter space at which these lines are produced at the observed k-ratios. Instead, they must have obtained the observed velocities prior to reaching these regions.

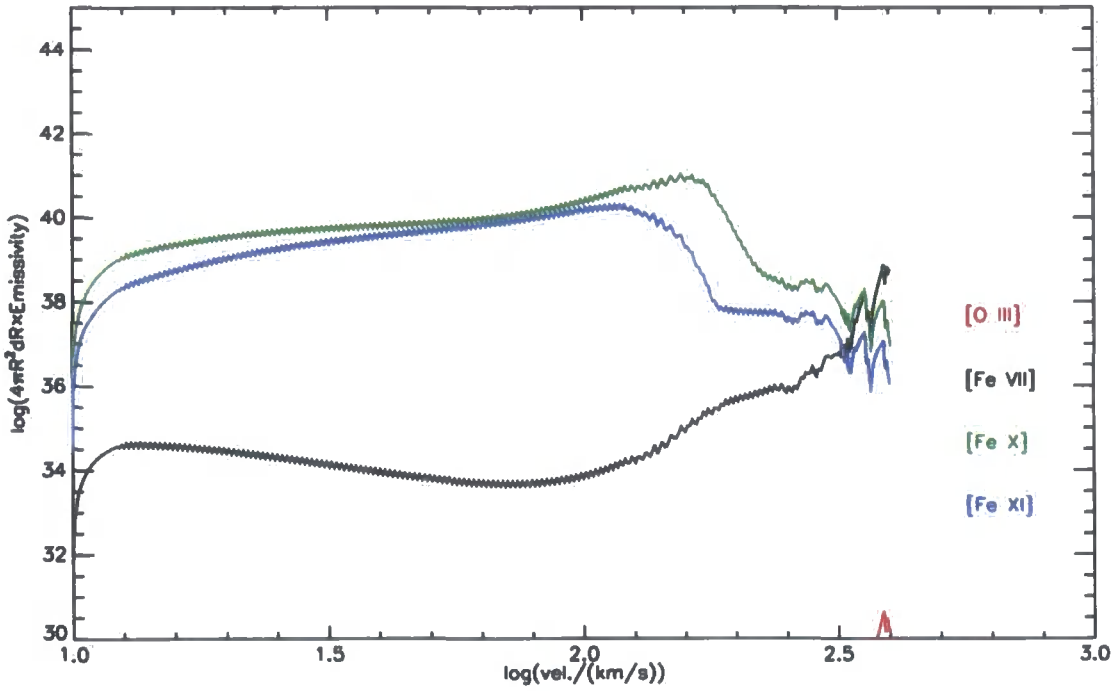

Figure 5.12: Same as Fig. 5.11 but for clouds at $R = 10^{17}$ and $n_H = 3 \times 10^9$. Although the [Fe X] and [Fe XI] emission peaks at higher velocities in this region of the parameter space, these speeds are still lower than observed. Furthermore a significant proportion of the line flux is produced at lower velocities.

Although regions of the parameter space with $\log(U) = -0.4$ can explain the low blueshift [Fe X] component and the observed k-ratios it cannot account for the higher velocity [Fe X] component. A possible source of this emission are regions of the parameter space with $\log(U)$=0.1 (see Fig. 5.12). Here, the luminosity of the [Fe X] and [Fe XI] lines peak at velocity $v \sim$160 km s^{-1}. However, the integrated [Fe X] and [Fe XI] flux at $v \leq$110 km s^{-1} correspond to 35% and 70% (respectively) of the total line flux. We would therefore expect to see significant flux at low blueshifts even at this higher value of the ionisation parameter where the clouds are most strongly driven.

In placing limits on the [O III] flux (relative to [Fe VII] flux) we are able to derive upper limits on the thickness, ΔR, of the clouds before this line dominates the emission (see §5.3.1). We find that in the case of the [Fe VII] emitting clouds with $\log(U)$=-0.4, ΔR is typically $< 1\%$ of R corresponding to a column density $N_H \sim 10^{22}$cm^{-2}. Prior to reaching this depth, the [Fe VII] emissivity falls by two orders of magnitude over the final 70% of the cloud. This implies that no *FHIL* flux is lost in introducing the [O

III]/[Fe VII] >6.2 limit. In the case of the clouds described in the previous paragraph (with log(U)=0.1) the models are stopped when the column density limit (= 10^{24} cm^{-2}) is reached. As expected, the emissivity of the [Fe X] line drops significantly before this depth is reached.

5.3.3 Discussion

The results from the models described here indicate that both SEDs are capable of producing the observed k-ratios along a narrow range of ionisation parameters. This implies that the blue wing of the [O III] emission in *Ark 564* can be produced by the same clouds as are responsible for the [Fe VII] line and the low velocity [Fe X] and [Fe XI] components. However, these models also indicate that neither SED is capable of producing sufficient radiative driving in the regions of the parameter space where the *FHILs* are most strongly produced. This suggests an alternative launching mechanism is required to accelerate the *FHIL* emitting clouds to the velocities seen in these lines' blueshifts.

In the previous section we showed that the region responsible for the observed k-ratios (log(U)=-0.4) could not be undergoing significant acceleration, otherwise we would see the effects of this acceleration in the profiles of the lines; there would be more [Fe X] flux than [Fe VII] flux at low blueshifts. These clouds must be accelerated to the observed velocities *prior* to emitting *FHILs*. A possible location for this accelerating process is in the previously mentioned [Fe X] and [Fe XI] emitting clouds with log(U)=0.1. However, despite the [Fe X] and [Fe XI] flux peaking at $v \simeq 160$ km s^{-1} in these clouds, a significant proportion of the total line flux will, again, be produced at lower velocities during the acceleration stage. Furthermore, our models suggest that even at these increased ionisation parameters, radiative driving still has difficulty in producing the observed line blueshifts ($\sim$500 km s^{-1} in the case of [Fe X] and [Fe XI]).

Our results indicate that *potential FHIL* emitting clouds undergo acceleration to the observed velocities prior to these lines being produced. Post acceleration, they then move outwards to larger radii until the conditions are suitable for *FHIL* production.

In Fig. 5.10 we show that radiative driving is capable of producing velocities of the order of those seen in the blueshifts of the [Fe X] and [Fe XI] lines at $10^{17} < R/\mathrm{cm} < 10^{18}$, corresponding to 0.03 – 0.3 pc. Our models show that, in the case of SED-X, dust grains would assume temperatures within the the range of 2500K to 800K; i.e. the same temperature a blackbody would have at these radii (the emitting gas at these radii is at a much higher temperature than this as the radiative processes taking place in gas

clouds means it cannot be described as a blackbody). These blackbody temperatures straddles at which dust undergoes sublimation (~1500K, Barvainis 1987) and is therefore the region of the inner edge of the putative dusty torus.

Our models are therefore consistent with the concept that an outflow is launched from the inner wall of this torus by evaporation due to the large flux of high energy photons (see later). From there it is driven outwards by radiative driving. As we have modelled *Ark 564* to be super-Eddington, this wind is quickly accelerated to the terminal velocity defined by its launch radius. The profiles of the lines indicate that if these winds are launched from $0.03 - 0.3$ pc, they will undergo little retardation before the ionisation parameter of the gas falls to a level suitable for the production of the [Fe X] and [Fe XI] lines.

Our model facilitates the production of [Fe X] and [Fe XI] in clouds across the large range of modelled densities yet showing similar kinematics as the terminal velocity of the clouds launched from these radii is largely independent of the density of the cloud.

A launch from the torus in *Ark 564* can therefore account for the high velocity component of the [Fe X] and [Fe XI] lines. Without modification, however, this model would also produce the [Fe VII] lines at these same terminal velocities. To account for the lower velocity shift of the [Fe VII] line (and the corresponding components in [Fe X] and [Fe XI]) a retardation force must be incorporated into this model at $R \gtrsim 3 \times 10^{18} - 10^{19}$ cm ($1 - 3$ pc). Beyond this radius our models indicate that more than 80% of the [Fe VII] flux, 37% of the [Fe X] flux and 35% of the [Fe XI] flux is produced, which is in rough agreement with the observed ratios given in Table 5.3.

A possible clue to a source of deceleration is that the stellar bulge of the host galaxy becomes an important factor at these radii. A full investigation of the influences of the host galaxy on the *FHIL* emitting region is beyond the scope of this thesis. However, an estimate of the radius at which the stellar bulge becomes important can be determined by assuming a bulge density distribution described by Hernquist (1990), a total bulge mass of $4.6 \times 10^{10} M_{\odot}$ (Bian and Zhao 2003) and an approximate half-light radius for *Ark 564* ~1 kpc (determined from 2MASS K-band images; this is similar in scale to the typical half-light radii for other SBb galaxy bulges found by Kent 1985). This reveals that the gravitational potential of the stellar bulge becomes important (i.e. greater than that potential of black hole) at $R = 0.03$ pc and the gravitational *force* of the bulge dominates the radiative+gravitational force of the black hole/accretion disk at ~10 pc. More generally Davies et al. (2007) showed that there is considerable emission from young stars within

the central few parsecs of an AGN-hosting galaxy. It is thus reasonable to consider that the kinematics of the outer *FHIL* emitting region can be affected by the host galaxy at radii of a few parsecs from the central engine.

A number of studies have suggested that winds could be launched from the inner edge of the torus (e.g. Krolik and Begelman 1986, Krolik and Begelman 1988). Recently, Dorodnitsyn et al. (2008) used hydrodynamic models to show that an outflow with velocities ranging from $\lesssim$500 km s^{-1} to 1000 km s^{-1} can be launched from the inner edge of an X-ray illuminated torus. The results presented here suggest that these same winds produce *FHIL* emission once they reach the optimal ionisation parameter for their production.

5.4 Summary

In this final science chapter we have attempted to use photoionisation models to reproduce the observed features of the *FHILs* discussed in previous chapters. The main results of this work can be summarised as follows:

- The clouds that are capable of producing the strongest *FHILs* are also strong absorbers of the soft X-ray photons. We use this result to deduce that the *FHIL* emitting clouds either do not lie along our line of sight to the continuum, or have a very low covering factor.

- The *FHIL* luminosities are highly sensitive to the shape of the ionising SED emitted by the central engine. A weaker dependence on the shape of the ionising SED is seen in the n_H and R values at which emission of a given line peaks. In particular, the density at which a given *FHIL*'s emission peaks is almost independent of the shape of the ionising SED.

- After summing the *FHIL* luminosities over the full parameter space, we can conclude that modest variations on the SEDs presented here would be capable of producing the full range of *FHIL* ratios measured in the previous chapters (for both type 1 and type 2 AGN).

- The *FHIL* emitting clouds must be accelerated to the velocities measured in the blueshifts of the lines *prior* to their emission of these lines. There is insufficient radiative driving in the regions where the *FHILs* are most strongly produced for these clouds to be accelerated from rest to the observed velocities at these radii.

- The observed blueshifts of the *FHILs* in *Ark 564* suggest they are accelerated from a region that straddles the dust sublimation radius of this AGN. This therefore supports the concept that *potential FHIL* emitting clouds are launched from the inner edge of the dusty torus. These clouds then flow outward and emit *FHILs* as they pass through the radii at which these lines are most efficiently produced.

- The lower velocity shift of the [Fe VII] line relative to that of the [Fe X] line (in the spectrum of *Ark 564*) suggests that the *FHIL* emitting clouds undergo decelaration between the radii at which these lines are most efficiently produced. We speculate that this retardation could be the result of the increasing influence of the host galaxy's stellar bulge at the larger of these radii.

Chapter 6 | *Concluding Remarks*

In this thesis we have seen how the study of emission line regions, in particular those that produce *FHILs*, can be tackled using three different techniques. In the first science chapter, we saw how we can utilise high S/N spectra to precisely determine the kinematics of these various regions, whereas in chapters 3 and 4 we utilised the vast resource of spectra in the *SDSS* database to determine general trends associated with the *FHILs* (and other prominent emission lines). Finally, in chapter 5 we used the power of photoionisation codes to help interpret the results from the previous chapters in terms of physical models for the *FHIL* emitting region. In this concluding chapter, we provide a summary of the major findings and suggest possible lines of future work that may lead on from the studies presented here.

6.1 An overview of presented work

6.1.1 Properties of the BLR of NLS1s and other AGN

One of our main findings from the first chapter was that to fit the profiles of the permitted lines of the NLS1s in our sample requires the inclusion of a third, broad component with FWHM typical of the permitted lines of BLS1s. We interpret this as evidence that the broad line regions of NLS1s contain some clouds that are travelling at velocities similar to those of the BLRs of typical BLS1s, but that the emission from these clouds is suppressed in NLS1s. We propose that this suppression may be the result of the destruction of this very broad line region by an energetic wind, or the the increased high energy photon flux that is commonly observed in NLS1s.

6.1.2 The *FHIL* emitting line regions of AGN

The majority of the work in this thesis has focussed on the the study of the *FHILs* emitted by AGN. The results presented here significantly enhance our knowledge and understanding of the regions in which these lines are produced.

Our study of the *FHIL* strengths and profiles using new data of a small sample of 10 AGN described in chapter 2 revealed that the [Fe VII] and [Fe X] lines are produced in two kinematically distinct regions, neither of which have similar kinematics to either the traditional BLRs of NLRs. In general we found that the *FHILs* were blueshifted with respect to the systematic velocity of the lower ionisation lines; this was interpreted as evidence that the *FHIL* emitting region is in outflow. We also noted that, despite the [Fe X]:[Fe VII] ratio within this sample having a relatively constant value of ~2, the [Fe XI]:[Fe X] ratio spanned a much larger range of values (between 0.03 to 1.0). We suggest that this is evidence that the [Fe XI]:[Fe X] ratio is sensitive to the shape of the (obscured) extreme UV to soft X-ray portion of the SED, and that it may be possible to use this ratio as a diagnostic for the obscured extreme UV to soft X-ray continuum of AGN.

The work described in chapter 2 was extended using the much larger samples defined in chapters 3 and 4. Comparison of the *FHIL* luminosities from both types 1 and 2 AGN revealed a strong systematic weakening of the [Fe X] line relative to [Fe VII] in the latter type. We rely on the standard model of AGN structure (BLR, Torus, NLR etc.) to determine that (on average) 50% of the [Fe X] line is produced within a region of the AGN that is obscured from our view by the dusty torus in type 2 AGN. This independently supports the results of earlier studies which indicate that a proportion of the [Fe VII] line region is obscured from our view in type 2 AGN. In our final science chapter, based on the results of the photoionisation models, we found that we could recreate the full range of [Fe VII]:[Fe X] ratios observed in both type 1 and type 2 AGN by using various different shapes of ionising SED and relative orientations of the obscuring torus.

Throughout this thesis we have made extensive use of the profiles of the *FHILs* to determine both the kinematics of the regions in which these lines are produced and further constrain the relative locations of these regions. In particular, we note that the FWHM of these lines suggest that the [Fe VII] line is produced in a region that is kinematically distinct from the [Fe X] and [Fe XI] emitting regions. However, although the results derived from the relative strengths of the [Fe X] and [Fe VII] lines (see above) suggest that the former is produced in a region closer to the central engine than the latter, there is no trend for the [Fe X] line to be broader than the [Fe VII] line. This is significant as it indicates that the broadening of these lines is not dominated by Keplarian motion under the gravitational influence of the central supermassive black hole, otherwise we would expect the [Fe X] line to be more broadened (on average) than the [Fe VII] line.

6.1.3 Outflows from AGN

All our results derived from the velocity shifts of the *FHILs* indicate that the region responsible for their emission is, in general, outflowing from the central source (based on the assumptions laid out in our introduction). Although there is evidence of the more highly ionised *FHILs* ([Fe X] and [Fe XI]) being more strongly blueshifted in a small number of individual objects (see chapter 2), when these shifts are measured in the general *FHIL* emitting population, there is no evidence that the [Fe X] line is necessarily more blueshifted than the [Fe VII] line. There is, however, some evidence in the larger samples that the [Fe XI] line is more strongly blueshifted than the other, lower ionisation iron lines. We interpret this in terms of a continuous flow of material travelling outwards from the inner regions at almost constant velocity. The various *FHILs* are produced as this outflowing gas passes through the radii at which line is emitted most efficiently. This model is similar to that proposed in the second half of chapter 5 to explain the detailed line profiles of the *FHILs* and [O III]λ5007 line in the NLS1 AGN, *Ark 564*. The results of the photoionisation models described in that chapter support the concept that this outflow is launched from the inner edge of the dusty torus and, in the case of *Ark 564*, is decelerated by the growing influence of the stellar bulge at the radii at which [Fe VII] is most strongly produced. This hints that the *FHIL* emitting region spans an important transition point in AGN; from deep within the central void of the obscuring torus to across the point at which the gravitational influence of the host galaxy becomes important.

6.2 Future work

The work described in this chapter has the potential to lead onto a number of different studies, which are summarised below:

- There are a number of objects in each of the samples derived in chapters 3 and 4 with *FHILs* that are particularly strong or have interesting profiles (e.g. strong asymmetries, particularly broad, etc.). It is hoped that these will form the basis of a dedicated observation programme to obtain further information on the kinematics and location of the *FHIL* emitting region (possibly via the use of integral field spectroscopy). With this in mind, we hope to publish our lists of *FHIL* emitting objects derived from the *SDSS* database as a resource future studies of the *FHIL* emitting

region.

- We have recently obtained access to near infrared (NIR) integral field spectra of the local type 1 AGN *NGC 3783* with the intention of studying the spatial and kinematic properties of the NIR *FHIL* emitting regions in this object. We expect that this will give us a much clearer impression of spatial extent of the *FHIL* emitting regions in type 1 AGN.

- The work described here has mainly focussed on the study of the *FHILs* emitted at optical wavelengths. A logical development of the work presented here would therefore be the study of *FHILs* emitted in the near infrared portion of the spectrum to determine if measurements of these lines corroborate the results described here.

- We hope to search our samples of *FHIL* emitters for evidence for the other [Fe VII] lines in the optical waveband (λ3758, 5720). As the ratios of these (and the λ6087) lines can be used as density and temperature diagnostics, their measurement will provide us with vital further information on the physical properties of the *FHIL* emitting region. For example, Fosbury and Sansom (1983) showed that the relative strengths of the [Fe VII]λ3758,5720 lines could be used to show that the gas responsible for these lines had a temperature that suggested that photoionisation ($\sim$40,000K) rather than shocks ($\gtrsim 10^6$K) were responsible for the production of these *FHILs* in Tololo 0109-383 and III ZW 77. Unfortunately these lines are typically much weaker than the [Fe VII]λ6087 line and have only been measured in a small number of individual cases. Our large sample of *FHIL* emitters enables a systematic search of these lines which could drastically increase the numbers of objects with [Fe VII]λ3758, 5720 measurements.

- As mentioned in our introduction, considerable work has been done on studying the outflows of AGN evident in the blueshifted *absorption* lines present in high spectral resolution UV spectra (see Crenshaw et al. 2003 for a review). Furthermore, some work has been done by Casebeer et al. (2006) in using the broad O VIλ1032 line (emitted in the U.V. part of the spectrum) to determine the intrinsic shape of the emitted AGN SED. It would be interesting to use the data derived from these types of studies with those presented here to determine whether they all point to a consistent physical model of the inner regions of AGN.

- Although our main conclusions are focussed astrophysical processes, the results of

this thesis have been arrived at by the development of robust emission line fitting routines. It is hoped that these routines will be useful in similar lines of study based on the accurate measurement of emission lines in large numbers of spectra (as promised by the next generations of spectral surveys).

Appendix A

Additional plots from Chapter 2

In the following plots of the line profiles, we only show the spectra for the galaxies in which the line is detected and measured. In each panel, the vertical dashed lines show the rest wavelength of the line of interest. Dotted lines reveal where we have removed a blended line to assist component fitting. Colour coding- Red: Full line model, Magenta, Green, Blue: Individual lines components (broadest to narrowest), Orange: Blended component not associated with measured line (e.g. [N II] blended with Hα)

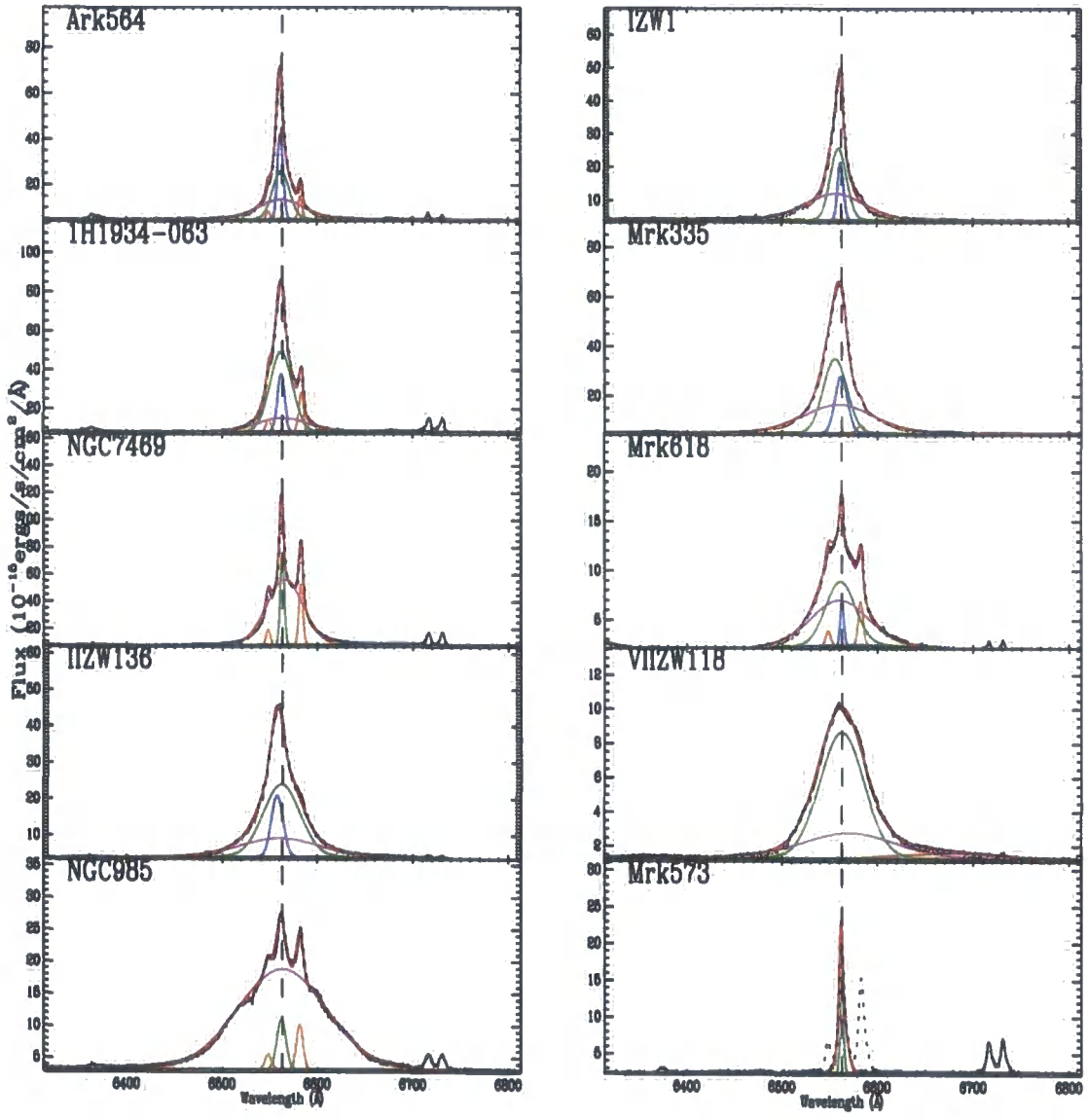

Figure A.1: For the case of Hα, shown here, we have removed the [N II] lines in Mrk573, as described in the text.

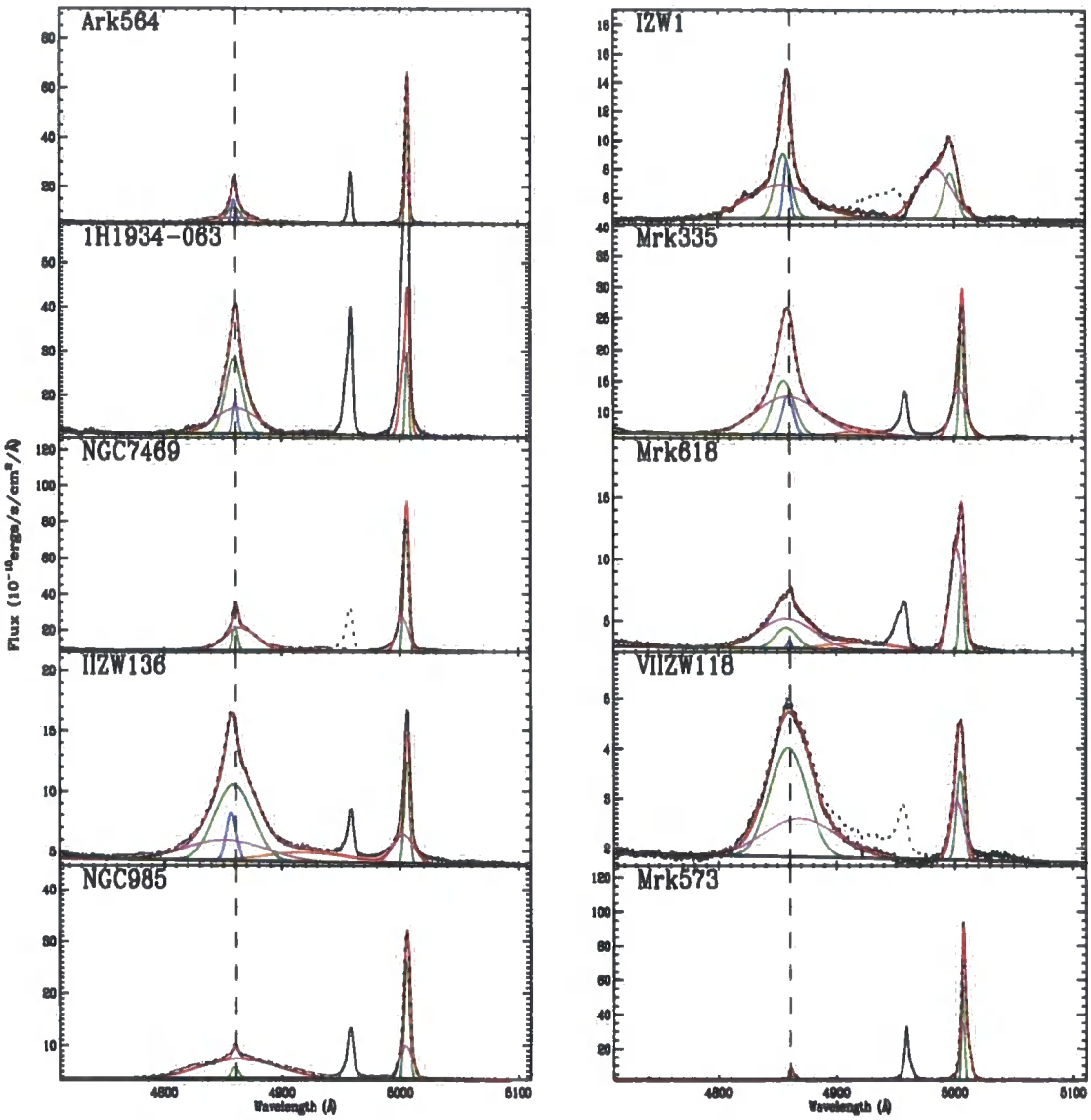

Figure A.2: Hβ & [O III]- Dotted lines show where we have removed the [O III]λ4959 line in order to more accurately fit the Hβ lines. In the case of VIIZW118, we have also removed the He Iλ4922 that forms a strong red shelf in this spectrum.

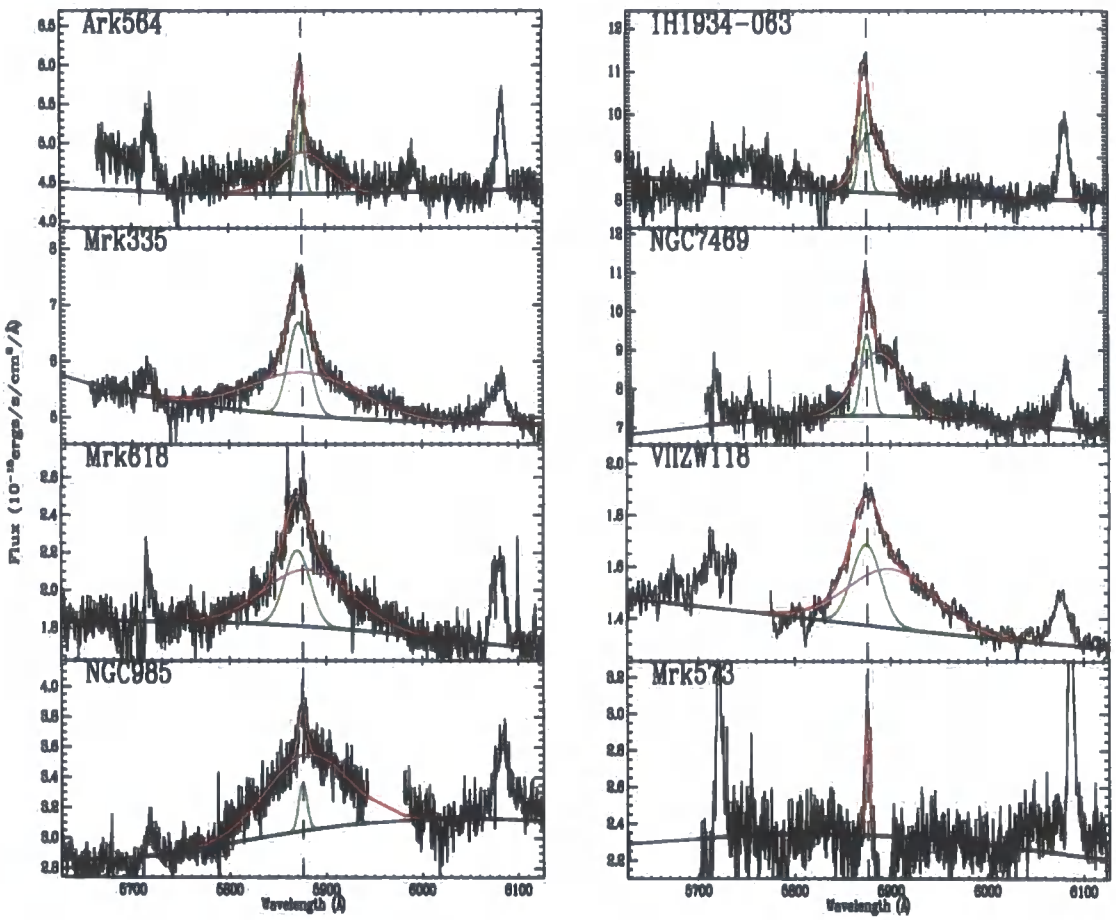

Figure A.3: He Iλ5876- IIZW136 appears to show evidence of a strong He I line, but unfortunately it could not be accurately measured, as its profile is interrupted by a gap introduced by the limited spectral range of each CCD.

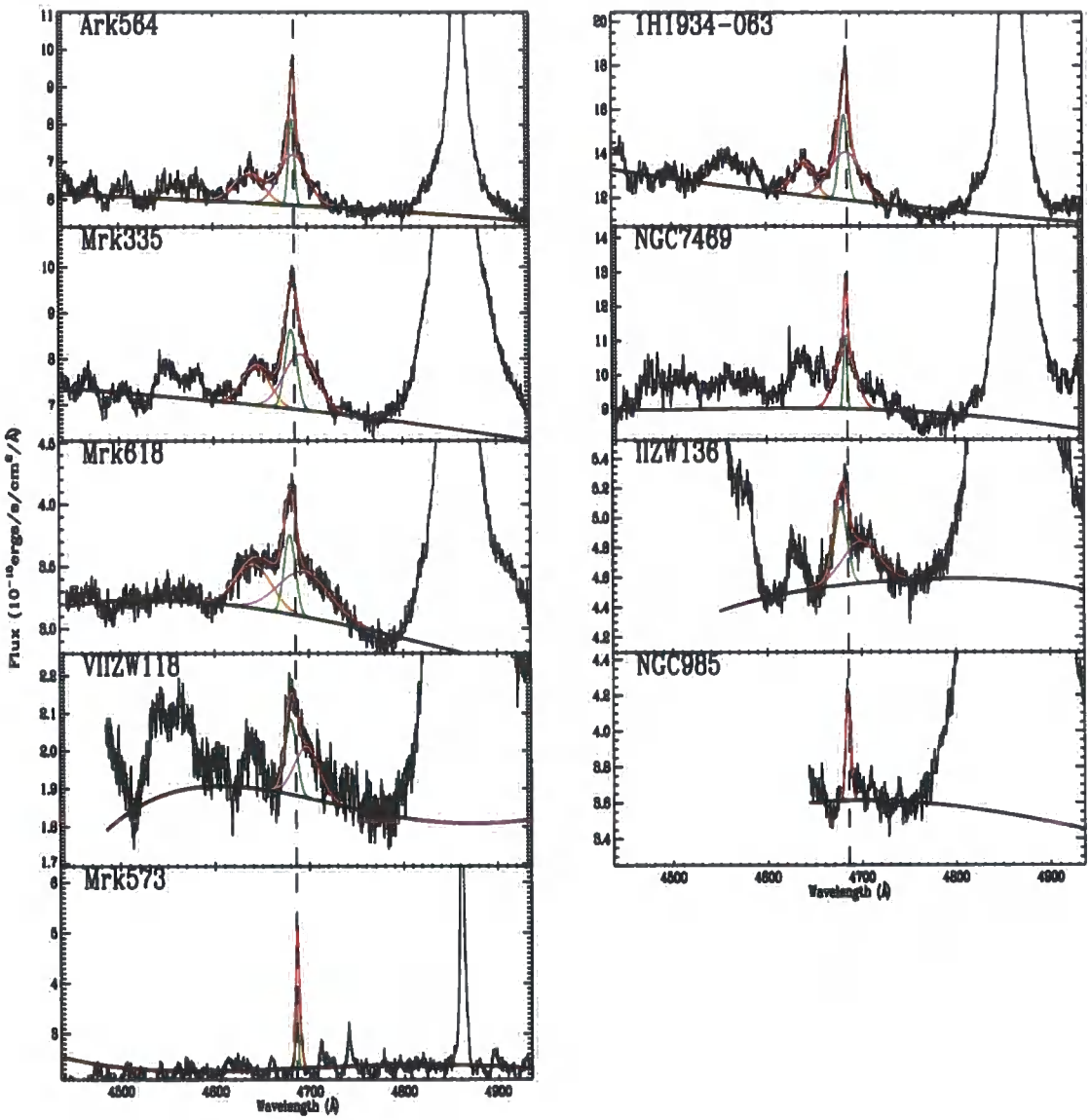

Figure A.4: He IIλ4686- We have deblended this line from the unknown line at ~4670Å, which is clearly a separate feature in a number of our targets (e.g. IIZW136, VIIZW118)

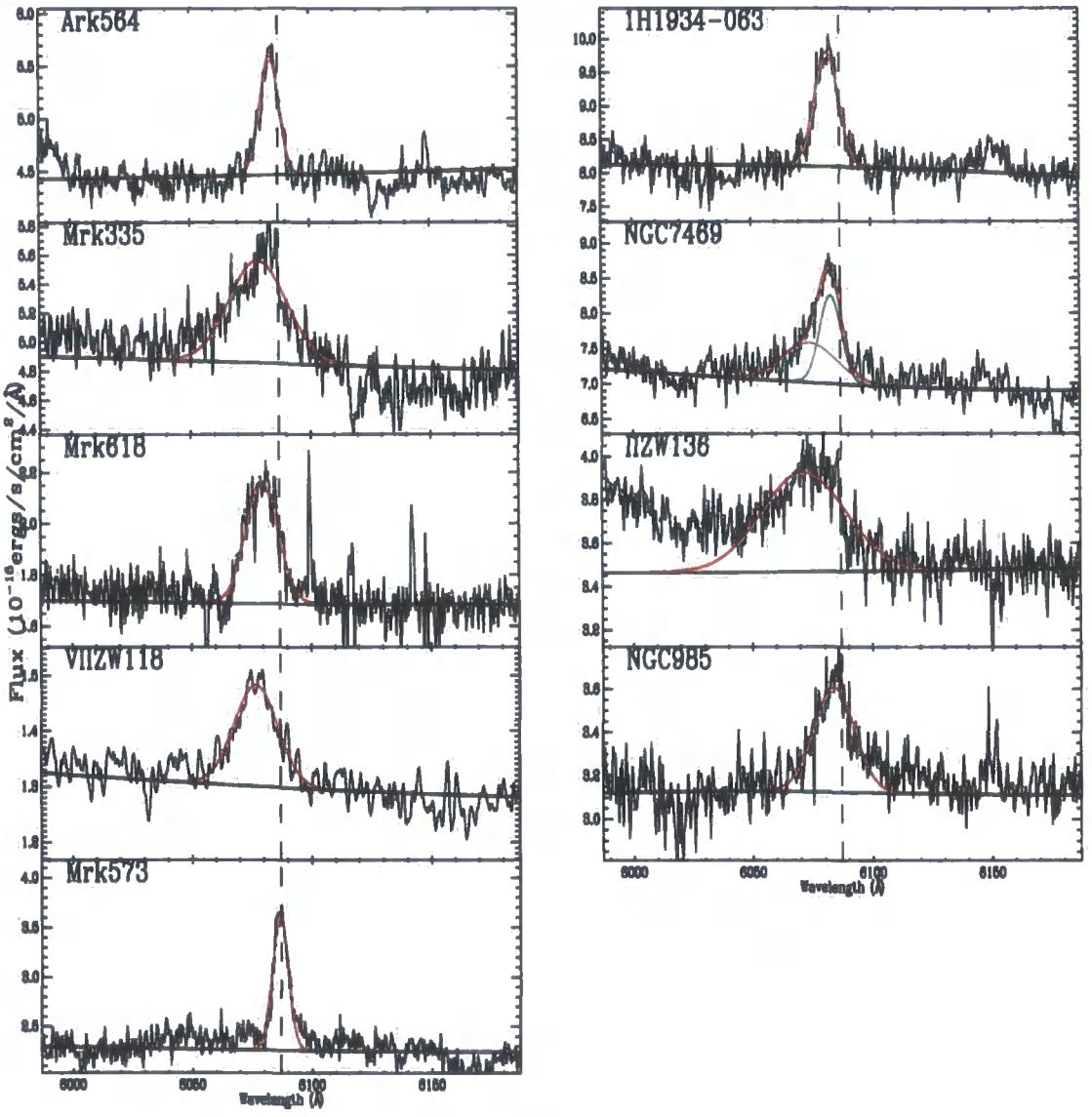

Figure A.5: [Fe VII]λ6087

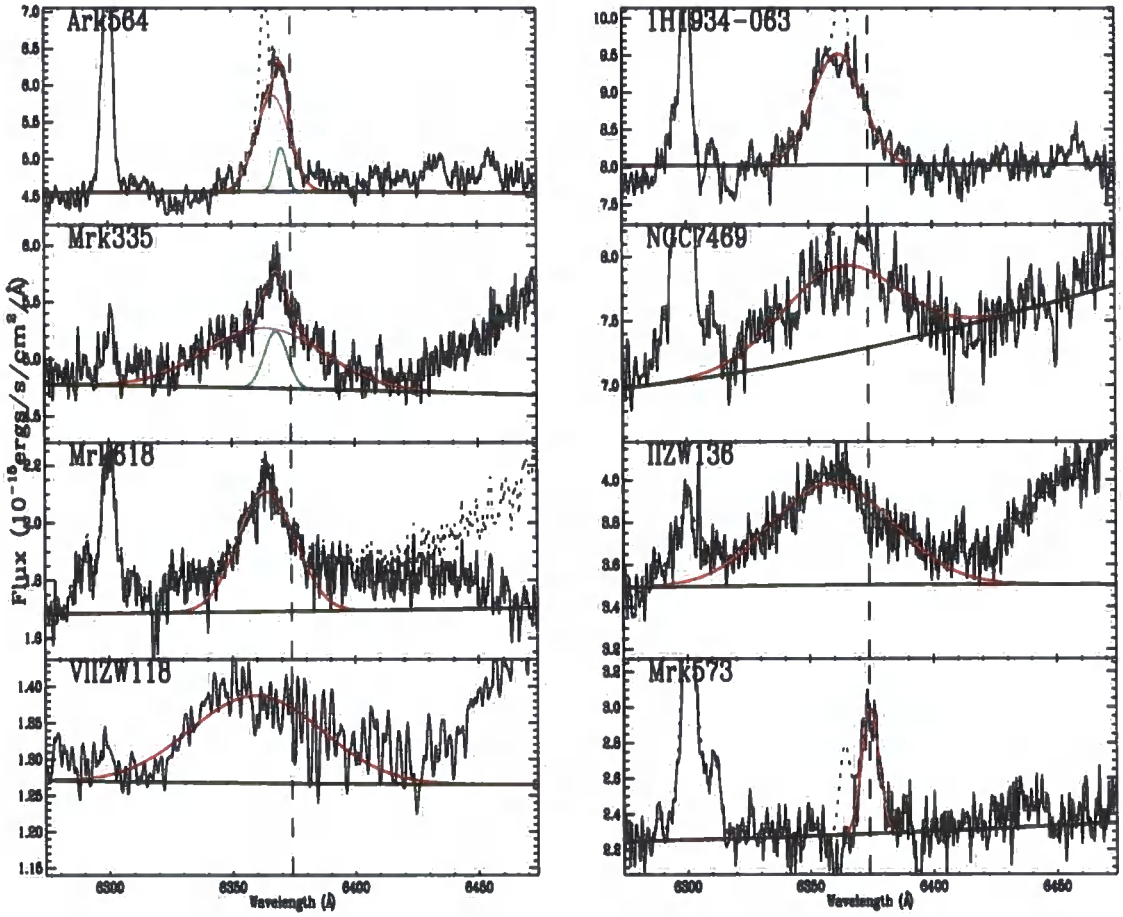

Figure A.6: [Fe X]λ6374- Dotted lines here are used to show where we have removed both the [O I] line that is blended with the [Fe X] line. Redward of some of the [Fe X] lines we have removed the blue wing of the Hα line that contaminated the [Fe X] line in some of the 'broader' NLS1s in our sample.

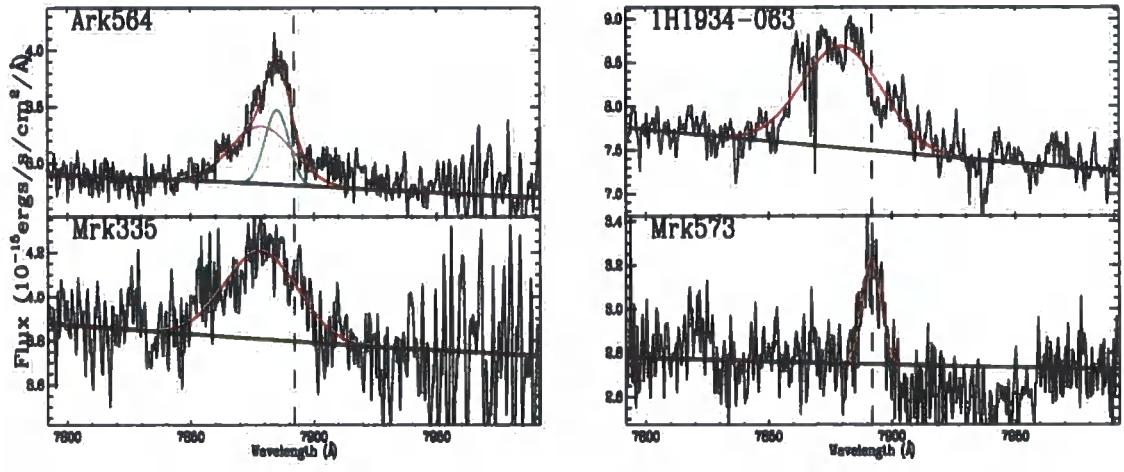

Figure A.7: [Fe XI]λ7892

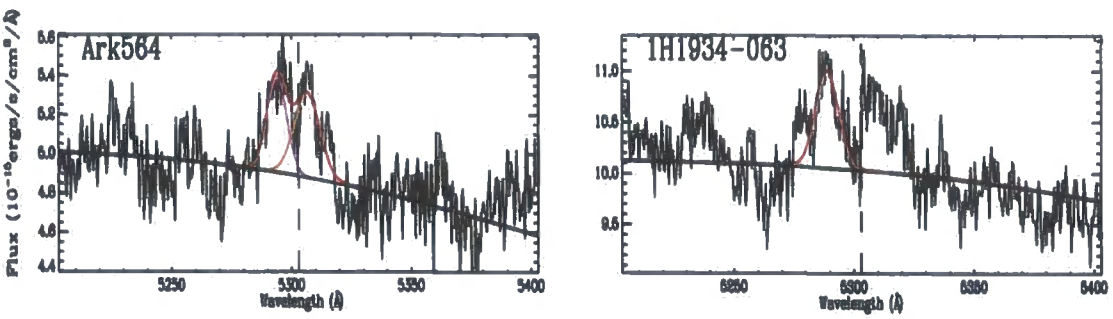

Figure A.8: [Fe XIV]λ5303- For Ark564, we have attempted to deblend this line from the [Ca V] line at 5309Å (shown here in orange).

Bibliography

Y. Almog and H. Netzer. The emission line spectrum of He I. *MNRAS*, 238:57–72, May 1989.

M. Almudena Prieto, O. Marco, and J. Gallimore. Morphology of the coronal-line region in active galactic nuclei*. *MNRAS*, 364:L28–L32, November 2005. doi: 10.1111/j.1745-3933.2005.00099.x.

R. R. J. Antonucci and J. S. Miller. Spectropolarimetry and the nature of NGC 1068. *ApJ*, 297:621–632, October 1985. doi: 10.1086/163559.

I. Appenzeller and R. Oestreicher. High-ionization line profiles of Seyfert galaxies. *AJ*, 95:45–57, January 1988. doi: 10.1086/114611.

J. N. Bahcall, S. Kirhakos, D. H. Saxe, and D. P. Schneider. Hubble Space Telescope Images of a Sample of 20 Nearby Luminous Quasars. *ApJ*, 479:642–+, April 1997. doi: 10.1086/303926.

J. Baldwin, G. Ferland, K. Korista, and D. Verner. Locally Optimally Emitting Clouds and the Origin of Quasar Emission Lines. *ApJL*, 455:L119+, December 1995. doi: 10.1086/309827.

J. A. Baldwin, M. M. Phillips, and R. Terlevich. Classification parameters for the emission-line spectra of extragalactic objects. *PASP*, 93:5–19, February 1981.

A. J. Barth, J. E. Greene, and L. C. Ho. Dwarf Seyfert 1 Nuclei and the Low-Mass End of the M_{BH}-σ Relation. *ApJL*, 619:L151–L154, February 2005. doi: 10.1086/428365.

R. Barvainis. Hot dust and the near-infrared bump in the continuum spectra of quasars and active galactic nuclei. *ApJ*, 320:537–544, September 1987. doi: 10.1086/165571.

W.-H. Bian and Y.-H. Zhao. Black Hole-Bulge Relation for Narrow-Line Objects. *PASJ*, 55:143–148, February 2003.

T. Boller, W. N. Brandt, and H. Fink. Soft X-ray properties of narrow-line Seyfert 1 galaxies. *A&A*, 305:53–+, January 1996.

T. A. Boroson and R. F. Green. The emission-line properties of low-redshift quasi-stellar objects. *ApJS*, 80:109–135, May 1992. doi: 10.1086/191661.

V. Botte, S. Ciroi, P. Rafanelli, and F. Di Mille. Exploring Narrow-Line Seyfert 1 Galaxies through the Physical Properties of Their Hosts. *AJ*, 127:3168–3179, June 2004. doi: 10.1086/420803.

A. H. Bridle and R. A. Perley. Extragalactic Radio Jets. *ARA&A*, 22:319–358, 1984. doi: 10.1146/annurev.aa.22.090184.001535.

J. A. Cardelli, G. C. Clayton, and J. S. Mathis. The relationship between infrared, optical, and ultraviolet extinction. *ApJ*, 345:245–256, October 1989. doi: 10.1086/167900.

D. A. Casebeer, K. M. Leighly, and E. Baron. FUSE Observation of the Narrow-Line Seyfert 1 Galaxy RE 1034+39: Dependence of Broad Emission Line Strengths on the Shape of the Photoionizing Spectrum. *ApJ*, 637:157–182, January 2006. doi: 10.1086/498125.

P. E. Christopoulou, A. J. Holloway, W. Steffen, C. G. Mundell, A. H. C. Thean, C. D. Goudis, J. Meaburn, and A. Pedlar. Evidence for an outflow from the Seyfert galaxy NGC 4051. *MNRAS*, 284:385–394, January 1997.

E. Churazov, M. Brüggen, C. R. Kaiser, H. Böhringer, and W. Forman. Evolution of Buoyant Bubbles in M87. *ApJ*, 554:261–273, June 2001. doi: 10.1086/321357.

S. Collin-Souffrin, J. E. Dyson, J. C. McDowell, and J. J. Perry. The environment of active galactic nuclei. I - A two-component broad emission line model. *MNRAS*, 232:539–550, June 1988.

A. Constantin and J. C. Shields. Ultraviolet and Optical Properties of Narrow-Line Seyfert 1 Galaxies. *PASP*, 115:592–608, May 2003.

D. M. Crenshaw, S. B. Kraemer, and I. M. George. Mass Loss from the Nuclei of Active Galaxies. *ARA&A*, 41:117–167, 2003. doi: 10.1146/annurev.astro.41.082801.100328.

R. I. Davies, F. Mueller Sánchez, R. Genzel, L. J. Tacconi, E. K. S. Hicks, S. Friedrich, and A. Sternberg. A Close Look at Star Formation around Active Galactic Nuclei. *ApJ*, 671: 1388–1412, December 2007. doi: 10.1086/523032.

M. M. De Robertis and D. E. Osterbrock. An analysis of the narrow-line profiles in high ionization Seyfert galaxies. *ApJ*, 286:171–185, November 1984. doi: 10.1086/162585.

G. de Vaucouleurs and A. de Vaucouleurs. An improbable coincidence in NGC 985 - A ring galaxy with a Seyfert nucleus. *ApJL*, 197:L1–L4, April 1975. doi: 10.1086/181762.

G. C. Dewangan, R. E. Griffiths, S. Dasgupta, and A. R. Rao. An Investigation of the Origin of Soft X-Ray Excess Emission from Ark 564 and Mrk 1044. *ApJ*, 671:1284–1296, December 2007. doi: 10.1086/523683.

M. Dietrich, D. M. Crenshaw, and S. B. Kraemer. Probing the Ionizing Continuum of Narrow-Line Seyfert 1 Galaxies. I. Observational Results. *ApJ*, 623:700–720, April 2005. doi: 10.1086/429121.

A. Dorodnitsyn, T. Kallman, and D. Proga. An Axisymmetric, Hydrodynamical Model for the Torus Wind in Active Galactic Nuclei. *ApJL*, 675:L5–L8, March 2008. doi: 10.1086/529374.

M. Elvis, T. Maccacaro, A. S. Wilson, M. J. Ward, M. V. Penston, R. A. E. Fosbury, and G. C. Perola. Seyfert galaxies as X-ray sources. *MNRAS*, 183:129–157, April 1978.

U. Erkens, I. Appenzeller, and S. Wagner. The nature of the FHIL winds from AGN. *A&A*, 323:707–716, July 1997.

E. A. Fath. Bulletin Number 149 - The spectra of some spiral nebulae and globular star clusters. *Lick Observatory Bulletin*, 5:71–77, 1908.

J. W. Ferguson, K. T. Korista, and G. J. Ferland. Physical Conditions of the Coronal Line Region in Seyfert Galaxies. *ApJS*, 110:287–+, June 1997. doi: 10.1086/312998.

G. J. Ferland, B. M. Peterson, K. Horne, W. F. Welsh, and S. N. Nahar. Anisotropic line emission and the geometry of the broad-line region in active galactic nuclei. *ApJ*, 387: 95–108, March 1992. doi: 10.1086/171063.

G. J. Ferland, K. T. Korista, D. A. Verner, J. W. Ferguson, J. B. Kingdon, and E. M. Verner. CLOUDY 90: Numerical Simulation of Plasmas and Their Spectra. *PASP*, 110:761–778, July 1998.

L. Ferrarese and D. Merritt. A Fundamental Relation between Supermassive Black Holes and Their Host Galaxies. *ApJL*, 539:L9–L12, August 2000. doi: 10.1086/312838.

R. A. E. Fosbury and A. E. Sansom. The high-ionization optical spectrum of the Seyfert galaxy Tololo 0109-383. *MNRAS*, 204:1231–1236, September 1983.

J. F. Gallimore, S. A. Baum, and C. P. O'Dea. A direct image of the obscuring disk surrounding an active galactic nucleus. 388:852–854, August 1997.

K. Gebhardt, R. Bender, G. Bower, A. Dressler, S. M. Faber, A. V. Filippenko, R. Green, C. Grillmair, L. C. Ho, J. Kormendy, T. R. Lauer, J. Magorrian, J. Pinkney, D. Richstone, and S. Tremaine. A Relationship between Nuclear Black Hole Mass and Galaxy Velocity Dispersion. *ApJL*, 539:L13–L16, August 2000a. doi: 10.1086/312840.

K. Gebhardt, J. Kormendy, L. C. Ho, R. Bender, G. Bower, A. Dressler, S. M. Faber, A. V. Filippenko, R. Green, C. Grillmair, T. R. Lauer, J. Magorrian, J. Pinkney, D. Richstone, and S. Tremaine. Black Hole Mass Estimates from Reverberation Mapping and from Spatially Resolved Kinematics. *ApJL*, 543:L5–L8, November 2000b. doi: 10.1086/318174.

K. Gebhardt, T. R. Lauer, J. Kormendy, J. Pinkney, G. A. Bower, R. Green, T. Gull, J. B. Hutchings, M. E. Kaiser, C. H. Nelson, D. Richstone, and D. Weistrop. M33: A Galaxy with No Supermassive Black Hole. *AJ*, 122:2469–2476, November 2001. doi: 10.1086/323481.

A. C. Gonçalves, P. Véron, and M.-P. Véron-Cetty. The emission-line spectrum of KUG 1031+398 and the intermediate line region. *A&A*, 341:662–666, January 1999.

R. W. Goodrich. Spectropolarimetry of 'narrow-line' Seyfert 1 galaxies. *ApJ*, 342:224–234, July 1989. doi: 10.1086/167586.

S. A. Grandi. /Fe XI/ lambda 7892 emission in Seyfert galaxies. *ApJ*, 221:501–506, April 1978. doi: 10.1086/156051.

P. Gröningsson, C. Fransson, P. Lundqvist, T. Nymark, N. Lundqvist, R. Chevalier, B. Leibundgut, and J. Spyromilio. Coronal emission from the shocked circumstellar ring of SN 1987A. *A&A*, 456:581–589, September 2006. doi: 10.1051/0004-6361:20065325.

D. Grupe, K. Beuermann, K. Reinsch, H.-C. Thomas, and H. H. Fink. Optical Properties of Soft X-ray Selected Bright New ROSAT AGN. In T. Courvoisier and A. Blecha, editors, *Multi-Wavelength Continuum Emission of AGN*, volume 159 of *IAU Symposium*, pages 508–+, 1994.

T. M. Heckman, G. K. Miley, W. J. M. van Breugel, and H. R. Butcher. Emission-line profiles and kinematics of the narrow-line region in Seyfert and radio galaxies. *ApJ*, 247:403–418, July 1981. doi: 10.1086/159050.

L. Hernquist. An analytical model for spherical galaxies and bulges. *ApJ*, 356:359–364, June 1990. doi: 10.1086/168845.

V. L. Jacobs, J. Davis, P. C. Kepple, and M. Blaha. The influence of autoionization accompanied by excitation on dielectronic recombination and ionization equilibrium. *ApJ*, 211:605–616, January 1977. doi: 10.1086/154970.

S. M. Kent. CCD surface photometry of field Galaxies. II - Bulge/disk decompositions. *ApJS*, 59:115–159, October 1985. doi: 10.1086/191066.

L. J. Kewley, M. A. Dopita, R. S. Sutherland, C. A. Heisler, and J. Trevena. Theoretical Modeling of Starburst Galaxies. *ApJ*, 556:121–140, July 2001. doi: 10.1086/321545.

E. Y. Khachikian and D. W. Weedman. An atlas of Seyfert galaxies. *ApJ*, 192:581–589, September 1974.

S. Komossa and N. Bade. The giant X-ray outbursts in NGC 5905 and IC 3599:() hfill Follow-up observations and outburst scenarios. *A&A*, 343:775–787, March 1999.

K. T. Korista and M. R. Goad. What the Optical Recombination Lines Can Tell Us about the Broad-Line Regions of Active Galactic Nuclei. *ApJ*, 606:749–762, May 2004. doi: 10.1086/383193.

J. Kormendy and D. Richstone. Inward Bound—The Search For Supermassive Black Holes In Galactic Nuclei. *ARA&A*, 33:581–+, 1995. doi: 10.1146/annurev.aa.33.090195.003053.

A. T. Koski. Spectrophotometry of Seyfert 2 galaxies and narrow-line radio galaxies. *ApJ*, 223:56–73, July 1978. doi: 10.1086/156235.

J. H. Krolik and M. C. Begelman. An X-ray heated wind in NGC 1068. *ApJL*, 308:L55–L58, September 1986. doi: 10.1086/184743.

J. H. Krolik and M. C. Begelman. Molecular tori in Seyfert galaxies - Feeding the monster and hiding it. *ApJ*, 329:702–711, June 1988. doi: 10.1086/166414.

D. Kunth and W. L. W. Sargent. Spectrophotometry of six Seyfert galaxies from the Zwicky lists. *A&A*, 76:50–59, June 1979.

H. Landt, M. C. Bentz, M. J. Ward, M. Elvis, B. M. Peterson, K. T. Korista, and M. Karovska. The Near-Infrared Broad Emission Line Region of Active Galactic Nuclei. I. The Observations. *ApJS*, 174:282–312, February 2008. doi: 10.1086/522373.

K. M. Leighly. HST STIS Ultraviolet Spectral Evidence for Outflows in Extreme Narrow-Line Seyfert 1 Galaxies. In B. M. Peterson, R. W. Pogge, and R. S. Polidan, editors, *Probing the Physics of Active Galactic Nuclei*, volume 224 of *Astronomical Society of the Pacific Conference Series*, pages 293–+, 2001.

K. M. Leighly and J. R. Moore. Hubble Space Telescope STIS Ultraviolet Spectral Evidence of Outflow in Extreme Narrow-Line Seyfert 1 Galaxies. I. Data and Analysis. *ApJ*, 611:107–124, August 2004. doi: 10.1086/422088.

I. J. Lewis, R. D. Cannon, K. Taylor, K. Glazebrook, J. A. Bailey, I. K. Baldry, J. R. Barton, T. J. Bridges, G. B. Dalton, T. J. Farrell, P. M. Gray, A. Lankshear, C. McCowage, I. R. Parry, R. M. Sharples, K. Shortridge, G. A. Smith, J. Stevenson, J. O. Straede, L. G. Waller, J. D. Whittard, J. K. Wilcox, and K. C. Willis. The Anglo-Australian Observatory 2dF facility. *MNRAS*, 333:279–299, June 2002. doi: 10.1046/j.1365-8711.2002.05333.x.

K. O. Mason, E. M. Puchnarewicz, and L. R. Jones. The origin of the optical emission lines in the narrow-line Seyfert 1 galaxy RE J1034+396. *MNRAS*, 283:L26–L29, November 1996.

S. Mathur, J. Kuraszkiewicz, and B. Czerny. Evolution of active galaxies: black-hole mass-bulge relations for narrow line objects. *New Astronomy*, 6:321–329, August 2001. doi: 10.1016/S1384-1076(01)00058-6.

I. M. McHardy, E. Koerding, C. Knigge, P. Uttley, and R. P. Fender. Active galactic nuclei as scaled-up Galactic black holes. 444:730–732, December 2006. doi: 10.1038/nature05389.

S. L. Morris and M. J. Ward. Spectrophotometry of active galaxies. I - The observations. *MNRAS*, 230:639–669, February 1988.

S. L. Morris and M. J. Ward. Optically thin gas in the broad-line region of Seyfert galaxies. *ApJ*, 340:713–728, May 1989. doi: 10.1086/167432.

F. Mueller Sánchez, R. I. Davies, F. Eisenhauer, L. J. Tacconi, R. Genzel, and A. Sternberg. SINFONI adaptive optics integral field spectroscopy of the Circinus Galaxy. *A&A*, 454:481–492, August 2006. doi: 10.1051/0004-6361:20054387.

J. R. Mullaney and M. J. Ward. Optical emission-line properties of narrow-line Seyfert 1 galaxies and comparison active galactic nuclei. *MNRAS*, 385:53–74, March 2008. doi: 10.1111/j.1365-2966.2007.12777.x.

T. Murayama and Y. Taniguchi. Where is the Coronal Line Region in Active Galactic Nuclei? *ApJL*, 497:L9+, April 1998. doi: 10.1086/311264.

T. Nagao, Y. Taniguchi, and T. Murayama. High-Ionization Nudear Emission-Line Region of Seyfert Galaxies. *AJ*, 119:2605–2628, June 2000. doi: 10.1086/301411.

T. Nagao, K. S. Kawabata, T. Murayama, Y. Ohyama, Y. Taniguchi, R Sumiya, and S. S. Sasaki. Detection of the Polarized Broad Emission Line in the Seyfert 2 Galaxy Markarian 573. *AJ*, 128:109–114, July 2004. doi: 10.1086/421740.

J. B. Oke and W. L. W. Sargent. The Nucleus of the Seyfert Galaxy NGC 4151. *ApJ*, 151: 807–+, March 1968.

D. E. Osterbrock. The spectrum of III ZW 77 - an unusual, high-ionization Seyfert 1 galaxy. *ApJ*, 246:696–707, June 1981. doi: 10.1086/158966.

D. E. Osterbrock. The nature and structure of active galactic nuclei. *ApJ*, 404:551–562, February 1993. doi: 10.1086/172307.

D. E. Osterbrock and G. J. Ferland. *Astrophysics of gaseous nebulae and active galactic nuclei* Astrophysics of gaseous nebulae and active galactic nuclei, 2nd. ed. by D.E. Osterbrock and G.J. Ferland. Sausalito, CA: University Science Books, 2006, 2006.

D. E. Osterbrock and R. W. Pogge. The spectra of narrow-line Seyfert 1 galaxies. *ApJ*, 297:166–176, October 1985. doi: 10.1086/163513.

D. E. Osterbrock, J. P. Fulbright, A. R. Martel, M. J. Keane, S. C. Trager, and G. Basri. Night-Sky High-Resolution Spectral Atlas of OH and O2 Emission Lines for Echelle Spectrograph Wavelength Calibration. *PASP*, 108:277–+, March 1996.

M. V. Penston, R. A. E. Fosbury, A. Boksenberg, M. J. Ward, and A. S. Wilson. The Fe(9+) region in active galactic nuclei. *MNRAS*, 208:347–364, May 1984.

B. M. Peterson. Overview of Reverberation Mapping: Progress and Problems. In P. M. Gondhalekar, K. Horne, and B. M. Peterson, editors, *Reverberation Mapping of the Broad-Line Region in Active Galactic Nuclei*, volume 69 of *Astronomical Society of the Pacific Conference Series*, pages 1–+, 1994.

B. M. Peterson. *An Introduction to Active Galactic Nuclei.* An introduction to active galactic nuclei, Publisher: Cambridge, New York Cambridge University Press, 1997 Physical description xvi, 238 p. ISBN 0521473489, February 1997.

B. M. Peterson, M. C. Bentz, L.-B. Desroches, A. V. Filippenko, L. C. Ho, S. Kaspi, A. Laor, D. Maoz, E. C. Moran, R. W. Pogge, and A. C. Quillen. Multiwavelength Monitoring of the Dwarf Seyfert 1 Galaxy NGC 4395. I. A Reverberation-based Measurement of the Black Hole Mass. *ApJ*, 632:799–808, October 2005. doi: 10.1086/444494.

R. W. Pogge. Narrow-line Seyfert 1s: 15 years later. *New Astronomy Review*, 44:381–385, September 2000.

D. Porquet, A.-M. Dumont, S. Collin, and M. Mouchet. The Warm Absorber constrained by the coronal lines in Seyfert 1 galaxies. *A&A*, 341:58–68, January 1999.

K. A. Pounds, R. S. Warwick, J. L. Culhane, and P. A. J. de Korte. The soft X-ray spectrum of NGC 4151. *MNRAS*, 218:685–694, February 1986.

K. A. Pounds, C. Done, and J. P. Osborne. RE 1034+39: a high-state Seyfert galaxy? *MNRAS*, 277:L5–L10, November 1995.

E. M. Puchnarewicz, K. O. Mason, F. A. Cordova, J. Kartje, A. A. Brabduardi, E. M. Puchnarewicz, K. O. Mason, F. A. Cordova, J. Kartje, G. Branduardi-Raymont, J. P. D. Mittaz, P. G. Murdin, and J. Allington-Smith. Optical properties of active galaxies with ultra-soft X-ray spectra. *MNRAS*, 256:589–623, June 1992.

M. J. Rees. Tidal disruption of stars by black holes of 10 to the 6th-10 to the 8th solar masses in nearby galaxies. 333:523–528, June 1988. doi: 10.1038/333523a0.

J. N. Reeves, G. Wynn, P. T. O'Brien, and K. A. Pounds. Extreme X-ray variability in the luminous quasar PDS 456. *MNRAS*, 336:L56–L60, November 2002. doi: 10.1046/j.1365-8711.2002.06038.x.

J. N. Reeves, P. T. O'Brien, and M. J. Ward. A Massive X-Ray Outflow from the Quasar PDS 456. *ApJL*, 593:L65–L68, August 2003. doi: 10.1086/378218.

R. Riffel, A. Rodríguez-Ardila, and M. G. Pastoriza. A 0.8-24 μm spectral atlas of active galactic nuclei. *A&A*, 457:61–70, October 2006. doi: 10.1051/0004-6361:20065291.

R. A. Riffel, T. Storchi-Bergmann, C. Winge, P. J. McGregor, T. Beck, and H. Schmitt. Mapping of molecular gas inflow towards the Seyfert nucleus of NGC4051 using Gemini NIFS. *MNRAS*, 385:1129–1142, April 2008. doi: 10.1111/j.1365-2966.2008.12936.x.

A. Rodríguez-Ardila, S. M. Viegas, M. G. Pastoriza, and L. Prato. Near-Infrared Coronal Lines in Narrow-Line Seyfert 1 Galaxies. *ApJ*, 579:214–226, November 2002. doi: 10.1086/342840.

A. Rodríguez-Ardila, M. A. Prieto, S. Viegas, and R. Gruenwald. Outflows of Very Ionized Gas in the Centers of Seyfert Galaxies: Kinematics and Physical Conditions. *ApJ*, 653:1098–1114, December 2006. doi: 10.1086/508864.

Romano et al. The Spectral Energy Distribution and Emission-Line Properties of the Narrow-Line Seyfert 1 Galaxy Arakelian 564. *ApJ*, 602:635–647, February 2004. doi: 10.1086/381235.

R. J. Rudy, S. Mazuk, R. C. Puetter, and F. Hamann. The 1 Micron Fe II Lines of the Seyfert Galaxy I Zw 1. *ApJ*, 539:166–171, August 2000. doi: 10.1086/309222.

C. J. Ryan, M. M. De Robertis, S. Virani, A. Laor, and P. C. Dawson. The Central Engines of Narrow-Line Seyfert 1 Galaxies. *ApJ*, 654:799–813, January 2007. doi: 10.1086/509313.

E. E. Salpeter. Accretion of Interstellar Matter by Massive Objects. *ApJ*, 140:796–800, August 1964. doi: 10.1086/147973.

D. J. Schlegel, D. P. Finkbeiner, and M. Davis. Maps of Dust Infrared Emission for Use in Estimation of Reddening and Cosmic Microwave Background Radiation Foregrounds. *ApJ*, 500:525–+, June 1998. doi: 10.1086/305772.

M. Schmidt. 3C 273 : A Star-Like Object with Large Red-Shift. 197:1040–+, March 1963. doi: 10.1038/1971040a0.

C. K. Seyfert. Nuclear Emission in Spiral Nebulae. *ApJ*, 97:28–+, January 1943.

J. M. Shuder. On the physical conditions and the velocity fields in Seyfert 1 galaxies and QSOs. *ApJ*, 259:48–54, August 1982. doi: 10.1086/160145.

S. A. Stephens. Optical spectroscopy of X-ray-selected active galactic nuclei. *AJ*, 97:10–35, January 1989. doi: 10.1086/114953.

C. Stoughton *et al.* Sloan Digital Sky Survey: Early Data Release. *AJ*, 123:485–548, January 2002. doi: 10.1086/324741.

C. Tadhunter. An introduction to active galactic nuclei: Classification and unification. *New Astronomy Review*, 52:227–239, August 2008. doi: 10.1016/j.newar.2008.06004.

C. Tadhunter and Z. Tsvetanov. Anisotropic ionizing radiation in NGC5252. 341:422–424, October 1989. doi: 10.1038/341422a0.

R. C. Telfer, W. Zheng, G. A. Kriss, and A. F. Davidsen. The Rest-Frame Extreme-Ultraviolet Spectral Properties of Quasi-stellar Objects. *ApJ*, 565:773–785, February 2002. doi: 10.1086/324689.

R. Terlevich and J. Melnick. Warmers - The missing link between Starburst and Seyfert galaxies. *MNRAS*, 213:841–856, April 1985.

M. Türler, S. Paltani, T. J.-L. Courvoisier, M. F. Aller, H. D. Aller, A. Blecha, P. Bouchet, M. Lainela, I. M. McHardy, E. I. Robson, J. A. Stevens, H. Teräsranta, M. Tornikoski, M.-H. Ulrich, E. B. Waltman, W. Wamsteker, and M. C. H. Wright. 30 years of multi-wavelength observations of 3C 273. *A&ASS*, 134:89–101, January 1999.

T. J. Turner and K. A. Pounds. Variability of the soft excess in the Seyfert I galaxy MKN 335. *MNRAS*, 232:463–471, May 1988.

S. Veilleux, P. L. Shopbell, and S. T. Miller. The Biconical Outflow in the Seyfert Galaxy NGC 2992. *AJ*, 121:198–209, January 2001. doi: 10.1086/318046.

P. Véron, A. C. Gonçalves, and M.-P. Véron-Cetty. The "red shelf" of the Hβ line in the Seyfert 1 galaxies RXS J01177+3637 and HS 0328+05. *A&A*, 384:826–833, March 2002. doi: 10.1051/0004-6361:20020072.

M.-P. Véron-Cetty, P. Véron, and A. C. Gonçalves. A spectrophotometric atlas of Narrow-Line Seyfert 1 galaxies. *A&A*, 372:730–754, June 2001. doi: 10.1051/0004-6361:20010489.

M.-P. Véron-Cetty, M. Joly, and P. Véron. The unusual emission line spectrum of I Zw 1. *A&A*, 417:515–525, April 2004. doi: 10.1051/0004-6361:20035714.

W. Voges, B. Aschenbach, T. Boller, H. Bräuninger, U. Briel, W. Burkert, K. Dennerl, J. Englhauser, R. Gruber, F. Haberl, G. Hartner, G. Hasinger, M. Kürster, E. Pfeffermann, W. Pietsch, P. Predehl, C. Rosso, J. H. M. M. Schmitt, J. Trümper, and H. U. Zimmermann. The ROSAT all-sky survey bright source catalogue. *A&A*, 349:389–405, September 1999.

M. Ward and S. Morris. The reddening and high-excitation emission lines in NGC 3783. *MNRAS*, 207:867–881, April 1984.

D. W. Weedman. Seyfert galaxies, quasars and redshifts. *QJRAS*, 17:227–262, September 1976.

M. Whittle. Virial and jet-induced velocities in Seyfert Galaxies. II - Galaxy rotation as virial parameter. III - Galaxy luminosity as virial parameter. *ApJ*, 387:109–137, March 1992. doi: 10.1086/171064.

A. S. Wilson, J. A. Braatz, T. M. Heckman, J. H. Krolik, and G. K. Miley. The Ionization Cones in the Seyfert Galaxy NGC 5728. *ApJL*, 419:L61+, December 1993. doi: 10.1086/187137.

D. Xu, S. Komossa, H. Zhou, T. Wang, and J. Wei. The Narrow-Line Region of Narrow-Line and Broad-Line Type 1 Active Galactic Nuclei. I. A Zone of Avoidance in Density. *ApJ*, 670:60–73, November 2007. doi: 10.1086/521697.